The aqueous corrosion of borosilicate glasses studied in operando by in situ fluid-cell Raman spectroscopy

Dissertation

zur

Erlangung des Doktorgrades (Dr. rer. nat.)

der

Mathematisch-Naturwissenschaftlichen Fakultät

der

Rheinischen Friedrich-Wilhelms-Universität Bonn

vorgelegt von

Moritz Bernd Karl Fritzsche

aus

Wittlich

Bonn, 2022

Angefertigt mit der Genehmigung der Mathematisch-Naturwissenschaftlichen Fakultät der Rheinischen Friedrich-Wilhelms-Universität Bonn

- *Redaktionell korrigierte, genehmigte Fassung –*

1. Gutachter: Prof. Dr. Thorsten Geisler-Wierwille

2. Gutachterin: Prof. Dr. Boriana Mihailova

Tag der Promotion: 06.10.2022

Erscheinungsjahr: 2023

Preface

The results presented in this doctoral thesis were already presented in parts at various conference presentations, including poster presentations and talks. In addition, to the corresponding conference contributions, co-authored research articles, and theses that are related to the PhD project and produced during the project, are listed in the following:

Related co-authored articles:

Geisler, T., Dohmen, L., Lenting, C., Fritzsche, M.B.K. (2019) Real-time in situ observations of reaction and transport phenomena during silicate glass corrosion by fluid-cell Raman spectroscopy. *Nature Materials*, 18, 342-348. (https://doi.org/10.1038/s41563-019-0293-8)

Müller, G., Fritzsche, M.B.K., Dohmen, L., Geisler, T. (2022) Feedbacks and non-linearity of silicate glass alteration in hyperalkaline solution studied by in operando fluid-cell Raman spectroscopy. *Geochimica et Cosmochimica Acta*, 329, 1-21. (https://doi.org/10.1016/j.gca.2022.05.013)

Conference Abstracts (oral presentations):

Fritzsche, M.B.K., Lenting, C., Geisler, T. (2020) Untersuchung des Korrosionsverhaltens von Borosilikatgläsern in wässrigen Lösungen mit Hilfe der *In situ*-Flüssigzellen-Raman Spektroskopie. Conference Abstract, *Deutsche Mineralogische Gesellschaft,* Workshop.

Fritzsche, M.B.K, Lenting, C., Lönartz, M.I., Geisler, T. (2020) Formation of surface alteration layers under flow through conditions observed in operando by fluid-cell Raman spectroscopy. Conference Abstract, *GLASS MEETING 2020 ON WEB,* virtual conference.

Conference Abstracts (poster presentations):

Fritzsche, M.B.K., Lenting, C., Dohmen, L., Geisler, T. (2019) The interface-coupled dissolution-reprecipitation model of aqueous glass corrosion considering a solution boundary layer and interdiffusion. Conference Abstract, *25th International Congress on Glass*, conference.

Fritzsche, M.B.K., Lenting, C., Lönartz, M.I., Geisler, T. (2020) Glass corrosion under stagnant and flow conditions observed in operando by fluid-cell Raman spectroscopy. Conference Abstract, *Deutsche Mineralogische Gesellschaft,* virtual poster session.

Supervised Bachelor and Master theses:

Falkenberg, H. (2020) Untersuchung der Sol-Gel-Synthese von Silica-Gelen mit Hilfe der Ramanspektroskopie. Unpubl. *Bachelor thesis*, University of Bonn, pp. 44.

Egger, F. (2021) Quantitative determination of water transport through porous alteration layers of borosilicate glasses in situ and in real time using fluid-cell Raman spectroscopy. Unpubl. *Master thesis*, University of Bonn, pp. 45.

Abstract

The properties of glasses depend mainly on their chemical composition. Because of the large variety of compositions, the glass properties are also very variable, which opens up a multitude of possible applications. Borosilicate glasses are widely used because of their relatively high chemical resistance compared to other materials or commercially available soda-lime glass. However, glasses are metastable materials and are prone to corrode in contact with aqueous solutions or under high humidity. Although this effect is often not noticeable in most everyday applications, good chemical resistance of glasses is crucial for many special applications. Borosilicate glasses are used, for example, to immobilize high-level radioactive waste from the reprocessing of spent nuclear fuel, or as container glass for storing chemicals or medicines. There, as in many other technical applications, high corrosion resistance is important in order to prevent deterioration of the material properties or contamination of the container contents. In order to enable the optimal choice of glass for applications, to achieve a high chemical resistance when developing new glasses, or to reliably simulate long-term resistance, it is essential to understand the corrosion mechanism, the basic reactions, the transport processes, and possible feedback. Even though glass corrosion has been studied for many decades, there is still no consensus on a general glass corrosion mechanism that can explain all observations, especially the formation of complex chemical and structural patterns in the corrosion products. In the scientific community of nuclear waste glass, two different models are widespread, even if they have also merged into one another for certain conditions recently. Rather classical models assume, except hyperalkaline condition, a modification of the glass at the surface occurs due to an interdiffusion based leaching process, followed by a *in situ* restructuring of the glass structure without complete glass network dissolution. This model is challenged by the interface-coupled dissolution-precipitation (ICDP) model, which also applies to mineral replacement reactions and can be adopted for glass alteration. In the model, a complete stoichiometric glass dissolution is supposed, which is spatially and temporally coupled to the precipitation of amorphous silica and/or crystalline corrosion products, which gradually replace the glass. As soon as a corrosion rim has started to form, its properties, which, in turn, depend on environmental conditions, the glass composition and the stage of corrosion, have a decisive influence on the further course of the corrosion process.

At the beginning, the most important observations, reactions and transport processes and their dependencies, which are responsible for feedback effects that are known so far, are presented and discussed in relation to the ICDP mechanism. This represents the theoretical basis for a numerical simulation of the corrosion process. *In situ* fluid-cell Raman spectroscopy was used to experimentally investigate the corrosion mechanism and also the feedback between glass dissolution, precipitation of corrosion products, and the chemical transport between the reaction

front and the surrounding solution. With this new and innovative application of Raman spectroscopy, it is possible to study glass corrosion *in situ* with a micrometer resolution and in real-time, i.e., *in operando*. The method was further developed in this study to conduct long-term experiments. For the first time the corrosion of a reference glass (International Simple Glass, ISG) could be measured *in operando* in regular measurement sessions for relatively long time of corrosion, i.e., several months. The formation of crystalline corrosion products (kosnarite) at the outer sample surface and structural ripening of a silica-based amorphous surface alteration layer (am-SAL) over time can be observed. Furthermore, under strongly alkaline conditions in a carbonate-rich solution, the precipitation of zeolites was observed *in operando*, which was confirmed by supplementary *post mortem* analyses. The experimental results support the established assumption that the ICDP mechanism dominates at high pH values.

In addition, variation of the chemical composition and the structure of the am-SAL reflect the dynamics of the hydrochemical conditions at the reaction front, where the corrosion product precipitates. A third case study was performed, where the fluid-cell was combined with a syringe pump to simulate flow-through conditions. This is the first time that corrosion of a ternary sodium borosilicate glass (TBG) has been investigated *in operando* as a function of the solution exchange rate and composition using fluid-cell Raman spectroscopy. It should be emphasized that the formation of several layers of structurally different am-SALs were observed. This experimental observation supports the assumption that multiple corrosion layers observed in many altered glasses are the result of a self-organizing pattern formation process, i.e., not just a result of cooling and/or drying-induced shrinkage. So far, only the ICDP model has provided an explanation for these patterns. To further verify the model, a one-dimensional numerical reaction-transport model that considers the basic reactions of an ICDP mechanism was set up by using finite volume methods. Its spatial resolution was deliberately adapted to the resolution of *in situ* Raman spectroscopy. The first results have shown that the proposed model is promising for simulating glass corrosion based on an ICDP process, even if some assumed model parameters have not yet been empirically validated. However, the simulation results reported here should be considered as a first approach that needs to be further developed in future. The combination of experimental and numerical methods used in this study allows the results from both to be compared in order to iteratively further develop both approaches.

Zusammenfassung

Die Eigenschaften des Werkstoffs Glas hängen vor allem von der chemischen Zusammensetzung ab, welche aufgrund der großen Zusammensetzungsvielfalt sehr variabel sind und eine Vielzahl von Anwendungsmöglichkeiten eröffnet. Borosilikatgläser sind insbesondere wegen ihrer relativ hohen chemischen Beständigkeit, verglichen mit anderen Werkstoffen oder handelsüblichem Kalk-Natron-Glas, weit verbreitet. Allerdings sind Gläser metastabile Materialien und anfällig für Korrosion in Kontakt mit wässrigen Lösungen oder Wasserdampf. Auch wenn dieser Effekt sich in den meisten Alltagsanwendungen häufig nicht bemerkbar macht, ist eine gute chemische Beständigkeit von Gläsern für viele Spezialanwendungen entscheidend. Borosilikatgläser werden beispielsweise zur Immobilisierung von hochradioaktiven Abfällen aus der Wiederaufbereitung von Brennelementen, oder als Behälterglas zur Lagerung von Chemikalien oder Medikamenten verwendet. Dort, wie auch in vielen weiteren technischen Anwendungsfällen, ist eine hohe Korrosionsbeständigkeit wichtig, um eine Verschlechterung der Materialeigenschaften oder Verunreinigung von Behälterinhalten zu verhindern. Um eine optimale Glasauswahl für Anwendungen zu treffen, bei der Entwicklung von neuen Gläsern direkt eine hohe chemische Beständigkeit zu erreichen oder die Langzeitbeständigkeit belastbar zu simulieren, ist das Verständnis über den Korrosionsmechanismus, die zugrundeliegenden Reaktionen, die Transportprozesse sowie mögliche Rückkopplungen unerlässlich.

Auch wenn Glaskorrosion bereits seit vielen Jahrzehnten untersucht wird, gibt es bisher keinen Konsens über einen allgemeingültigen Glaskorrosionsmechanismus, der alle Beobachtungen, insbesondere die Entstehung von komplexen chemischen und strukturellen Mustern in den Korrosionsprodukten, erklären kann. In der wissenschaftlichen Gemeinschaft der nuklearen Abfallgläser sind vor allem zwei unterschiedliche Modelle verbreitet, welche zuweilen in Teilen auch ineinander übergegangen sind. Viele eher klassische Modelle nehmen an, sofern kein stark alkalisches Milieu vorliegt, dass die Veränderung des Glases an der Oberfläche als Auslaugungsprozess durch Interdiffusion stattfindet, gefolgt von einer Umstrukturierung der Glasstruktur, ohne diese vollständig aufzulösen. Dem gegenüber steht das grenzflächengekoppelte Lösungs-Fällungs-Modell (*interface-coupled dissolution-precipitation*, ICDP), welches ebenfalls für Mineralverdrängungsreaktionen gilt und auf Glasalteration übertragbar ist. Dabei wird von einer vollständigen stöchiometrischen Glasauflösung ausgegangen, welche räumlich und zeitlich an die Präzipitation von Korrosionsprodukten gekoppelt ist und so das Glas allmählich verdrängt. Sobald die Entstehung eines Korrosionssaums aus amorpher Kieselerde und/oder kristallinen Phasen begonnen hat, beeinflussen seine Eigenschaften, welche wiederrum von Umweltbedingungen, der Glaszusammensetzung, und dem Korrosionsstadium abhängen, die weitere Korrosion entscheidend. Zu Beginn der Arbeit werden

die bedeutendsten Beobachtungen und die nach aktuellem Kenntnisstand wesentlichen Reaktionen, Prozesse und deren Abhängigkeiten, welche für Rückkopplungseffekte verantwortlich sind, in Bezug zum ICDP-Mechanismus dargelegt und diskutiert, der auch die Basis für eine numerische Simulation des Korrosionsprozessen darstellt.

Um den Korrosionsmechanismus und auch die Rückkopplungen zwischen Glasauflösung, Präzipitation von Korrosionssäumen sowie dem Transport von Stoffen zwischen Reaktionsfront und der Umgebungslösung im Kontakt mit der Probe experimentell zu untersuchen, wurde die *in situ*-Flüssigzellen-Ramanspektroskopie angewendet, welche insbesondere für Langzeitexperimente weiterentwickelt wurde. Mit dieser neuen und innovativen Anwendung der Ramanspektroskopie ist es möglich, die Glaskorrosion *in situ* mit einer Mikrometerauflösung und in Echtzeit, *in operando,* zu untersuchen. Dadurch konnte erstmals die Korrosion von einem Referenzglas (*International Simple Glass*, ISG) *in operando* in regelmäßigen Messsequenzen über relativ lange Zeiträume von mehreren Monaten und dabei die Entstehung von kristallinen Korrosionsprodukten (Kosnarite) an der Oberfläche der in saurer Lösung korrodierten ISG-Probe und eine strukturelle Reifung eines Korrosionssaumes, der primär aus amorphem Kieselgel basiert, mit der Zeit beobachtet werden. Unter stark alkalischen Bedingungen in einer Carbonat-reichen Lösung konnte des Weiteren die Präzipitation von Zeolithen *in operando* beobachtet werden, was durch ergänzende *post mortem*-Analysen bestätigt wurde. Die experimentellen Ergebnisse unterstützen die etablierte Annahme, dass bei hohen pH-Werten der ICDP-Mechanismus dominiert. Zudem reflektiert die Variation der chemischen Zusammensetzung und Struktur des Korrosionssaums, dass die hydrochemischen Bedingungen an der Reaktionsfront, wo das Korrosionsprodukt präzipitiert, dynamisch sein müssen.

Für eine dritte Fallstudie wurde die Fluidzelle erstmals mit einer Spritzenpumpe kombiniert, um Durchflussbedingungen zu simulieren. Damit wurde die Korrosion eines ternären Natrium-Borosilikatglases (TBG) erstmals *in operando* in Abhängigkeit von der Lösungsaustauschrate und -zusammensetzung untersucht. Dabei ist hervorzuheben, dass die Entstehung mehrerer Lagen aus strukturell unterschiedlicher, amorpher Kieselerde erstmals in Echtzeit beobachtet werden konnte. Diese experimentelle Beobachtung stützt die Annahme, dass die in vielen alterierten Gläsern beobachteten mehrlagigen Korrosionssäume Ergebnis eines selbstorganisierenden Musterbildungsprozesses darstellen und nicht durch Abkühlung und/oder durch Trocknung induzierte Schrumpfungseffekte entstanden sind. Bislang liefert nur das ICDP-Modell eine Erklärung für deren Entstehung.

Um das Modell durch eine numerische Simulation zu überprüfen, wurde ein eindimensionales numerisches Reaktions-Transport-Modell mit der *Finite Volumen*-Methode entwickelt, das auf dem ICDP-Mechanismus basiert. Die räumliche Auflösung des *Finite Volumen*-Modells wurde bewusst an die Auflösung der *In situ*-Ramanspektroskopie angepasst. So ist es möglich, die

Ergebnisse aus den Experimenten und den numerischen Simulationen direkt miteinander zu vergleichen und beide Ansätze iterativ weiterzuentwickeln. Die ersten Ergebnisse haben gezeigt, dass der Modellansatz vielversprechend zur Simulation der Glaskorrosion auf Basis eines ICDP-Prozesses ist; auch wenn einige angenommene Modellparameter bislang noch nicht empirisch validiert sind. Durch den Fokus dieser Arbeit auf die experimentelle Untersuchung des Mechanismus und der Weiterentwicklung der Analysemethoden ist die numerische Simulation als erster Ansatz zu verstehen, auf dem zukünftig ein erweitertes numerisches Korrosionsmodell aufgebaut werden kann.

Contents

1

Introduction and objectives of this study

Silicate glasses are used frequently in daily life and various technical applications because of their high chemical flexibility, ease of production, and durability compared to other solid materials [12]. The well-established production of glasses and the possibility to incorporate a wide variety of radionuclides are reasons for being the favored matrix material for the immobilization of high-level radioactive waste (HLW) [1,3–7]. This property is important when looking at the long list of radioisotopes contained in spent fuel elements and the liquid waste from nuclear spent fuel reprocessing. Added to this is the nuclear waste from nuclear weapon programs, scientific research, and nuclear medicine. Consequently, a large variety of radioisotopes needs to be fixed by a matrix that is sufficiently resistant to chemical corrosion and intrinsic radiation damage. Therefore, the most widely used technology for immobilization of HLW is its vitrification in either a borosilicate or phosphate glass matrix [1,7].

Understanding aqueous glass corrosion is, however, also of high interest for glass industry to (i) avoid delamination of possibly formed surface alteration layers (SALs) in pharmaceutical glass vials which are used for storage of sensitive drugs [8], (ii) improve the chemical resistance of glassware, and (iii) to minimize the alteration of construction and design glasses that are exposed to natural weathering. Nevertheless, most literature deals with long-term glass durability related to nuclear waste glasses. One reason for this might be the fact that the corresponding quality test frequently performed in industry only runs for a few hours to days, instead of years to decades. Furthermore, these results are often not available because they are not published by the companies due to their economically motivated confidentiality policy.

Glass is a metastable material and corrodes in contact with water [2,4,6,7,9–11] or under high humidity [9,10,12–14]. Even though the glass specific alteration rates are low over several years under ambient conditions, the alteration rate can be high under extreme pH conditions, high temperatures, and/or over long time-periods [2,4–6,15–19]. Depending on these parameters, distinct silica-rich SALs are formed, which can induce passivation of the underlying glass and a slowdown of the corrosion rate typically by orders of 3 to 5 [20,21]. The scientific interest in glass corrosion has developed over more than 150 years [22–24] and was initially mainly based on the investigation of weathered historical glasses [11,24–28]. Until now, numerous additional corrosion experiments with well-defined glass cuboids or powders under different conditions have been performed to determine glass alteration rates [7] and/or to understand the complex alteration reactions [29,30] and the glass corrosion mechanism(s) [20,31]. Concerning the use as matrix for nuclear waste, the corrosion mechanism needs to be understood and numerical models to be developed to simulate the alteration and release of encapsulate HLW over long time-scales up to one million years. The modelling of glass corrosion, especially over long timescales, is important to predict the integrity of the matrix of vitrified high-level radioactive waste (HLW). Even though the safety concepts are primarily based on the radionuclide retention capacity of the surrounding geological formation and/or on the barrier effect of the repository container, the waste matrix itself also contributes as the first barrier to the safety of a multi-barrier system [7,32]. In addition to the correct prediction of glass corrosion rates over long-time scales, understanding the glass corrosion mechanism opens up new avenues to customize the glass selection for specific applications and conditions. Since the chemical durability of glass depends on the glass type and many environmental parameters, more knowledge about specific feedbacks of solution composition on glass dissolution and *vice versa* is a promising way for an ideal glass selection to ensure minimal alteration under certain conditions. Furthermore, the understanding of glass corrosion is important for a correct interpretation of corrosion features observed for historical or natural glasses [24–27,33], where the initial glass composition usually shows large differences and the environmental conditions often have changed over time extremely.

Therefore, the aim of the present study was to get a better understanding of the glass corrosion mechanism and the underlying molecular reactions to be able to explain all glass corrosion phenomena observed so far. Identification of the basic molecular reactions and their interdependency is crucial to correctly model the physical and chemical reactions that are involved in the glass corrosion process.

This study aimed to identify all relevant reactions, feedbacks, and corrosion features and to portray their role in the ICDP model for glass corrosion [11,29,31,34–38] in order to get a better and more complete understanding of this process and its internal consistency. Along with new experimental Raman data on two different borosilicate glasses, the identified reactions and transport steps should provide the basis to develop a numerical model that is able to reproduce the observations at the micrometer scale. Therefore, the ICDP mechanism and the basic reactions and feedback loops are described in great detail in Chapter 3, in which also the most important models for long-term glass corrosion are reviewed critically with respect to the ICDP model. Recent scientific findings support an ICDP-based corrosion mechanism [30,31,38–41], at least under certain conditions or for certain stages of the corrosion process [11,20]. However, especially for acidic conditions, an interdiffusion based leaching mechanism is still unchallenged, apart from a few exceptions [11,30,31]. Therefore, one of the main goals was to test the hypothesis that an ICDP process is able to explain SAL formation over the entire pH range.

Conventional glass corrosion studies are mainly based on *post mortem* studies of corroded glass samples and the leaching solution. However, it is not fully understood whether quenching affects the frequently metastable, hydrous corrosion products and whether the observed corrosion features are artificially induced by the drying procedure. Therefore, to clarify the glass corrosion mechanism *in situ* fluid-cell Raman spectroscopy was used, which is a powerful method that allows studying glass alteration *in operando* and thereby spatially and temporally resolved. Three different case studies were performed to investigate how the ISG behaves under hyperalkaline and acidic conditions and how glass corrosion is affected by changing solution compositions and exchange rates. This required to further refine the fluid-cell Raman technique in order to be able to also perform long-term experiments and to enable continuous solution exchange. Furthermore, *in situ* Raman data were complemented by compositional bulk solution analysis to compare the overall corrosion rates with those derived from spatially-resolved, *in operando* Raman data.

Case study I: Since the ICDP model seems to be capable to explain formation of the manifold corrosion features (compare Chapter 2.1), some recent studies [11,20,30] make it necessary to provide evidence that the ICDP mechanism is also suitable for complex and Al-containing glasses. Therefore ISG, a six component refence glass, was studied under hyperalkaline conditions to

(i) test the suitability of the further developed *in situ* Raman method for monitoring glass alteration over longer time periods in several separate measuring sessions instead of merely two to maximum of three weeks of continuous measurement which completely blocks the instrument [30,31,40–42],

(ii) monitor the inwardly directed replacement of ISG by an SAL *in situ* and *in operando* for the first time,

(iii) clarify how the formation of secondary phases and their formation kinetics are related to the glass corrosion rate, and

(iv) to demonstrate the importance of local thermodynamic conditions for the overall corrosion rate (Chapter 5.7).

Case study II: There is a broad scientific consensus about a coupled dissolution and precipitation mechanism under hyperalkaline conditions [43], at least for the formation of crystalline secondary phases. However, a universal glass corrosion mechanism must also be able to explain the formation of the corrosion products under neutral and acidic conditions. This is why the same glass (ISG) of case study I was corroded a second time in a strongly acidic solution, enriched in dissolved phosphate species for pH buffering and monitoring. In this way,

(i) the compatibility of the ICDP model with the dynamic corrosion behavior of ISG under acidic conditions, based on real-time *in situ* data, and

(ii) possible pH changes, differences, and/or gradients in the bulk, pore, and the presumed interface solution may become visible by the pH sensitive phosphate speciation, which can be deduced from Raman spectra (Chapter 7).

In this way, the extensive data from the two endmember-type corrosion experiments of case study I (hyperalkaline) and II (hyperacid) allow proving the hypothesis that the ICDP model is also valid for Al-containing borosilicate glasses independent of pH.

Case study III: So far, formation of multiple layered corrosion products formed by glass corrosion was just observed by analysis of the samples after they were quenched and dried (*post mortem*) [11,25,26,39,44]. Such complex chemical and structural patterns were often assumed to be drying induced shrinking features and little attention has been paid to lamella formation, possibly reflecting the fact that an ID-based mechanism cannot explain this common corrosion feature. On the other hand, the ICDP model has so far provided a good theoretical framework to explain the origin of patterned SALs [11,31,36,39]. To support this theory, a simple Na-borosilicate glass (TBG) was studied in different solutions under varying solution exchange rates. Three different fluid-cell Raman experiments with TBG were performed to

(i) test the method at varying solution exchange and to study the interdependence of bulk solution renewal and glass alteration dynamics,
(ii) test whether boric acid can be used as an *in situ* pH tracer to provide a further alternative to the carbonate [40,42,45] and phosphate systems (Chapter 7),
(iii) observe multiple am-SAL formation *in operando* by applying silica-supersaturated conditions,
(iv) to monitor longer durations compared to past fluid-cell Raman experiments with TBG [29–31,41,42] and
(v) to determine the impact of initially silica-supersaturated conditions on the initial alteration rate and the SAL structure (Chapter 8).

Finally, based on the review of the involved reactions, the identified feedbacks, the results presented in the case studies, and several existing glass corrosion models, some implications for upcoming numerical models for (long-term) glass corrosion are discussed in Chapter 9. Furthermore, a first approach for a simplified 1D reactive transport model for TBG corrosion in water was set up, which is assumed to lead to the self-organized formation of multiple SALs. The approach is qualitatively consistent with the experimental observations and allows the realization of an ICDP-based glass corrosion mechanism in aqueous solutions at a similar spatial resolution as the *in situ* Raman method used here.

2 Introduction to silicate glass corrosion

2.1 Glass corrosion features

The aqueous corrosion of silicate glasses leads to several corrosion features, compositional changes of the reacting solution, and variations of macroscopic reaction rates with time. Before taking a deeper look at the individual reactions involved in the corrosion process, most of the relevant observations made so far on naturally and experimentally altered glasses will be summarized in the following. These include but not restricted to

- the formation of chemical and structural self-organized patterns [11,24–26,34,35,39,45–50] (Chapter 2.1.1),
- the observation of a sharp interface between the SAL and the pristine glass revealed by atom probe tomography (APT) [10,38,51–53] (Chapter 2.1.2),
- the indications for the existence of a interstitial fluid film such as a frequently observed gap between the SAL and the pristine glass [31,39,40], the detection of a water-rich interstitial zone between the SAL and the glass by *in situ* fluid-cell Raman spectroscopy [31,40,41], and the observation of a hydrogen enrichment at the reaction interface, often detected by ToF-SIMS analysis [20,38,43,53,54] (Chapter 2.1.3),
- the microstructure that is partly controlled by the spherical shape of the primary silica particles of the SAL [20,26,31,34–36,39,41] and the SAL porosity [31,34,55,56], which in turn may cause passivating properties of SALs [5,9,21,31,34–36,38,40,41,57–60] (Chapter 2.1.4).

In addition, the different kinetic stages of glass corrosion [2–4,9,10,17,19,42,43,58,61–65] are briefly reviewed (Chapter 2.2) by considering their dependence on

- temperature and solution pH under far from equilibrium conditions [17,44,63,66,67] (Chapter 2.3.1),
- fluid flow rates in flow through corrosion experiments [15,68–70] (Chapter 2.3.2),
- the initial bulk solution chemistry [9,18,40,42,46,47,58,67,68,71–78] (Chapter 2.3.3),
- the ratio of sample surface area to solution volume (SA/SV) [9,10,58,61,73,78,79] (Chapter 2.3.4), and
- of radiation damage on the glass structure and corrosion rates [42,55,56,80–83] (Chapter 2.3.5).

2.1.1 Surface alteration layer and their chemical and structural patterns

The analysis of cross sectioned corroded glass samples by optical and electron microscopes often revealed that the SAL has a fine laminated structure with layer thicknesses in the range from the nanometer to millimeter scale [11,24–26,34,39,45–49,84,85]. However, there is a huge variety of patterns that have been observed in nature and experiment [25,26,39,44].

Figure 1 shows a representative selection of such structural patterns observed so far. These include parallel alteration layers, pseudomorphic replacements by lamellae and crystalline phases on top, wavy layering structures, concentric rings of lamellae, dendritic structure, and zigzag banding [25,26,39,44]. While a lot of these corrosion features are apparent to the eye, chemical and structural patterns can also be observed at nanometer scale, depending on the glass and the environmental conditions [26,34,46,47,50]. Additionally, chemical patterns can also be observed in SALs, as shown in Figure 2 for a Ti-bearing and Ce-bearing borosilicate glass that was altered under acidic conditions at 150 °C. The observed chemical oscillation within the silica corrosion product was explained by a periodically-coupled dissolution and precipitation process [35].

Based on the observation of laminar structures on naturally weathered samples, Brill and Hood [24] found a direct relation between the number of lamella and the annual temperature and moisture cycles of the soil in which the glass was buried. However, it has been shown that layered patterns also form in closed systems in laboratory experiments under isothermal conditions, indicating a self-organizing pattern forming process [25,31,35,39,45,48,49]. Cox and Ford [25] gave a detailed summary on the unique features observed on naturally corroded glass specimens and highlighted the advantage of studying naturally weathered glass samples as they are already altered by geochemical reactions at ambient temperatures over relatively long time periods. Geisler and coworkers [35] were the first to suggest that chemical patterns observed in static experiments with a Ce-bearing borosilicate glass, that was compositionally based on the German nuclear waste glass (WAK), were the result of a self-organization process. Later, Dohmen and coworkers [39] and Schalm and Anaf [26] found that in some cases the lamellae are composed of random close packing of silica nano-particles with slightly varying particle size. Recently, Schalm and coworkers [11] provided a detailed phenomenological model of the feedback reactions that lead to pattern formation via an ICDP-based process.

A dark-colored Mn enrichment between the SAL and dendritic structures is often observed in ancient stained-glass windows. Schalm et al. (2011) [27] concluded that the Mn enrichment represents an secondary degradation process involving the oxidation of mobile Mn(II) ions to Mn(IV) in between the previously formed SAL, leading to Mn(IV) precipitation within pores and gaps.

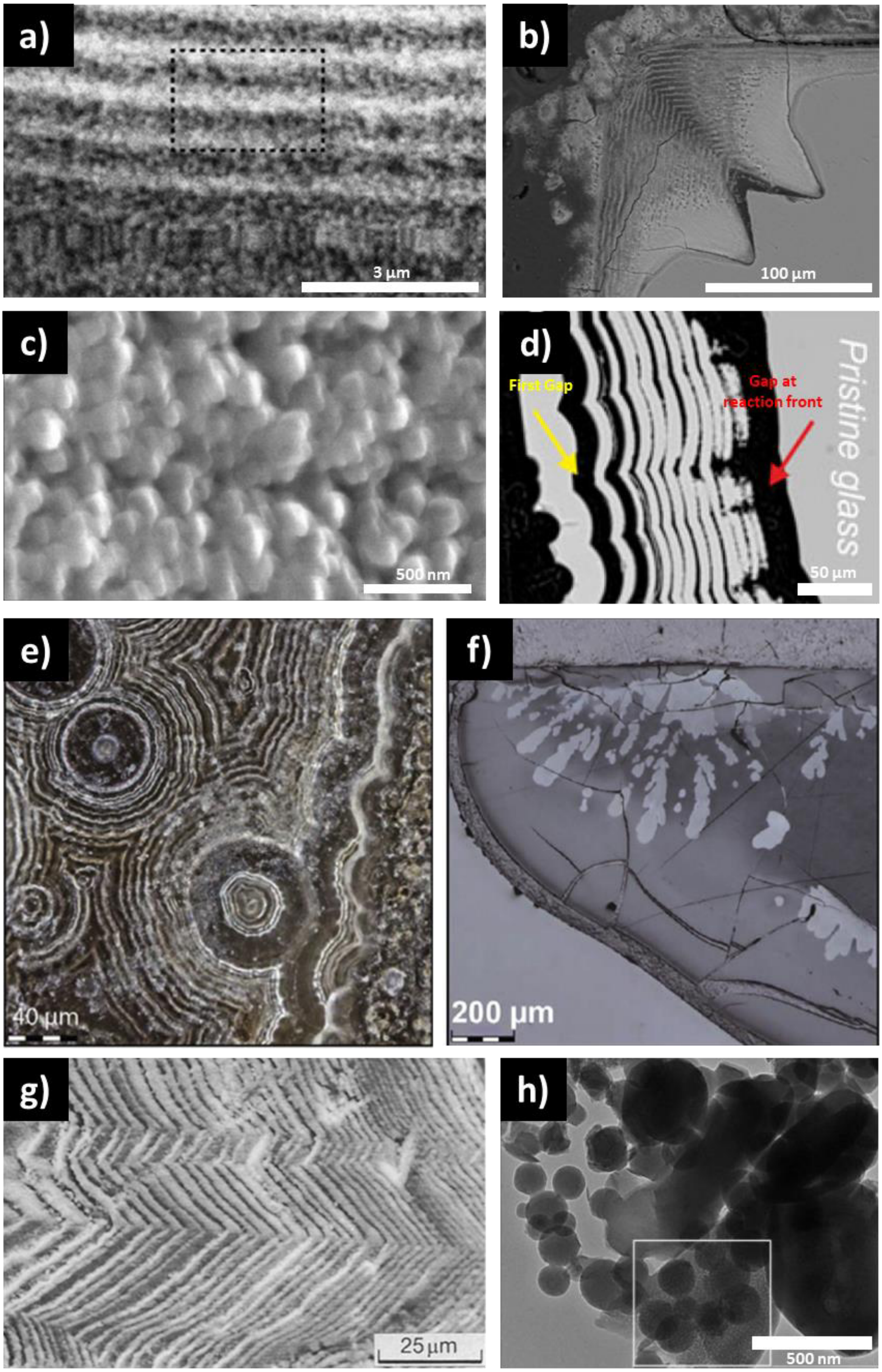
a)
3 µm
b)
100 µm
c)
500 nm
d)
First Gap
Gap at reaction front
Pristine glass
50 µm
e)
40 µm
f)
200 µm
g)
25 µm
h)
500 nm

Figure 1 (see previous page): Structural patterns and surface features of artificial and naturally weathered glasses. **(a)** and **(c)** SE images of a freshly broken surface of a historical glass sample from the 16-17th century from an excavation site in Antwerp (Belgium), **(b)** BSE image of a cross-sectioned International Simple Glass (ISG) coupon that was altered for 540 days in a hyperalkaline Ca(OH)$_2$ solution showing pseudomorph replacement of the glass by laminar corrosion layers and crystalline precipitates onto the outer surface of the SAL, **(d)** wavy corrosion layers covering a pristine sodium borosilicate glass after 7 days of alteration in an initially acidic solution (pH$_{90°C}$ 2), **(e)** optical dark field and **(f)** bright field image from historical glass samples from the 16-17th century from an excavation site in Antwerp (Belgium) showing varying colored lamellae and Mn-rich dendrites, respectively, **(g)** zigzag banding of the corrosion layer on the surface of a historical glass sample older than 1650 AD from the Eltham Palace in Kent (United Kingdom) [25], **(h)** bright field TEM of a Al-free corroded glass powder corroded for 21.4 years at pH$_{90°C}$ 9 (a), (c), (e), and (f) taken from Schalm and Anaf [26]; (b) taken from Backhouse et al. [44]; (c) taken from Cox & Ford [25]; (d) taken from Dohmen et al. [39]; (h) taken from Gin et al. [20].

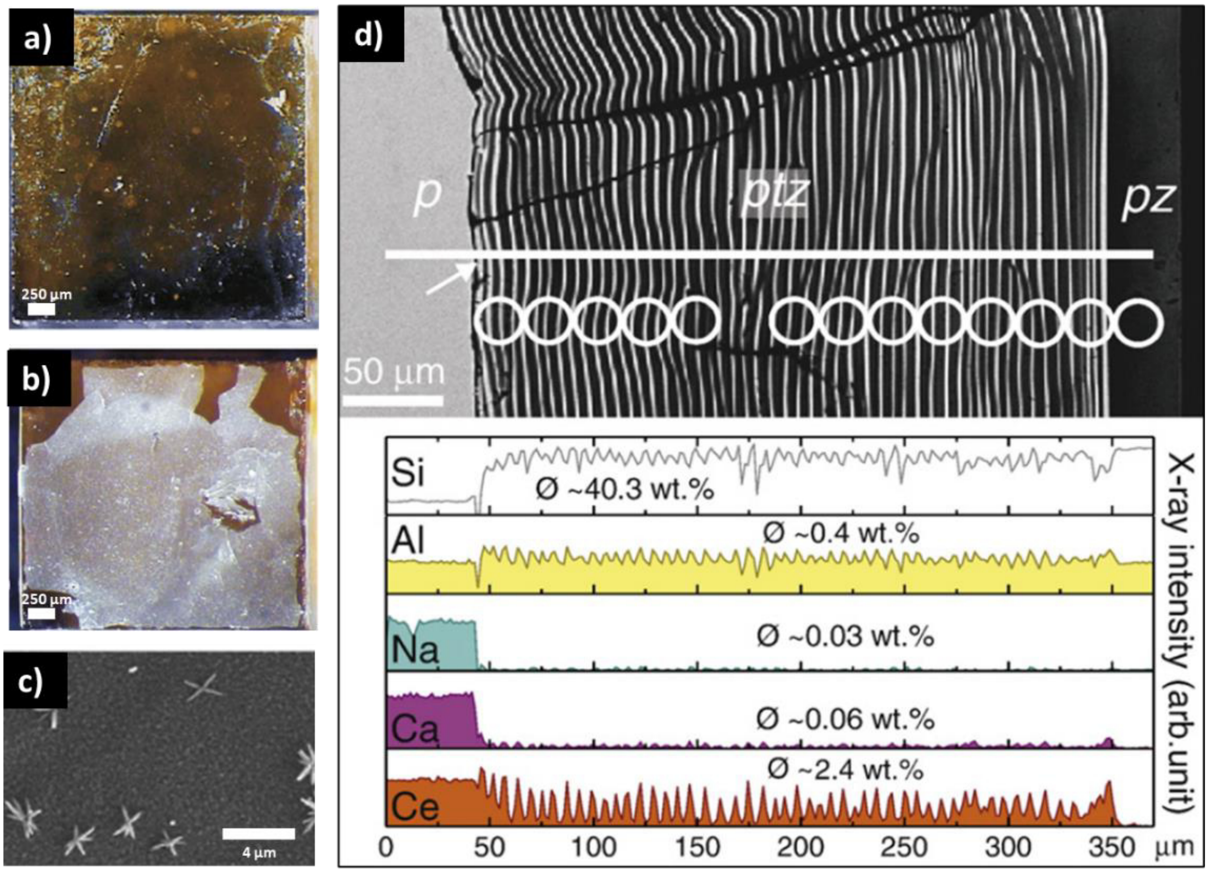

Figure 2: Selection of textural characteristics and chemical patterns of altered borosilicate glass treated for 96 h at 150 °C in a 1*M* HCl solution (pictures taken from Geisler et al. [35]). **(a)** and **(b)** Optical images of the glass sample before and after experimental alteration, espectively, revealing the formation of a surface alteration layer. **(c)** Secondary electron image of rutile (TiO$_2$) crystals at the outer surface of the alteration layer of the sample shown in (b). **(d)** Backscattered electron image of the cross sectioned corrosion zone that can be subdivided in an outer plain zone (pz) and an inner zone that is characterized by oscillatory banding patterns (ptz). The pristine glass is labelled p. The lower part of (d) shows the results of quantitative electron microprobe analysis that was performed along the white line and that reveals chemical oscillations.

2.1.2 Atomically sharp interface

In the past, several studies proposed a glass corrosion mechanism that is mainly based on interdiffusion (ID) reactions, except for strongly hyperalkaline conditions, because the elemental release of B and alkali elements into the solution was often found to follow an inverse square root of time dependency and elemental profiles crossing the interface have shown sigmoidal shaped concentration gradients [10,11,37,38,53,73,86–88]. Indeed, both observations can basically be attributed to an interdiffusion-type process. Although the elemental profiles were determined by using high resolution techniques, such as (ToF-)SIMS or TEM [37,53,73,87,88], some APT analysis revealed an atomically sharp reaction front, while (ToF-)SIMS profiles showed a sigmoidal shaped concentration profile for readily soluble elements [38,53]. These conflicting results point to the possibility of artificial detected apparent diffusion profiles and support a dissolution reaction at the reaction front, instead of a pure ID type reaction. Nevertheless, some authors mentioned that the sharp interface observed in atom probe analyses itself is an artefact producing artificially sharper interfaces due to difficulties in the reconstruction of APT data of multilayer structures [51,53]. More precisely, Gin and coworkers [53] argued that a high-to-low evaporation field transition, i.e., the glass-to-SAL transition will artificially compress the low evaporation field layer in the reconstructed volume. Indeed, such analytical artifacts can falsify the reconstructed APT data [89]. However, concerning the corresponding study, the concentration profiles of some less soluble elements (e.g., Al, Zr) do not show any anomalies, which should be the case if a compression of the whole reconstructed volume would be responsible for an atomically sharp interface, which is indicated by the concentration gradient of the readily soluble elements at the SAL-glass interface.

2.1.3 Indications for the existence of an interstitial fluid layer

Between the SAL and at the reaction front, often gaps can be observed, especially if the corrosion layer has reached a µm scale thickness (c.f. Figure 1b & d) [35,39,40]. Furthermore, the formation of a water-rich interface between the glass and SAL was directly observed by *in situ* fluid-cell Raman spectroscopy during corrosion of a silicate glasses [30,40,41,45]. Another observation that indicates the occurrence of a water-rich reaction interface are high hydrogen concentration at the reaction front, observed in several ToF-SIMS analysis crossing the SAL/glass interface of corroded glass samples [38,43,53,54,56,90]. A selection of such ToF-SIMS profiles is shown in Figure 3 where the hydrogen profiles are highlighted by a dashed red line.

Note that Collin and coworkers [91] recently showed that H and ^{18}O concentration profiles are probably not affected by ion beam sputtering in contrast to weakly bonded cations (e.g., Li, K). The observation that ^{18}O and H were not displaced during the measurements proves that the hydrogen enrichment at the interface is a real feature and therefore must be explained by a reliable mechanistic model for glass corrosion.

2.1.4 Microstructure, passivation, and rate limiting species

The microstructure, including porosity and pore connectivity as well as the (silica) particle size of SALs, depends on the original glass composition [20,56], solution composition [47], solution pH [50], reaction time [9,55,92] and temperature [34]. The SALs of some corroded glass specimens is *inter alia* made up of spherical shaped particles (c.f. Figure 1a, c & h) of an amorphous, silica-rich phase [11,20,26,34–36,39]. However, such particles were often not identified in SEM or TEM analysis of the SALs formed by corrosion of Al and Zr bearing glass samples [43,51,55,56].

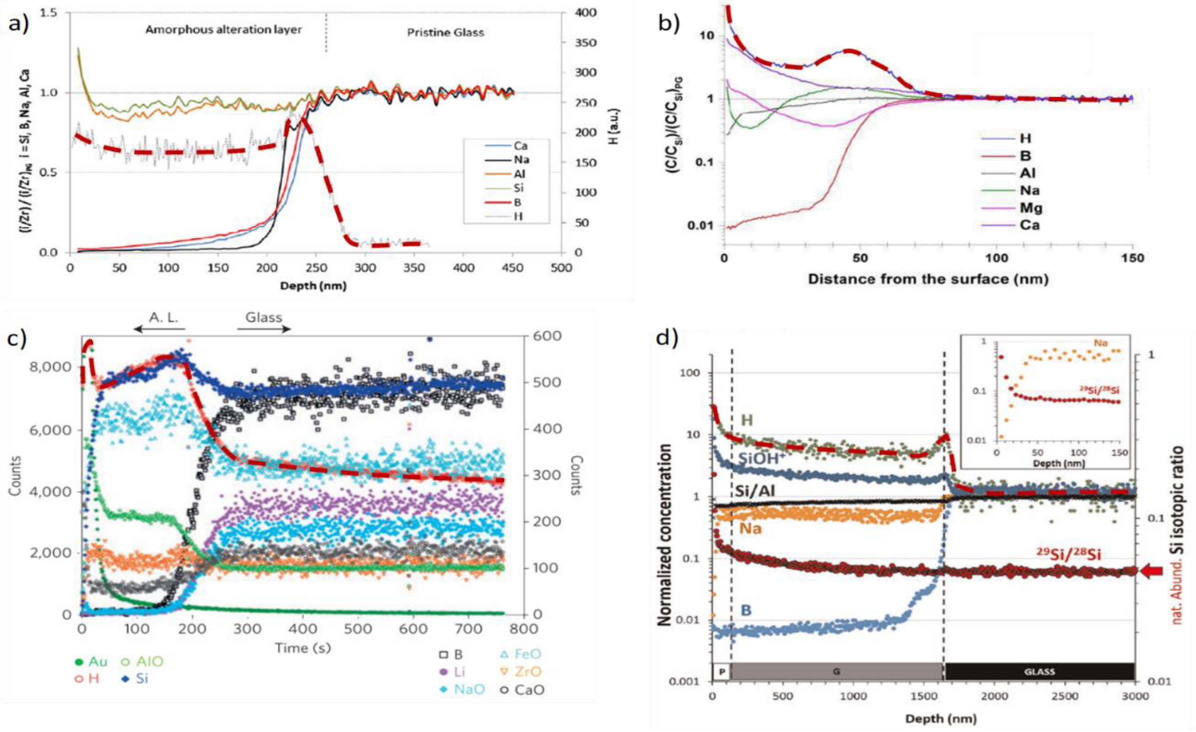

Figure 3: Selection of ToF-SIMS profiles from the literature from differently altered glass samples, which all show an enrichment of hydrogen at the reaction interface. The hydrogen profiles are highlighted by a tracing dashed red line. (Images are taken from **(a)** Gin et al. [43]; **(b)** Narayanasamy et al. [54]; **(c)** Hellmann et al. [38]; **(d)** Mir et al.[56]).

It should also be mentioned that the microstructure may be a transient feature, i.e., it may change over time, as recently has indeed been observed by *in operando* fluid-cell Raman spectroscopy [30]. This was also observed for amorphous corrosion layers that experimentally formed during the replacement of crystalline materials [37,93] and for SALs of corroded nuclear waste glasses [9,56,92].

There is broad scientific consensus that the formation of an SAL may protect the underlying glass from further corrosion even though the extent of this passivating effect depends on various factors [6,7,9,20,21,31,35,36,38,40,57–60,77,94]. The passivating property of the SAL, in turn, is assumed to reflect the fact that the SAL forms a diffusion barrier for the reactive or rate limiting species and therefore strongly depends on its microstructure [10,21,31,34,43,58,60,86,94,95]. Isotope tracer experiments have suggested that the transport of silicon containing species through the SAL can be limited, depending on its density and/or porosity [36,40,95]. In contrast, other isotope tracer experiments revealed that hydrous species are probably not rate limiting, because they can be transported relatively quickly to the reaction front [31,34,40,55]. Additionally, Gin and coworkers [53] performed ToF-SIMS analyses on International Simple Glass (ISG) coupons altered for different time periods up to 875 days, which revealed that a hydrous species (more precisely hydrogen) still diffused progressively into the glass, whereas the interface of B, Na and Ca remained at the approximately same position between 209 and 875 days. This hydrogen distribution consequently cannot be explained by an ID process, because no cation (e.g., such as Na) shows a mutual concentration gradient. The ISG is an international reference glass and has a simplified borosilicate nuclear waste glass composition (mentioned in Chapter 5.8.1), based on the non-radioactive SON68 French nuclear waste glass.

2.2 Glass corrosion mechanisms

The debate about a general glass corrosion mechanism has mainly revolved around two different basic theories for several years. The still largely accepted and more classical theory assumes that the SAL, frequently also called gel, is formed by interdiffusion (ID), hydrolysis, and *in situ* recondensation reactions once saturation is reached with respect to amorphous silica [20,53,90]. A new competing mechanistic model has been suggested by Geisler et al. [35,36] that is based on the stoichiometric dissolution of the glass, which is spatially and temporally coupled to reprecipitation of an amorphous, silica-rich phase at an inwardly moving reaction front. This model has later also been adapted by other authors, at least under certain conditions [20,38]. In this interface-coupled dissolution-precipitation (ICDP) process, the dissolution-reprecipitation reactions are mediated and directly coupled by a thin interface solution between both solid phases. The spatial coupling of dissolution of the glass and precipitation of corrosion product(s) with an inwardly moving reaction front will progressively replace the glass if no passivating processes comes into effect. An important kinetic constraint of such a replacement reaction is that the rate of silica precipitation, r_p, has to be coupled to the glass dissolution rate, r_d, i.e., $r_d - (r_p + u) = 0$, where u accounts for the quantities of elements that are released into solution per unit time [35,36]. Hence, both rates are not equal.

Recent experimental results suggest that an overall glass corrosion model must consider both endmember like mechanisms, because none of both can explain all features observed in glass corrosion studies [20,34,53]. A unifying, refined ICDP mechanism has recently been proposed by Lenting and coworkers [31,34] and specified more recently by Schalm and coworkers [11] to explain the lamella formation frequently observed under neutral to alkaline conditions. This model is based on rather concurrent reactions and rate limiting processes, instead of consecutive reactions. More precisely, the formation of amorphous or crystalline corrosion products onto the glass surface is assumed to take place via ICDP reactions. The ID reactions become more relevant, when the glass dissolution rate is slowed down and diffusional ion exchange ahead the dissolution front will not be overprinted by following network dissolution. If this is the case, an ID zone will be established ahead the ICDP reaction front, resulting in a hydrated, alkali exchanged/depleted glass layer. Note that this reaction can be crucial over long time periods by triggering resumption of the dissolution rate, but the actual formed distinct SALs are assumed to be formed by precipitation from solution after stoichiometric glass dissolution [31,34].

Recently, another general mechanism was proposed that assumes a dissolution/precipitation reaction followed by *in situ* reorganization for a readily soluble ternary sodium borosilicate glass [20], which is partially similar to the model proposed by Lenting et al. [31]. However, based on results from experiments performed with a glass containing additional Al it has been proposed that the alteration mechanism switches to a pure *in situ* reorganization mechanism without an initial ICDP stage for Al-containing glasses under the same conditions [20]. The authors concluded that the glass composition, environmental conditions, and the stage of reaction progress determine the type of SAL forming mechanism, i.e., whether it is formed by ICDP or *in situ* reconstruction. In summary, there is agreement that corrosion of silicate glasses, especially over long time periods, cannot be explained sufficiently by a single overall, rate limiting reaction step [10,20,34,53,67]. It is rather a mechanism that involves competing parallel and/or successive rate limiting reactions. The actual reaction that is rate limiting under certain conditions depends on the reaction stage, initial glass composition, temperature, (local) pH, and (local) solution composition. It should be emphasized that the rate limiting reaction will probably change over time and feedbacks [11,31,45] as well as catalytic reactions may (re-)accelerate corrosion rates. In fact, the discussion of an unifying, general mechanism of corrosion has reached a point where the various models mentioned above have been partially merged and some differences are more a matter of terminology.

2.3 Glass corrosion kinetics

Although the glass corrosion process and the formation of SALs are not fully understood so far, a general observation made in most of the glass corrosion experiments is a change of the corrosion rate with time, reflecting the kinetics of individual reactions involved in the replacement process. The temporal evolution of the macroscopic corrosion rate of glass is typically subdivided into three different stages, highlighted schematically in Figure 4, where the corrosion rate ($d\xi/dt$) and extent of the reaction (ξ) are plotted as a function of time. During *Stage I* the alteration rate is assumed to depend on solution chemistry, glass composition, pH, reaction temperature [2–4,9,17,19,43,53,58,61–64], and irradiation-induced structural damage of the glass [42,55,56,80,83]. At this stage, it is supposed that no SAL is formed which may affect the corrosion rate and the solution stays highly undersaturated with respect to the glass constituents, i.e., affinity effects are more or less negligible [9]. Under these circumstances the glass specific, intrinsic forward dissolution rate can be approximately determined, which is also often named *initial* or *forward rate* and denoted as r_0 in Figure 4 [9,43,64]. Once the glass dissolution has led to a significant enrichment of glass components in solution, formation of an SAL can usually be observed. At this stage, the corrosion rate is commonly reduced after a transition period to a second, relatively low corrosion rate regime that is called *Stage II* with a *residual rate,* denoted as r_r [9,43,61,64]. Both, the formation of a transport limiting, passivating SAL and the chemical affinity of the solution are suggested to be responsible for the rate drop [9,40,94].

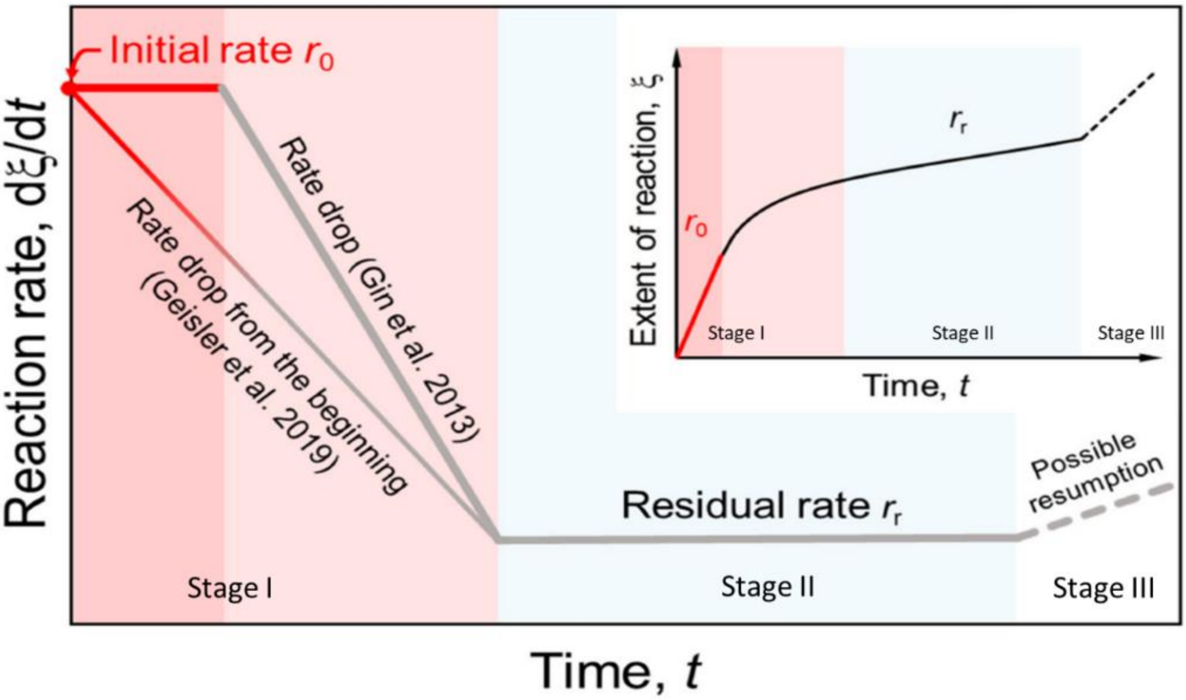

Figure 4: Different kinetic stages of glass corrosion presented as reaction rate dξ/dt and extent of the reaction ξ (inset diagram) over time (taken from Lönartz et al. [42]). Here ξ represents the amount of stoichiometric dissolved glass. In contrast to an initially constant corrosion rate as proposed by Gin et al. [3]. Geisler et al. [40] observed a linear decrease already from the beginning of glass corrosion, likely due to affinity effects [42].

In some cases, a *resumption of alteration* (*Stage III*) has been observed, which is typically associated with the precipitation of new, silica-rich crystalline corrosion products [17,38,50,58,61,76,91,93–96]. Although the scientific research on glass corrosion is going on for several decades, there is still a lack of precise thermodynamic data and the understanding of formation mechanism(s) of the SAL, the rate limiting steps, and the trigger(s) of *Stage III*. This makes a prediction of long-term glass durability and corrosion rates still highly uncertain [2,4,9,43,62,64,96,96].

2.3.1 Impact of pH and temperature

A lot of effort has been made to identify the impact of temperature and pH on the *forward dissolution rate* of different silicate glasses. The frequently proposed empirical rate equations, that are based on the *transition state theory* (TST), usually allow predicting reliable dissolution rates, especially under silica undersaturated conditions [7,9,17]. The impact of pH on the individual reactions will be discussed in more detail in the following chapters, but some general facts can already be anticipated:

- The temperature dependence of the glass network dissolution can be given by an Arrhenius equation with an empirically determined activation energy (E_a) and the pH dependence is approximated by hydrogen activity to the power of an empirically determined reaction order coefficient (η) [16,63].
- The extent of glass dissolution increases with temperature and the activation energies in rate laws typically range from 60 to 80 kJ/mol [17,67].
- In general, the dissolution rate has a V- or U-shaped pH dependency with a minimum between values ranging typically from 6 to 8 [9,44,48,63,66].

2.3.2 Impact of fluid dynamics

Intrinsic forward dissolution rates are usually determined by using special experimental setups which ensure a highly undersaturated solution to avoid any affinity effects or formation of SALs. This can be achieved by single path flow through (SPFT) systems with sufficiently high flow rates [10,15,68,69] or reaction vessels with high solution volume and turbulent stirring conditions [7,70]. Experiments conducted using SPFT systems revealed a clear correlation of fluid flow rates and glass dissolution rates [15,68,69]. Experiments performed with fast flow rates showed a higher glass dissolution rate compared to slow flow rates. However, the interdependence is highly nonlinear and at a specific threshold, no significant increase of the dissolution rate is observed with further increase of the flow rate [15,68,69]. This apparent rate maximum is assumed to represent the *forward dissolution rate*. Concerning the passivating properties and microstructure of the SAL, mentioned in Chapter 2.1.4, it should be noted that SALs of very low density are formed at high flow rates compared to those formed in static dissolution tests [10].

2.3.3 Impact of solution composition on glass dissolution and surface alteration layer formation

The corrosion rates of glasses are assumed to strongly depend on silica activity of the surrounding solution, frequently referred to as affinity effects [15,18,40,42,67,68,97]. The affinity effect describes the dissolution rate dependency of minerals and glasses on the approaching equilibrium or steady state conditions with respect to the rate limiting component in solution, e.g., amorphous SiO_2 [15]. It is remarkable that even small amounts of dissolved silica much below the saturation level of known SiO_2 polymorphs were found to have a large effect on the forward dissolution rate [15,68,97]. Nevertheless, even if the presence of dissolved Si in solution can dramatically change the forward dissolution rate, its impact on the residual rate is assumed to be negligible [9,58].

In contrast to this, Oelkers and Gislason performed experiments under flow through conditions at $pH_{25°C}$ 3 and 11 using a basaltic glass and concluded that the dissolution rates are independent of aqueous silica activity [72]. Nevertheless, the interpretation of the results was questioned because the dataset includes analysis of experiments performed under different conditions, e.g., different reactive surface areas, fluid flow rates, and input solution compositions. A reduction of the dataset to those data, which just show the dissolution rate in dependence of the initial Si concentration reveals the existence of an affinity effect also for basaltic glasses.

Because of the failure of some affinity limiting rate laws based on saturation state of amorphous SiO_2 to correctly describe the corrosion of several silicate glasses, efforts been made to improve this approach by, e.g., including the Al activity [72,98] into the affinity term. Indeed, the accumulation of other glass constituents in solution also affects the corrosion rate [10]. However, experimental results indicate that the effect of silicic acid activity on the chemical affinity rate is dominating [15,67,68,97]. In addition to this, solution pH and the presence of other dissolved species (e.g., ions, organic buffers/acids) are found to affect the alteration rate [46,75–78], the composition of the SAL, and its physical properties [46,47,78,99].

It has also been reported that the presence of K and Cs in the solution seems to decrease the glass alteration of ISG at $pH_{90°C}$ 7 and the reaction kinetics decrease with increasing concentration of these elements [77]. Interestingly, no significant effect was observed in the presence of Li and Na [60,77]. Furthermore, it was observed that the forward dissolution rate increases with increasing Ca content of the glass [73] and in the presence of a Ca-rich solution at neutral or slightly basic pH [69,78]. In general, Ca tends to be incorporated in the SAL, but will prefer to form CSH phases at high pH and reaction progress [10,78,100] and enriches in certain layers or nodules, depending on pH [11]. In contrast to this, Fe, Mg, Zn, Ni, and Co will rather not become incorporated in the SAL structure in significant amounts [46,47,58]. Instead, if the concentrations are high enough, the pH dependent and affecting precipitation of other secondary phases onto the SAL or in its porosity space can be observed, which coincides with an increased glass alteration rate [47,58,74,100,101].

It is further known that organic acids and pH buffers within the reacting solution may also change the glass corrosion rate [7,72,75]. Tournié et al. [75] , for instance, showed that the dissolution kinetics of borosilicate glasses are accelerated by TRIS molecules, while they have no significant influence on soda-lime glass corrosion. Oelkers and Gislason [72] revealed an increasing dissolution rate of basaltic glass in the presence of oxalic acid containing solutions at pH 3, while no significant effect was observed at pH 11. Recently, an *in operando* fluid-cell Raman experiment with a Na borosilicate glass and TRIS buffer clearly demonstrated a profound influence on the dissolution kinetics, i.e., the buffer cannot be considered to be inert with respect to the glass-water reaction process [41]. However, the impact of organic acids and buffers on glass dissolution is still poorly studied and therefore poorly understood, only assumptions have been made about how such organic substances change or impact the reaction kinetics and/or mechanism(s).

2.3.4 Impact of surface area to solution volume ratio (SA/SV ratio)

According to literature, the amount of glass that is altered in a given time is increased with decreasing the SA/SV ratio, frequently also called S/V [9,10,58,61,78]. This behavior can be easily explained by assuming a constant surface area value of a certain glass that corrodes in different solution volumes [61]. It is obvious that more glass has to be dissolved in a large volume of solution compared to a lower volume to reach the same concentrations of glass constituents, which, in turn, determine the saturation states of corrosion products and the extent of a chemical affinity effect [10,58,61]. In addition to the solution volume, the reaction kinetics and the total amount of dissolved glass that is necessary to reach supersaturation with respect to a certain product phase can be controlled by adjustment of the reactive SA of the glass. In practice, this is achieved by using a glass powder with a high SA instead of monolithic samples [58]. Values for reactive surface area of glass powders are typically estimated by the geometric particle size, assuming an ideal spherical particle shape. Even if this method underestimates the reactive surface area due to exclusion of small cavities, adhered fine particles, and an actually rough initial particle surface, this approach leads to a better estimate of the reactive surface area than other approaches, such as Brunauer-Emmett-Teller (BET)-specific surface area measurements [7,68,102]. It should be noted that the use of a ´shrinking core´ model is also recommended for normalizing the dissolution rates to the reactive surface area when solution samples are sampled in regular time intervals, because the reactive geometric surface area decreases with ongoing dissolution [7].

2.3.5 Impact of radiation damage

While several studies investigated the (long-term) corrosion behavior of surrogate glasses, the impact of radiation damage induced by radioactive decay of confined radionuclides has so far only been little studied. Nevertheless, it is already clear that radiation damage induced artificially, e.g., by bombardment with multi-energy ions [42,55,80,81,83], by doping of glasses with radioactive elements [80], or by treatment with high energy radiation [82,83] changes the glass structure and eventually the corrosion behavior. So far it has been shown that radiation damage can both increase [80,82] or decrease [42,83] the polymerization state of glasses, depending on the glass composition and radiation conditions. Irrespective of this, the extent of corrosion, i.e., the thickness of corrosion layers or magnitude of dissolution rates, seems to be generally increased by irradiation damage of the glass structure [42,55,81]. Mir and coworkers [56] also showed that irradiation can change the microstructure of SALs after its formation and change its porosity, which may also affect the corrosion rate. Systematic and more complex studies dealing with the effect of self-irradiation damage of nuclear waste glasses on their corrosion resistance, particularly in contact with stainless steel of a nuclear glass mould, are still missing.

3

The interface-coupled dissolution-precipitation mechanism for glass corrosion

3.1 Introduction

An interface-coupled dissolution-precipitation process was proposed by Geisler and coworkers in 2010 [35] for the formation of amorphous SALs during glass corrosion. In the following years, more experimental results that support this proposed corrosion mechanism were published [11,31,36,38–40]. In turn, those observations led to the recently published refined version of this corrosion model that considers ID in the glass ahead the dissolution front, when the glass dissolution rate becomes significantly lower than the diffusion velocity of hydrous species inside the pristine glass [11,31,34].

Hellmann and coworkers [38] also proposed an interface dissolution-reprecipitation mechanism for glass corrosion based on findings of APT and TEM analysis. The atomically sharp interface of B is a strong evidence for a network dissolution front as opposed to the diffusion type profiles of Li and H. Similar APT results were already published two years earlier by Gin et al. [52], but the authors interpreted this unexpected sharp B profile as a hydrolysis front of the silicate network, excluding a complete network dissolution. Another more recent study of this working group used APT in combination with other high-resolution techniques (TEM, ToF-SIMS) to investigate corroded samples of ISG [53]. Again, an atomically sharp interface of B, Na and Ca was observed after 209 days of alteration at 90°C in a silica-saturated solution with pH 9. Beside this atomically sharp interface, which can be interpreted as a dissolution front, ToF-SIMS analysis of four ISG samples, corroded over different time periods (7, 209, 363, 875 days) under the same conditions showed an ongoing diffusion of hydrous species across the atomically sharp and practically stationary SAL-glass interface. This observation and the results of isotope tracer experiments, which showed ion exchange reactions ahead of the dissolution front [31,34], makes it obligatory to consider the diffusion of hydrous species and ID in the pristine glass also in ICDP-based corrosion models for SAL formation. Such a unifying model was already proposed by Lenting and coworkers [31,34] and will be summarized, further detailed, and discussed below.

In a silica-undersaturated aqueous solution corrosion will start with the stoichiometric dissolution (Figure 5a) of the glass (*Stage I*). The molecular reaction includes a stepwise hydrolysis of the glass network and a catalytic effect of H_3O^+ and OH^-, discussed in detail in 3.2.2. Glass dissolution will rise the monomeric silicic acid (MSA) concentration, especially in a boundary layer close to the glass surface. Beside Si, most other dissolved glass constituents will change the solution chemistry as well (e.g., pH, salinity) [40,41,45] and affect further dissolution and the silica saturation state. It seems obvious that the diffusional or convective equilibration of released glass constituents at the dissolution front with the surrounding bulk solution will not occur instantaneously. In contrast, a surface near solution boundary layer with chemical gradients was observed, including also a pH gradient at the glass surface, revealed by *in situ* and *in operando* fluid-cell Raman spectroscopy [40,41]. Even under turbulent conditions, where equilibration of the solution is enhanced, surface effects likely define the local conditions at the glass surface.

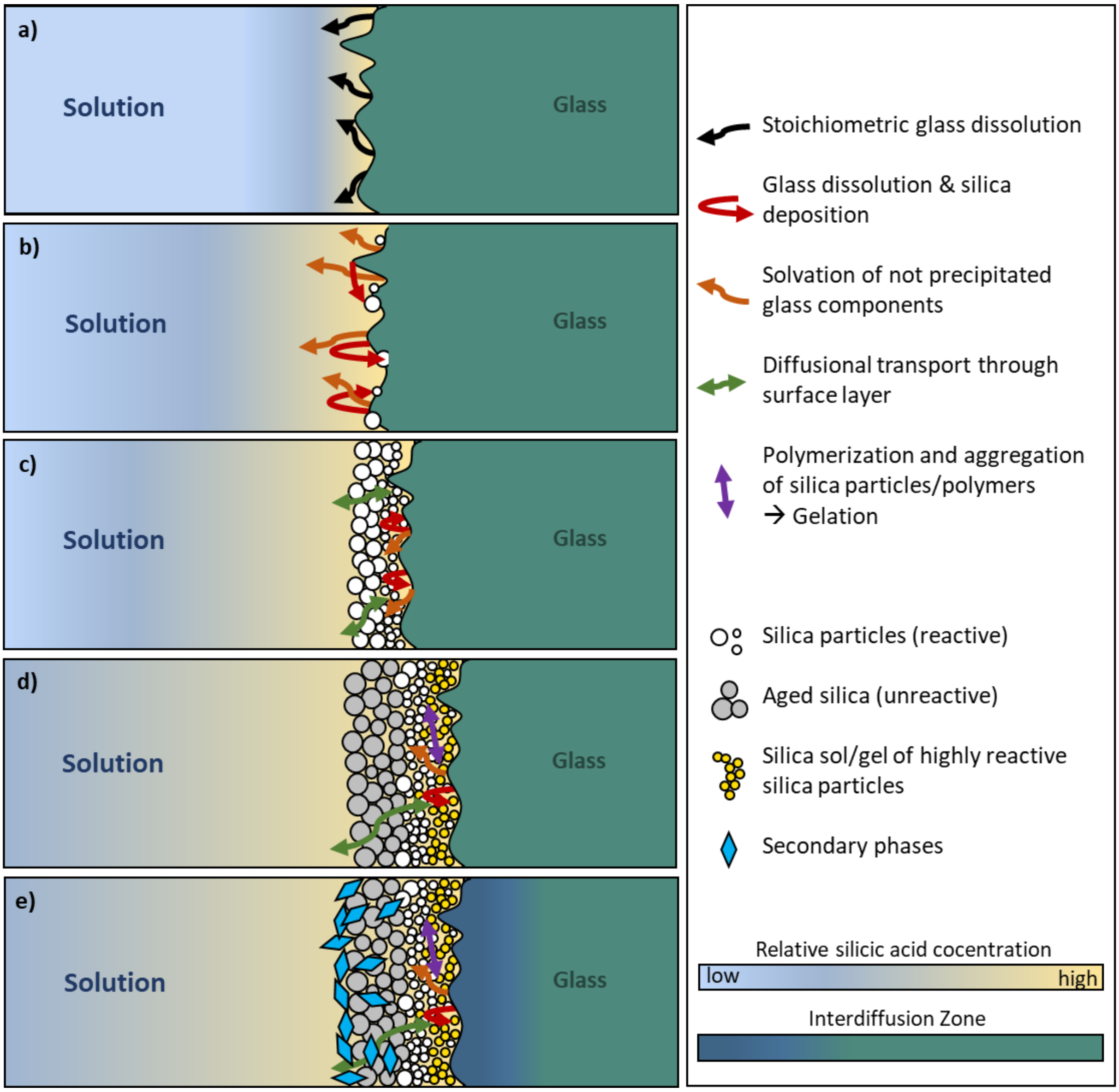

Figure 5: Schematic outline of the refined interface-coupled glass dissolution and silica precipitation (ICDP) mechanism, also considering interdiffusion (ID) reactions at different stages of corrosion (based on Lenting et al. [31,34] and Geisler et al. [36]).

Nevertheless, the initial forward dissolution rate continuously decreases with ongoing dissolution under stagnant conditions, even if no surface layer has formed at this stage that can cause passivation effects (2.1.4) [40,42]. This is in line with the observation that even small amounts of Si have an significant effect on alteration rate and explained by the decreasing chemical affinity for further glass dissolution due to the increasing SiO_2 saturation level in solution (2.3.3) [15,68,97].

However, it was found that an affinity effect alone cannot be responsible for the drop of the corrosion rate towards a residual rate that is observed in the following *Stage II* [103].

What else is responsible for the rate drop observed during *Stage II*? Due to ongoing glass dissolution, the MSA concentration in the solution will rise, especially in the direct vicinity of the glass surface, and, subsequently, supersaturation with respect to amorphous silica will be achieved and polymerization of MSA to oligomers (Chapter 3.2.3) will result in the formation of stable silica nuclei (Figure 5b). In addition to the high silica concentration at the interface, the reactive sites (e.g., $\mathrm{Si-O^-}$) at the glass surface will promote the nucleation of amorphous silica onto the glass [11]. This is because of the lower energy barrier for heterogenous nucleation in presence of impurities or reactive surfaces sites (surface $\mathrm{Si-O^-}$) [104].

The precipitation of amorphous silica and the simultaneously ongoing dissolution of the underlying glass will cause a separation of both solid phases. This creates a new interstitial, water-rich zone in between for which indications were found by Raman spectroscopic experiments [40,41,45]. The existence of an interface fluid is also supported by the enrichment of hydrogen at the reaction front as revealed by several ToF-SIMS analysis [38,43,53,54,56,90] of altered glass samples (Chapter 2.1.3). It is difficult to envisage how a diffusion process can be responsible for such an enrichment, which would require a high driving force for uphill diffusion.

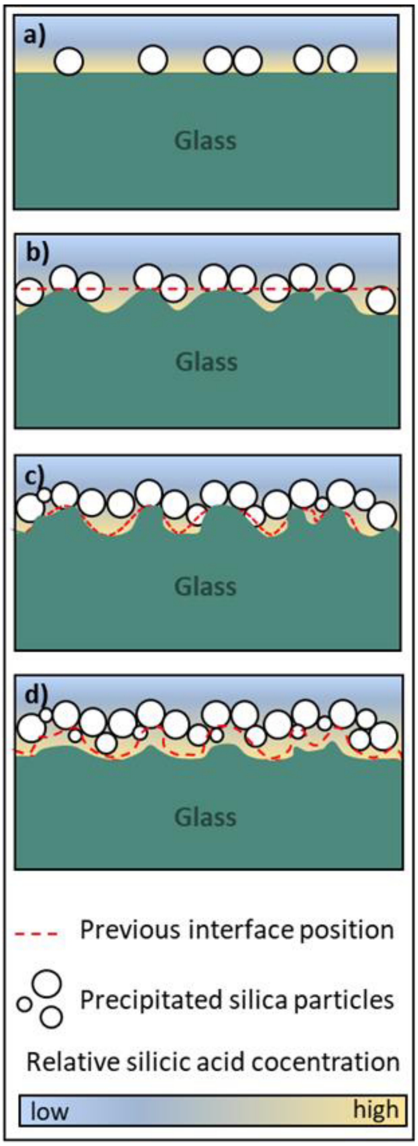

Figure 6: Proposed mechanism of silica rim detachment and interface solution formation.

For better understanding of the formation of an interface solution or an interface fluid film, the stepwise silica rim detachment and formation of the interface solution is visualized in Figure 6. At the beginning, primary silica particles will deposit locally onto the glass surface (step a and b). The underlying glass is less prone to dissolve compared to the regions exposed to the solution and may lead to a wavy reaction front when glass dissolution proceeds, as also observed in some SALs of corroded glass samples [26,39,49] (c.f., Figure 1d and e). Further glass dissolution and precipitation of silica due to the ongoing release of MSA and polymerization by glass dissolution will result in a complete coverage of the surface by a silica rim (Figure 6c) that will eventually detach by continuous dissolution of the underlying glass (Figure 6d).

After the formation of an SAL, the dissolved glass components must pass the porous layer via diffusion to be released into the bulk solution (Figure 5c). The porous SAL will reduce the transport velocity from the inner glass surface into the bulk solution or even inhibit the transport of some species by acting as a molecular sieve, depending on the pore size, pore connectivity, and molecular size of the dissolved species (2.1.4) [34,36,40,60,94]. This is supported by isotope tracer experiments suggesting a transport limitation of Si though the SAL, depending on its density and/or porosity [20,34,36,56,94,95,105].

Both dissolution and precipitation reactions take place in this interface solution simultaneously and are interdependent. Furthermore, after creation of an SAL, the reactions depend mainly on the properties of the interface solution and less on the bulk solution properties. With ongoing glass dissolution and silica precipitation the SAL thickness increases. It can be assumed that it becomes energetically favored for silica to nucleate at the surface of already formed amorphous silica. However, this can change again if the distance between the SAL and the glass surface becomes too large and spatial decoupling of the dissolution and precipitation reaction takes place.

The precipitated phase is generally not a pure, amorphous SiO_2 phase. Such an assumption is a strong simplification in this model, but is valid, e.g., for ternary Na borosilicate glasses [29,30,41] corroded in chemically simple aqueous solutions. Depending on glass and solution composition, some other elements (e.g., Fe, Al, Zr and Ca) can be incorporated in the amorphous silica network [46,47,76,78,90,100], which is also well known from silica particles synthesized via sol-gel methods [50,106–109]. Under certain conditions the SAL can also consist exclusively of crystalline phases, so observed for a Ba-bearing silicate glass altered in a hyperalkaline carbonate solution [45]. Although the focus is on describing the formation of amorphous SALs, as these are most frequently observed and assumed to be responsible for passivation, it should be noted that the proposed mechanism works independently of the product phase. It is currently the main process used to explain the pseudomorphic replacement of crystalline materials [110–112].

The dimension of the interface fluid film depends mainly on the initial glass composition, temperature, and pH at the interface, because these parameters will determine the amounts of elements that may exceed the solubility limit and will be incorporated in the SAL and that determine the thermodynamically stable product phase(s). Consequently, glasses containing a high amount of well soluble elements are replaced by a smaller volume of SAL, even if its density is typically lower. A significant relative volume difference may lead to a relatively thick fluid layer in the order of several micrometers [40,41].

The interface-coupled dissolution-precipitation reactions are thermodynamically driven by the solubility difference between the primary glass and the precipitated silica rich corrosion product, which is also the case for solution-mediated mineral replacement reactions [36,93,111,112]. Thus, the glass can theoretically be replaced completely by amorphous silica, by an interface-coupled process of glass dissolution and silica precipitation along an inwardly moving reaction front. However, in most of the glass corrosion experiments the reaction slows down after an SAL of a sufficient thickness has been formed, which somehow passivates the underlying glass [94]. A reasonable explanation for this passivating behavior within the framework of an ICDP mechanism is the decoupling of the interface solution at the reaction front from the bulk solution due to transport limitations. A decreased removal rate of dissolved glass species will increase their concentrations in the interface solution and therefore the local salinity and pH will change as observed by Geisler et al. [40]. Higher pH values at the reaction front in turn increase the SiO_2 solubility and promotes further glass dissolution. This represents one of the identified feedbacks which results directly from the ICDP mechanism and is explained in more detail in Chapter 3.2.5. Such a self-acceleration of glass dissolution [48,67], coupled with an transport limitation due to the SAL may lead to a highly saline interface solution containing high amounts of dissolved silica [34]. Under these conditions, the coagulation of silica particles is also known to be triggered by a high salt concentration, leading to aggregation of the primary silica particles instead of growth and attachment to the SAL [108]. The primary particles are assumed to condense together to form a widespan, continuous structure throughout the interface solution (Figure 5d). Such a sol-gel is made up by very small primary particles connected by fewer linking bonds than those within themselves [108]. This ridged network is highly porous with a small pore size and is rather a solid than an aqueous solution. The gelation reaction driven solidification of the interface region in turn inhibits further glass dissolution at the reaction front, i.e., it slows down the glass corrosion rate [31,34]. Such a phenomenon was already observed by *in situ* fluid-cell Raman spectroscopy, revealing a slowdown of the corrosion rate coinciding with establishment of a water-rich interface [30,40]. Consecutive solution exchange with deuterated water also indicated high mobility of hydrous species, which therefore cannot be rate limiting [29]. These observations are in accordance with the idea of a silica gel that is interpenetrated by pore water and an SAL that has a specific transport limiting effect to different dissolved species.

It is assumed that after the ICDP reaction is slowed down, ID can become the dominating alteration process [31,34], though the resulting structural changes to the glass network seems to be negligible on typical laboratory time scales. However, ID (i.e., exchange of H and alkali elements) might play a role in triggering the *resumption* of the alteration rate over long term commonly referred to as *Stage III* (Figure 5e) [31,34]. The *resumption* is often correlated directly with the precipitation of secondary phases, which in turn are linked to bulk solution properties and the prevailing temperature [10,43,67,99,113,114]. The *secondary phase* formation and its feedback on the passivating properties and glass alteration rate will also be discussed in Chapter 3.2.8. In general, the precipitation of secondary minerals, e.g., alumo-silicates onto the surface or within the SAL will consume dissolved SiO_2 from bulk and/or pore solution, which reduces the chemical affinity with respect to amorphous silica. This possibly enables redissolution of the gel-like interface layer and the SAL, which, in turn, allows further diffusional transport of Si containing species into the bulk solution. This sequence of reactions ultimately permits further glass dissolution, i.e., *resumption* of glass alteration.

So far it has been shown that the proposed ICDP mechanism is suitable to explain

(i) the observed hydrogen enrichment and water-rich zone at the reaction front that reflects an interstitial fluid (2.1.3),
(ii) the porous microstructure and silica particles, which is an argument for precipitation of a silica-based phase known from sol-gel chemistry (2.1.4),
(iii) the atomically sharp reaction front that represents the dissolution front (2.1.2), and
(iv) the opposing curves of alkali metals and hydrogen within glass after the corrosion rate has been slowed down, reflecting ID reactions and inwardly directed diffusion of hydrous species ahead the dissolution front [34,53].

Following this understanding, the (micro-)structural (e.g., density, porosity), chemical, and phase variations within the SAL perpendicular to the reaction front reflect fluctuating conditions in the interface region at a specific point in space and time [35,36,39]. According to sol-gel chemistry, the sphere size, network structure, and chemical composition of amorphous silica is strongly dependent on the pH and the presence of salts. As already explained above, these solution parameters will change with time due to the dissolution of glass and enrichment of its constituents, especially in the interface solution. Therefore, an abrupt change in SAL composition and/or its microstructure is a consequence of the feedbacks between dissolution, transport, and precipitation reactions that are trigger by changing local solution properties. The feedbacks of solution composition and pH on SAL formation and on chemical and microtextural self-organization of the SAL will be discussed in detail in Chapter 3.2.6 and Chapter 3.2.8, respectively.

3.2 Identified reactions and feedback loops

In the following, the most important reactions involved in the glass corrosion process are described in more detail and their feedbacks in relation to the ICDP mechanism are discussed. The plausibility of the ICDP mechanism becomes even clearer by having a look to the reactions on the molecular level and the effect of parameters, e.g., pH, can be evaluated. Those reactions include the formation of an interface equilibrium at the glass surface, ID reaction, the stoichiometric glass dissolution, the condensation of MSA, and silica precipitation. The creation of surface gradients, the role of dissolved ions, the formation of SALs and their transport limiting effect, as well as the formation of secondary phases will be discussed with a focus on the feedbacks controlling the corrosion process. The aim of this review, which also includes the research into a number of fundamental aspects that have not yet been addressed in the literature, is to highlight that all observations made so far are consistent with the ICDP mechanism proposed in the previous section, which also serves as a framework for developing a numerical model for an ICDP-based glass corrosion process.

3.2.1 Interdiffusion and the solution boundary layer

When a silicate glass is immersed in an aqueous solution a heterogeneous, interface equilibrium between the functional groups at the glass surface and the ions in solution will be established immediately [115,116]. This equilibrium is named heterogeneous because the terminal surface $\mathrm{Si-O}$ groups ($\mathrm{Al-O}$ or other groups, depending on composition) can have an acidic ($\mathrm{Si-O-H}$) or salt ($\mathrm{Si-O-M}$) form, depending inter alia on the activity of $\mathrm{H^+}$ and alkali ions in solution. Beside these forms of functional groups, a minute amount of negatively charged $\mathrm{Si-O^-}$ groups will be formed, creating an electrochemical potential at the glass/solution interface, which incidentally is also the basis for pH glass electrodes. The dissociation of silanol groups is described by reaction Equation (I), whereas further protonation of the surface is expected only under extreme acidic conditions [108,117].

$$(\equiv \mathrm{Si-OH})_{(s)} + \mathrm{H_2O} \rightleftharpoons (\equiv \mathrm{Si-O^-})_{(s)} + \mathrm{H_3O^+_{(aq)}} \tag{I}$$

The surface charge density is controlled by the ionic strength and pH of the bulk solution [117,118]. Even if the function of pH glass electrodes is not of major interest here, the fact that an electrochemical potential can be measured is strong evidence for such a rapidly formed interface equilibrium at the outermost glass surface. Note also that a 50 µm long pH gradient of about one log unit was observed within the first hour of a fluid-cell Raman experiment from the glass surface towards the bulk solution [40]. Concerning glass corrosion, the surface coverage with hydrogen will induce a chemical gradient between the glass surface and the underlying glass, which is the driving force for ID inside the glass that is commonly written as follows [27,67,90,119]:

$$(\equiv \mathrm{Si-O-M})_{(s)} + \mathrm{H_3O^+_{(aq)}} \rightleftharpoons (\equiv \mathrm{Si-O-H})_{(s)} + \mathrm{M^+_{(aq)}} + \mathrm{H_2O} \tag{II}$$

In contrast to the rapidly formed interface equilibrium at the glass surface, the ID within the glass is relatively slow at temperatures far below T_g, even if the gradient in chemical potential is large. This assumption is supported by modeling results of ID reactions. For example, Rieke and coworkers [120] showed that the ability of the GRAAL model (summarized in 3.3.3.1) to reproduce empirical glass corrosion data can be improved significantly by assuming a steeper drop in water concentration at the glass surface. This was achieved by introducing non-linear diffusion and can be interpreted by a rapid ion exchange/hydrolyzation at the glass surface, whereas ID inside the glass is several orders of magnitude slower. This is also in accordance with binary diffusion modelling, performed by Hellmann et al. [37], showing that a simple ID mechanism cannot explain the step function-like jumps of cation concentration at the reaction front, as observed in altered minerals.

Consequently, if dissolution of the glass network is not hindered, ID ahead the reaction front is likely to be overwhelmed by matrix dissolution and is therefore the main process causing the release of glass constituents into the bulk solution respectively environment. Therefore, ID reactions just become relevant if the dissolution rate of the glass is slowed down by passivation of the SAL [31]. At this *Stage II*, an ID zone ahead the ICDP interface may be established if the network dissolution rate is smaller than the diffusion rate of the slowest individual species that is involved in the diffusional ion exchange reaction. Note that the diffusion coefficients, and consequently the ID velocities, depend on the participating and/or competing alkali ions. Neeway and corworkers [121] showed experimentally and by calculations that the diffusion coefficients of alkali ions in glasses can vary in orders of magnitude depending on temperature and type of glass (including reference nuclear waste glasses, such as ISG and SON68). The authors assume D_H values ranging from $1 \cdot 10^{-18}$ to $1 \cdot 10^{-25}$ $m^2 s^{-1}$ at temperatures ranging from 150 °C to 25 °C, respectively.

3.2.2 Stoichiometric glass dissolution - network hydrolysis

Far from equilibrium conditions, also referred to as highly undersaturated conditions with respect to glass components (especially SiO_2), are frequently applied in experiments and models to determine intrinsic dissolution rates of minerals and glasses. It is assumed that the glass specific forward dissolution rate is then just a function of both, temperature and solution pH and can be well described by TST type rate laws [7,9,16,19,44,122]. Note that the experimentally determined dissolution rate strongly depends on the method that is applied [7] and that the rate can vary when determined under different conditions, e.g., ionic strength, silica saturation state, and the possibly unexpected presence of an SAL. Nonetheless, at the beginning of a corrosion experiment performed in pure water, the corrosion starts with stoichiometric dissolution, even if the measured rate can already be affected by chemical affinity from the very beginning [40,42]. This is even more relevant under acidic solutions since here the solubility of amorphous SiO_2 is the lowest (see Figure 10) and can be reached very quickly, especially at the glass surface.

The stepwise hydrolysis of the $\mathrm{Si-O-Si}$ bonds is a crucial process for stoichiometric dissolution of silicate glasses and can be described by following reactions [36]:

$$\equiv \mathrm{Si-O-Si} \equiv_{(s)} + \mathrm{H_2O} \rightleftharpoons \ \equiv \mathrm{Si-OH}_{(s)} + \mathrm{HO-Si} \equiv_{(s)} \quad \text{(III)}$$

$$\equiv \mathrm{Si-OH}_{(s)} + \mathrm{H_2O} \rightleftharpoons \ = \mathrm{Si-(OH)_{2}}_{(s)} \quad \text{(IV)}$$

$$= \mathrm{Si-(OH)_{2}}_{(s)} + \mathrm{H_2O} \rightleftharpoons -\mathrm{Si-(OH)_{3}}_{(s)} \quad \text{(V)}$$

$$-\mathrm{Si-(OH)_{3}}_{(s)} + \mathrm{H_2O} \rightleftharpoons \mathrm{H_4SiO_{4}}_{(aq)} \quad \text{(VI)}$$

Most of the free $\text{Si}-\text{O}$ bonds located at the surface of the glass are going to be hydrolyzed immediately due to the established heterogenous interface equilibrium [115]. Further hydrolysis will break the $\text{Si}-\text{O}-\text{Si}$ bonds located at the surface and according to the stepwise chemical reactions ((III) to (VI)). This results in fully hydrated, dissolved MSA. Even though breaking of the $\text{Si}-\text{O}-\text{Si}$ bonds can be theoretically well described by the equations above, the total hydrolysis of a central Si atom, i.e., dissolution of the main glass network former of most glasses, strongly depends on the pH and is therefore much more complex [17,63]. Furthermore, the glass structure may contain other network formers and cross-linking elements (e.g., B, Al, Zr) and add other bond types (e.g., $\text{Si}-\text{O}-\text{B}$, $\text{Si}-\text{O}-\text{Al}$, $\text{Si}-\text{O}-\text{Zr}$) with different binding energy and hydrolytic resistance [10,20,51,58,107], which makes an overall hydrolyzation rate prediction difficult. This is even more challenging for complex multicomponent nuclear waste glasses, containing a broad variety of radionuclides.

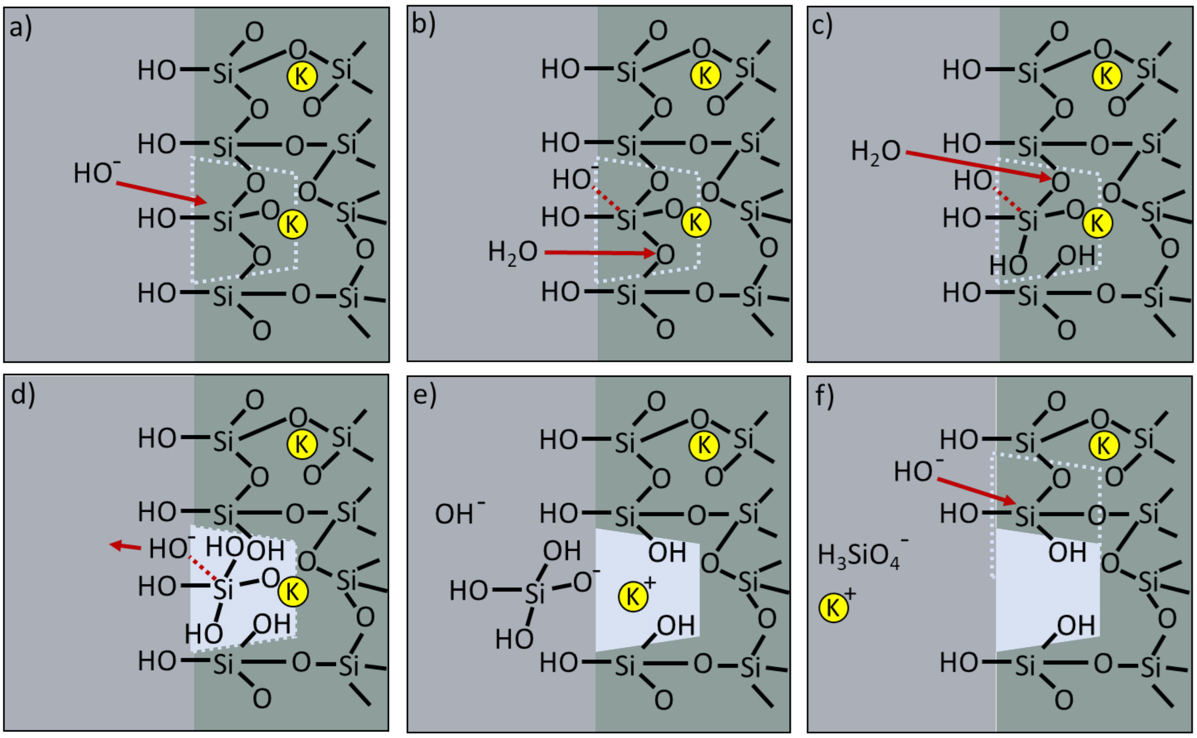

Figure 7: Proposed mechanism of OH^--catalyzed glass dissolution based on ideas from Iler [108].

The pH dependency of glass dissolution can be explained by catalyzation of the hydrolysis reaction by H_3O^+ and OH^- (F^- in HF as well at pH < 2) [108,122,123], because these ions weaken the siloxane bonds of surface located silicon atoms to the underlying network. The reason for this is chemisorption of the ions, which increases the coordination number of a surface located silicon atom [108,122]. How such a catalyzation may take place in alkaline solutions is proposed in Figure 7. The chemisorption of OH^- ends up with a polarization of the $\text{Si}-\text{O}$ bonds. This in turn weakens the surrounding $\text{Si}-\text{O}$ bonds, hydrolyzation proceeds by ongoing attack of hydrous species (H_2O), and MSA will be released [108,122].

According to this surface complexation model, the pH effect can be expressed by empirical rate equations with a minimum rate at the zero point of charge (ZPC), where the concentration of charged surface sites is (almost) zero [122]. Considering the catalytic effect of H_3O^+ and OH^-, it seems obvious that the pH dependence of the glass dissolution rate is one of the most crucial parameters in modeling long-term durability of glass, especially because the glass dissolution itself will change the solution pH with time [40,48,121]. However, it should be recalled that the pH of the bulk solution does not necessarily equals the pH of the solution at the glass surface [29]. It seems obvious that the glass dissolution rate and the diffusion of silica species in solution control the width of such a surface solution boundary layer.

3.2.3 Polymerization of dissolved silicic acid and formation of amorphous silica

Beside glass dissolution other key processes to understand the formation of an SALs are the polymerization of MSA and nucleation of amorphous silica in aqueous solutions, followed by aggregational or monomeric growth, gelation, and/or precipitation. Silica polymerization in aqueous solutions has been studied very intensively in the past [108,109,118,124–132]. In general, MSA ($Si(OH)_4$) is just stable in diluted solutions and tends to polymerize at even low supersaturation level [108,125,130]. It is widely accepted that polymerization of silicic acid takes place primarily by a reaction between an ionized and non-ionized silicon monomer, which incidentally is proposed to be the reason for the low condensation rate of colloidal silica at its ZPC (pH ~2), as shown in Figure 10 [108,126,130]. Consequently, the MSA polymerization is also catalyzed by hydronium and hydroxyl ions, according to following reactions [108,109,129]:

acid-catalyzed

$$\equiv Si-OH + H_3O^+ \rightleftharpoons \equiv Si-OH_2{}^+ + H_2O \tag{VII}$$

$$\equiv Si-OH_2{}^+ + HO-Si\equiv \rightleftharpoons \equiv Si-O-Si\equiv + H_3O^+ \tag{VIII}$$

base-catalyzed

$$\equiv Si-OH + OH^- \rightleftharpoons \equiv Si-O^- + H_2O \tag{IX}$$

$$\equiv Si-O^- + HO-Si\equiv \rightleftharpoons \equiv Si-O-Si\equiv + OH^- \tag{X}$$

Even if the solution is slightly supersaturated with respect to amorphous silica, condensation will occur and take place according to the molecular mechanism illustrated in Figure 8 [130,132]. After the attachment of an ionized siloxane group of a MSA to the silicon atom of another neutral MSA, the penta-coordinated intermediate molecule will release a water molecule in a second reaction step and further polymerization is possible at the new ionized $Si-O^-$ site [132].

3.2 Identified reactions and feedback loops

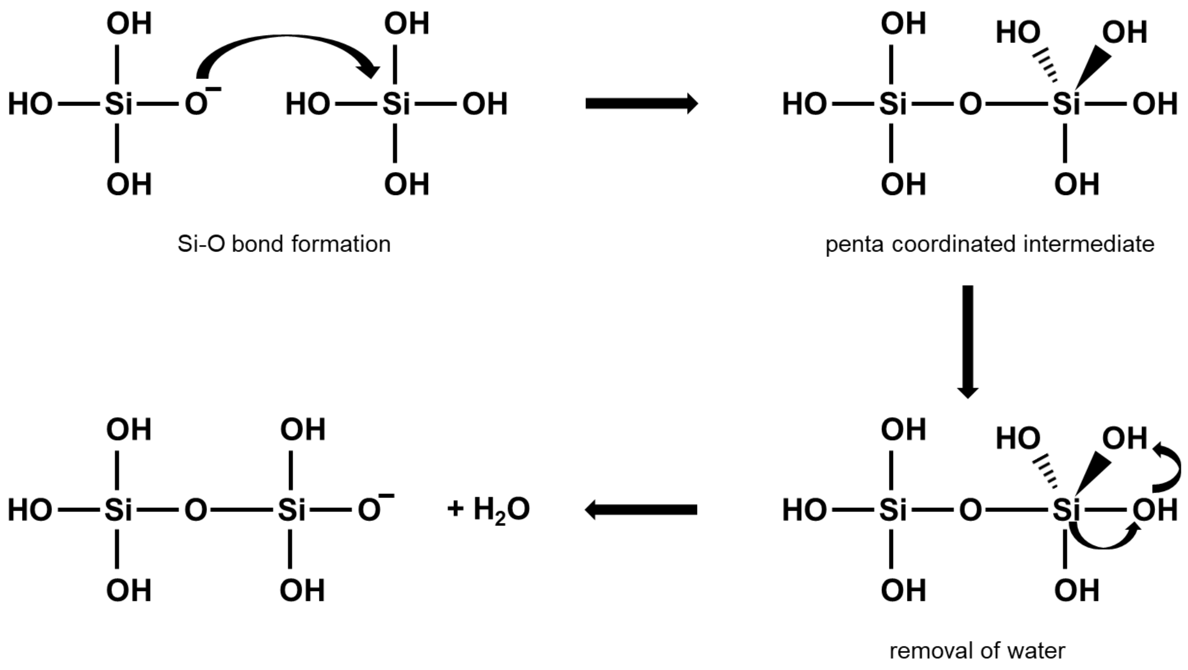

Figure 8: Mechanism of silica condensation (redrawn after Pavlova et al. [132]).

In most of the studies dealing with the formation of silica sols and gels, the reactant is a silica supersaturated solution which represents both the SiO_2-source and the reaction medium [108,109,118,125–131]. In contrast to this, in glass corrosion experiments using initially silica free solutions the dissolving glass is the source for SiO_2. Furthermore, the glass surface becomes covered with active surface sites when terminal non-bridging oxygens (NBO) are hydrolyzed and/or ionized. Silica oligomers and nuclei represent primary particles which can attach to the surface as shown exemplary in Figure 9 for a silica trimer. Thus, the silicate glass surface acts as a nucleating agent, analogously to colloidal silica particles typically used to investigate the growth of silica particles via molecular growth [118,127,128].

Furthermore, analogously to the condensation of two silicic acid monomers, the condensation of an oligomer onto a silica glass surface is also favored between an ionized and non-ionized silanol group. It seems plausible that such a condensation reaction (Figure 9a) will release a hydroxyl ion that, in turn, ionizes another NBO of the glass or silica oligomer (Figure 9b). Further condensation of other silanol groups should lead to a strong connection between the oligomer and the silica skeleton of the glass (Figure 9c & d). Reprecipitation on the glass surface at the beginning, followed by the preferred precipitation on the detached silica layer after it is established, could explain chemical and structural differences of the outermost part compared to the rest of the SAL [20].

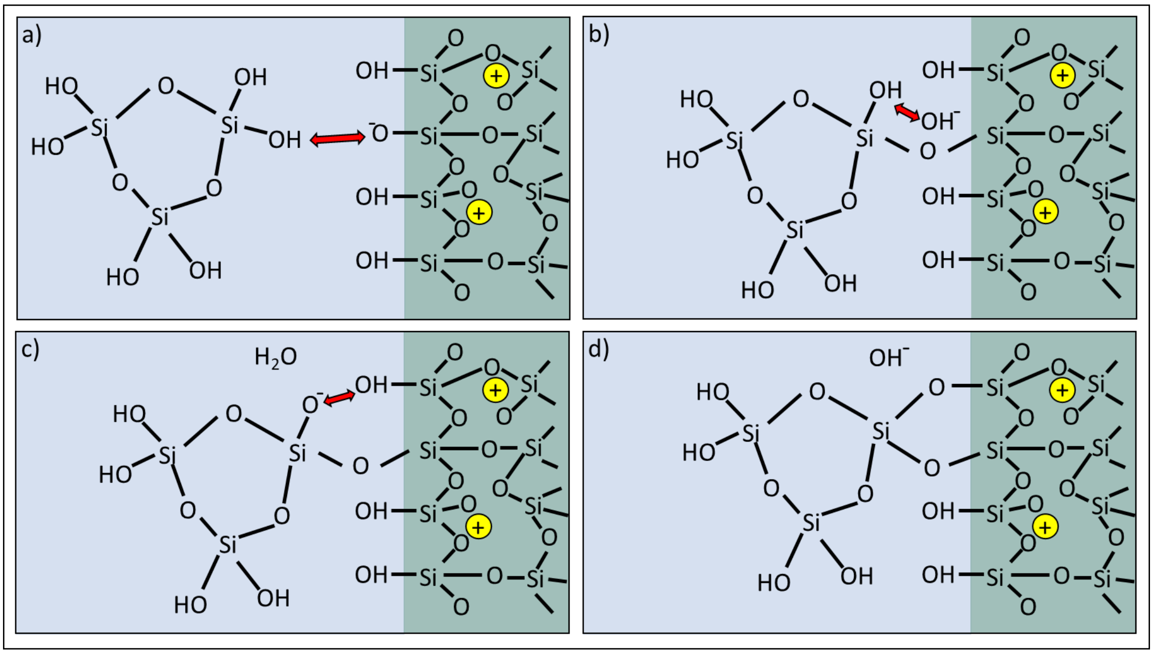

Figure 9: Proposed mechanism of silica deposition and initial silica precipitation.

3.2.4 Impact of temperature and solution pH on hydrolysis and condensation reactions

While the impact of temperature and pH on the glass dissolution rate can be determined under far from equilibrium conditions (2.3.1), the methods and corresponding models may fail to calculate overall glass corrosion rates in silica saturated solutions. This is because the SAL formation, which can include an amorphous silica-rich corrosion layer and eventually formed secondary phases, also depends on pH and temperature in a very different way like network hydrolysis and therefore the glass specific rate law parameters are not sufficient to correctly describe the overall reaction.

I must be emphasized that both dissolution of the glass and polymerization of dissolved silica strongly depend on the pH due to the catalytic effect of H_3O^+ and OH^- (3.2.2 and 3.2.3). However, the ZPC of glass and silica is located at different pH values, and the reaction rates for glass dissolution and silica condensation have different, even contrary pH dependencies, as contrasted in Figure 10. While the ZPC of pure silica is well defined, the ZPC of silicate glasses varies depending on glass composition, e.g., the Al_2O_3 content [116], but is usually located at slightly higher pH (3 to 4) [2]. These and other aspects are summarized in Figure 10, including the silicic acid speciation at 25 °C, the amorphous silica solubility at 25, 30, 55, 70 and 90 °C, and the relative sol stability/gel time. The speciation and solubility curves were calculated with the geochemical software PHREEQC [133]. Note that for the lower pH region, the Cherkinskii equation (black dashed line) describes a comparatively slight increase in silica solubility with decreasing pH (with the minimum at pH 7) [108]. Even though the reason for the slightly higher solubility between pH 2 and 7 is not known, it has been confirmed by various experiments, reviewed by Iler [108]. Below pH = 2, the formation of cationic silica is assumed [108,134], which can explain the observed changes in relative gel time and silica condensation rate due to the acid-catalyzed condensation reactions (VII) and (VIII). The calculated solubility curves and silica speciation in strongly acidic pH regime must be taken with caution as a cationic silica species is not implemented in the used database. The exponential increase of silica solubility with rising pH values above approximately 10.5 at 25 °C can be attributed to the formation of deprotonated silicic acid ($H_3(SiO_4)^-$ and $H_2(SiO_4)^{2-}$), which both were considered in the calculations. Under this hyperalkaline conditions, silica prefers to dissolve and crystalline secondary phases may become thermodynamically more stable. The opposite course of the silica condensation rate and sol stability curves is not surprising, since the condensation reaction between two silica monomers and particles are essentially the same, i.e., condensation occurs between an ionized and non-ionized $Si-OH$ group [108,132]. Therefore, a higher condensation rate automatically decreases the stability of a sol, because they will attach faster to each other. However, it should be mentioned that the sizes of the silica species, including monomers, dimers, and higher polymerized species changes their ionization properties. For example, the pK_A value is 9.9 of an $Si(OH)_4$ monomer an therefore much higher than that of higher polymerized oligomers which is about 6.7 [108,109]. Hence, their ionization state is different. Correspondingly, the agglomeration rate of primary silica particles or oligomers also depends on their size and not just the pH value of the surrounding solution. Due to the higher ionization of silica particles and oligomers, they repel each other because of electrostatic repulsion allowing the stabilization of silica sols under alkaline conditions in salt free solutions. However, counter ions can cover the negative surface charge, which reduces the gel time and thereby changes the SAL microstructure. If the salinity is high enough, silica will rather precipitate to an aggregate that has a higher concentration of silica than the original sol via coagulation [108].

Considering an Arrhenius behavior, reaction rates are usually accelerated by increasing the temperature by orders of magnitude. Regarding the polymerization of MSA the temperature dependency seems to be in contradiction to this, since results of Rothbaum and Rhode [125] revealed decreasing polymerization rates between 50 and 120 °C in geothermal waters. However, the polymerization rate is just the result of a forward and backward reaction, i.e., condensation and hydrolysis of dissolved silica species. Therefore, the rising temperature probably rises the reaction kinetics of both condensation and hydrolysis, but to a different degree, which is ultimately reflected in the microstructure and grade of polymerization of the SAL for corroded glass samples. Lenting et al [34] showed that the diameter of silica spheres building up the SAL depends on temperature. Under the same experimental conditions ($pH_{90°C}$ 7, silica free solution) a quaternary borosilicate glass (QBG), containing 65.9 mol% SiO_2, 17.9 mol% Na_2O, 11.9 mol% B_2O_3, 4.2 mol% Al_2O_3, and 0.09 mol% of CaO, was replaced by larger silica spheres at 150 °C (~15 nm diameter) than at 90 °C (~5 nm diameter). This is in accordance with observations made by Rothbaum and Rohde [125] that show the favored formation of less but larger polymers and preferred silica deposition above 90°C. Accordingly, it seems logical that fewer but larger silica particles will from after densification and phase separation. This is also supported by a strong temperature dependency of silica sphere size to particles that can grow even to 150 nm in diameter at 350°C [108].

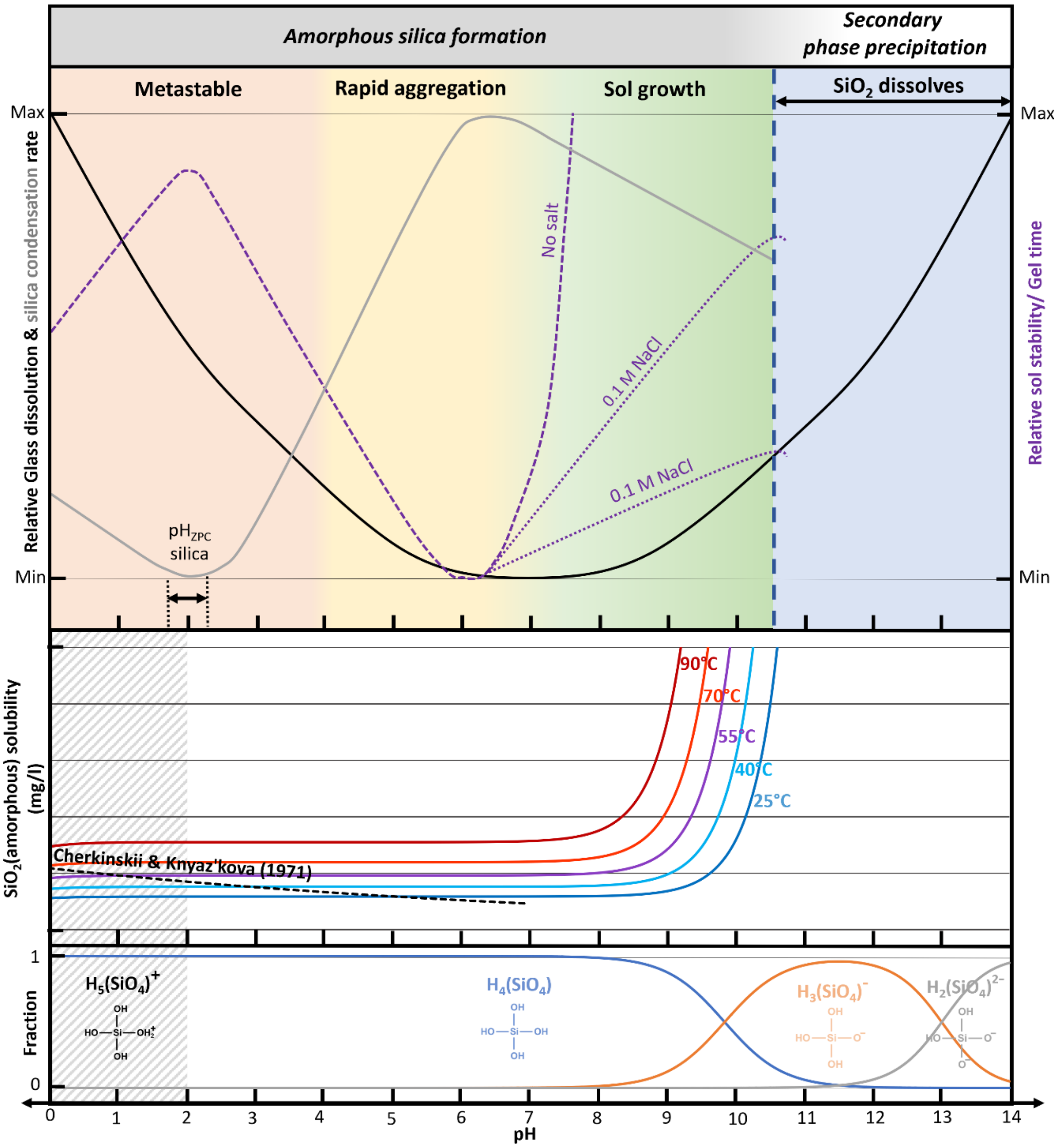

Figure 10: Effect of pH on (*top*) glass dissolution rate (black line) and silica condensation rate (gray line), and the sol stability/gel time (purple dashed and dotted lines) including the lowest rates at the zero point of charge (ZPC) of silica and the altered gel time in presence of salts (NaCl) [108,131,135], (*center*) amorphous silica solubility in mg/l for the different temperatures, with the dashed line calculated from Cherkinskii-equation $\log C_M = -2.44 - 0.053(pH)$ (after Ref. [108]), and (*bottom*) speciation of dissolved silicic acid calculated for 25 °C and a solution containing 200 ppm of SiO_2. The software PHREEQC [133] and the SIT database (thermodynamic database Thermochimie V9b [136]) were used for calculations. Note that a cationic species $H_5(SiO_4)^+$ as was not existing in the database, but $H_5(SiO_4)$ will form at pH values below 2 [108,134]. Therefore, the data in the gray hatched area are not as accurate, but show the general trends of the properties of aqueous silica in highly acidic solution.

The impact of pH and temperature on the saturation state of amorphous silica, dissolution kinetics, the thermodynamic stability of amorphous and crystalline reaction products, and the kinetics of condensation and gelation are of crucial importance to understand the feedbacks that occur during glass corrosion. Therefore, the dependencies of the identified reactions, transport processes, and their feedback is summarized by Figure 11, for (a) initially undersaturated conditions, (b) (over-)saturated conditions, (c) the presence of an interface fluid film after silica precipitation, and (d) the possibly occurring resumption of glass alteration.

3.2.5 Feedback I: Local solution properties and glass dissolution

A concentration gradient between the initial surface of the glass and the bulk solution will immediately form when the pristine glass starts to dissolve in the adjacent boundary layer. This gradient drives diffusion of all solute glass components and leads to their fractionation in space and time, depending on the specific diffusion coefficients. Naturally, these concentration gradients will equilibrate by diffusion in the bulk solution. However, it can locally be superimposed by ongoing glass dissolution. As an alternative to a purely diffusion-based transport process, perturbation of the solution by thermal convection of the solution, stirring or continuous solution exchange can reduce the extent of such gradients and homogenize the solution. Depending on whether purely diffusive or diffusive and convective solute transport takes place, the ratio between transport and dissolution rate must determine the solution properties at the glass surface and the extent of surface gradients. This is consistent with experimental observations showing a totally different corrosion behavior when the solution is renewed instead of applying static conditions, even if the bulk solution remains very diluted [104] and can be attributed inter alia to surface near affinity effects by formation of a boundary layer. If the bulk solution becomes more enriched in glass constituents at a certain time, the smaller gradients between the boundary layer and bulk solution will in turn result in reduced diffusional fluxes from the reaction interface into the bulk solution.

Another solution parameter that is probably the most relevant for aqueous glass corrosion and any changes with time and space [40,41,65] is the solution pH. Numerous experiments, that have been performed under different conditions using various types of glasses, showed a pH change of the bulk solution if no buffering or pH adjustment was conducted [36,39,79]. The pH change and the local solution composition adjacent to the glass surface will influence the local glass dissolution rate, which in return affects the amount of glass constituents being released into solution [48,67,121]. This feedback effect, labeled with I in Figure 11a and 11c, may increase or decrease the dissolution rate by several orders of magnitude and is thus of key importance to predict the long-term durability of glasses. To capture this feedback of solution advance on further glass dissolution Wang and coworkers [48] postulated that the release of cations causes a rise of the pH, because the concentration of OH^- anions must increase by increasing cation concentration to ensure charge

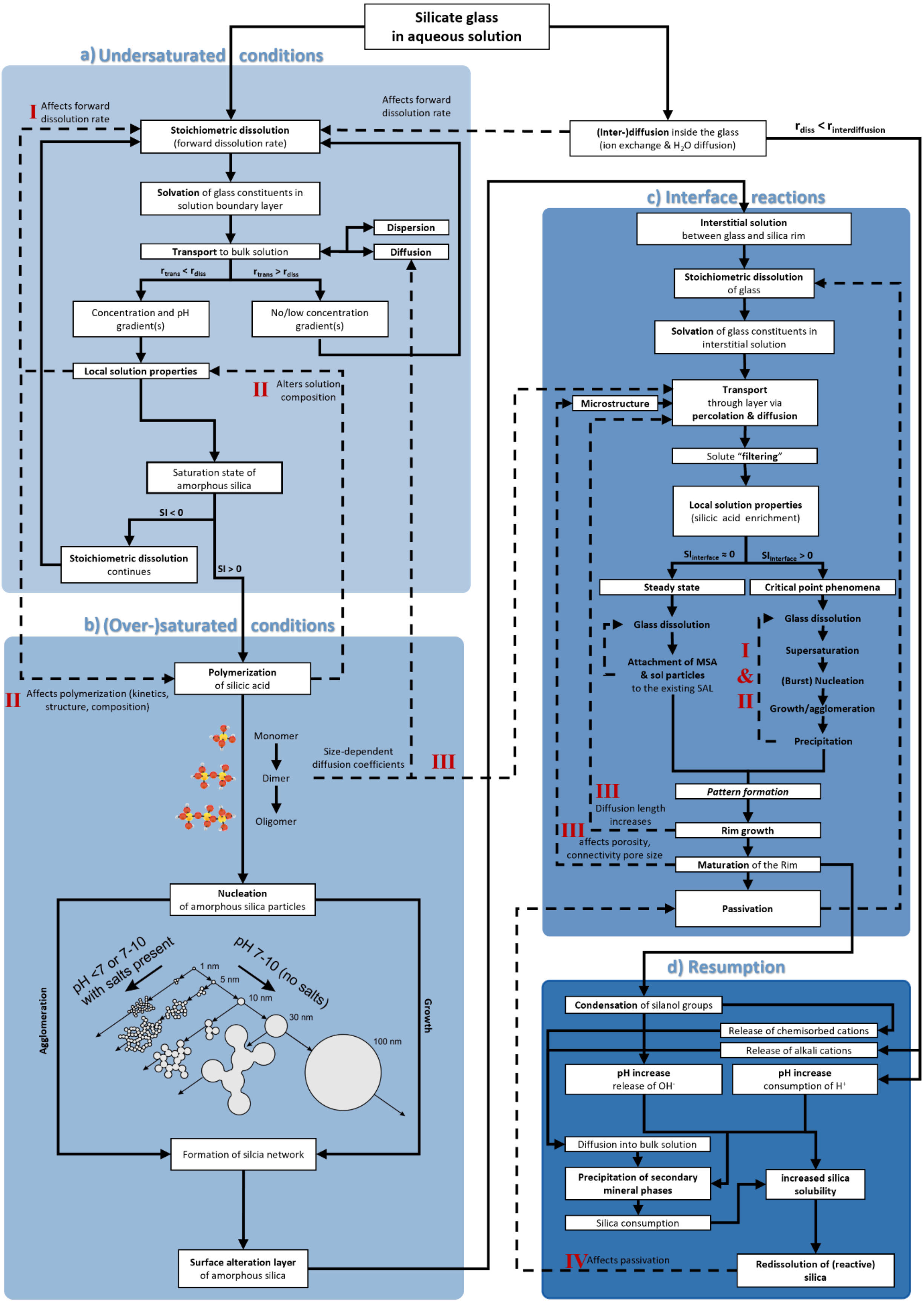

Figure 11 : Flow chart of reactions and feedback loops (labeled with red colored Roman numbers) in the proposed ICDP model (modified after Lenting [31] and subdivided into four main sections). The polymerization scheme of silica (left side) was redrawn after Iler [108].

balance ($\Delta[OH^-] \approx \Delta[\text{cation}]$). In turn, this may autocatalytically accelerate the dissolution reaction according to the discussed pH effect in Chapters 2.3.1, 3.2.2 and 3.2.4, because of the typical V/U-shaped pH dependence, and result in higher cation release and further pH rise.However, the mechanism of hydroxyl ion formation was not discussed by Wang and coworkers. Keeping charge balance is mandatory, but if OH^- is formed by simple dissociation of water, the pH value will not change, and the charge will not be balanced because the chemical reaction Equation (XI) produces the same amount of H^+:

$$H_2O \rightleftharpoons OH^-_{(aq)} + H^+_{(aq)} \tag{XI}$$

Therefore, the pH can only rise if the concentration of H^+ will be reduced or OH^- be produced by another reaction. One reason for the changing pH is probably the formation of hydroxyl ions by complete hydrolyzation of the oxidic alkali and earth alkali glass components, according to reaction Equation (XII)

$$M_2O + H_2O \rightleftharpoons 2\,M^+_{(aq)} + 2\,OH^-_{(aq)} \tag{XII}$$

Based on this, the coupled overall changes of cation and OH^- concentrations proposed by Wang [48] is reasonable. Another OH^- source may be the production by the hydrolysis of ionized silanol groups by H_2O or the reduction of H_3O^+ by a reaction with the surface sites according to reaction Equations (XIII) and (XIV), respectively:

$$\equiv Si - O^-_{(s)} + H_2O \rightleftharpoons \equiv Si - O - H_{(s)} + OH^-_{(aq)} \tag{XIII}$$

$$\equiv Si - O^-_{(s)} + H_3O^+_{(aq)} \rightleftharpoons \equiv Si - O - H_{(s)} + H_2O \tag{XIV}$$

Such surface reactions probably have a minor effect on the bulk solution pH in high solution volumes compared to the changes induced by alkali/earth alkali oxide dissolution according to reaction Equation (XII), but can be highly important for the local solution pH in the boundary layer [40] or at high (local) SA/SV ratios (c.f., Chapter 2.3.4).

In addition to the known effect of the solution pH, it has been observed that the presence of some dissolved cations [46,76–78] and the chemical affinity (approaching equilibrium/steady state conditions with respect to a certain product phase, e.g., amorphous silica) [15,18,40,42,67,68,97] also affect the dissolution reaction and SAL formation (2.3.3). Note that the competitive reaction Equation (XV) of binding alkali cations (e.g., Na^+) instead of H_3O^+ (13) may happen simultaneously and the extent of this reaction depends on the alkali cation concentration [115]. This reaction may also reduce the bond strength of the surrounding $Si - O$ bonds and facilitates the hydrolyzation of glass network [69,78]:

$$\equiv Si - O^-_{(s)} + M^+_{(aq)} \rightleftharpoons \equiv Si - O - M_{(s)} \tag{XV}$$

It follows that the ongoing release of glass constituents by stoichiometric dissolution complexly influences further glass dissolution, here referred to as feedback I. Due to the increasing MSA concentration when a glass dissolves, the decreasing chemical affinity reduces the dissolution rate already from the beginning of a dissolution experiment [40,42], even if the bulk solution is highly undersaturated with respect to amorphous silica [15,68,97]. The underlying molecular mechanisms of how alkali and alkaline earth elements affect dissolution reaction is poorly understood, but it is assumed that some alkaline earth and alkali ions occupy surface sites of the glass and make the surrounding $Si-O$ bonds more easily hydrolysable [69,78].

3.2.6 Feedback II: Local solution properties and SAL formation

If a solution is sufficiently supersaturated with respect to amorphous silica, previously formed oligomers will densify by intramolecular condensation reactions. The reduced amount of functional silanol groups is the reason for separation of solidified silica particles, which no longer belong to the dissolved species [108,131]. Instead, they have become solid, dispersed particles. These primary silica particles may grow via monomer addition to larger silica particles or aggregate, depending on their size and the solution properties [108,109,124]. The effect of ionic strength, pH, presence of specific metal ions, and temperature has been examined very intensively in sol-gel literature [108,109,124] and helps to understand similar interdependencies observed in SALs formed under equivalent conditions [106,137]. As shown in the scheme of silica polymerization in Figure 11b, differences in pH and salinity have a great influence on particle size and the degree of branching of precipitated silica gels. Especially under acidic conditions, the MSA polymerizes to linear chains and finally forms a dense gel network with no visible primary particles compared to the relatively big, spherical shaped, primary particles of highly branched clusters formed under rather neutral and alkaline conditions [106,108,109].

Concerning glass alteration, a few studies [46,47,73,77,78] merely correlate the presence of different alkali, alkaline earth, and transition metals with changing macroscopic corrosion rates (c.f., 2.3.3), already mentioned in the previous section of feedback I. But it was also observed that the presence of certain elements also affect the physical SAL properties and its composition [31,34,56,73,106,137]. However, a detailed discussion about how these ions affect the mechanism and the kinetics of SAL formation on a molecular level is missing. A universal glass corrosion model should be able to describe the influence of the solution composition on the mechanism to develop a numerical model that correctly considers these effects. Nevertheless, data from such studies are very helpful for statistical correlations and machine learning approaches and help to understand the interconnections and influence of specific parameters on overall corrosion rates in such complex systems, because an explicit description of all possible molecular reactions and SAL phases may be an unsolvable challenge.

3.2 Identified reactions and feedback loops

In sol-gel chemistry, the effect of salts and electrolytes is explained in general by acting as a coagulant at pH values above 6 if their concentrations are high enough. This is indicated in Figure 10 by a reduced gel time compared to salt free solutions [108,130]. Sol destabilization with respect to particle-particle agglomeration is based on charge compensation and reduced repulsion of the negatively charged primary silica particles. Consequently, the particles can attach to each other more easily and get linked together by condensation of surface silanol groups. It is also known that the effect of divalent cations (e.g., Mg^{2+}, Ca^{2+}) are much stronger than that of monovalent cations (e.g., Na^{+}) [130]. In addition to the reduced gel time, a high salt concentration lowers the amorphous silica solubility and increases the polymerization rate [125]. Since the ICDP mechanism is based on analogous reactions, the knowledge from sol-gel chemistry is helpful to understand how the presence of alkali and alkali earth metals affect the SAL formation, especially the growth and agglomeration of primary silica particles.

Some cations will also be incorporated in the SAL, rather than just affecting its formation kinetics and microstructure, depending on the initial solution and glass composition [46,47,76]. For example, Ca^{2+} can catalyze the condensation reactions of silica [73], enable CSH precipitation above $pH_{90°C}$ 10 [56,73,78], and modify the microstructure of the formed SAL. At $pH_{90°C}$ values above 9 and if the solution reaches an apparent saturation state of silica, dissolved Ca has a rate-decreasing effect and will be incorporated in the so-called gel layer [47,73,76,78,100]. It is suggested that it does not matter if Ca originates from the glass or the solution [73]. However, the presence of other elements within the glass may also have a significant impact on glass corrosion. Zn and Fe were shown to increase the dissolution resistance of glasses, compared to reference glasses which are having the same SiO_2: B_2O_3: Na_2O molar ratio of 4.7:1.3:1 in a study of Gin and coworkers [58]. This results in a lower dissolution rate during *Stage I* by increasing the hydrolytic resistance that is also known from other heteroatoms when they are added to the glasses [10] or amorphous silica [51,107] (e.g., Zr, Al). Nevertheless, the *residual rate* in *Stage II* still can be higher, because of possibly reduced passivating properties of the SAL and the formation of precipitates (e.g., Fe silicates) formed under certain conditions [58,107]. The effect of Fe in direct contact with water was recently studied by Guo and coworkers [138], who found that ISG that is in direct contact to stainless steel creates different corrosion regimes. The different local chemical environment created localized corrosion of metal and the authors also suggest that the glass corrosion rate was also enhanced in the presence of metal ions. However, this effect strongly depends on the leaching solution.

It is usually not known whether the alkali/earth alkali elements are incorporated in the silica network, chemisorbed at reactive surface sites, or merely trapped in the pore solution during the corrosion process. However, the role as counter ions is accepted for most of the mechanistic models for SAL formation. In contrast to this, *inter alia* Al and Zr, which also act as network formers in the parental glass phase [123,139], can be incorporated in structure of synthetic silica gels [106] and can be found in SALs formed by alteration of different reference glasses (e.g., ISG, SON68) [34,100,137]. The reactions required for this are probably the same as for pure silica, i.e., condensation of hydrolyzed metal cations. Especially, silica stabilization by Zr and Al crosslinking with Si might be the reason for stabilization of silica-rich SALs, even if the SiO_2 solubility is quite high.

As mentioned already before, the ICDP mechanism is not limited to the precipitation of pure silica. Compatible elements are rather incorporated into the SAL structure, similar to silica gels of SAL like compositions formed by sol-gel methods [106,137]. And furthermore, mobile elements such as alkali metals may be chemisorbed at the reactive surface sites for charge compensation according to reaction Equation (XV). The stable SAL/silica gel modification and its composition, in turn, depends on the local solution properties and the thermodynamic conditions.

It can be concluded that the evolving solution properties at the ICDP interface, including pH, the ionic strength, and saturation state of amorphous silica or another amorphous silica-rich product phase, will affect the composition and polymerization, growth, and agglomeration kinetics of primary SAL particles. The polymerization and precipitation of a silica-rich SAL will deplete the local solution next to the glass surface with respect to compatible elements, which, in turn, influences further glass dissolution and following polymerization reactions. This feedback is denoted by II in Figure 11. As clearly shown in the flow chart, both feedback cycles, I and II, relate to each other by the local properties of the interface fluid that directly couples the dissolution and precipitation reactions.

3.2.7 Feedback III: Transport through SAL and local solution properties

Once the glass surface is covered by an SAL, the ongoing glass dissolution underneath will lead to the formation of a gap in between that is filled with dissolved species, which was detailed in the introduction to the ICDP mechanism (3.1). As already mentioned in Chapter 2.1.3, there is evidence for the existence of an interstitial fluid layer, such as the direct observation of a water-rich interface by fluid-cell Raman spectroscopy [40,41] and the hydrogen enrichment at the reaction front observed in *post mortem* ToF-SIMS analyses of experimentally formed SALs [38,43,53,54,56,90]. In this chapter, the effect of an SAL on the reactions and feedbacks within the interface solution will be discussed. First, it should be clear that both the reactions and feedbacks are essentially the same whether they take place in the interface solution or while the glass surface is directly exposed to the bulk solution. Thus, the glass dissolves as long as free water molecules are present at its surface. A silica-rich phase will precipitate once a critical oversaturation is reached or MSA is consumed by growth of the silica particles (Figure 11b), and especially the local solution conditions are affected by these reactions and *vice versa*.

What comes into effect in the third part (c) of Figure 11 is the fact that the SAL separates the interface solution from the bulk solution by slowing down the diffusion velocity and/or even act as a selective molecular sieve if the pore size is in the range of the hydrodynamic radii of the solvated species [31,94]. This can dramatically change the solution conditions of this interface fluid layer and result in an MSA-enriched, highly saline interface solution, which in turn can alter the nature of silica gel that forms. The ongoing replacement of glass by the SAL, also called rim growth in Figure 11c, and its maturation will increase the diffusion length and affects its porosity. The porosity, connectivity, and pore size are summarized here as SAL microstructure, which is assumed to be a transient feature [9,56,92].

Most of the tracer experiments in literature show a significant difference between the isotopic composition of the outermost part of the SAL, representing the first silica precipitated onto the glass surface, and the rest of the SAL [20,34,56,94,105]. There are silicon isotope studies, where the corrosion rim was observed to consist almost entirely of Si that originates from the glass itself, even if the solution initially contained dissolved MSA [36,94]. Nevertheless, Si originating from the bulk solution was also found to be incorporated in the precipitated silica if the SAL is less dense and allows diffusional transport of Si-species through this layer [36,105]. Because the porosity and pore connectivity of the SAL, depending on several solution parameters (*c.f.*, Chapter 2.1.4) and may change with time, the diffusional transport conditions through the SAL also change during the corrosion process. An ICDP mechanism, where the precipitated SiO_2 can incorporate silicon isotopes according to the actual isotopic composition of the boundary layer by the mechanism proposed (Figure 5), is in accordance with the isotope tracer studies mentioned here. Once the glass surface is covered completely by silica, the equilibration of MSA originating from the glass and MSA originating from the bulk solution can be inhibited by reduced diffusional transport through the SAL [36,40]. Therefore, the isotopic ratio of the silica gel can vary gradually, with increasing thickness by extension of the diffusional transport distance between the reaction (dissolution and precipitation) front and the bulk solution, as observed by Valle and coworkers [105].

The microstructure, thickness, and the species-dependent diffusion coefficients are all denoted by a red colored III in Figure 11 and affect the diffusional transport through the SAL. This will determine the local solution properties of the interface (and pore) solution as a function of time. Because the solution properties will, in turn, determine the further growth and maturation of the SAL, the SAL transport properties and interface solution properties represent the third feedback loop that was identified. How the rim growth will happen is described in more detail in the following, considering the frequently observed chemical and structural patterns [24–26,34,39,46–49,84,85].

3.2.8 Feedback IV: Passivation properties of the surface alteration layer and secondary phase formation

There is still no agreement about a universal mechanism that is responsible for the formation of a surface alteration layer (SAL) formation, even if the previous sections showed that the ICDP mechanism seems to be the best candidate. Nevertheless, it seems to be obvious that the lowered corrosion rate is related to the formed SAL that can act as a diffusion barrier between the reaction front and the bulk solution [5,10,21,40,59,60](c.f., Chapter 2.1.4). It follows that the growth of the SAL increasingly drives the interface solution away from equilibrium with the bulk solution, which is, as feedbacks are, a prerequisite for self-organized pattern formation [140].

As mentioned already before, the glass dissolution rate is slowed down by increasing SiO_2 concentration, because of increasing chemical affinity effects. On the one hand, glass dissolution will enrich the solution (especially near the surface and in the interstitial solution) with glass constituents, but, on the other hand, SAL formation will consume SAL compatible elements, especially Si. Neither SAL growth via steady state nor growth via sequential burst nucleation events (c.f., Chapter 3.2.8) provides an easy explanation for the passivation effect. The dissolution of glass and formation of silica, mediated and coupled by an interface solution, theoretically should proceed, even if diffusional exchange between the interstitial and bulk solution is inhibited. This is based on the thermodynamically driven inherent character of the replacement reactions of metastable glasses, based on the relative solubility difference between glass and the corrosion product [36,93,111,112].

This leads to the question: What causes the passivation and stops further growth of the SAL? As anticipated already in the introduction to the ICDP model (Chapter 3.1) and in Chapter 3.2.7, an increasing SAL thickness and potential densification will increase the diffusional transport distance along the pore space of the SAL between the interface and bulk solution [34]. This in turn reduces diffusional transport for all dissolved species and water through the SAL and results in a highly saline interface solution with a pH that in the most cases will be higher than the bulk solution pH (with the exception of extremely high initial bulk solution pH values), because of the alkaline character of alkali-(boro)silicate glass dissolution. These assumptions were confirmed experimentally for a ternary Na borosilicate glass (TBG) by electron microprobe chemical analyses and pH monitoring using fluid-cell Raman spectroscopy [40,41].

Besides triggering burst nucleation, passing a critical supersaturation can also lead to the transformation of the interstitial solution to a porous, polymeric silica gel that is interpenetrated by the residual water [108,109]. Such a gel is made up of agglomerated primary silica particles attached to each other, forming branched chains and ends up with a three-dimensional network that occupies the total volume of the interface [108]. The interface solution is then rather a continuous solid network with a high amount of pore solution, which inhibits solution movement through the porous gel and transport of Si species. At this stage, further dissolution of glass is also suppressed due to the lack of free water and the condensation of the water-rich interstitial gel with most of the reactive surface sites of the glass. Indeed, the primary SiO_2 particles here can be very small (1 - 10 nm) cyclic or polycyclic polymer units and the particle size and gel structure depend on both, the local solution pH and salinity as illustrated in Figure 11b [108,109,124]. This is because the agglomeration and growth rate depend on these parameters and determine for how long these particles can grow before they are linked together to precipitate or gel, which is emphasized in Figure 10 as gel time/sol stability.

A gel that is formed this way is still partly hydrolyzed and interpenetrated by pore solution, which makes it more reactive compared to a densified, completely condensed silica particle or precipitate. This is in line with (i) the observed high hydrogen concentrations at the reaction front revealed by several ToF-SIMS analyses of corroded samples [38,43,53,54,56,90] and with (ii) fluid-cell Raman experiments, revealing a water-rich silica layer between the SAL and the pristine glass [30]. The general assumption of an interpenetrating pore solution is also supported by results of other fluid-cell Raman experiments, which showed a strong water signal within the SALs, the presence of many surface $Si-OH$ groups, and H_2O/D_2O diffusion through the SAL [31,40,41,45,141].

In principle, one could even make use of such a passivation to improve the chemical durability of technical glasses. However, the most crucial point in predicting the long-term stability of (nuclear waste) glasses is *Stage III* of glass corrosion, i.e., the possible *resumption* of the glass alteration rate, because its estimation bears a lot of uncertainties. The *resumption* of the corrosion rate often coincides with the formation of crystalline and/or amorphous precipitates, so called secondary phases (e.g., zeolites, phyllosilicates, and C-S-H phases), on the surface of the amorphous corrosion layer or in its pore space [43,99,101,114]. The formation of secondary phases can be described by precipitation when reaching a local supersaturation with respect to a certain phase. This will trigger SAL redissolution and further glass dissolution, because the consumption of MSA will lower the chemical saturation state of silica in solution controlling the chemical affinity.

The reactions during the *residual rate* stage that influences the solution chemistry and destabilizes the silica gel can be, e.g., ID [31,34], residual stress [9], and maturation/syneresis [109,114] of the silica gel layer (Figure 11d). Syneresis of the silica gel by proceeding condensation of silanol groups will reduce the concentration of reactive surface silanol groups and will release water:

$$(\equiv \mathrm{Si-O-H}) \; + \; (\mathrm{H-O-Si} \equiv) \quad \rightleftharpoons \quad (\equiv \mathrm{Si-O-Si} \equiv) \; + \; \mathrm{H_2O} \qquad \text{(XVI)}$$

Such densification reactions and water expulsion can induce stress and crack formation. Furthermore, a local release of molecular water in the pore space may increase the solubility and thus locally cause the redissolution of the SAL or enables further glass dissolution at the reaction front. Ngo and coworkers [9] also mentioned that residual stress within the SAL may lead to crack formation, and in turn allows direct contact between the bulk solution and the reaction front, which could trigger *Stage III* by reducing the passivating properties of the SAL.

Due to the competing effect of alkali elements and H^+ ions to occupy the NBO positions [115] of negatively charges surface sites, some alkali ions, especially at high concentrations, are also chemisorbed at the silica surface. On the microscale, such an effect is called salt retention for colloidal silica particles [108] and is based on the role of alkali metals as counter cations. The condensation of a hydrolyzed NBO and an NBO linked to an alkali element, e.g., Na^+, will release OH^- and Na^+ and change the pH and salinity of the pore solution, which can be written as:

$$(\equiv \mathrm{Si} - \mathrm{O} - \mathrm{Na}) + (\mathrm{H} - \mathrm{O} - \mathrm{Si} \equiv) \quad \rightleftharpoons \quad (\equiv \mathrm{Si} - \mathrm{O} - \mathrm{Si} \equiv) + \mathrm{Na}^+ + \mathrm{OH}^- \qquad \text{(XVII)}$$

This reaction is just another possible reason for an increasing concentration of alkali metals within the pore/interface solution and induce pH variations which may trigger the *resumption* of glass alteration. In turn, an undersaturation of the interface, pore, and/or bulk solution with respect to amorphous silica, likely enables redissolution of the amorphous SAL.

The thermodynamic stability of the secondary phases also depends on pH, which usually changes with time during glass corrosion [9,36,39–41,79]. In fact, the pH value may increase or decrease during the glass corrosion process, depending on the kinetic stage, glass composition, and initial solution, i.e., its pH and composition. A resumption at, e.g., $pH_{90°C}$ 11 can lead to a decrease of the solution pH [9], which, in turn, allows the redissolution of certain precipitates that are no longer stable. The pH-reducing effect of *secondary phase* precipitation grounds on the alkali element (e.g., Na, K) consumption [43,101,142]. It was also observed that the dissolution of a ternary Na-borosilicate glass, starting at $pH_{90°C}$ 7, increased the solution $pH_{90°C}$ up to about 9 already after a few days of corrosion [36,40]. In fact, the pH value is known to change significantly during glass corrosion, caused by the glass dissolution process itself [48] and the alkaline acting basic molecular reaction Equations (VII), (VIII), and (IX). Apart from this, when the dissolution reaction of the glass network is slowed down, the pH of the interface solution can still change with time by the release of alkali elements via ID processes [48,121].

But what is the consequence if a *secondary phase* becomes more stable than the amorphous silica phase that is present at a certain location within SAL? The answer seems obvious based on the results of the literature review in the previous chapters. The SAL phase will be replaced via ICDP reactions by the *secondary phase*, because of its solubility difference, analogous to the glass replacement reaction. It is suggested here that the ICDP mechanism is also an important mechanism that allows the re-equilibration of the SAL phase assemblage, i.e., a *secondary phase* may be replaced by another phase provided it has a lower solubility. Nevertheless, it is not clear if the secondary phases may precipitate from solution directly, without affecting the primarily formed gel-type SAL, i.e., re-dissolve it. It is also unclear if the *secondary phase* formation is just kinetically inhibited during the *residual rate* or if changes in solution chemistry and destabilization of the silica gel triggers this event [9]. This thermodynamically based ICDP concept, that assumes local equilibria, is also in accordance with the observation that glass is replaced directly by crystalline phases instead of an amorphous intermediate phase, which has recently been observed during the corrosion of a Ba-bearing silicate glass [45]. The notion of very local equilibria is also supported by the observation that a silica-based SAL can form, although the bulk solution is not saturated in amorphous silica [35]. Different SA/SV ratios also affects the nucleation time, shape, and composition of secondary phases, such as zeolites formed during corrosion of a quite complex surrogate glass at 50°C under hyperalkaline conditions ($pH_{50°C}$ 12.6) [142]. However, the limiting components in the experiments for zeolite formation (Al, Si, or alkali metals) originate from the glass and are released by dissolution. Therefore, it seems obvious that the higher the SA/SV ratio, the less glass must be dissolved to reach saturation with respect to the thermodynamically stable *secondary phase*. It can be concluded that the SA/SV ratio rather accelerates alteration kinetics than changing the glass corrosion mechanism. In general, the advantage of performing experiments under high SA/SV ratios is that shorter reaction times are necessary to pass the different kinetic stages of glass corrosion and reach supersaturation with respect to precipitating corrosion products [9,14,58,61,73,79]. In this way the long-term durability of glass can be investigated more efficient in terms of time, because the SA/SV ratio is assumed to have no or minor effect of the magnitude of the residual rate [9,58]. Apart from the relevance of an overall parameter, the local SA/SV ratio is also important when considering interface solution films between the glass sample and surrounding materials [138], pore fluids, and experiments performed under H_2O vapor or partially immersed conditions [13,14]. In all these cases, the small volume of solution next to the glass surface without sufficiently fast equilibration with a larger bulk solution volume may strongly change the local solution chemistry (e.g., pH, salinity) and saturation state with respect to a secondary corrosion product phase dramatically over short time periods [9,10,14,78,138].

In general, the formation of secondary phases may be kinetically inhibited and strongly depend on the (local) solution composition. Re-equilibration by Ostwald ripening processes and changing environmental properties may induce stabilization of thermodynamically more favored crystalline secondary phases, compared to a previously formed amorphous silica-rich SAL, which in turn destabilizes the SAL and enable its replacement, again via a ICDP-based reaction mechanism. This is because redissolution or maturation of the initially formed protective layer can reduce its passivating effect (labeled with a red IV in Figure 11). It follows that the identified feedbacks III and IV are connected by the passivating properties of the SAL.

3.2.9 Surface alteration layer growth and pattern formation: Steady state vs. critical point phenomena

In previous chapters, it has been shown that the growth of an SAL drives the interface solution, where the ICPD reactions take place, away from equilibrium with the bulk solution, which is a critical prerequisite for self-organization of the SAL. The microstructure of the SAL has great impact on the transport properties between the interface and bulk solution [10,21,31,34,43,58,60,86,94]. The microstructure depends on several parameters, such as glass composition [20,56], solution composition [47], solution pH [50], reaction time [9,55,92] and temperature [34]. It is remarkable that the SALs are usually not homogeneous, but rather represent a sequence of different layers, which clearly indicate non-equilibrium conditions during their formation. The layers can have both a chemical and structural differences and are seen in the form of nanometer to micrometer scaling patterns [11,24–26,34,39,45–49,84,85]. A representative selection of very impressive patterns is given by Figure 1. With the exception of the ICDP mechanism, none of the existing models is able to explain these striking and frequent corrosion features. The elegance of the ICDP mechanism is given by the fact that the glass dissolution, silica-rich SAL precipitation, and their spatial and temporal coupling by an interface solution, including several feedbacks, are sufficient to explain all observed corrosion features reviewed in Chapter 2.1. This, in particular, includes the intriguing structural and chemical patterns. A varying microstructure and chemical composition of the SAL reflects the variations in the interface solution compositions at a given point in time and space. Based on sol-gel chemistry of silica, the growth via a continuous steady state route takes place by attachment of excess silicic acid in the interstitial solution at the already precipitated silica via monomer-addition [118,125,127,128,130], or continuously form new primary silica sol particles which attach to the SAL [108,109,131]. While the interface solution is slightly supersaturated and no steric inhibition of further glass dissolution occurs, the silica rim may grow continuously. As glass dissolution progresses, it can then theoretically reach a steady state growth rate. The glass is then replaced by amorphous silica, and/or by other secondary phases, by an inwardly moving reaction front. In practice, such a steady state replacement reaction is at odds with the generally observed rate drop (2.2), except under certain conditions [43,45].

But what is the reason for the alternating layers of amorphous, silica rich SALs and free void space (gaps) in between? The multiple SALs that are separated by free space can be explained by a large loss of volume associated with the replacement reaction. In addition to a high proportion of well soluble components (e.g., alkali elements, B), which can be responsible for such a high loss of volume, a high pH increases the solubility of SiO_2 and less silica will reprecipitate. That is probably the reason, why the formation of gaps was observed in micrometer scale exclusively for altered, corrosion-prone glasses [25,26,39–41] or such that have been corroded under hyperalkaline conditions [44,45].

3.2 Identified reactions and feedback loops

As long as the interface solution is supersaturated with SiO_2, the MSA and sol particles probably attach to the already precipitated silica-rich rim and thus the rim will grow in direction of the dissolving glass. The dissolution and precipitation reactions may change the interface solution properties (feedback I, II in Figure 11) and the related SAL growth affects the transport between interface and bulk solution (feedback III). Beside pure continuous growth of the SAL, which may explain gradual changes of the SAL chemistry and microstructure, a second competing process is proposed [31]. A steady state competing *critical point phenomenon* might explain abrupt and oscillatory pattern formation (Figure 11c, right side) that also recently specified by Schalm et al. (2021) [11], focusing on the pH dependence of the silica microstructure. In general, the study of Schalm et al. confirms the assumption made earlier [35,36,39] that an ICDP mechanism is suitable to explain self-organized pattern formation.

Such patterns are a result of sequentially precipitation events, triggered by local chemical instabilities of a supersaturated boundary solution by exceeding tipping points. A critical point phenomenon takes place if the system reaches a certain threshold representing such a tipping point, which is a decisive prerequisite for pattern formation [11,31,45]. Therefore, a high supersaturation is required that will break down by rapid nucleation of silica particles, followed by growth and/or agglomeration. This effect is known as burst nucleation that was proposed by LaMer and Dinegar in 1950 [143] to explain the formation of monodispersed hydrosols, which is illustrated in the lower part of Figure 1. After the monomer concentration passes the critical concentration level n^*, the supersaturation is high enough to allow the rapid formation of many almost equally sized nuclei. This burst nucleation event decreases the MSA concentration quickly down to a metastable zone (MSZ) between the critical concentration n^* and the saturation concentration n^{sat}, where particle growth is allowed and further nucleation suppressed. With respect to the SAL formation in glass corrosion experiments, this instability at a critical supersaturation level can be induced by

(i) small pH changes under alkaline conditions, where the silica solubility curve are characterized by steep positive slopes, as shown in Figure 10 [11],
(ii) changes of salinity, and
(iii) temperature fluctuation,

because these parameters have a great impact on the amorphous silica solubility [108,125,144]. In other words, the local solution properties (pH and composition under isothermal conditions) will determine the SAL formation according to the feedback loop II (Figure 11). What is most important here is to recognize that the saturation state at any point in time and space must be considered. After an interface fluid layer of significant thickness has been established, as emphasized in the upper part of Figure 12, another silica layer may precipitate on the glass surface instead of contributing to the growth of the already established SAL. In this case, the glass dissolution reaction is spatially decoupled from the precipitation and growth of the first SAL. Instead, the dissolution is coupled to the precipitation on the second SAL from now on. The formation of a second SAL is enabled as soon as critical supersaturation with respect to amorphous silica (or any other saturated phase) is reached again at the glass surface. Consequently, (burst) nucleation will occur (Figure 12, yellow star No. 2). At the same time, the concentration of MSA in bulk solution may be at equilibrium level (Figure 12, yellow star No. 1) and within the MSZ in the interface solution (Figure 12, yellow star No. 3). Note that the growth in the MSZ is equivalent to the steady state growth route for the SAL shown in Figure 11c.

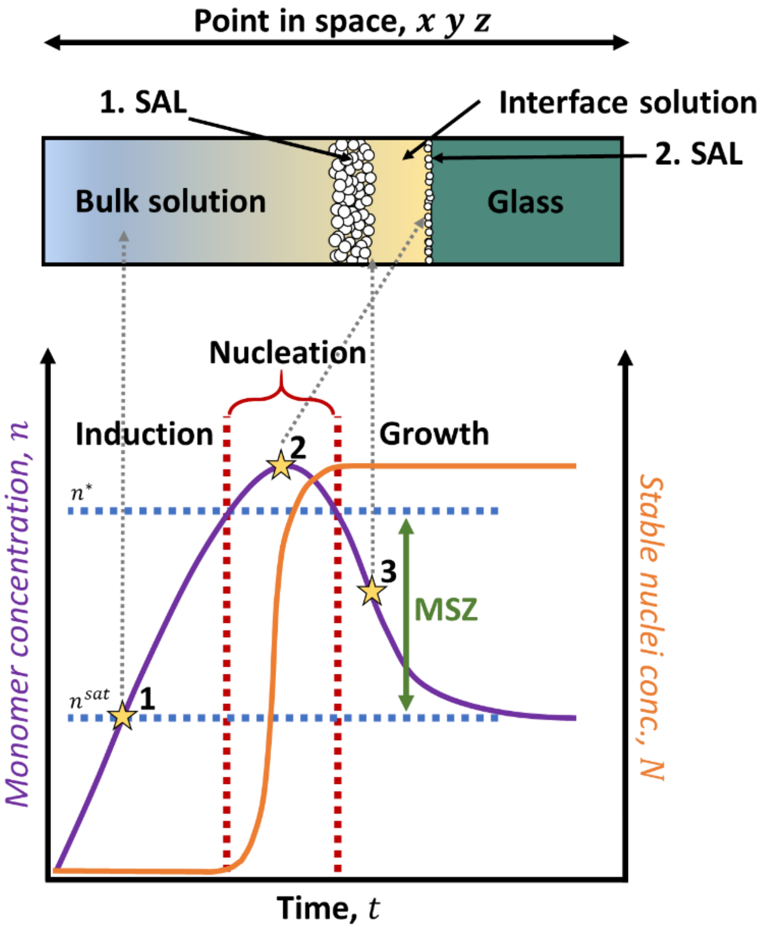

Figure 12: The LaMer-Dinegar model of burst nucleation (lower part)[143]. n^* and n^{sat} is the monomer concentrations, where nucleation begins and at saturation, respectively. MSZ is the metastable zone, where growth of existing stable clusters occurs (modified after Baronov et al.[145]). The yellow colored stars and references to the upper sketch emphasize that the saturation state of amorphous silica in the bulk solution, the interface solution, and at the glass surface may differ at a certain point in space and time.

3.3 Models for long-term glass corrosion

Many different mechanistic and related numerical kinetic models for glass dissolution and corrosion have been proposed and further developed in the last decades[20,21,31,34–36,59,66,86,90,99,101,104,114,146–149]. In the following, the most important of these models will briefly be reviewed, with particular reference to the ICDP mechanism, beginning with kinetic models for glass dissolution that do not account for SAL formation before those that do. Figure 13 schematically illustrates the reactions and transport processes, interfaces, and involved phases in the various models that consider SAL formation. In some cases, the differences between the model seem to be minor or sometimes rather semantic. However, differences can be identified and will be discussed with regard to the validity of the models for explaining the observed glass corrosion characteristics in nature and experiment.

3.3.1 Models that do not consider the formation of a surface alteration layer

As mentioned already in Chapter 2.3.1, the pH, temperature and saturation state dependency of glass dissolution rates are often described using an expression for the overall rate of a chemical dissolution reaction, which is based on the TST and the *surface complexation model* and looks like the following [7,9,17–19,63,64,149–152]:

$$\mathrm{r} = \mathrm{r}_{+}10^{\pm\eta\cdot\mathrm{pH}}\exp\left(-\frac{\mathrm{E_a}}{\mathrm{RT}}\right)\left[1-\left(\frac{\mathrm{Q}}{\mathrm{K_g}}\right)\right] \tag{1}$$

where r is the forward dissolution rate (g m^{-2} d^{-1}), r_{+} is the intrinsic dissolution rate constant (g m^{-2} d^{-1}), η the unitless pH power coefficient, $\mathrm{E_a}$ the apparent activation energy (J mol^{-1}), R the ideal gas constant (J mol^{-1} K^{-1}), T the absolute temperature (K), Q the ion activity product and $\mathrm{K_g}$ the pseudo-equilibrium constant of amorphous silica [17–19]. The idea of a TST based dissolution rate law grounds on the hypothesis that there is a quasi-equilibrium between the reactants and a surface-activated complex and that the transition state and the conversion rate to the final products can be calculated to describe the overall reaction kinetics. More information about the TST and the *surface complexation model* can, for instance, be found in a recent review of Wang et al. [152] and references therein.

Concerning the rate law of Equation (1), it is commonly assumed that the last term, enclosed in square brackets, can be neglected if the silicic acid concentration is sufficiently low. However, this assumption is questionable, because extremely small amounts of dissolved silica can affect the apparent forward dissolution rate [15,40,40,42,68,97].

A high degree of correlation between experimental results of different nuclear waste glasses and a kinetic rate model based on TST can be observed [17,19]. However, the kinetic rate models just work well for alkaline and near neutral pH values, but not under acidic conditions and are not capable of predicting the long-term glass corrosion. Strachan [63] fitted different experimental data reported in literature to these kind of dissolution models to describe the pH dependency of the dissolution rate for several glasses. Although the data fitted well for alkaline solutions, a single term rate equation failed to model the entire pH range. The author concluded that separate activation energies are necessary to describe the dissolution rates depending on the pH value. The formation reaction of the rate limiting activated complex consequently differs, depending on pH region of interest. Based on a mineral dissolution rate law of Köhler and coworkers [151], a modified equation for glass dissolution was proposed using an intrinsic rate constant that is affected by three different terms depending on hydronium, hydroxide, and water activity [63].In general, the reason for the misfit is that TST rate equations are actually not the adequate tool to describe complex mechanisms if the rate is not limited by a single elementary reaction [10,153]. Nevertheless, apart from some necessary modifications for dissolution under acidic conditions, these rate laws are very useful to predict the *forward dissolution rates* of glasses and minerals under varying pH and temperature conditions in silica undersaturated solutions. Since the determination of the glass specific parameters η, E_a, and r_+ in these rate equations requires a lot of experimental effort, methods of predicting these coefficients are desired [9,17,19]. Therefore, the calculation of corrosion rates and specific parameters by using machine learning approaches is already being done [153,154] and probably will gain in importance in the future. However, all previously mentioned rate equations neglect the formation and influence of SALs, which will form under realistic nuclear waste glass storage conditions. Furthermore, even if it is true that the bulk solution is undersaturated, oversaturation and precipitation of silica at the glass surface may happen because the solution properties at the glass surface were shown to be much different [36,40,41]. This could also be the reason why the TST based rate laws do not work well for acidic conditions, because then the silica solubility is quite low and oversaturation in a solution boundary layer at the surface can be reached rapidly. Consequently, the required far from equilibrium conditions are no longer present. In order to exclude that no secondary SAL has been formed, the altered samples need to be investigated, but usually only the solution chemistry is analyzed to determine the *forward dissolution rate* [15,68,69]. An additional check of the solid samples for possible SAL formation after the end of the experiment is often not reported in the literature, which raises serious doubts about the validity of the data interpretation.

3.3.2 Models considering the formation of a surface alteration layer

Most of the older glass corrosion models are based on the ideas of interdiffusion (ID), *in situ* network hydrolysis, and reconstruction of the glass in the solid state if the $pH_{90°C}$ is below 11.5 [43]. This *´classical corrosion theory´* was summarized by Gin et al.[90] and is redrawn in Figure 13a, including the possible dissolution of the gel and precipitation of secondary phases under certain conditions (e.g., high pH). Note that it was recently admitted that dissolution and precipitation reaction can also happen at lower pH, e.g., $pH_{90°C}$ 9, depending on glass composition, and that the corrosion mechanism may switch to an *in situ* reconstruction type after an initial ICDP sequence [20]. Crovisier et al.[104] suggested already 30 years ago that the formation and growth of SALs generated during corrosion of basaltic glass is based on glass network dissolution and precipitation of a silica-rich phase as a corrosion product due to supersaturation of the bulk solution (Figure 13b).

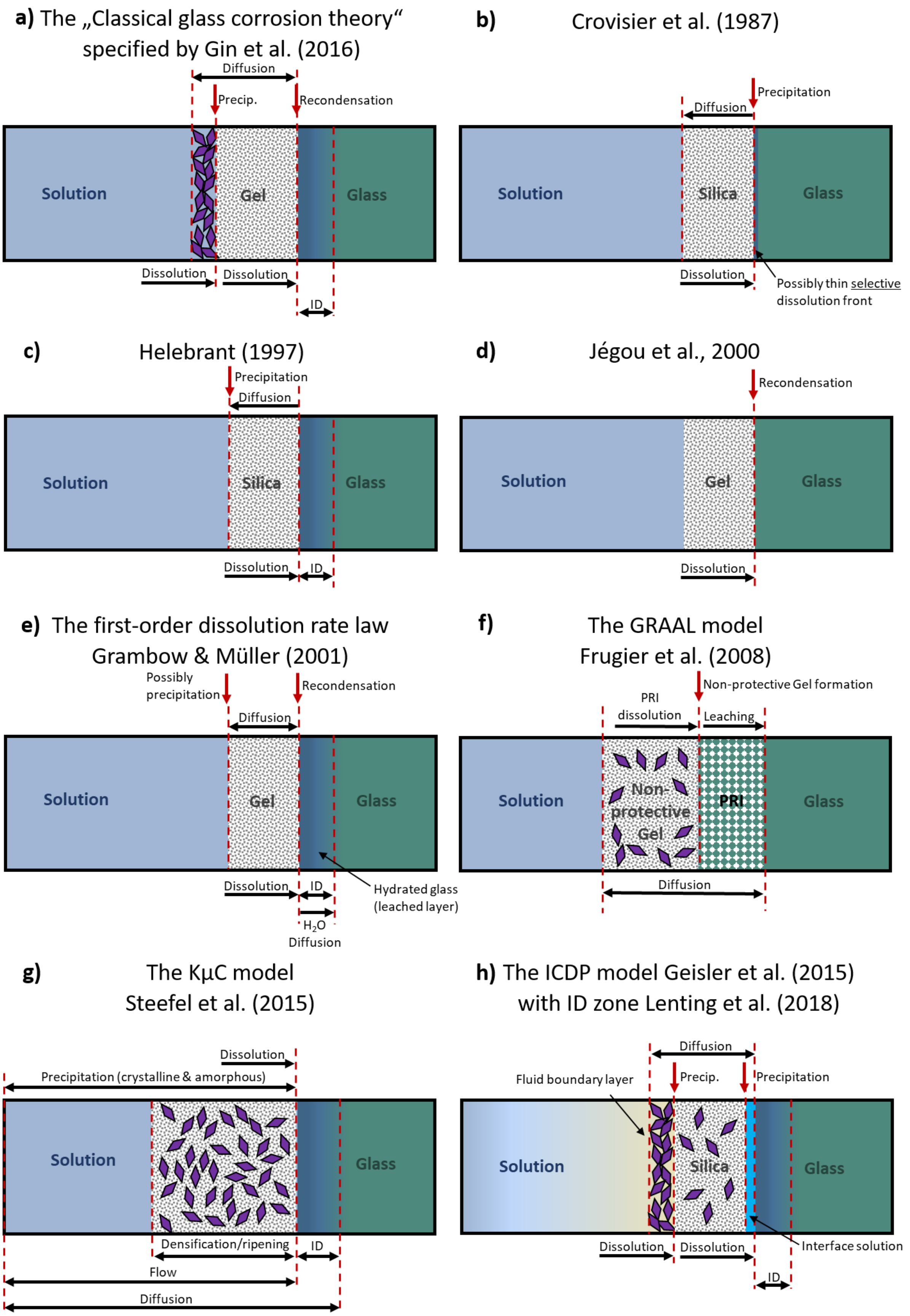

Figure 13: Schematic representation of selected important mechanistic and numeric glass corrosion models, showing the main processes, interfaces, and involved phases [31,36,59,86,90,104,146–148].

In accordance with the notion of the ICPD mechanism, the authors admitted the possibility of a thin selective dissolution front that progresses with a constant thickness of a few tens of angstroms. Nevertheless, they also concluded that this thin front can be neglected if it exists at all. Another, more recent study of Munier, Crovisier, and Grambow [155] simulated the SAL formation based on this proposed theory. Even the simulations where in good agreement with the experimental results for two different reference glasses, the authors concluded that the dissolution-precipitation process is just a suitable way to mathematically describe the kinetics of gel formation, which in the authors opinion represents a residual, reorganized, and hydrated glass.

Helebrant [147] was the first who considers simultaneous ID and precipitation reactions during glass dissolution (Figure 13c). Based on the ideas of Doremus and Boksay [156], he further developed his model by adding a time dependent rate of dissolution. This kinetic model includes glass dissolution, formation of a precipitated layer (made up by amorphous and/or poorly crystalline phases) onto the glass surface and ID processes ahead the dissolution front. The dissolution rate in the reviewed model is limited by the diffusion-limiting properties of the precipitated layer and the affinity effect. Additionally, the time dependent interdiffusion coefficient is assumed to be affected by the concentration of diffusing species and structural changes in glass surface. Though, at first glance, the model considers most of the reactions that are involved in the ICDP mechanism proposed in Chapter 3.1, no interface solution between the glass and the precipitated layer is assumed. Furthermore, instead of an inwardly moving and spatially- and temporally-coupled dissolution and precipitation front, Helebrant proposed that the dissolved species will be transported through the precipitated layer first into the bulk solution and that the precipitation and growth of this layer then take place at the outer surface of the SAL that is exposed to the bulk solution. Thus, the growth of the SAL is assumed to be outwardly directed, which is evidently not the case for the amorphous SiO_2-rich layers, as directly observed by *in situ* Raman experiments [40,41]. However, one of the case studies presented in Chapter 5.7 impressively show that crystalline secondary phases, such as zeolites and carbonates, may form at the outer SAL surface und grow into the solution, i.e., outwardly directed.

Jégou et al. [148] tried to model the silica gel formation via precipitation assuming the formation of a boundary layer close to the glass surface. The saturation with respect to amorphous silica in this layer was assumed to lead to so-called gel formation. The authors tested the proposed model with numerical calculations, but a misfit to the experimental results was observed. Although the calculated saturation with respect to amorphous silica was reached after 13 hours, the authors rejected a dissolution-reprecipitation mechanism to be responsible for the silica gel formation. They argued that the conducted experiments showed a divergence between B and Si normalized mass loss values, indicating that non-stoichiometric dissolution occurred already after 2 to 3 hours. However, the temporal difference can be just a result of the simplifications made in the model. For example, the assumption that the glass grains and their boundary layers have a constant distance is far from reality because especially at a thin water film between two grains, the surface boundary layer can be smaller and saturation with respect to amorphous silica can be reached quickly, because of the high local SA/SV ratio [10,61,78] (explanation for this local SA/SV-effect is given also in Chapter 2.3.4). Additionally, the concentration gradient in the boundary layer is assumed to be linear, but a clearly non-linear pH, und thus, indirectly, also silica solubility gradient has recently been observed by fluid-cell Raman experiments [40]. This is in line with calculations of Ruiz-Agudo and coworkers [65] for the wollastonite-to-amSiO_2 transformation, which indicate that supersaturation with respect to amorphous silica only at the mineral-fluid interface of wollastonite under the given conditions. This explains the observations that wollastonite is replaced by amorphous silica, although the bulk solution is silica undersaturated, which is also a common observation in glass corrosion experiments [35].

Finally, the authors concluded that another approach must be used to reach local saturation with respect to amorphous silica and proposed a dissolution/recondensation model outlined in Figure 13d [148]. Even if the calculations of this model fitted well with experimental observations, this approach just describes the Si concentration development in solution until a SAL is formed and not how this layer can influence the ongoing reaction progress by changing the transport properties.

A first-order dissolution rate law was proposed by Grambow and Müller [59] and grounds on an advection/dispersion/reaction equation, an affinity/TST-based dissolution rate, and an SAL growth rate (Figure 13e). The rate-limiting step is assumed to be the diffusion of water and the associated hydrolysis of the glass network. The already restructured part of the glass, which is considered as a distinct phase, limits the mass transfer of dissolved silica from the reaction interface into the bulk solution and therefore may cause a protective effect by affecting the chemical affinity at the gel-glass interface. The authors state that the glass corrosion process works via ID, followed by *in situ* restructuring of a residual, leached glass. Interestingly, their model mathematically describes the so-called *in situ* transformation as a matrix dissolution and precipitation process.

3.3.3 Reactive transport models

Another approach to model glass corrosion is to use geochemical reactive transport codes [18,21,66,99,114,146,157]. Geochemical modeling software is highly promising to model the long-term behavior of glasses in aqueous solutions on a macroscopic scale and allows the validation against measurable bulk parameters [21]. This approach further allows considering the transport limiting properties of the SAL and can describe the solution chemistry including the saturation state of precipitating phases principally very well [21], provided that internal consistent thermodynamic and kinetic data are available.

3.3.3.1 *The GRAAL model – Frugier et al. (2008)*

The probably most advanced and validated numerical model in terms of long-term glass corrosion is the so-called GRAAL (glass reactivity in allowance of the alteration layer) model (Figure 13f) [9,18,21,86,99,114,146]. It was proposed by Frugier and co-workers already in 2008 [21,86] and some extensions and improvements have been made till today in order to also consider, e.g., the impact of zeolite precipitation and non-linear diffusion [21,99,114,120].

The GRAAL model is a diffusion-reaction model and the basic equations are implemented in the geochemical transport code *CHESS/HYTEC* [21]. Compared to the other models presented so far, the GRAAL model is able to describe the composition and solubility of the different SAL phases by setting up an reference phase (end-member) model [21,99]. Another key element of the GRAAL model is the so-called *passivating reactive interface* (PRI) that represents a part of the SAL (so-called *amorphous gel*) [21] and lowers the corrosion rate by acting as a diffusion barrier for H_2O [18,86,146]. Its thickness determines the glass alteration rate and is affected by creation and transformation to a non-protective layer. Even if the GRAAL model allows reproducing trends in experimental data [21,99,114], recently improved by adding non-linear diffusion coefficients [120], ID and water diffusion in the glass are ignored. The formation of an amorphous layer and its passivation effect on the molecular level cannot be modeled in this way [21,146]. Additionally, the frequently observed chemical and structural patterns [11,24–26,34,39,46–49,84,85] are not considered and cannot be explained or simulated by the GRAAL model.

3.3.3.2 *The KμC model – Steefel et al. (2015)*

Another reactive transport model is the *Kinetic Micro-Continuum* (KμC) model, which was proposed by Steefel and co-workers and is built upon the *CrunchFlow* code [146,157]. This model considers (i) the dissolution of glass by using a TST-type dissolution rate law with an affinity term, (ii) multicomponent diffusion through the solution and corrosion products, (iii) H_2O diffusion into the glass, (iv) convective flow of the solution, (v) precipitation of corrosion products (thermodynamically and/or kinetically driven), (vi) kinetically controlled densification of the corrosion products, and (vii) diffusional ion exchange. In Figure 13g the features of the model are schematically summarized in order to make the considered reactions and transport processes comparable to the others. As mentioned before and also pointed out by the authors as well, the disadvantage of micro-continuum modeling approaches is that the pore-scale cannot be modeled correctly and the fluid-mineral interface cannot be resolved explicitly. Furthermore, the impact of the local solution properties next to the glass interface on the glass dissolution rate is not considered in the simplified description of dissolution and precipitation rate laws. Nevertheless, it should be noted that in this model no single passivating or rate limiting process is specified, which is probably close to reality. The overall reaction rate is rather a result of several interdependent reactions, including diffusional transport, precipitation of corrosion products, and glass dissolution. Consequently, the rate limiting process may change with reaction progress [10,20,31,67]. It can be further concluded that the frequently observed chemical and structural patterns within the SALs reflect this dynamic.

3.4 Interface-coupled dissolution-precipitation versus *in situ* reconstruction

In general, a universal ICDP mechanism for the SAL formation during glass corrosion has not yet been accepted in the glass (corrosion) community as a universal mechanistic framework to model the glass corrosion process, although it has partly been accepted for corrosion under (hyper-) alkaline conditions, especially $pH_{90°C}$ values above 9 [43,56,79] and specifically for glasses that do not contain Al [20,56]. The SAL forming mechanism under neutral and acidic conditions is mainly still assumed to be pure ID and *in situ* reconstruction and the SAL is assumed to be a residual, chemically modified glass [43,48,49,79]. Some conflicting points will be discussed in the following to finally evaluate whether ICDP or *in situ* reconstruction or even a combination of both provides a full explanation for all observations made so far by glass corrosion experiments.

An argument against an ICDP model is the absence of a visible gap between the SAL and the pristine glass in some corroded samples that reflects the space occupied by an interface solution [31,34,50,52,53]. Furthermore, as pointed out by Gin et al. [90] a film of water between both phases would allow to separate them easily from each other, which is often not the case. Indeed, such a fluid interface between the pristine glass and the precipitated reaction product is an intrinsic feature of the ICDP mechanism [35,111]. But as already discussed by Lenting and coworkers [34], the presence of another inner, water-rich SAL zone [30,31,34,57] between the outer SAL and the pristine glass is more likely the result of a silica supersaturated interface solution instead of being a pure water film. Such a silica-rich solution might already be highly polymerized or gelled during the corrosion experiment, what can cause passivation (described in detail in Chapters 3.1 and 3.2.8, or may solidify rapidly if the sample is quenched and dried [31,34].

It must be emphasized that the thickness of this interstitial zone can vary from a few nanometers to micrometer size depending on the experimental conditions and the glass composition and is not of primary importance for the basic mechanism, but for the kinetics. This has also been postulated based on various evidence for numerous mineral replacement reactions [37,65,93,111,112]. The interface-coupled dissolution and precipitation reactions are assumed to take place already in a few monolayers of ordered water, representing the interface solution and even a monolayer of a dissolving parental phase then allows to reach supersaturation with respect to a certain product phase [37,93,111,112]. A key point of the ICDP mechanism is that the solubility difference between the glass and amorphous silica or, in general, the product phase thermodynamically drives the ICDP process and determines the coupling between the dissolution and precipitation rate [93,111,112]. To estimate this delta is impossible while dealing with glasses, because they are metastable and determining an equilibrium constant is based on thermodynamic phase equilibrium, which cannot be achieved due to the absence of a backward precipitation reaction for glasses [10,21,67]. This problem is doubly challenging in most cases because the primary product phases are also often amorphous and metastable. Nevertheless, it can be assumed that the solubility of a glass in water is higher than the solubility of any amorphous SAL, because the latter can be precipitated from aqueous solutions containing dissolved silica in contrast to the irreversible glass dissolution reaction.

Whether a relatively thick gap between the glass and SAL will form, depends on the fraction of SAL compatible elements in the parental glass and the density difference between the parent and product phase. For example, corrosion of glasses containing a high amount of highly soluble elements (e.g., TBG) is replaced by SALs containing a significant smaller fraction of the original glass components. Even if the density of such an amorphous silica layer is smaller than that of glass, the final volume occupied by the replacing solid can be much smaller if a lot of well soluble components (e.g., B, Na) will not be incorporated in the SAL structure and remain dissolved. A significant volume difference between the glass and the replacing corrosion product leads to the formation of porosity, and sometimes, a relatively large gap between both phases arises [29,39,41], which is demonstrated also in one of the following case studies (Chapter 8). Multiple sequences of dissolution, precipitation, and gap formation is also addressed to be the reason for the impressive structural patterns showed in Figure 1 and was discussed already in detail above (Chapters 2.1.1 and 3.2.8). This can be even amplified by maturation of the SAL, as observed for hydrogels [109] and also by *in situ* fluid-cell Raman spectroscopy for an SAL formed under acidic conditions [30,31] and in the mentioned case study about TBG corrosion under varying fluid exchange rates (Chapter 8).

Another aspect, rarely illuminated in more detail so far, is the frequently observed hydrogen enrichment adjacent to the reaction front (c.f., Chapter 2.1.3). Although such observation does not alone proof the existence of an interstitial fluid film that solidified to a silica gel already during the process and/or during quenching and drying [30,42], it is another indication for its existence that cannot be explained by any of the other proposed corrosion mechanisms. Assuming an ID process in a porous *in situ* restructured glass, relic being responsible for this hydrogen concentration would indicate an uphill diffusion process for which the driving force would be completely unknown. Furthermore, the question arises why the extension of the SAL via ID and hydrolysis does not proceed, but even comes to a near standstill, although hydrous species are piled up at the interface [38,43,53,54,56,90]. Gin et al. showed, e.g., that hydrous species are even able to diffuse inside the glass, while the other components of the glass remain constant [53]. It follows that the observed hydrogen enrichment at the interface reflects a water-rich zone at the reaction front, which is an inherent feature of the ICDP mechanism.

A mechanism based on ID and *in situ* reconstruction also fails to explain discontinuities in concentration profiles in different parts of the SAL, formed during corrosion of a QBG glass sample at 90 °C followed by further corrosion at 150 °C [31,34]. Nano-SIMS results of Lenting and coworkers [34] are displayed in Figure 14, which revealed significant different compositions of two parts of the SAL formed at different temperatures. The incorporation of B as well as the high concentration of K, that originated from solution, in the SAL formed at 150 °C are also at odds with leaching of the so-called “soluble” glass components and reconstruction of a residual network caused by the condensation of silanol. Boron has so far been assumed to merely become incorporated in corrosion products for strong alkaline solutions [78] and is thus commonly used as a quantitative dissolution at lower pH. However, B incorporation in the SAL under neutral to slightly alkaline conditions ($pH_{RT} = 8$) was observed by Lenting and coworker [34], which makes its use as a quantitative dissolution tracer questionable [158]. The retention of B and simultaneous depletion of Ca in the high temperature SAL region also excludes a formation of calcium borates, even if it might be the be a reason for boron enrichment in SAL pores in some cases, especially under alkaline conditions [158]. So far it is not clear how B is incorporated in the SAL under these conditions, but the Raman spectra reveal the presence of $B(OH)_3$ vibrations and indicates the presence of boric acid [31].

The absence of Ca in the high temperature part of the SAL and its presence in the SAL formed at low temperature are in contradiction to a simple unimpeded diffusional transport across the SAL into the bulk solution, because the diffusion would then take place against the concentration gradient for which no driving force is apparent. These observations can be best explained by a precipitation mechanism for SAL formation, whereby the SAL composition and microstructure is determined by the local conditions at a certain point in space and time, allowing the precipitation of the momentarily thermodynamic stable silica gel.

Recently, another study of Gin et al. [158] also showed a B incorporation in ISG samples of SAL parts that were formed at pH 3 and pH 5. The authors concluded that the use of B as a corrosion tracer can be problematic and that the retention is probably the result of a generally reduced pore size of the SAL. Furthermore, the pH dependency of B dissolution, more precisely $B - O - Si$ bond hydrolyzation, was postulated to also depend on local $B_{(aq)}$ and $Ca_{(aq)}$ concentration, which in turn enable borate mineral precipitation in the pores. The described effect leads to a passivating gel that act as a trap for well-soluble glass elements.

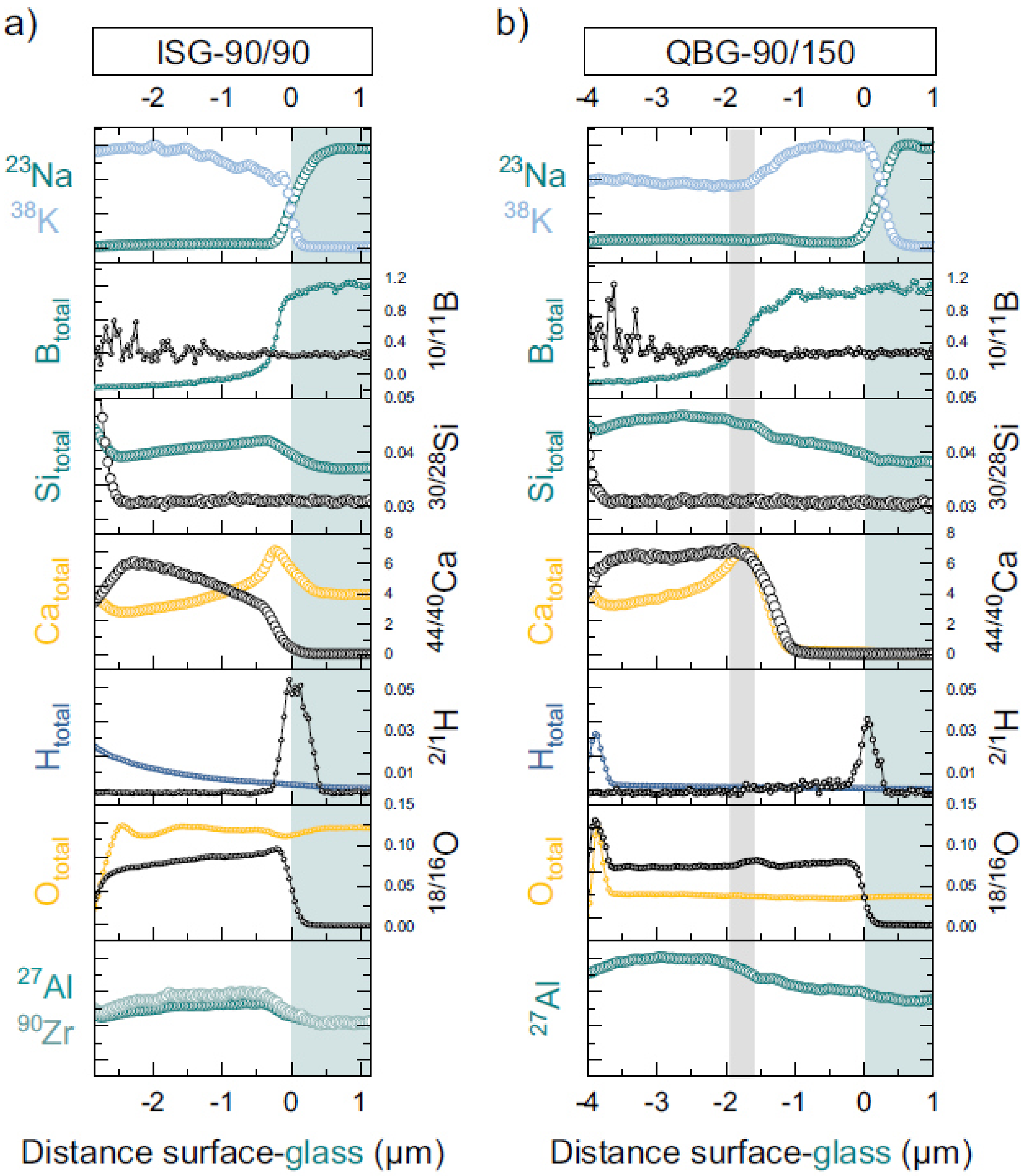

Figure 14: NanoSIMS profiles across the SAL into the pristine glass of a quaternary borosilicate glass (QBG) formed after pre-corrosion for three month at 90 °C in a ^{30}Si-bearing solution at initial pH$_{RT}$ of 7 and a consecutive corrosion at higher temperature (150 °C) for 3 month [31,34]. The symbol size matches the estimated NanoSIMS probe diameter. The gray area indicates the location of an additional STEM analysis that has been performed as well and can be found in the original references of Lenting and coworkers [31,34]. The green area marks the glass phase.

Another criticism concerns the fact that some corrosion products of the spherical silica particles are often not observed in SEM or TEM analysis but are inherent to the ICDP model. However, primary spherical silica particles can be exceedingly small, that is, down to 1 nm depending on solution chemistry and temperature [31,34,108,109,124,130]. Different silica gel structures are for example known to depend strongly on pH, leading to polymerized linear chains forming a dense gel network under acidic conditions, compared to a gel that consist of highly branched clusters of relatively big silica spheres formed under basic conditions [106,108,109]. This can also be the reason for the observed pH dependency of porosity and in turn the B retention that was discussed above.

Recently, Reiser et al. [106,137] tried to synthesis silica gels, containing Si, Al, Ca, Na, and Zr using sol-gel methods to compare aerogels with similar composed SALs formed by corrosion of ISG under different pH values. The pore size (1 - 10 nm) and composition of these artificial gels showed some similarities to the SALs formed during glass corrosion [106]. Gels and SALs formed at higher pH (9, 11) were found to have more pore volume and bigger skeletal structures compared to those formed at a lower pH of 3 [137]. This is in line with the assumed SAL formation mechanism in the ICDP model that grounds on ideas of sol-gel chemistry. However, there are significant differences between the SALs and aerogels, which are not surprising considering the different synthesis conditions (e.g., room temperature vs. 90 °C) and precursors (MSA vs. alkoxides) [50].

3.5 Conclusion

In this chapter, it has been demonstrated that the ICDP mechanism (including ID reactions) summarized in Chapter 3.1 provides a suitable mechanistic framework to understand several observations which cannot be explained by the more “classical” mechanistic models. This includes

(i) the extremely sharp interface between the SAL and the pristine glass (Chapter 2.1.2),
(ii) the spherical shape of the primary silica particles of the SAL and their absence under rather neutral to acidic conditions,
(iii) the porosity in the corroded region that strongly depends on the reaction kinetics, glass composition, temperature, pH, and solution composition (Chapter 2.1.4),
(iv) the formation of chemical and structural patterns (Chapters 2.1.1 and 3.2.8), and
(v) the water-rich interface/gap between the SAL and the pristine glass and the hydrogen enrichment at the reaction front (Chapter 2.1.3).

It is shown here that these observations can all be explained by a mechanistic framework of an ICDP model, considering ID reactions when the ICDP reaction is decelerated for some reasons [31,34], and knowledge from of sol-gel chemistry.

It can further be concluded that both end member like models, i.e., the ICDP and *in situ* reconstruction model, basically describe the same molecular reactions. The alteration of glass occurs via several coupled physico-chemical reactions, including

(i) the rapid hydrolyzation of the surface near free NBO by hydrous species,
(ii) ID, i.e., the diffusional ion exchange of alkalis from the glass against $\mathrm{H_3O^+}$ (or other alkalis) from solution which may also result in hydrolyzation of NBOs,
(iii) further hydrolysis by breaking up $\mathrm{Si-O-Si}$ or equivalent network forming bonds (e.g., $\mathrm{Si-O-Al}$, $\mathrm{Si-O-Zr}$),

(iv) condensation of hydrolyzed and ionized NBO ($\mathrm{Si-O^-}$, $\mathrm{Si-OH}$) leading to a silicon rich corrosion layer onto the pristine glass,

(v) aging of the silicon rich SAL that possibly changes its microstructure with time and, in turn, its transport properties,

(vi) formation of secondary corrosion products, i.e., crystalline or amorphous secondary phases (e.g., CSH-Phases, zeolithes, clays, silicates) at the outer surface and in the pores of already existing corrosion layers.

Distinguishing between the two models using terms such as repolymerization/condensation and dissolution/precipitation can be misleading, since both mechanistic models actually assume that Si originating from the glass is repolymerized via condensation reactions after a previous hydrolysis reaction. It is rather the case that the terms hydrolysis and condensation have similar meanings to dissolution and precipitation reactions on the nanoscale [93].

The major difference between both models is that all glass components are assumed to be completely hydrolyzed and detached from the glass network, at least for a short period of time, in the ICDP model [20,31]. In contrast, the hydrolyzation in the *in situ* reconstruction model is assumed to be incomplete, i.e., not all bonds of the network forming cations (e.g., Si, Al, Zr) are being hydrolyzed simultaneously [20,50,56]. Some indications for an interstitial fluid layer were reviewed here (2.1.3), but it might even be that some strong bonds, e.g., $\mathrm{Si-O-Zr}$, stay untouched, left behind as remnant, and are as such incorporated into newly formed silica-based SALs. In other words, the dissolution process leaves out the strongest bonds if they are isolated in the network which has certain similarities with models assuming an incomplete hydrolyzation of the glass network [20,50,56].

To put an end to the debate of the SAL forming mechanism, numerical models which includes the transport (diffusion, convection) and molecular reaction (ion exchange, hydrolyzation, condensation) on pore scale are required, because these models may correctly reflect the positive and negative feedbacks, which are probably responsible for self-organization and pattern formation in SALs. Indeed, most numerical models describe glass corrosion regardless of the initial SAL forming mechanism and apply kinetic rate equations to describe the overall glass dissolution and the formation of the SAL (3.3). But such rate equations are just mathematical descriptions of the rate of the slowest, rate controlling reaction process and must be applicable and ultimately applied in a spatially differentiated manner. If not done that way, the simplification can end up with a lot of uncertainties for the prediction of, in particular, the long-term durability of nuclear waste glasses because the rate limiting reaction can change significantly over time [10,20,31,34].

It follows that merely a few basic assumptions are necessary to provide an ICDP mechanism for glass corrosion that is able to explain all basic features observed so far. These include:

- the local solution chemistry,
- the stoichiometric dissolution of the glass (hydrolysis on molecular level),
- the presence of a (possibly very thin) water-rich interface solution at the reaction front,
- the precipitation of amorphous silica (via condensation/polymerization) or any other replacing phase, depending on the local thermodynamic conditions,
- the species depending, (transient) transport properties of the SAL.

These sub-processes and their coupling are illustrated in Figure 15, which is a simplified and more universal visualization of the flow chart in Figure 11. Apart from solution properties (composition, pH and ionic strength), the dissolution (rate) of glasses depends primarily on the resistance against hydrolyzation, which, in return, is affected by the glass composition, structure/topology, reactive surface area, and system temperature. Once oversaturation is reached in the solution boundary layer at the glass surface, the grade of supersaturation and presence of nucleating agents (such as solid silica, reactive glass surfaces, and impurities) determines whether precipitation of the SAL forming phase (amorphous or crystalline) will occur, a pre-existing phase will grow continuously, or whether the solution will remain slightly oversaturated and glass dissolution will continue.

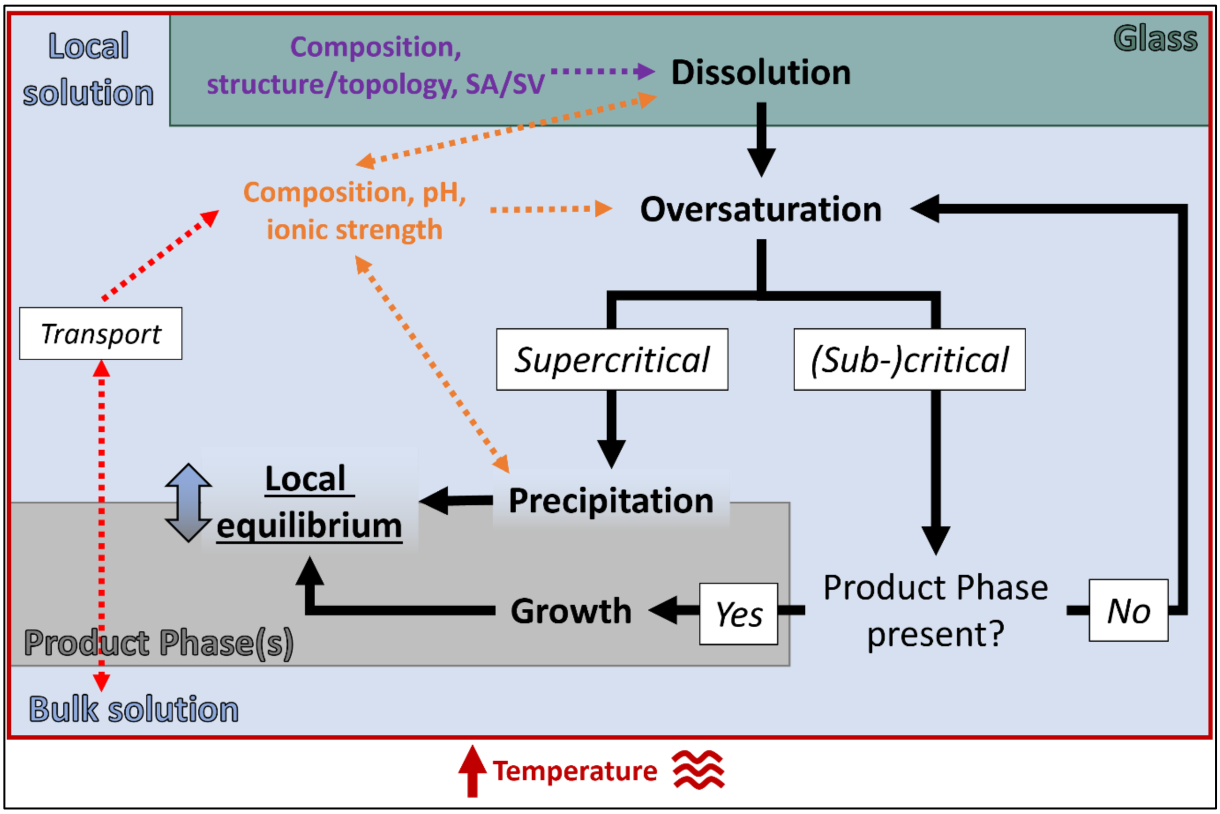

Figure 15: Generalized summary of the reactions, transport processes, and feedbacks governing the ICDP mechanism for glass corrosion.

After an SAL has formed, microstructure and thickness will affect the chemical and molecular transport through the SAL towards the interface solution by, for instance, acting as a molecular sieve for some dissolved species. This solute filtering affects the local solution properties and feedbacks the dissolution and precipitation reaction. Such a general framework is also suitable for describing the formation of secondary phases, which could similarly replace the previously formed amorphous silica because of being thermodynamically more stable, i.e., having a lower solubility in the local solution volume than amorphous silica. It should be noted that this replacement, if the thermodynamic conditions favor it, is reversible and could reach equilibrium. It follows that the most important aspect is to consider the local thermodynamic (quasi) equilibria and transport properties on the pore scale in a sufficiently discretized model instead of trying to describe the overall system by using simple continuum approaches.

4 A brief introduction to Raman spectroscopy

Raman Spectroscopy is widely used for structural analysis and identification of substances from the characteristic spectral patterns or for semiquantitative analysis of a substance in a sample [159]. Although the method has a few problems, such as fluorescence, sample degradation [159], as well as spherical aberration [160–163] when using confocal Raman microscopes, novel instruments allows analyzing aqueous solutions and (transparent) solid samples placed in reaction vessels with high spatial resolution and in real time [29,30,41,42,45]. Raman spectroscopy is a vibrational spectroscopic technique that takes advantage of interaction of electromagnetic radiation with atoms and molecules, more precisely, the inelastic scattering of photons by molecules. A monochromatic light source, such as a laser, of an excitation wavelength, lying between or near the visible spectrum of light, is used and focused on or into a (transparent) sample, where the photons interact multifariously with the molecules. The inelastic scattering goes along with a small shift of the incident laser photons energy, which is defined as the Raman effect. The Raman effect was predicted already by A. Smekal [164] in 1923, but was first observed experimentally by C.V. Raman and K.S. Krishnan in 1928 [165].

The fraction of Raman scattered photons is very small (one of 10^6 to 10^8 photons) and most of the photons are scattered elastically (Rayleigh scattering) without any change of energy. Furthermore, absorption of the incident photons is possible when the energy of an incident photon corresponds to the energy gap between ground and excited state of a certain molecule [159]. This absorption is used in absorption spectroscopy and depending on the electromagnetic wavelength, other spectroscopic techniques, such as infrared adsorption, electronic adsorption, and fluorescence emission spectroscopy can be used for analyses.

Raman and infrared spectroscopy are vibrational spectroscopic methods that excite atomic motions. In infrared spectroscopy the excitation of a molecule is caused by absorption of a certain frequency of the incident radiation. In contrast to this, Raman spectroscopy uses monochromatic radiation and the energy difference of inelastically scattered photons from elastically scattered photons is measured. Scattering itself occurs when light polarizes the electron cloud of nuclei of molecules by inducing an electrical dipole moment to form a short-lived virtual state [159]. The induced dipole moment $\mu(t)$ is proportional to the electrical field strength ε and relates to the polarizability constant α, according to the following equation:

$$\mu(t) = \alpha\varepsilon(t) \tag{2}$$

The polarizability constant α expresses the ease with which a distortion of the electron cloud of a certain molecule can occur. Caused by the fluctuating, time dependent electric field of the excitation laser, a fluctuating dipole moment of the same frequency is produced, which can be expressed as:

$$\mu(t) = \alpha\varepsilon_0 \cos(\omega_0 t) \tag{3}$$

where ε_0 is the equilibrium field strength, ω_0 is the angular frequency of the radiation, and t is time.

Here, the induced dipole of frequency ω_0 will emit or scatter a photon of the same frequency. In other words, the electron cloud distortion is resolved back into its original form and the photons are scattered with the same frequency as the incident radiation, known as elastic scattering in general and named Rayleigh scattering for molecules [159].

Since the polarizability of molecules changes during vibration, the value for a small vibrational amplitude is given by Equation (3), which considers the normal mode's coordinate q:

$$\alpha = \alpha_{(0)} + \left(\frac{\partial\alpha}{\partial q}\right)_0 q \tag{4}$$

A substitution of Equation (3) in (4) and a combination with a description of the harmonic oscillator (Equation (5)):

$$q = q_0 \cos(\omega_{Os} t) \tag{5}$$

to consider the time dependence of the normal coordinate yields to Equation (6):

$$\mu(t) = \left(\alpha_{(0)} + \left(\frac{\partial\alpha}{\partial q}\right)_0 q_0 \cos(\omega_{Os} t)\right) \varepsilon_0 \cos(\omega_0 t) \tag{6}$$

Rewriting this equation as

$$\mu(t) = \alpha_{(0)}\varepsilon_0 \cos(\omega_0 t) + \frac{1}{2}\left(\frac{\partial\alpha}{\partial q}\right)_0 \varepsilon_0\, q_0 \cos\big((\omega_0 t - \omega_{Os})t\big) \tag{7}$$
$$+ \left(\frac{\partial\alpha}{\partial q}\right)_0 \varepsilon_0\, q_0 \cos\big((\omega_0 t + \omega_{Os})t\big)$$

shows the three different polarizability terms, where the first one describes the Rayleigh scattering, the second term Stokes, and the third term anti-Stokes Raman scattering. Considering this equation, the polarizability of the molecule must change during a vibration when it is Raman active. The Stokes and anti-Stokes frequencies differ in being positive or negative, respectively, but in fact have the same wavenumber shift relative to the excitation wavelength.

The different scattering processes observed in Raman spectroscopy are idealized and illustrated based on the relative energy levels in Figure 16. Most of the photons will return back to the lowest vibrational level m after excitation to a virtual state. In this case, if the starting vibrational energy level corresponds to the final level, this is called Rayleigh scattering. When a photon starts from ground vibrational state *m* to a higher energy state *n*, this inelastic scattering is called Stokes Raman scattering. However, the opposite process can occur where molecules, which may be present initially in an excited state *n,* and scattering from these states to ground state *m* is called anti-Stokes Raman scattering. The latter effect becomes more frequent with increasing temperature, because the initially excitation of some molecule's origin by the thermal energy. However, at ambient conditions most molecular vibrations are at the lower ground level, which is why the Stokes bands are more intense and are commonly measured [166]. For more specific information on Raman spectroscopy the textbooks of Smith and Dent [159] and Gardiner and Graves [166] are highly recommended.

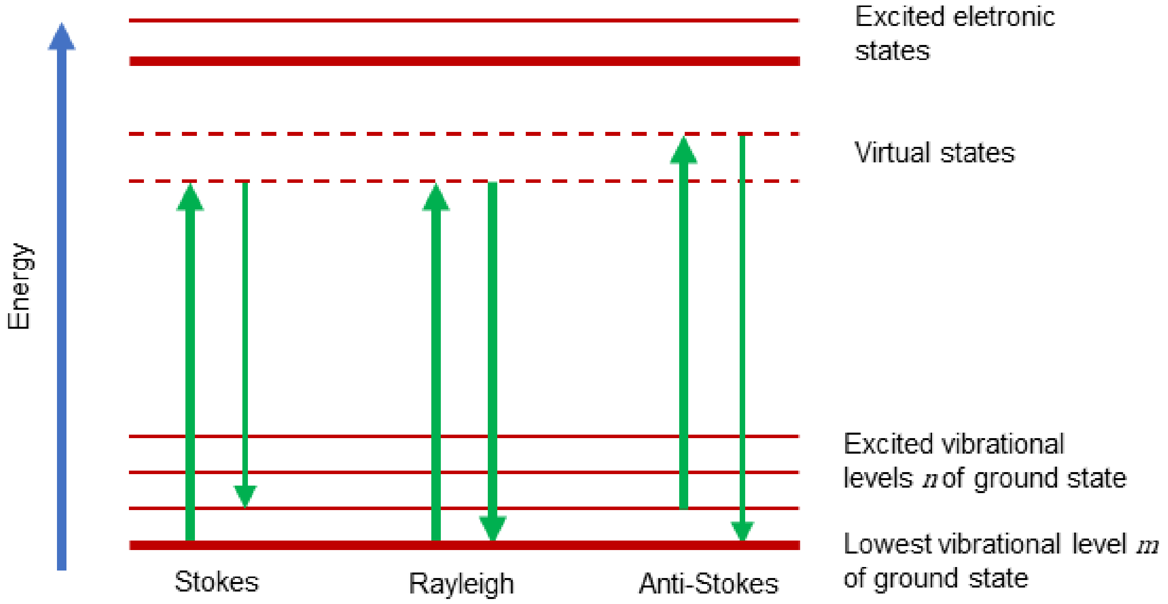

Figure 16: Idealised illustration of the Rayleigh scattering, Stokes Raman scattering, and anti-Stokes Raman scattering processes. The vibrational ground state *m* has the lowest energy vibrational state und the higher vibrational energy levels *n* above are representing the excited energy states. The different start and end levels reflect the possible energy change depending on the process. This figure was redrawn after Smith and Dent [159].

The result of a Raman measurement is a Raman spectrum that shows the relative Raman scattering intensity as a function of the Raman frequency shifts, usually in cm^{-1}, relative to the frequency of the excitation wavelength, i.e., the Rayleigh scattering. Such a spectrum can be characteristic to a certain phase or also be a convoluted combination of several phases, depending on the spatial resolution of the method and the purity or homogeneity of the analyzed sample. To analyze localized regions by Raman spectroscopy, the Raman mapping method can be used. Raman mapping describes a sequential measurement of an individual Raman spectrum at each adjacent spots for a defined region of a sample is acquired by focusing the laser at each measuring spot, until the whole mapping region has been covered by measurements [167]. Raman hyperspectral images can be generated based on the structural and chemical information that are present in the multitude of Raman spectra, one for each pixel. Therefore, false-color images can be produced by visualization of the spatial distribution of specific spectral features, such as phase characteristic Raman bands. By sequential Raman mapping at different environmental conditions (e.g., temperature) or at different times, hyperspectral Raman images can be used to visualize the phase distribution and transformation, temporally and spatially resolved. This makes the method a powerful tool to investigate, e.g., high-temperature ceramic sintering reactions and phase transformations [168–171] and glass corrosion [29,31,41,42,45] *in operando* and on the micrometer scale, whereby the possibility to study glass corrosion by fluid-cell Raman spectroscopy should be further developed in this thesis.

5 Materials and methods

5.1 In situ fluid-cell Raman spectroscopy

5.1.1 Experimental setup

In situ fluid-cell Raman spectroscopy allows investigating the glass corrosion process *in operando*, i.e., in real time, and spatially resolved. The technique offers the possibility to extract isothermal dissolution and precipitation rates from only a single experiment in contrast to conventional approaches where numerous quench experiments over different time periods have to be performed [43,44]. With this method, it is possible to clearly differentiate between phases and structural features formed during the corrosion process and those that may be induced by quenching/cooling, drying, and preparation of the sample. *In situ* fluid-cell Raman spectroscopy was first introduced by Geisler et al. [29], who studied a ternary sodium borosilicate glass (TBG). The technique allows collecting hyperspectral Raman images crossing the glass/SAL/solution interfaces *in operando*, i.e., while the reaction proceeds without quenching and disturbing the corrosion process [29,30,41,42,45]. For the long-term alteration experiments of the following chapters the method has been modified to enable the acquisition of Raman data in regular time intervals without blocking the Raman spectrometer for the entire duration of the experiment. Therefore, the reaction cell was stored on a heating stage between the measuring sessions. Reference spots at the surface of the reaction vessel allowed the repositioning with a reproducibility better than ± 1 µm.

The fluid-cell for *in situ* Raman experiments is sketched in Figure 17, holds a volume of 4.75 ± 0.10 ml, and is located at an automated x-y-z stage below the objective of the Microscope (Olympus BX41) that is linked to the confocal *Horiba* HR800 Raman spectrometer of the Institute for Geosciences of the University of Bonn, Germany. A solid state Nd:YAG laser (532.09 nm) (Nd:YVO_4 (532.11 nm) for Exp. II of case study III) with laser output power of nominally 2.2 W, a 100x long working distance (LWD) objective with a numerical aperture of 0.8, and a 600 grooves per mm grating, a confocal hole of 1000 µm, and spectrometer entrance slit width of 100 µm was used for all *in situ* measurements. The nominal temperature for all experiments presented here was set to 90°C, but due to a temperature gradient within the reaction vessel, the actual temperature at the glass for this setup was 82.9 ± 2.2°C [29,42,45].

Before each session, the Raman spectrometer was calibrated based on the first order optical phonon band of a silicon single-crystal with a maximum at 520.7 cm^{-1} [172]. Additionally, a Ne lamp was placed alongside the beam path of the scattered light to continuously record the intense Ne line at 1707.06 cm^{-1} (for a 532.09 nm excitation wavelength) [173]. This was done to correct possible spectral shifts of the spectrometer due to mainly temperature fluctuations in the laboratory of ± 0.5°C during long measurement periods. The spectral resolution was about 4.9 cm^{-1} as given by the full-width at half-maximum (FWHM) of the Ne line.

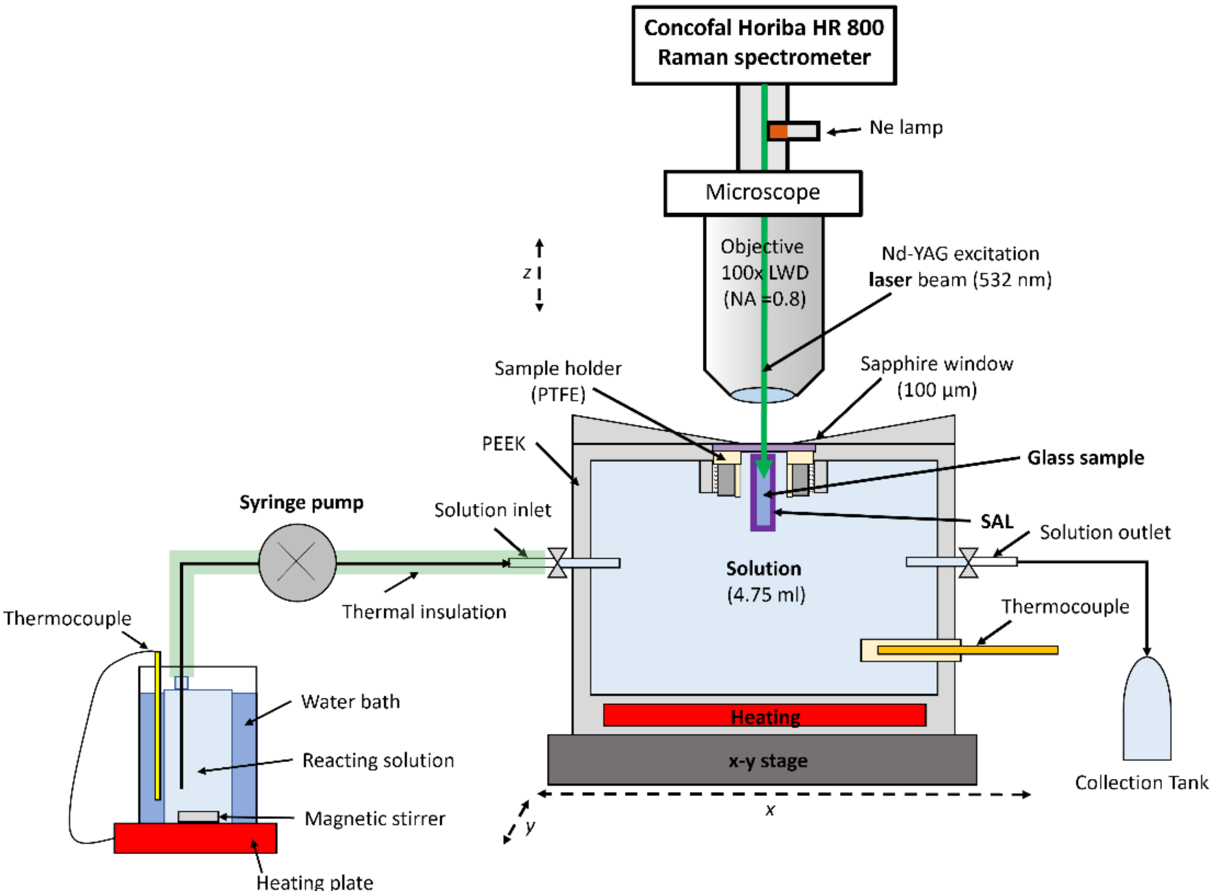

Figure 17: Schematic sketch (not to scale) of the experimental setup for fluid-cell Raman spectroscopy. The laser beam of a Raman spectrometer is aligned parallel to the direction of the reaction front and the focal point is continuously monitoring the reaction interface(s), i.e., acquire Raman spectra, by moving the x-y stage. The reaction cell is equipped with a heating at the bottom and an inlet and outlet for optional solution exchange. For corrosion experiments under flow-through conditions with different solution exchange rates, the fluid cell can be linked to a preheated leaching solution reservoir via a syringe pump. To collect the exchanged solution, the outlet is then also connected to a collection tank that can be replaced in regular time intervals for regular solution sampling and analysis.

A higher lateral resolution compared to the spatial resolution in depth profiling is the reason for the applied arrangement of the sample in the fluid cell, with the laser beam running parallel to the solid-water interface. The lateral resolution in such setups was found to be between 6 to 20 µm, worsens with increasing depth of measurement [29,41,45], and can be determined empirically as shown in Chapter 5.1.4. More details about the temperature gradients in the fluid cell and how it was determined are given in Chapter 5.1.2.

To prevent the thermocouple from corrosion in acidic solutions such as those used in the second case study, it was sheathed by PTFE. For the flow-through experiments in case study III, the setup was extended by a syringe pump connected to the inlet valve. Both valves were kept open to enable solution exchange and the continuously stirred solution reservoir of 1 liter was preheated at about 80°C in a water bath. The syringe pump enables pumping of fresh reacting solution via a thermal insulated PTFE hose into the reacting cell. With this setup, the replaced solution can be sampled an analyzed to obtain information about the dynamically changing bulk solution composition and bulk pH. Furthermore, by tuning the pump rate, the glass retreat rate can be measured *in situ* for different pump rates and/or under stagnant conditions.

All studied glass coupons were prepared as described in Chapter 5.8.1, including the additional top side polishing to minimize the reactive surface area and the related top side corrosion. Taking a look at the setup in Figure 17, it becomes clear why this is necessary. Significant top side corrosion is problematic, because the laser beam must pass the corroded part on top of the glass to acquire Raman spectra across the glass/SAL/solution interfaces at the actual measurement depth. Especially at late reaction progress, this reduces the quality (signal-to-noise ratio) of the spectra and the spatial resolution of the method, because the corrosion products formed along the beam path will scatter and absorb both, the incident and scattered light.

5.1.2 Temperature correction, calibration, and gradients in the fluid cell

The Raman spectra for fluid-cell temperature calibration and for data evaluation in the case studies were corrected for temperature and frequency dependent scattering intensity [174] by application of the following equations, originally proposed by Long in 1977 [174,175]:

$$I = I_{obs} \times R \tag{8}$$

$$R(\nu) = {\nu_0}^3 \left[1 - \exp\left(\frac{-hc\nu}{kT}\right)\right] \frac{\nu}{((\nu_0 - \nu)^4} \tag{9}$$

where the observed intensity I_{obs} is multiplied with a correction factor R to get the intensity I according to Equation (8). The correction factor can be calculated using Equation (9) where ν_0 is the incident laser wavelength (Nd-YAG, 532.09 nm, ν_0 =18793.81308 cm^{-1}), h the Planck constant (h = 1.05458 Js), k the Boltzmann constant (h = 1.380066·10^{23} JK^{-1}), c the speed of light (c = 2.9979·10^{10} ms^{-1}), T the absolute temperature that was assumed to be 358.15 K for the *in situ* Raman experiments and ν the measured wavenumber in cm^{-1} [174].

Due to the design of the experimental setup, described in Chapter 5.1.1, a significant distance exists between the heating at of bottom and the sample position near the lid of the fluid cell. This is why the actual temperature at the corroding glass sample was different to the nominal temperature. *In situ* temperature calibration (Chapter 5.1.2.1.1) and depth correction (Chapter 5.1.3) were carried out in order to estimate the temperature deviation and gradient in the fluid cell (Chapter 5.1.2.2).

5.1.2.1.1 Temperature calibration measurements and data evaluation

To estimate the temperature distribution within the reaction cell, a 3-D Raman map was recorded at nominal 90 °C. The fluid cell was filled with a $0.5M\ Na\mathrm{HC}O_3$-solution and a glass cuboid (ISG) was placed into the sample holder to create conditions very similar to those in the corrosion experiments. Because the spectral position of the Raman band of aqueous $\mathrm{HCO_3^-}$ depends on temperature, spatially resolved recording of Raman spectra allows conclusions to be drawn about the temperature distribution within a bicarbonate solution. To investigate the temperature distribution within the fluid-cell, a 3D hyperspectral Raman image of the solution below the sapphire window to a depth of about 1.2 mm was recorded. For this, Raman spectra were collected in x-, y-, and z-direction, that is, in x-direction from 0 to 500 µm in 25 µm steps, in y-direction from 0 to 150 µm in 25 µm steps, and in z-direction from -125 to 750 µm in 50 µm Steps, whereby at y = 0 the interface between the sapphire window and the underlying solution was located.

To be able to convert the frequency of the $\mathrm{HCO_3^-}$ vibration to temperature, a 0.5 M bicarbonate solution was analyzed at 16 different temperatures ranging from 25 to 110 °C. Three Raman spectra were taken at each temperature step at a nominal depth of - 50 µm below the sapphire window. Because the thermocouple that records the temperature in the fluid-cell is placed at the bottom, a second thermocouple was inserted for calibration and located directly below the sapphire window. All Raman spectra were acquired close to this thermocouple (precise within ± 0.1 °C). This temperature is referred to as the actual temperature and its difference to the nominal temperature increases with rising target nominal temperature from 1 °C at 25 °C up to about 5 °C at 110 °C.

Beside spectral position correction using silicon and the Ne lamb as external and internal standards, respectively, a consecutive crosscalibration using the stretching band of oxygen (O_2) at 1556.4 $\mathrm{cm^{-1}}$ [176] was also performed this time before background calibration. The oxygen signal originates from air in the beam path that is also excited by the laser.

Following data processing procedure was performed:

1. Spectrometer shift correction using the Ne at 1707.06 $\mathrm{cm^{-1}}$ line and the stretching band of O_2 at 1556.4 $\mathrm{cm^{-1}}$.
2. Extraction of the spectral regions between 950 and 1100 $\mathrm{cm^{-1}}$.
3. Subtraction of a linear baseline (10 base points and 10 noise points).
4. Extraction of the spectral regions between 955 and 1045 $\mathrm{cm^{-1}}$.
5. Second subtraction of a linear baseline (10 base points and 10 noise points).

Least-squares fitting of the HCO_3^- band near 1016 cm^{-1} at 25 °C [177] was carried out using a combined Pseudovoigt function (PsdVoigt1 in OriginPro® 8G) that is a combination of a Gaussian and Lorentzian function and defined as:

$$y = y_0 + A\left[m_u \frac{2}{\pi}\frac{w}{4(x-x_c)^2+w^2} + (1-m_u)\frac{\sqrt{4\ln 2}}{\sqrt{\pi}w}e^{-\frac{4\ln 2}{w^2}(x-x_c)^2}\right] \tag{10}$$

5.1.2.2 Determination of the temperature gradient in the fluid cell

The $\nu_5(HCO_3)$ band position is plotted as a function of temperature in Figure 18. To account for the high interdependence of the intercept a and slope b of a linear least-squares fit, the covariance between a and b, $cov(a,b)$, was considered and calculated with Equation (11) for error propagation to estimate the error [178] of the temperature σ_T obtained from the $\nu_5(HCO_3)$ frequency and the calibration line:

$$\sigma_T^2 = \left(\frac{\delta T}{\delta a}\right)^2 \sigma^2(a) + \left(\frac{\delta T}{\delta b}\right)^2 \sigma^2(b) + 2\left(\frac{\delta T}{\delta a}\right)\left(\frac{\delta T}{\delta b}\right) cov(a,b) \tag{11}$$

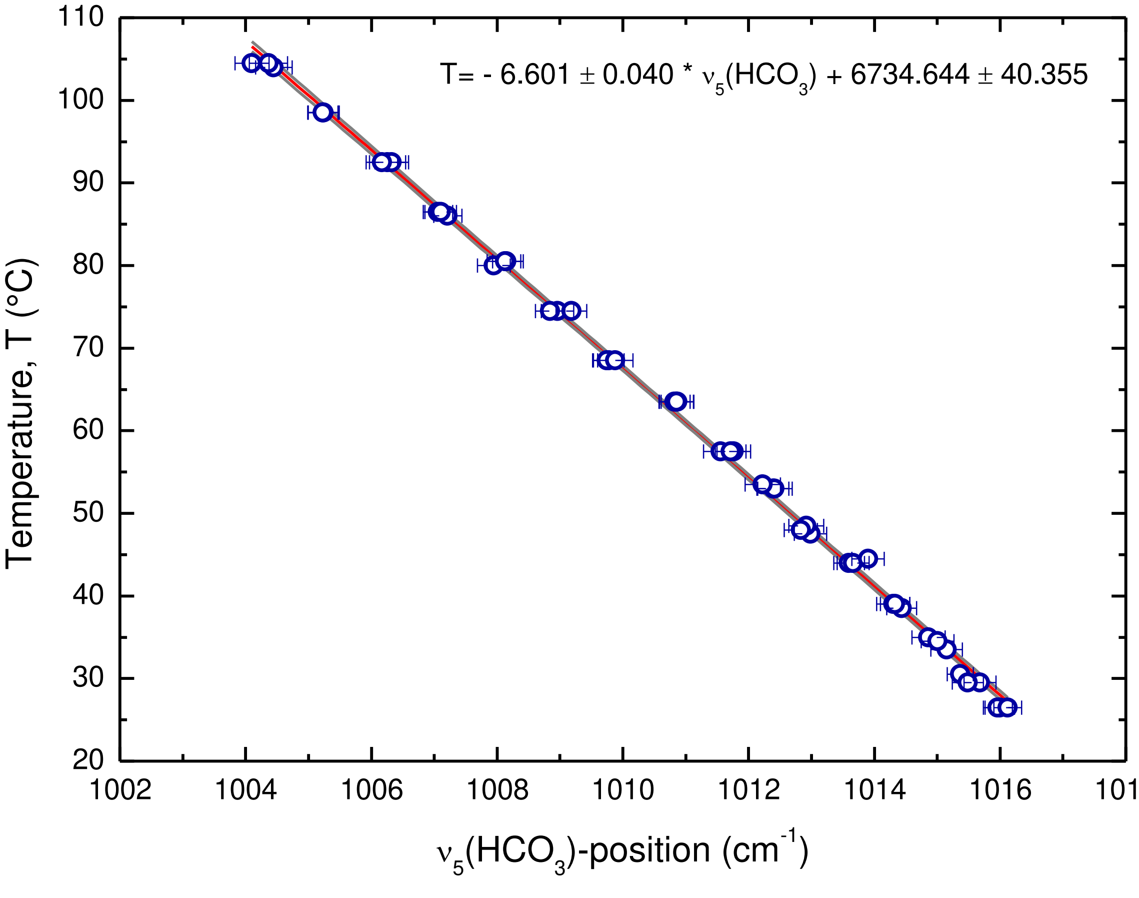

Figure 18: The actual solution temperature as a function of the $\nu_5(HCO_3)$ band position. The errors mark the 95 % standard confidence interval from the fitting procedure. The red line is a least-squares fitted linear function that was used to determine the temperature from the $\nu_5(HCO_3)$ band position and the grey lines outlines its 95 % confidence interval.

As mentioned above, a hyperspectral 3D Raman image of a solution volume was recorded (364 spectra in total: 26 in the horizontal *x*-*y* plane at 14 different vertical *z* positions). All Raman spectra were processed similarly to the calibration dataset as described in the previous section and no significant horizontal (*x* and *y* direction) temperature fluctuations were observed in the measured volume. Therefore, all horizontally distributed band position values were averaged for each *z* position to increase the robustness of the depth temperature profile. The standard deviation of the mean band position values was then calculated from following equation:

$$\overline{\sigma_x} = \sqrt{\frac{1}{N(N-1)}\sum_{j=1}^{N}\left(v_j - \overline{v_x}\right)^2} \tag{12}$$

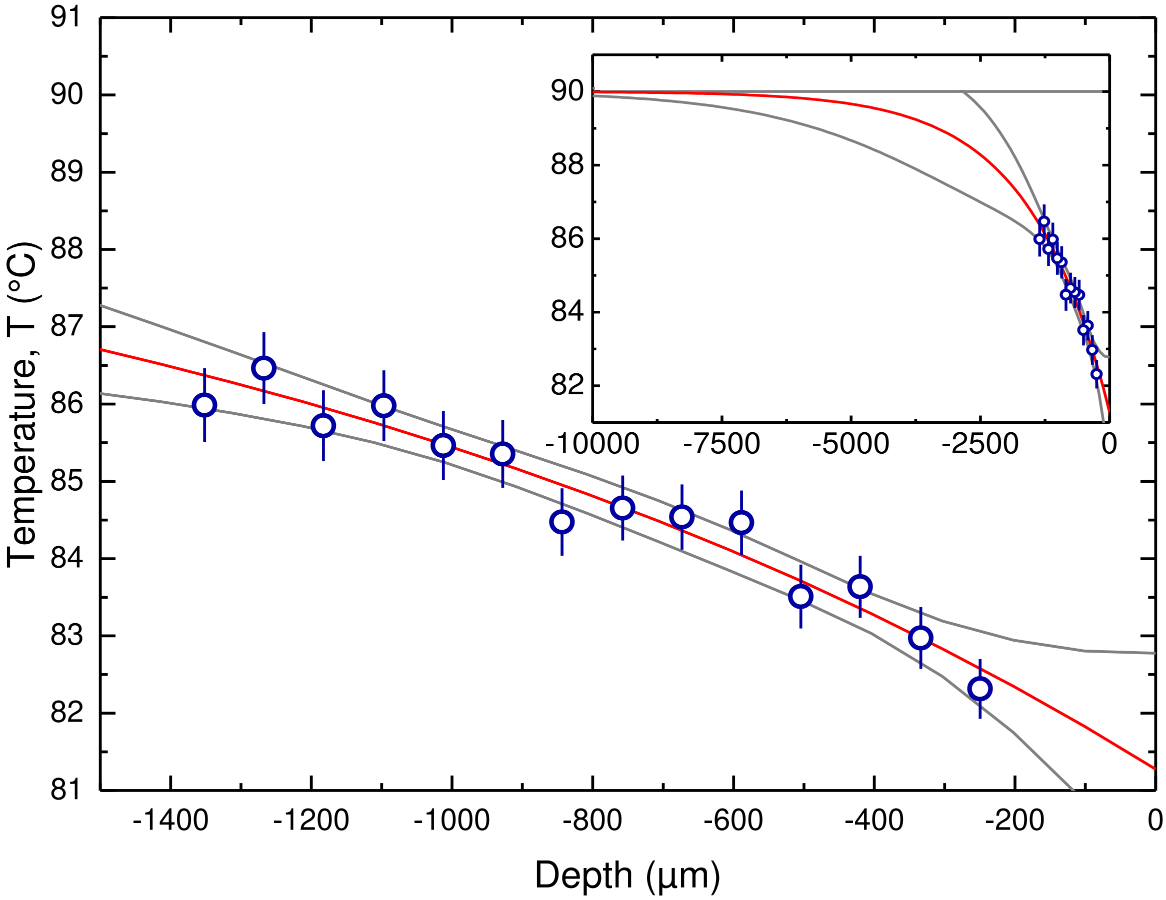

Figure 19: Solution temperature determined from the frequency of the $\nu_5(\mathrm{HCO_3})$ band as a function of depth in the fluid-cell used for Raman spectroscopic *in operando* experiments. The red curve represents a fitted Boltzmann function ($y = A_2 + (A_1 - A_2)/1 + \exp((x - x_0)/dx)$) and the grey lines outline the 95 % confidence interval of the fitted curve. In the inset diagram the fit is shown as an extrapolated curve to the total depth of the fluid cell. The fitting parameter A_1, that describes the temperature at the bottom of the reaction cell at 10 mm depth, was fixed to 90 °C. The other parameters were $A_2 = -1930 \pm 528925$, $x_0 = 8352 \pm 409422$, and $d_x = 1535 \pm 1108$ with an R^2 of the fit of 0.943. The error bars are given at the 95 % confidence level. The depth (= z position) has been corrected for multiple refraction effects (c.f., Chapter 5.1.3).

As shown already for $\mathrm{HCO_3^-}$, the temperature dependent frequency shift of dissolved $\mathrm{CO_3^{2-}}$ can also be used for *in situ* temperature measurement [29,177]. This can be particularly useful under hyperalkaline conditions, where $\mathrm{HCO_3^-}$ is not the dominating dissolved carbonate species. Therefore, a second calibration experiment was performed using a 0.25*M* KOH, 0.25*M* $\mathrm{K_2CO_3}$

solution and the Raman spectra were collected next to the thermocouple inside the cell for 17 different temperatures ranging from 25 to 105 °C.

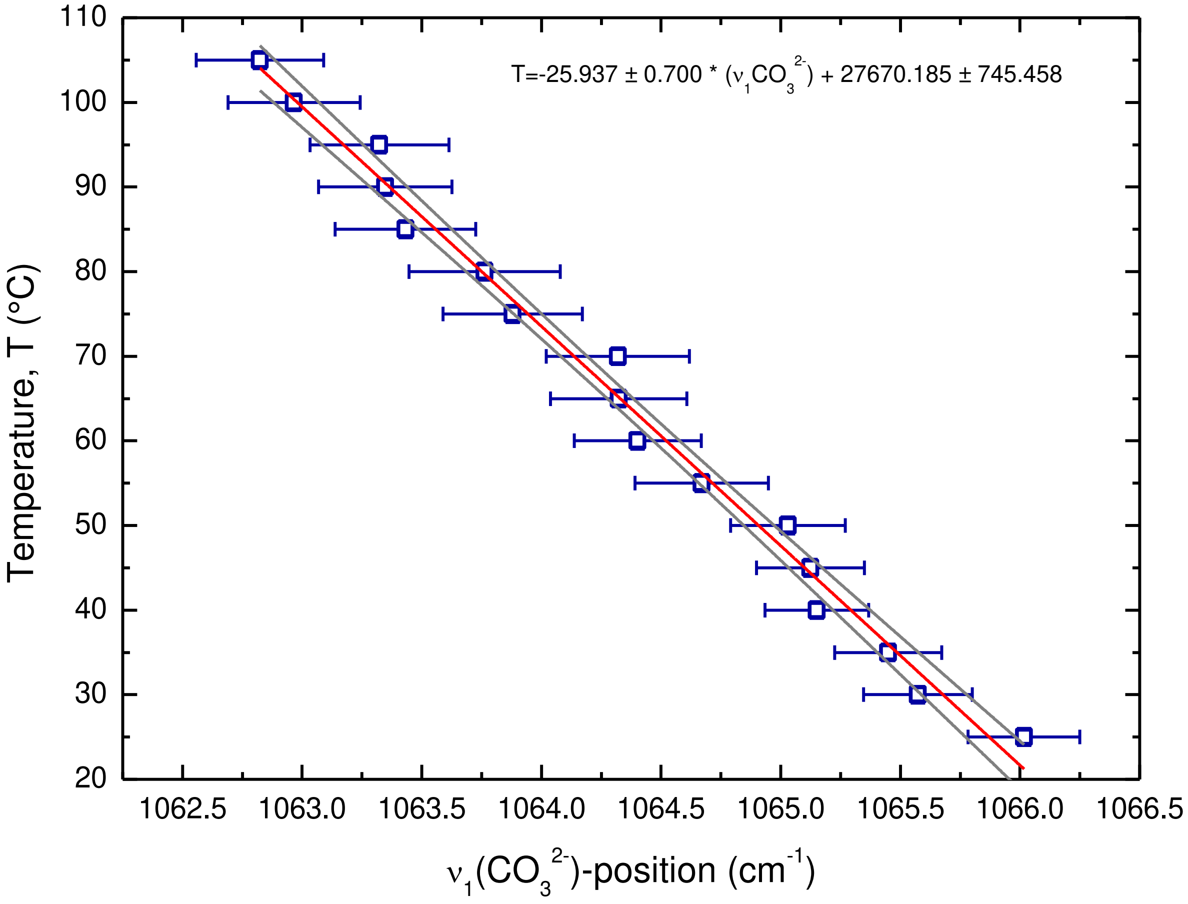

Figure 20: The actual solution temperature as a function of the $\nu_1(CO_3^{2-})$ band position. The red line is a linear least-squares fit to the data and the grey lines outline its 95 % confidence interval.

After the spectra were treated similar to those of the HCO_3^-, the calibration dataset shown above and a clear linear relationship between the band position and temperature was revealed (Figure 20). However, because of the much sharper HCO_3^- band around 1016 cm^{-1} at less alkaline pH and the resulting a much higher uncertainty of temperature estimation based on CO_3^{2-} band around 1065 cm^{-1}, which is also due to the about four times less intense shift by increasing the temperature from 25 to 105 °C [29,45], the temperature gradient was determined by using a bicarbonate solutions at moderate pH.

5.1.3 Determination of the depth resolution

For the correct localization of the laser focus, i.e., of the analyzed volume of a Raman measurement recorded deep in a transparent sample, refraction phenomena between air and sample have to be considered [160–163]. In addition to refraction, which can be partially be overcome by using immersion objectives, spherical aberration of the incident laser beam influences the depth resolution (R_z) obtainable by confocal Raman microscopy. As a matter of fact, the actual and apparent depth may vary by orders of magnitude, depending of the focal depth and optical arrangement. However, the depth resolution and actual depth from which a Raman signal is acquired can be calculated with reasonable accuracy from geometrical and optical considerations. In general, R_z increases linearly with the apparent depth (Δ_z) and is given by [162,163]:

$$R_z = \Delta_z \left[\left[\frac{NA^2(n^2-1)}{(1-NA^2)} + n^2 \right]^{1/2} - n \right] \tag{13}$$

Here NA is the numerical aperture of the objective and n is the refractive index of the sample. This equation works well for a single interface, but cannot be directly transferred to the *in operando* measurements, where the laser beam crosses at least two interfaces, i.e., the air-sapphire and the sapphire-solution interface. In Figure 21, the multiple refraction of the laser beam, its spherical aberration, and the depth resolution is schematically illustrated. Note that an increase of the depth of focus causes more out of focus signals to contribute to the Raman spectrum and thus a worsening of the depth resolution. In such a multiple refractive system, the refractive index is not constant, but a sum function of the pathlength fraction and the refractive indices of each individual phase. Based on the geometrical considerations made by Everall [160–163], one arrives to Equation (14) to estimate the refractive index n used to calculate the depth resolution displayed in Figure 21:

$$n = n_2 \cdot \left(\frac{d_{saph}}{d_{total}}\right) + n_3 \cdot \left(\frac{d_{saph}}{d_{total}}\right) \tag{14}$$

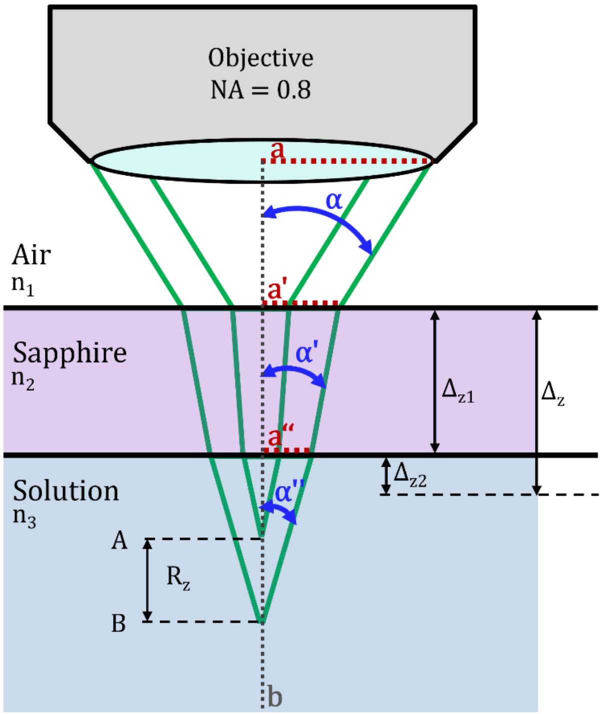

Figure 21: Schematic illustration of the optical pathway, laser beam refraction and spherical aberration, and depth resolution for a multilayered optical system.

As indicated in Figure 21, the actual depth can be calculated for each depth by apply trigonometric principles and the law of refraction:

$$n_1 \sin\alpha = n_2 \sin\alpha' \tag{15}$$

Based on these basic laws and some assumptions on the materials' refractive indices, the actual depth was calculated and finally used in the depth *versus* temperature plot shown in Figure 19. The exact procedure is explained in more detail in the following (Equation (16) to (26)).

For the depth calculation, a thickness (d_{sph}) of 100 µm and a refractive index of 1.77 was used for the sapphire window, which is reasonable for the used excitation wavelength of 532.11 nm when considering wavelength- and temperature-dependent literature data [179]. The refractive index of the solution was assumed to be 1.33 (similar to water at ambient conditions) and its temperature dependence was neglected for the calculations. A reasonable decrease to 1.32 at 90 °C [180] would have an effect of less than 1 % on the calculated depth for the used laser. The objective used for the measurements was an Olympus 100x long-working-distance objective with a numerical aperture of 0.8.

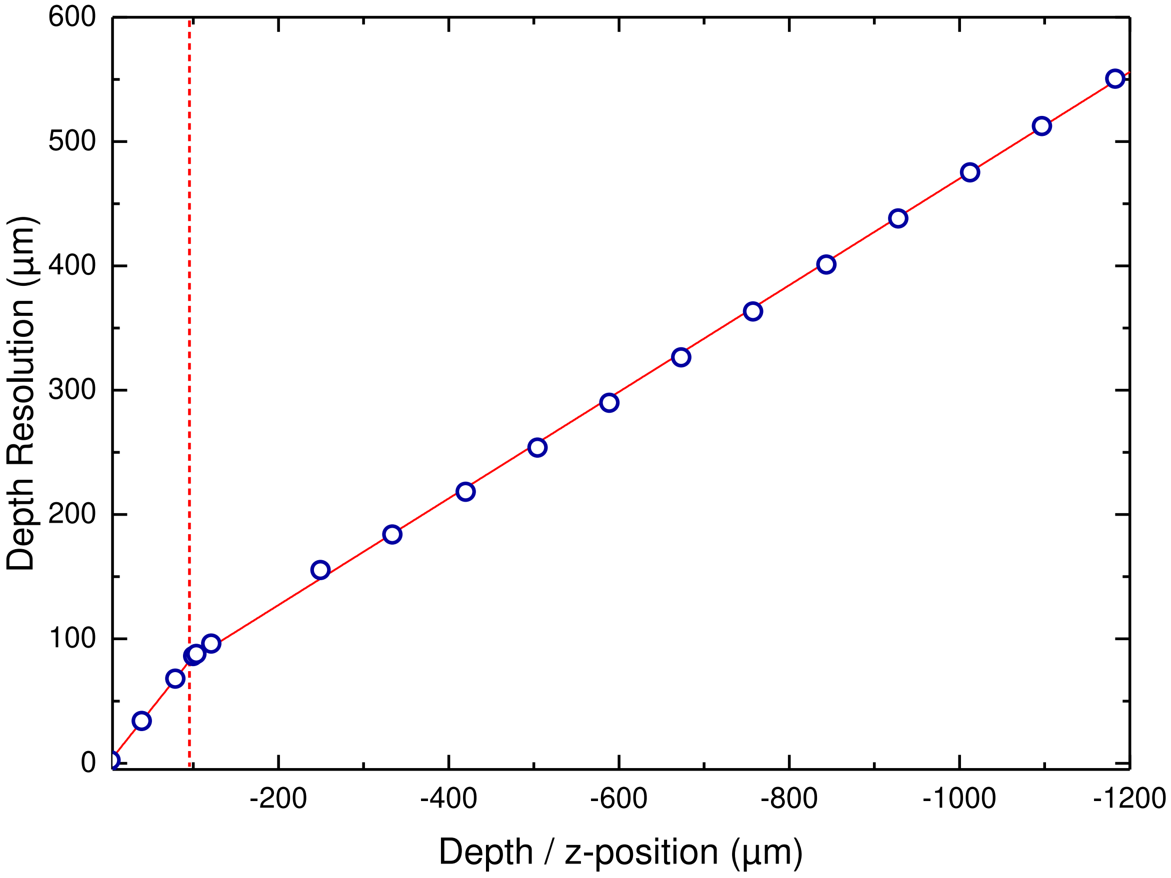

Figure 22: Depth resolution as a function of nominal depth. The two-part linear trends are due to the change of the overall refractive index of the sample below a focal depth of 96 ± 9 µm which represents the sapphire-water interface (red dashed line). The solid red line represents a piecewise linear fit to the data.

Because air is located between the objective and the sample object, the refractive index n_1 equals one and therefore $\sin\alpha$ is NA according to the following equation:

$$\sin\alpha = \frac{NA}{n_1} \tag{16}$$

Because the refractive index of air n_1 equals one, α' and α'' are:

$$\sin\alpha' = \frac{NA}{n_2} \tag{17}$$

$$\sin\alpha'' = \frac{\sin\alpha' \cdot n_2}{n_3} \tag{18}$$

The length a', corresponding to the radius of the circular laser beam area which hits the surface of the sapphire window, was calculated from the depth Δ_z and the objective angle α:

$$\mathrm{a}' = \Delta_z \cdot \tan\alpha \tag{19}$$

From this, the corresponding actual depth that considers the refraction at the air/sapphire interface ($d_{air/sph\ cor}$) can be calculated:

$$d_{air/sph\ cor} = \frac{\mathrm{a}'}{\tan\alpha'} \tag{20}$$

Considering the second refraction at the sapphire/solution interface when the actual focal depth is below the sapphire window, i.e., greater than d_{sph}, the actual depth in the solution $d_{sph/sol\ cor}$ is given by:

$$\mathrm{a}'' = \left(d_{air/sph\ cor} - d_{sph}\right) \cdot \tan\alpha' \tag{21}$$

$$d_{sph/sol\ cor} = \frac{\mathrm{a}''}{\tan\alpha''} \tag{22}$$

The equations (16) to (22) are summarized in the following expression for the described air-window-solution sequence to calculate the corrected depth d_{cor}:

$$d_{cor} = d_{sph} - \frac{(|\Delta_{cor}| - \Delta_{cor})}{2} + \frac{\left(\frac{(|\Delta_{cor}| + \Delta_{cor})}{2}\right) \cdot \tan\alpha'}{\tan\alpha''} \tag{23}$$

when

$$\Delta_{cor} = \frac{\Delta_z \cdot \tan\alpha}{\tan\alpha'} - d_{sph} \tag{24}$$

The terms in Equation (23), which contains the expression Δ_{cor} from equation (24), accounts for the constant and depth independent refraction caused by the lid window and the depth depending refraction that originated from the second refraction at the window-solution interface.

When using the *in situ* fluid-cell Raman technique to study glass corrosion reaction, it is also necessary to consider at least one additional refractive interface. More precisely the solution/glass sample interface. In the used *in situ* Raman setup the laser beam passes the air between the objective lens and the top of the lid, then the window followed by a tenth of µm thick solution layer before it is focused either in the solution or the glass underneath. The actual depth within the glass sample (d_{gls}) can be estimated by modifying the corrected depth (d_{cor}) as follows:

$$d_{gls} = d_{cor} + \frac{2(|\Delta_g|+\Delta_g)}{\Delta_g} \cdot \frac{\Delta_g \cdot \tan\alpha''}{\tan\alpha'''} \tag{25}$$

When

$$\Delta_g = d_{cor} - (d_{sph} + d_{sol}) \tag{26}$$

Here the Δ_g considers the thickness of the sapphire window and the solution layer thicknesses d_{sol}. The first multiplier in the second term automatically becomes zero, when the actual depth value (d_{cor}) is smaller than the sum of the sapphire window and solution layer thickness. Note that the thickness of the solution layer d_{sol} has to be known for this correction.

5.1.4 Determination of the lateral resolution

The spatial resolution, i.e. the lateral resolution, that is limiting the accuracy of the actual interface positions was determined analogous to other *in situ* fluid-cell Raman experiments [29,41,45]. Assuming the glass/solution interface to be atomically sharp, passing the interface would theoretically coincide with a gradual, opposite intensity transition of the glass and the solution bands intensities. In practice, instrumental limitations lead to a sigmoidal shaped intensity transition across the interface that was fitted by a dose response function. The lateral resolution d_l can be estimated by:

$$d_l = 2 \cdot (x_{Y0.25} - x_{y0.50}) \tag{27}$$

where $x_{y0.50}$ is the inflection point and $x_{y0.25}$ the corresponding *x* value of the quarter-maximum intensity (*y* value) of the sigmoidal fitted intensity curve. An overall lateral resolution was found to be 3.3 ± 1.4 µm for the experiment of ISG in hyperalkaline solution (Chapter 5.7). However, depending on the measuring depth and the chosen characteristic frequency range, whose intensity jump is used to determine the interface position, the resolution can be worse but still on the micrometer scale (e.g., 11 to 16 µm [45]).

5.1.5 Acquisition parameters for Raman spectroscopy

All Raman spectra were measured with a confocal *Horiba* HR800 Raman microscope at the Institute for Geosciences of the University of Bonn, Germany. The wavenumber ranges from 100 to 1735 cm^{-1} and from 2800 to 4000 cm^{-1} were measured in two distinct spectral windows with different acquisition times. In general, the acquisition time and the number of accumulated spectra had to be increased as the duration of the experiment increased, because the signal intensity was lowered by simultaneous corrosion of the top side of the glass sample, which attenuated the laser intensity at depth. Due to the top side corrosion of the glass, the nominal measurement depth below the covering sapphire window was also increased with time. Note that the actual depths are probably larger in the order of tens of microns, because of refraction effects along the beam path [160]. In Table 1, the acquisition parameters are summarized for all experiments presented in this thesis. Spectra acquired *post mortem* were measured with an acquisition time of 15 s for 5 accumulations. The laser power had to be reduced for the *post mortem* measurements, because the am-SAL stability was quite sensitive to the thermal energy induced by the excitation laser.

Table 1: Acquisition parameters for all *in situ* Raman measurements presented in this thesis.

Experiment	*Acquisition time (s)*		*Accumulations*	*Apparent depth (µm)*
	100 - 1735 cm^{-1}	2800 - 4000 cm^{-1}		*(relative to focus on sapphire surface)*
Case study I	7 - 8	1 – 2	6 - 10	170 - 270
Case study II	6	1	7	200 - 160
Case study III, Exp. I	8	2	5	130 - 250
Case study III, Exp. II	5	1	5	200 - 250
Case study III, Exp. III	8	2	5	170

Although the measuring depth was increased in most of the experiments, it was *vice versa* in case study II. In fact, the nominal measurement depth below the covering sapphire window was 200 µm for the first four measurement sessions, i.e., the first 17 days of the experiment, and was then reduced to 160 µm to improve the lateral resolution for the rest of the Raman measurements, because *Stage II* was already assumed to be established and therefore almost no ongoing top side corrosion was expected.

5.1.6 Raman data evaluation

For determination of glass retreat and SAL layer thickness, all Raman spectra were first normalized by the standard normal variate method, which means a normalization in which each spectrum is centered and then scaled by dividing by its standard deviation, and corrected for temperature and scattering according to the equation proposed by Long [175] for an estimated reaction temperature of 85 °C (c.f., Chapter 5.1.2). For the low frequency range, the region between 100 and 1250 cm^{-1} was extracted and a linear baseline with 10 baseline points was subtracted. The high frequency range between 3000 and 3800 cm^{-1} was baseline corrected the same way to obtain a measure of the H_2O signal given as the integrated signal intensity between 3050 and 3750 cm^{-1}.

5.1.6.1 Determination of the glass/solution interface position

To determine the location of the glass interface, the specific bands of the glass and the solution can be used. The typically sigmoidal shaped intensity profiles were fitted by a sigmoidal function ("dose response function in OriginLab®), defined as:

$$y = A_1 + \frac{A_1 - A_2}{1 + 10^{(\log x_0 - x)p}} \tag{28}$$

Here the position of the inflection point x_0 is assumed to represent the actual interface position that is used for glass retreat estimation [40], p is a shape parameter, and A_1 and A_2 define the upper and lower limit of y, respectively. While the fitting procedure was the same in all case studies, the fitted signal intensity curves were individually derived from the integrated intensities of specific spectral ranges for each of the different case studies.

Because of the absence of any Raman band overlap in the high frequency region, the water signal was preferred for case study I and II. The integral signal intensity of the normalized (SNV-normalization) and baseline corrected (linear baseline, 10 basepoints) water bands (range from 3050 to 3750 cm^{-1}) were determined. This approach leads to a better lateral resolution of the glass interface estimation compared to previous approaches that used the Q^n species band (1000-1250 cm^{-1} for TBG) [40]. However, to compare the glass retreat with previous *in situ* Raman corrosion experiments using TBG [30,31,40–42], the glass interface was determined by the intensity distribution of the Q^n signal (typical glass signal between 1000 - 1250 cm^{-1} [40]) for case study III. However, the Q^n signal was of low quality in Exp. III of case study III after about 110 hours due to intense top side corrosion. Therefore, the glass retreat was determined based on the more intense H_2O signal after 110 hours for this experiment.

5.1.6.2 Determination of am-SAL and zeolite layer growth

The SAL that replaces the glasses usually consist of a highly porous, hydrolyzed, amorphous surface alteration layer (am-SAL). The am-SAL was additionally covered a layer of crystalline zeolites in case study III. To estimate the thickness evolution of these distinct corrosion layers with time, the region of 100 to 1250 cm^{-1} was extracted from the corrected Raman spectra and then a linear baseline (10 basepoints) was subtracted.

To visualize the zeolite and the am-SAL layers in hyperspectral Raman images, the integral intensity of the spectral ranges that include the characteristic bands of all corrosion products were determined. In contrast to the sigmoidally shaped glass or water intensity profile at a single glass/solution interface, the intensity profile of the amorphous and the zeolite layers are characterized by two interfaces (left- and right-hand side). Therefore, a Gaussian function was fitted to the intensity distribution in x-direction according to Equation (29).

$$y = y_0 + \frac{A}{w\sqrt{\pi/2}} e^{-2\frac{(x-x_c)^2}{w^2}} \tag{29}$$

The full width at half maximum (FWHM) is assumed to approximate the thickness of the distinct corrosion layers and can be calculated from the width (w) by the following equation:

$$FWHM = w \times \sqrt{\ln(4)} \tag{30}$$

The FWHM-data with an w error > 10 % were excluded from the whole dataset to ensure that just robust fitted data are considered.

For each case study, an individual specific spectral range was used as am-SAL signal. This was necessary because the am-SAL structure in all case studies was very different and therefore the intensity contrasts becomes clear through different bands in the spectra, i.e., different integrated ranges of the spectra.

For example, in case study I, the characteristic Raman bands of the amorphous alteration products are located near 490, 530, and 970 cm^{-1} (c.f., Chapter 6). However, just the integral signal intensity between 850 to 1000 cm^{-1} was chosen for the am-SAL signal, because the Si-OH stretching mode at 970 cm^{-1} and closely located other non-bridging Si-O-X bonds are the most unambiguous am-SAL bands, because they do not overlap with pristine ISG bands. It turned out that for case study II the spectral range between 200 and 500 cm^{-1} is best suitable to derive the am-SAL thickness from the *in situ* Raman data and in case study III the spectral intensity between 200 to 525 cm^{-1} was used.

The zeolites in case study I were best represented by using the ratio of the base corrected zeolite/aqueous carbonate integral signal intensity ratio (200 - 500 cm^{-1}/1050 - 1075 cm^{-1}). This can be explained by the fact, that the formation of zeolites automatically displaces the dissolved carbonate ions at this place in the solution volume. Even if there is still a relatively strong carbonate band visible in the Raman spectra of regions that are assigned to zeolites, this is probably due to out of focus signals and interpenetration of carbonate ion bearing pore solution within the zeolite layer.

5.1.6.3 Determination of structural parameter R_n

To study structural maturation of the silica-based am-SAL, the parameter R_n was determined, which was defined as the ratio of the integral signal intensities between 250 and 460 cm^{-1} and 250 and 600 cm^{-1} by Geisler and coworkers [29]. Therefore, the spectra used were not corrected for temperature and scattering effects and not normalized by normal variate method to allow the comparison with previous studies [29–31,41]. Instead, the low frequency range between

200 and 1250 cm^{-1} of the calibrated spectra was first background corrected by a 2nd order polynomial baseline (10 basepoints). Subsequently, the spectral range of 250 to 600 cm^{-1} was extracted and a linear baseline (10 baseline points) was subtracted before the R_n ratio was determined. Thus, a higher value represents the formation of larger silica ring structures and thus could indicate maturated and aged amorphous silica or initially less dense oligomers.

5.1.6.4 Altered glass fraction ($f_{AG_{Raman}}$)

The altered glass fraction based on Raman data was determined by assuming that the locally measured glass retreat is homogeneous for the whole glass sample. By knowing the initial size of the glass cuboid and assuming a homogenous glass retreat at all sides, a glass retreat in % can be calculated by the following equation:

$$f_{AG_{Raman}} = \frac{(l_{x,t-1} - 2 \cdot R_t) \cdot (l_{y,t-1} - 2 \cdot R_t) \cdot (l_{z,t-1} - 2 \cdot R_t)}{V_{glass,ini}} \times 100\ (\%) \tag{31}$$

Where $l_{x,t-1}$, $l_{y,t-1}$, and $l_{z,t-1}$ are the dimensions of the glass cuboid (in µm) at time $t-1$, R_t is the retreat in µm at time t, and $V_{glass,ini}$ is the initial glass volume in µm^3.

5.2 Solution analysis data evaluation

5.2.1 Altered glass fraction (f_{AG})

In accordance with Gin and coworkers [43], the fraction of altered glass (f_{AG}) was calculated based on solution analysis for each sample by the following modified equation:

$$f_{AG}(\%) = \frac{(C(\mathrm{B})_t - C(\mathrm{B})_{ini}) \times V}{m \times x_B} \times 100\ (\%) \tag{32}$$

here $C(\mathrm{B})_t$ is the concentration of B at the end of the corresponding experiment, $C(\mathrm{B})_{ini}$ the initial boron concentration that was set to zero, because it was below the detection limit, V the solution volume, m the initial mass of the glass sample, and x_B the B mass fraction of the pristine glass.

In the corresponding study of Gin and coworkers [43] the leaching solution of the reaction vessel contained several glass coupons and was sampled regularly. Furthermore, glass coupons were removed after certain periods of time to characterize the samples at different reaction stages. Both effects were considered in the calculation of $f_{AG,t}$ at time t by using the following equation:

$$f_{AG,t} = f_{AG,t-1} + \frac{(C(\mathrm{B})_t - C(\mathrm{B})_{ini}) \times V_t}{\sum m_t \times x_B} \tag{33}$$

Where $f_{AG,t-1}$ is the previous f_{AG} value (zero for the first one), V_t is the solution volume at the duration t, and $\sum m_t$ is the overall mass of the glass coupons still placed in the vessel at the duration t. The corresponding $f_{AG,t}$ values were multiplied by 100% to allow comparison between both studies.

5.2.2 Normalized glass dissolution rate

According to Inagaki an co-workers [102], the boron normalized dissolution rate r_{BN} was calculated using the following equation:

$$r_{BN}\ (g/m^2/d) = \frac{(C(\mathrm{B})_t - C(\mathrm{B})_{t-1}) \times V}{\Delta t\ \times SA \times x_B} \tag{34}$$

Here, $C(\mathrm{B})_t$ is the concentration of B in the solution sample after the experiment, $C(\mathrm{B})_{t-1}$ is the concentration of the previous sample. Δt is the time difference between the samples taken at t and t−*1*, and SA the geometric surface area.

5.2.3 Calculation of the fraction of glass constituents in the SAL

Based on B concentration, the equivalent amounts of other released glass constituents was calculated, assuming stoichiometric dissolution of the ISG. The difference between stoichiometric glass dissolution and measured concentrations of the corresponding oxides was calculated as follows, after the blank (initial solution) was subtracted from the measured concentrations:

$$f_x(\%) = \frac{\left(C(x)_{boron\_equivalent} - C(x)_{measured}\right)}{C(x)_{boron\_equivalent}} \times 100\ (\%) \tag{35}$$

Here $f_x(\%)$ is the fraction (in %) of a certain oxidic component x that is removed from solution by the corrosion products, $C(x)_{boron\_equivalent}$ is the concentration of component x equivalent to the measured B concentration, and $C(x)_{measured}$ is the actual measured concentration. This calculation is also based on the assumption that B is not incorporated in any corrosion products. Therefore, the B_2O_3 retention was set as 0 %. The Zr concentration was below the detection limit for all measurements, indicating a complete retention. Therefore, an $f_x(\%)$-value of 100% is assumed for ZrO_2. Although ISG is nominally free of K, it was highly concentrated (0.375M K_2O corresponds to the amount of KOH and K_2CO_3) in the initial leaching solution. Therefore the $f_x(\%)$ value of K_2O was calculated as well, whereby the boron equivalent amount was set to the nominal initial concentration of dissolved K_2O.

5.3 Electron microprobe analysis (EMPA)

The quenched and dried samples were embedded into epoxy resin, polished (3 µm diamond paste), and coated with an approximately 20 nm thick carbon layer to texturally and chemically characterize the corroded samples by electron microprobe using a JEOL 8200 Superprobe at the Institute for Geosciences of the University of Bonn, Germany. The device is equipped with five spectrometers, a cathodoluminescence, a secondary electron (SE), and a backscattered electron (BSE) detector. The elemental distribution within the SALs were mapped with a 0.5 µm step size in x-y direction in the wavelength-dispersive mode for 1 second at each point with 2 accumulations.

5.4 Inductively coupled plasma mass spectrometry (ICP-MS)

Before analysis by inductively-coupled plasma mass spectroscopy (ICP-MS), the pH of solution samples was measured after quenching the experiment at room temperature (RT, usually 21 °C) with a Mettler Toledo pH microprobe. Afterwards, aliquots from the leaching solutions were transferred with an Eppendorf® pipette in vials and diluted by a dilution factor of 1:5 by adding HNO_3 (2.5 wt.%). The solutions were then analyzed using a Thermo Element XR ICP-MS at the Institute for Geosciences of the University of Bonn, Germany.

For analysis of the alkaline ISG alteration experiment (case study I, Chapter 5.7) the solutions were further diluted to a final dilution ratio of 1:500. Because of the extremely high K concentration with respect to the other elements, the measurement of K was performed using a higher diluted aliquot (1:500000). Solution samples from the acidic ISG alteration experiment (case study II, Chapter 7) were diluted 1:10 for analyzing the dissolved glass constituents and 1:100000 for the highly concentrated K and P in the corroding solution. Exchange solutions of the corrosion experiments performed with TBG (case study III, Chapter 8) were diluted by 1:50 for the initial solution and 1:125 for all following samples of Exp. II. The samples of Exp. III were diluted by 1:500 for the initially silica-rich solution and 1:50 for the silica-free solutions at the end.

All samples were measured twice and the concentration values were averaged. For Si and B, the concentration was determined based on two different isotopes (^{28}Si, ^{29}Si, ^{10}B, and ^{11}B) to check for their natural isotopic ratio. In this way, significant molecular interference, e.g., by different Si and N species [43], could be ruled out. The naturally most abundant isotope of Ca (^{40}Ca) could not be quantified, because of a strong interference with ^{40}Ar of the transport gas. Consequently, the less abundant isotope ^{43}Ca was monitored. Because the Zr concentration was assumed to be below detection limit due to its low solubility, it was not calibrated and measured. Al, Na, and K concentrations were determined based on the isotopes ^{27}Al, ^{23}Na, and ^{39}K, respectively. All elements were measured at medium mass resolution, except ^{39}K that was measured at high resolution to avoid interference with $^{38}ArH^+$.

5.5 Micro-Computed Tomography (µCT)

To evaluate the homogeneity of the glass corrosion reaction for the whole sample and to estimate an overall altered glass fraction to validate the solution data, some corroded TBG samples were analyzed by using a SkyScan 1272 desktop µCT device of Brucker microCT (Kontich, Belgium) with a detector size of 4,904 px × 3,280 px. To avoid unintentional changes of the samples they were kept in the sample holder of the *in situ* experiment which in turn was fixed with plasticine for the µCT scans to avoid movement artifacts during scanning. The scanning parameters are summarized in Table 2 for both measurements that were performed over 180° without frame averaging. The relatively big size of the samples limited the maximum voxel resolution.

For the estimation of the glass volumes in case study III (c.f., Chapter 8), the 3D images were treated as follows. Using the software Fiji [181], each reconstructed dataset composed of 16-bit TIFF images was modified to an 8-bit TIFF image stack, rotated using the TransformJ plugin, and finally cropped along all three axes using the Crop function. Based on the prepared datasets, the non-corroded areas of each scanned glass block were specifically segmented using the software Amira 6.1 (Thermo-Fisher Scientific, Waltham, MA, USA). Segmentation was carried out using the Segmentation Editor and its threshold-based Magic Wand tool with subsequent manual improvements using the Brush tool. The segmented label field was then surface-rendered using the SurfaceGen module with unconstrained smoothing activated. The resulting surface mesh was reduced to 1,000,000 faces using the Simplifier tool. The 3D visualization of the simplified mesh was conducted using the SurfaceView module. The surface-rendered model was displayed using orthographic projection mode. In addition, a volume-rendering was blended in using the Volren module to visualize the corrugated areas in greyscale. Finally, scaled snapshots were taken using the Snapshot function. The volume of the segmented, surface-rendered, simplified glass block was calculated based on voxel size dimensions using the SurfaceArea module. A second more simple volume estimation was done by measuring the size of the residual glass cuboid manually and assuming the residual glass volume would be a cuboid. Point-by-point measurements were done by using the DataViewer 1.5.6.2 (Brucker microCT, Kontich, Belgium) software. The initial glass volume was estimated based on geometric measurements of the samples before running the experiments and was 86 ±2 mm^3 for Exp. II and 77 ± 2 mm^3 for Exp. III.

Table 2: Scanning parameters for µCT scans of the corroded glass samples from Exp. II and Exp. III.

Scanning Parameter	*Experiment II (Exp. II)*	*Experiment III (Exp. III)*
Source voltage	80 kV	80 kV
Source current	125 µA	125 µA
Rotation step size	0.2°	0.4°
Filter	Al (1 mm)	Al (1 mm)
Acquisition time	1 h 33 min 5 s	1 h 2 min 51 s
Isotropic voxel resolution	7.5 µm	10 µm

5.6 Data evaluation software

For data treatment of the Raman spectra, including the temperature correction, Raman shift calibration, extraction of spectral regions and baseline correction, the software HORIBA Scientific's LabSpec 6.5.1.24 Spectroscopy Suite was used and the specific procedure is described in Chapter 5.1.5.

The data analysis and graphing software OriginPro® 8G was used for fitting of sigmoidal and Gaussian shape functions to the Raman intensity profiles, for creation of the various data plots, and for fitting of linear and polynomial functions to determine slopes, respectively rates.

For dataset preparation of the µ-CT data, the software Fiji [181] was used. The consecutive segmentation and 3D visualization were performed with the software Amira 6.1 (Thermo-Fisher Scientific, Waltham, MA, USA). For visualization and point-by-point measurements the DataViewer 1.5.6.2 (Brucker microCT, Kontich, Belgium) was also used.

For all aqueous geochemical calculations, i.e., calculation of solution pH at different temperatures, several solubilities and saturation states, and activity of dissolved species PHREEQC Version 3 [133] with the Thermochimie V9b [136] database was used, which considers the specific ion interaction theory (SIT), which is particularly accurate for high ionic strength solutions. Specific input parameters for specific calculations for the different case studies are given in the corresponding chapters.

MATLAB® was used to generate the false color Raman maps using the *viridis* color palette, for customized scripting to evaluate data, to run batches of PHREEQC calculations (using the IPhreeqcCOM module, Version 3.7.3), and for setting up a simple numerical 1D ICDP-based glass corrosion model (more details in Chapter 0).

5.7 Conventional batch experiments

Complementary to the *in situ* fluid-cell Raman experiments, some hydrothermal experiments were carried out in PTFE lined steel reactors. The size of cylindrical fluid-cell volume is 12 mm in diameter and 24 mm in height. All PTFE inlays were cleaned first to remove any contaminants from fabrication and the mobile fluorine by the following procedure: the inlays were cleaned in an ultrasonic bath for 1 hour at 60 °C in Milli-Q® that was mixed with a commercial rinsing agent. Subsequent the PTFE-inlays were rinsed by Milli-Q® and boiled in an HNO_3 solution (16.25 wt.%) for 48 hours at 90 °C. The third cleaning step was boiling in HCl (18.5 wt.%) for 24 hours at 90 °C. Finally, the PTFE parts were rinsed with Milli-Q® and dried in a clean bench. For the experiments, 2 ml of the corresponding solution was added into the reactors, measured with a piston-operated Eppendorf® pipette. After closing the vessels, they were transferred to in-house build ovens, in which they were heated at 90 ± 1 °C for different periods of time. After termination of the experiments, the reactors were removed from the furnaces and cooled down to room RT before they were opened. The experimental solution was pipetted off and, after drying in a desiccator, the solid samples were prepared for further analysis.

5.8 Glass synthesis, characterization, and preparation

5.8.1 Glass synthesis and preparation

The TBG is an in-house borosilicate reference glass and characterized by a relatively low corrosion resistance. As a result, TBG usually forms am-SALs several micrometers thick after just a few days, making it ideal for the technique used here and in previous experiments [29–31,39,41,42]. For synthesis, a powder mixture of SiO_2, B_2O_3, and Na_2CO_3 was prepared to get a target glass composition of 60 mol.%, 20 mol.%, and 20 mol.%, respectively. The powder was melted two times at 1400 °C for 3 hours to ensure chemical homogeneity and tempered at 560 °C for 6 hours after quenching to reduce tension.

The ISG was produced in 2012 by MoSci Corporation (Rolla, Mo, USA) and was distributed to different research groups that deal with the scientific research on long term stability of nuclear waste glasses [3,6,43]. This reference benchmark glass has a typical composition of the main components making up most of the boro-aluminosilicate nuclear waste glasses (composition in mol.%: 60.2 SiO_2, 16.0 B_2O_3, 12.6 Na_2O, 3.8 Al_2O_3, 5.7 CaO, 1.7 ZrO_2 [3]).

All studied glass coupons were cut with a diamond saw and their faces were polished with SiC papers. The top side of the samples used for *in situ* fluid cell Raman spectroscopy were additionally polished properly twice with diamond paste (3 µm and 1 µm) to minimize the reactive surface area and in turn to reduce top side corrosion. Why this is important for data quality is explained in more detail in Chapter 5.1.

5.8.2 Characterization of the pristine glasses by Raman spectroscopy

Representative Raman spectra of pristine ISG and TBG that were acquired *in operando* in corrosion experiments of case study II and III are shown in Figure 23. The structure of both glasses based on Raman spectroscopy has already been discussed intensively in the literature [41,42,80,83] and is briefly summarized in the following. Even if some of the Raman bands are the same, there are differences of their relative intensity ratios, which are visible to the naked eye. The intense band around 485 cm^{-1} is observed in both spectra and can be assigned to breathing modes of fourfold Si-O-Si ring structures (D_1 band) [177]. Another band that is typical for silicate glasses, the so called D_2 band, is usually localized around 600 cm^{-1} and reflects threefold ring structures [182]. However, this band was not detected. For ISG it is known to appear after structural modification caused by ion irradiation [80,83]. The band near 630 cm^{-1} is also present in the spectra of both glasses and can be addressed to danburite-like ring structures [42,80,83,183], which reveal the formation of a borosilicate structure and tetrahedrally coordinated borate (BO_4^-) [183]. It should be mentioned, that an absence of this band in the am-SAL spectra would be in line with the still widespread general assumption that B is not incorporated in the silica structure of glass corrosion products [43]. However, under certain conditions the retention or incorporation within the am-SAL was observed [31,34,158]. The convoluted Q^n bands, usually located between 850 and 1250 cm^{-1}, represent stretching motions of Si-O bonds and SiO_4 tetrahedra. The relative proportion of the underlying individual bands reflects the degree of polymerization of neighboring SiO_4 tetrahedra, i.e., the amount of non-bridging oxygens [42,80,83,182,183]. Individual bands near 850 cm^{-1} (Q^0), around 930 cm^{-1} (Q^1), between 980 and 1000 cm^{-1} (Q^2), between 1050 and 1100 cm^{-1} (Q^3), and around 1150 cm^{-1} (Q^4), are addressed to tetrahedra with zero, one, two, three, and four non-bridging oxygens for ISG, respectively [80,183]. Equivalent bands were observed by Lönartz et al. (2019) [42] for TBG near 905, 978, 1061, and 1128 cm^{-1}, which have been assigned to Q^1, Q^2, Q^3, and Q^4 species. Based on NMR analysis and modeling results of ISG structure, Peuget et al. (2018) [80] postulated that the band in the ISG spectrum around 980 cm^{-1} probably corresponds to fully polymerized SiO_4 tetrahedra in which two bridging oxygens are linked to network formers other than Si (i.e., B, Al, or Zr), so called Q^a units. The fact that this strong band was not observed in the Al- and Zr-free TBG supports this assumption. Beside this characteristic difference, the higher Boron content of TBG (c.f., Chapter 5.8.1 for composition of both glasses) is also reflected in a much more intense danburite-like band. In Figure 23 the Raman signals of the reaction cell components (e.g., sapphire at 418, 574, and 750 cm^{-1}, PTFE at 734 cm^{-1}) were labeled as B_{RC} and are inevitably found in the *in situ* data.

5.9 Solution preparation

All solutions used here were prepared with deionized, pure water (Milli-Q®) and the added powders were weighed in on an analytical balance from Sartorius AG with an accuracy of 0.1 mg. Nitric acid solutions were prepared by dilution of a pure (68 wt.%) stock solution from Carl Roth GmbG & Co. KG. Hydrochloric acid was also produced by dilution of a stock solution with 37wt.% HCl EMSURE for analysis from Merck KgaA. For pH adjustment several NaOH of different concentrations were prepared from dissolving NaOH (Merck KGaA, ≥ 97 %) in Milli-Q®. For the corresponding experiments presented here, Phosphate and carbonate bearing corroding solution were prepared from KH_2PO_4 (Merck KgaA, analytical grade) and $NaHCO_3$ (Merck KgaA, analytical grade), respectively. A Si oversaturated solution was prepared by dilution of pure sodium silicate ($Na_2O(SiO_2)_x{\cdot}xH_2O$) from Merck KgaA.

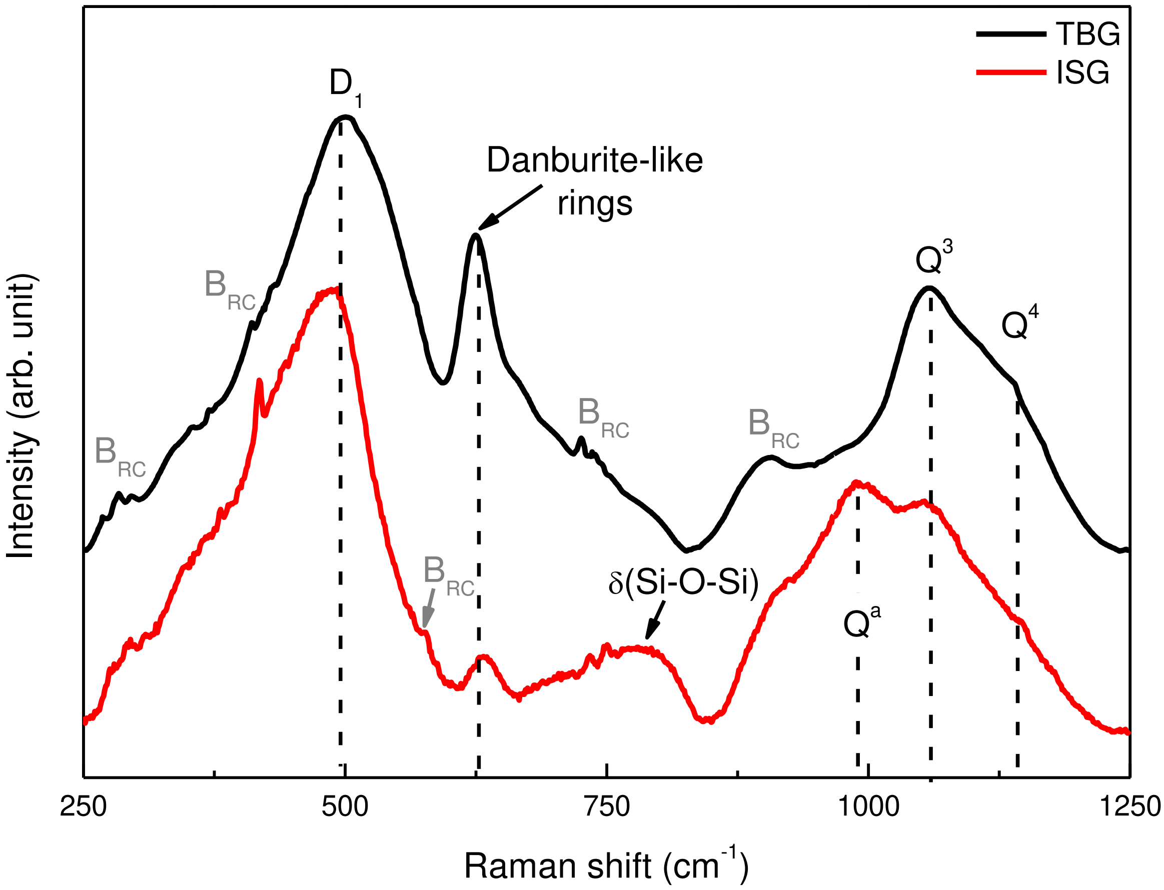

Figure 23: Representative background-corrected Raman spectra from pristine ISG (red) and TBG (black), acquired during the experiment at ~85 °C. Some bands that can be assigned to the background signal of the reaction cell components were labeled B_{RC}.

6

Case study I: International simple glass (ISG) corrosion under alkaline conditions

6.1 Introduction

The corrosion of silicate glasses (and minerals) in aqueous solutions involves a multitude of transport and reaction processes occurring simultaneously or subsequently, including diffusion and ion exchange, sorption, surface complexation, hydrolysis, condensation, dissolution and precipitation [10,20,31,34,60]. Depending on the physicochemical conditions, the interaction of glasses with an aqueous solution leads, at a macroscopic scale, to congruent and/or incongruent dissolution of the glass. Incongruent glass dissolution is observed when a certain product phase is supersaturated in the reacting solution, frequently causing in formation of a complex surface alteration layer (SAL) [26,39]. The kinetics and extent of alteration, the microstructure and composition of the SAL depend on the composition of the parental phase, its structure, and environmental parameters such as pH, temperature, and solution composition [5,31,46,47]. When using silicate glasses as a matrix material to immobilize high level radioactive waste, the impact of radiation damage on the corrosion behavior must also be taken into account [42,80,81].

The whole SAL can be made up by (multiple layered) hydrated, amorphous and/or crystalline corrosion products, primarily depending on pH and elemental composition of both the parental glass and solution [43,44,184]. Nevertheless, there is a lack of clarity about the underlying mechanisms that are responsible for the different types of SALs formed under neutral or weakly alkaline pH [20,31,36,43,90]. Over the last decade, an interface-coupled dissolution-precipitation model for glass corrosion competes with the idea of an interdiffusion-based corrosion mechanism that includes a solid-state reconstruction, i.e., local hydrolysis and recondensation, at pH values below $10.5_{90°C}$ [20,43,185]. It should be noted that the basic molecular reactions (hydrolysis and condensation) are essentially the same for both models, but the mechanistic framework is different. For instance, the ICDP model postulates stoichiometric dissolution of the glass in a thin interface fluid film at the reaction front between the parental glass and the bulk solution or SAL [20,29,34–36,38,39], which is temporally and spatially coupled to the precipitation of the SAL. In contrast to this, the *in situ* reconstruction/interdiffusion model rather assumes a partial hydrolysis of the glass network without a complete hydrolyzation, followed by silanol recondensation reactions [20,90,137]. More recent studies seem to rather indicate a combination of both model endmembers. It was proposed that the mechanism may switch from ICDP to an *in situ* reconstruction mechanism for more readily soluble, Al free glasses [20,56]. Furthermore, the ICDP model was also refined by consideration of ID reactions, which, however, is not the decisive reaction for SAL formation [31,34]. Even if there is no consensus on a universal glass corrosion mechanism (yet), it now seems to be widely accepted that the amorphous and crystalline corrosion products observed under hyperalkaline conditions ($pH > 10.5_{90°C}$) are formed by ICDP reactions, even for Al-bearing glasses [43,44,184].

Here, data from an *in situ* fluid-cell Raman corrosion experiment with ISG in a hyperalkaline carbonate solution (0.25*M* KOH and 0.25*M* K_2CO_3) is presented. The total corrosion time was about 198 days and after continuously monitoring by *in situ* Raman spectroscopy for 137 hours, the reaction cell was placed on a heating stage and several times measured in varying time intervals.

A strong alkaline environment similar to the initial experimental conditions at $pH_{90°C}$ 13.5 ± 0.2 is indeed realistic for specific nuclear waste disposal scenarios that use cementitious backfill material in the near-field of nuclear waste in deep geological repositories [44,78]. At these pH conditions, the formation of crystalline corrosion products, such as zeolites, phyllosilicates, and calcium silicate hydrates (CSH-phases) were observed [43,44,71,142,186,187]. The high carbonate content in this study can be used to potentially recognize a significant pH drop caused by dissolution of the glass, as this would produce dissolved bicarbonate that can be identified in Raman spectra of the solution by its $\nu_5(HCO_3)$ near 1006 cm^{-1} at RT [29]. The speciation of carbonate measured by Raman spectroscopy has already been used in previous fluid-cell Raman experiments to *in situ* estimate the pH during the experimental corrosion of a ternary sodium borosilicate glass (TBG) [29,41,42].

Fluid-cell Raman spectroscopy offers the possibility to extract isothermal dissolution and precipitation rates from a single experiment, in contrast to conventional approaches where numerous quench experiments over different time periods have to be performed [43,44]. With such methods it is possible to clearly differentiate between phases, textural, and structural features formed during the corrosion and those probably induced by quenching, i.e., cooling, drying, and preparation of the sample. Complementary batch/quench experiments were performed to compare both approaches and to be able to analyze samples of the glasses and solution at certain intermediate stages (c.f., Table S 3 for experimental parameters and sample names).

Therefore, five polished ISG monoliths were altered for different periods of time (8, 31, 80,166, and 274 days) in PTFE-lined steel autoclaves, already described in Chapter 5.7, at 90 °C in the same solution used for the *in situ* experiment. The SA/SV ratio was higher (0.45 ± 0.30 to 0.48 ± 0.30 m^{-1}) compared to the *in situ* experiment (0.26 ± 0.3 m^{-1}). The drying procedure of the *ex situ* samples was also modified to reduce any structural changes of the alteration products. After rinsing the samples with Milli-Q®, the glass specimens were placed in ethanol for 48 hours that was renewed two times during this time, before the samples were dried at 90 °C for 48 hours. The aim of this procedure was to exchange the adhesive and pore water within the am-SAL, since the lower surface tension of ethanol reduces the collapse of the porous, gel-like structures [188].

Furthermore, formation of precipitates, especially carbonates and also zeolites, within the pores and at the SAL surface during drying were observed in quenched samples under similar conditions [45]. The procedure aimed to avoid such drying features. The samples altered for 166 days could not be further analyzed, as it was disintegrated before it could be embedded and stabilized in resin.

The general aims of this study were (i) to further develop the methodology enabling the *in operando* investigations of more durable glasses over long reaction time-scales, (ii) to study the effect of dissolved carbonate on ISG alteration under hyperalkaline conditions, and (iii) to investigate zeolite formation and its relationship to the phenomenon of resumption of alteration rates during long-term corrosion.

6.2 Results

6.2.1 *In operando* and *in situ* observations

The first Raman scans across the glass-solution interface were acquired 1.5 hours after start of the experiment. In Figure 24 the movement of the glass-solution interface, the replacement of the glass by an amorphous, silica-rich and hydrolyzed phase, here called am-SAL, and the zeolite layer thickness is visualized as a function of space and time. The signal intensity of Raman bands that can be assigned to molecular water (specific band region 3050 - 3750 cm^{-1}) is shown in Figure 24a. The false color space-time resolved image in Figure 24a reveals nonlinear glass dissolution at the beginning, especially for the first 140 hours which becomes even clearer when having a look on the glass retreat vs. time plot for this period in Figure 26. In addition to the H_2O signal, the amorphous SAL replacing the glass was highlighted by showing the intensity of phase specific Raman bands between 850 and 1000 cm^{-1} in Figure 24c. The Raman data indicate the onset of precipitation after approximately 50 - 60 hours of congruent glass dissolution. However, it should be noted that due to the spatial and detection limitations, the first µm of the SAL could have formed already earlier. In combination, the false color images of the H_2O and am-SAL signal reveals a replacement of glass by an amorphous phase, producing a tens of micrometer thick alteration layer after just two weeks. To get information about the glass dissolution and SAL formation kinetics over longer time periods, Raman mappings were carried out at different time step until 198 days (4761 h) of corrosion in total. The experiment was terminated, because most of the glass was already corroded and the top side corrosion of the sample had progressed so far that it was no longer possible to record Raman spectra from the water/am-SAL and am-SAL/glass interfaces below. Corresponding to Figure 24a and b, Figure 24c and d show the H_2O and am-SAL signals, indicating a progressive replacement of glass by the am-SAL. Moreover, it is noteworthy that both signal intensities at the initial interface position decreased in time, beginning after 1849 hours. This low intensity region extends in both directions and correlates well with the rising zeolite signals in Figure 24e. Zeolite crystals that formed right below the sapphire window significantly affected the Raman signals by absorption and scattering of the excitation laser, which is the reason for a blurred SAL interface. Moreover, it must be considered that this effect is likely to be intensified by increased corrosion on the edges of the glass monolith above the scanned area, so that the am-SAL layer thickness may be underestimated. The deteriorating signal quality is also

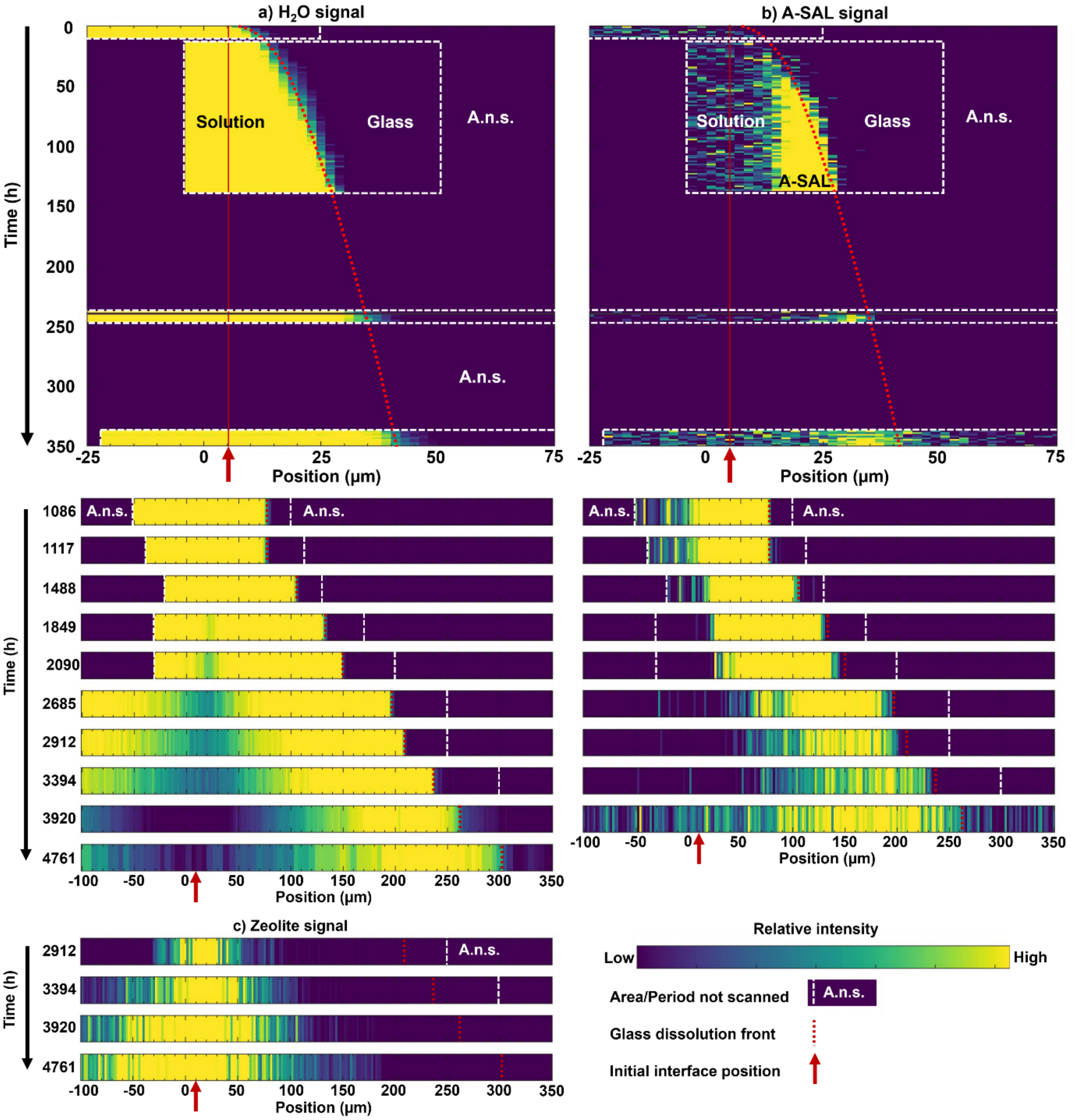

Figure 24: Temporospatial evolution of the glass-solution interface monitored *in situ* and *in operando* at 85 °C using fluid cell Raman spectroscopy. In these hyperspectral Raman images, yellow reflects a high intensity of **(a)** water (H_2O; bands between 3050 - 3750 cm^{-1}), **(b)** the amorphous surface alteration layer (am-SAL; bands between 850 - 1000 cm^{-1}), and **(c)** zeolites (ratio of bands between 200 - 500 cm^{-1} and 1050 - 1075 cm^{-1}). Regions (positions in x-direction) and time periods (rows in y-direction) of which no measurements were performed during the experiment are colored with minimum intensity and delimited from the measured area by dashed white lines. The red dotted line shows approximately the position of the glass surface/reaction front and for glass retreat estimation this interface was determined by fitting a sigmoidal distribution function to the H_2O signal intensity for each row.

the reason for the missing SAL signal plot of the final scan after 198 days in Figure 24d. The H_2O signal at the glass/am-SAL interface is less affected because of its high Raman scattering factor and the absence of possible interferences with other Raman bands in the high frequency region. Nevertheless, because the overall signal intensity decreased in response to zeolite formation, the water signal near the solution-am-SAL interface weakened as well. Zeolite crystals were observed to occur for the first time already after 1849 hours and grow significantly until 2685 hours. Up to this point in time this time, a clear estimation of the zeolite layer thickness was not possible, because it was difficult to obtain Raman spectra of zeolites with good signal-to-noise ratios. This is because these phases are highly dispersed and have a low Raman scattering cross-section [189]. In addition, the complex optical conditions in the setup hindered the acquisition of a good signal-to-noise ratio with good spatial resolution. Nevertheless, the extracted zeolite specific signal intensities (ratio of bands between 200 - 500 cm^{-1} and 1050 - 1075 cm^{-1}) were sufficient to reliably record zeolite growth over time.

Representative Raman spectra of different zeolite phases, collected after quenching to RT, are shown with reference spectra in Figure 25. In addition, representative Raman spectra of the zeolite layer at 1850 and 3920 hours and the am-SAL at 1850 hours are shown in the appendix (Section 0). However, due to limitations of the spatial resolution, it was impossible to *in situ* obtain a pure and clear spectrum of each phase. Nevertheless, it was possible to render the zeolite layer indirectly by the much lower signal intensity compared to the background and identify the phase by the spectral differences compared to the am-SAL (e.g., no Si-O-H and ZrO_8 bands), although it is not possible to visually distinguish between the am-SAL and zeolite bands between 480 and 490 cm^{-1}. The same applies to the second zeolite fundamental band near 424 cm^{-1} that was observed after quenching the experiment, but overlaps with the symmetrical stretching band from the sapphire window. In summary, to clearly identify zeolite in this experimental setup, analysis of the quenched samples were found to be more suitable, especially when it comes to recognizing different zeolites.

During the first 140 hours of the experiment, the glass-solution interface was continuously scanned to record the initial changes of the dissolution rate and, potentially, the first formation of an amorphous corrosion product. The continuous drop of the glass retreat vs. time plot in the inset diagram of Figure 26 also shows the dynamic shift of the reaction front. The initially nonlinear evolution of dissolution rates can be reasonably fitted by a 4th order polynomial function with the intercept anchored at zero. A strong decrease of the alteration rate at the beginning becomes even clearer by plotting the glass retreat rate vs. time as shown in the supplementary material (Figure S 3). The relatively low dissolution rate, the short time intervals between measurements in one measuring session, and the uncertainty of the determined glass/solution interface result in artificial fluctuations of the alteration rate that merely reflect the uncertainty of the method at low alteration rates. Because of this, such a rate vs. time plot highlights the strong initial decrease of the dissolution rate very well, but is less suitable for the overall rate behavior than it is for Figure 26. The initial glass dissolution rate at t = 0 was 0.43 ±0.01 µm/h. Between 238 and 2699 hours the dissolution proceeded with a linear rate of 0.0767 ± 0.0003 µm/h. During this period, the am-SAL thickness also increases, replacing the glass at an inwardly moving reaction front. A second, further reduced rate of 0.0510 ± 0.0008 µm/h occurred after 2699 hours and remained constant until the end of the experiment. This deceleration of the glass corrosion rate coincides with the appearance of the zeolite layer covering the outer am-SAL surface. Because of the relatively long period of time between 2090 and 2699 hours for which no Raman data exists, the conditions at the onset of zeolites growth are not known. However, the detection and growth of zeolite are synchronous to a stagnation of the am-SAL growth. Then both layers increase in thickness and their sum exceed the thickness of the replaced glass thickness ('am-SAL + Zeol.' in Fig.4).

Although the amorphous SAL is presented in Figure 24 as a single layer that replaced the glass, a detailed look at the Raman spectra of the am-SAL at different positions reveals significant spectral differences, reflecting local variations in molecular structure, hydrolysis states, and composition. Figure 27 shows four representative, background corrected and spatially averaged Raman spectra from the scan that was acquired after 1117 hours and exhibit systematic changes in the shape of the convoluted bands within the wavenumber ranges of 400 - 600 cm^{-1} and 850 - 1000 cm^{-1}.

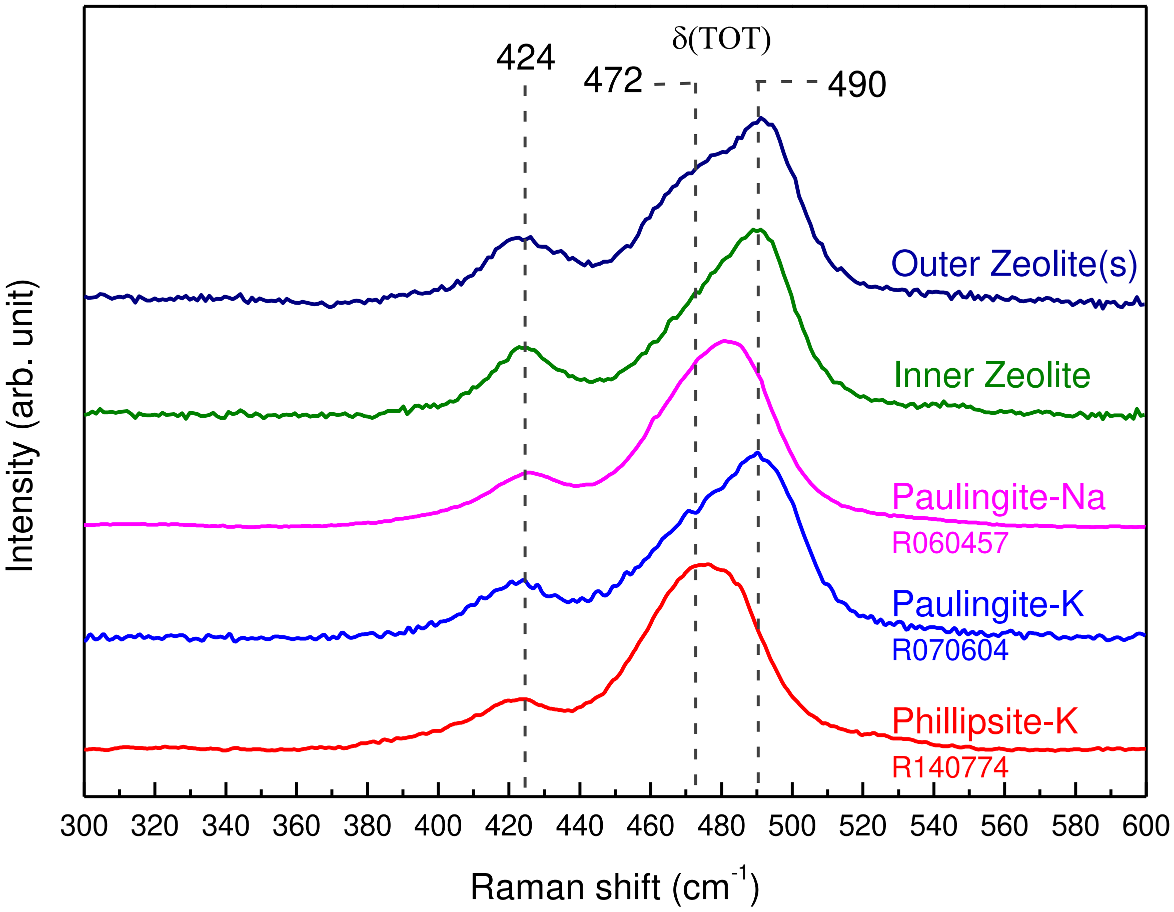

Figure 25 (see previous page): Background-corrected Raman spectra of the zeolites formed during the corrosion of the ISG under hyperalkaline conditions (blue and green spectrum). Raman spectra of paulingite-Na (R060457), paulingite-K (R070604), and phillipsite-K (R140774) from the RRUFF database [190] are shown as reference. The green spectrum was measured right next to the surface of the outer am-SAL, while the blue spectrum was measured in a distance of 5 µm outwardly directed with respect to the underlying pristine glass. The symmetric bending modes δ(T-O-T) (T = Al, Si) between 480 and 520 cm^{-1} [191,192] are characteristic for S4F-Zeolite-group minerals [45]. The reference spectra indicate that K-bearing paulingite and phillipsite were formed.

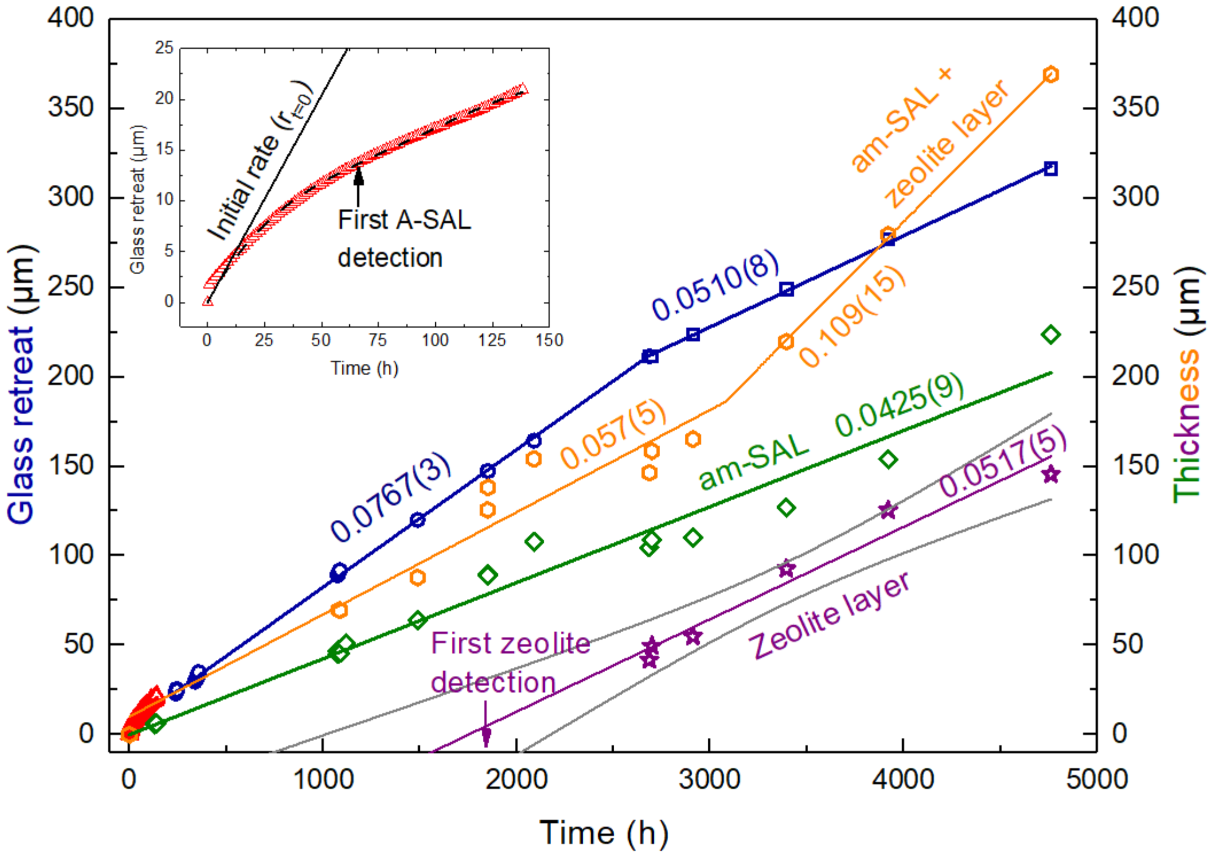

Figure 26: Glass retreat and thickness of individual corrosion layers as a function of time. The glass retreat with time can be subdivided at least three different kinetic regimes. The fitted blue lines reveals a retreat rate of 0.0767 ± 0.0003 and 0.0510 ± 0.0008 µm/h, respectively (first blue line: R^2= 0.9994, 30 data points; second blue line: R^2= 0.9988, 6 data points). The summed total layer thickness of am-SAL (green circles) and Zeolites (purple stars) is displayed by orange hexagonal symbols, fitted by a piecewise function (R^2=0.97782) and exceed the total thickness of dissolved glass after almost 4000 hours. Errors are smaller than symbol size and increases with time due to the increased scattering caused by top side corrosion of the sample. The initial stage is more clearly displayed in the inset diagram and characterized by a strong flattening of the data trend. The red curve is a 4rd order polynomial fit to the data (r^2= 0.9936, 91 data points). The derived initial rate rt=0 was found to be 0.43 ± 0.01 µm/h. The other rates were 0.0425 ± 0.0009 µm/h for am-SAL growth (R^2= 0.9889), 0.00517 ± 0.00005 µm/h for zeolite layer growth (R^2= 0.9456), 0.05712 ± 0.00528 µm/h for am-SAL & zeolite layer growth for the first rate regime, and 0.10902 ± 0.01461 µm/h for am-SAL & zeolite layer growth for the second rate regime.

The occurrence of the symmetric stretching $\nu_1(CO_3)$ band at 1063 cm^{-1} clearly proves the presence of CO_3^{2-} ions within the pore solution of the am-SAL. The amplitude of this band was used to normalize spectra as its intensity is approximately constant in all spectra shown here. The solid am-SAL is characterized by the D_1 band around 490 cm^{-1} that is attributed to $Si-O-Si$ rocking modes of four-fold siloxane rings and can be found in many (boro)silicate glasses and spectra of SALs [29,31,80,182,193]. It is partly overlain by a band near 550 cm^{-1} that can be assigned to cubic zirconia type ZrO_8 groups incorporated in the amorphous silica structure, so observed in heat-treated ZrO_2-SiO_2 gels [194]. It is noteworthy that an increased intensity of this band relative to the D_1 band can be observed in the outermost am-SAL spectrum (Figure 27).

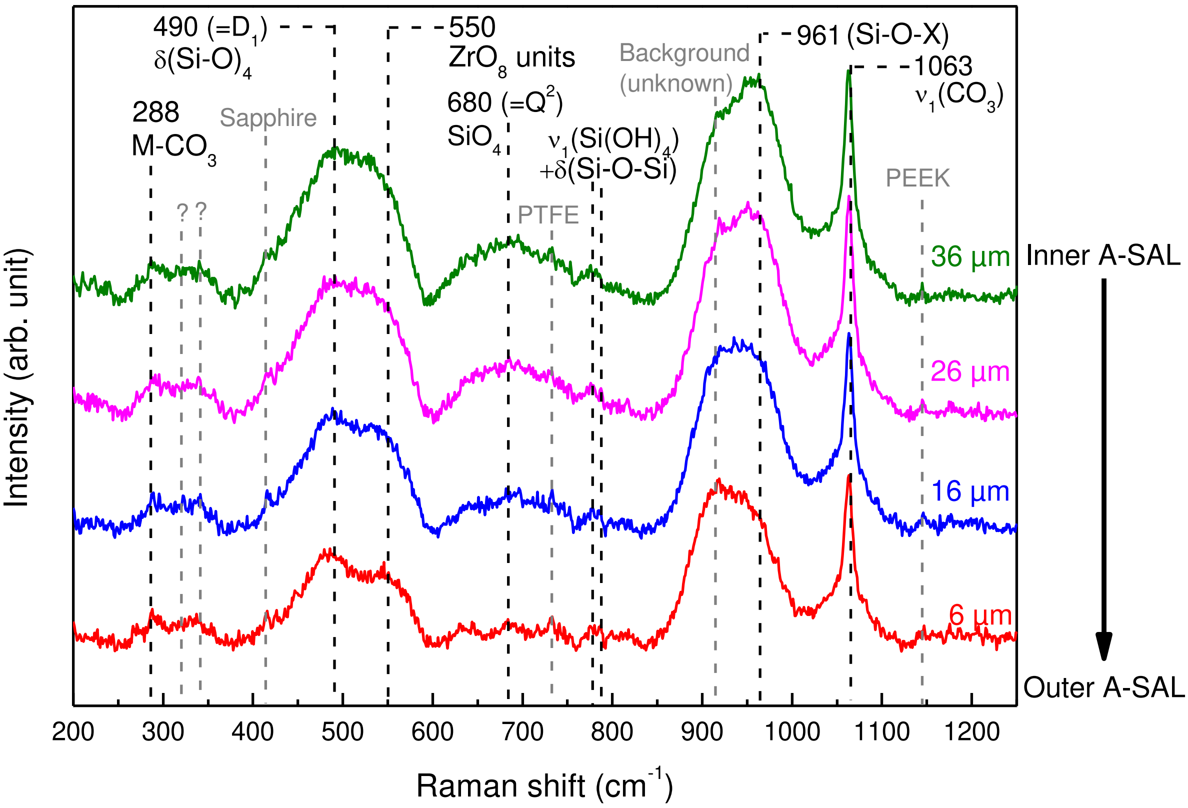

Figure 27: Representative background-corrected Raman spectra of the am-SAL collected in situ after 1117 hours of corrosion at 85°C. The spatial position (6, 16, 26, and 36 µm) refers to the position in the corresponding line scan of Figure 24c & d and each spectrum was generated by averaging 5 neighboring spectra (from 2 - 10 µm, 12 - 20 µm, 22 - 30 µm, and 32 - 40 µm). The most prominent bands near 490, 550, 961, and 1063 cm^{-1} can be assigned to the breathing mode of four-fold Si-O-Si rings, ZrO8 units, surface silanol groups, and dissolved carbonate anions, respectively. The differences between the inner and outer am-SAL spectra reflect different molecular structures, hydrolysis states, and composition. Unknown background bands between 300 and 350 cm^{-1} are labeled with a question marks and other assigned background signal bands (Carbonates, PTFE, and PEEK) are labeled grey are colored in grey.

The intense convoluted bands in the region between 850 and 1000 cm^{-1} are characteristic for the am-SAL and were therefore used to highlight its distribution in the hyperspectral time-position images (Figure 24). The $\nu_1(Si-OH)$ stretching mode at 961 cm^{-1} is higher at the inner side, right next to the reaction front, indicating a higher concentration of hydrolyzed nonbridging $Si-O-H$ surface sites [31]. Usually, this band appears at higher wavenumbers near 975 cm^{-1} [31,193,194] at RT, but is shifted here by temperature. In addition to surface siloxane, the symmetric vibration of other nonbridging $Si-O-$ (Na, K, negative charge) [195] groups appear between 900 to 950 cm^{-1}, which is in line with studies conducted on bioactive glasses [196], sol-gel derived silicate glasses [31,193], and sodium metasilicates [195]. Considering the chemical composition of the am-SAL and the presence of ZrO_8 units, vibrations of $Si-O-Zr$ linkages are also likely. Lee and

Condrate [194], for instance, assigned a band near 954 cm^{-1} to $Si - O - Zr$ linkages in sol-gel derived glasses. In accordance with this study, Celestian et al. [197] also described $Si - O - Zr - O$ chain stretching modes near 938 cm^{-1} in the mineral gaidonnayite ($Na_2ZrSi_3O_9 \cdot 2H_2O$). However, since these vibrational modes are also located in the range of nonbridging Si-O groups and their temperature-dependent shift is unknown, it is not possible to unambiguously assign the bands between 900 and 950 cm^{-1}. Most likely, these bands represent a combination of both symmetrical, non-bridging $Si - O - (X)$ and $Si - O - Zr - O$ chain vibrations, an interpretation supported by chemical analysis (see below).

The intensity of the broad hump between 600 and 750 cm^{-1} with a maximum near 680 cm^{-1} is increasing from the outer to the inner side of the am-SAL. The band is usually assigned to Q^2 species of SiO_4 [198] and clearly shows a different am-SAL structure at the outer and inner side. Note that the signal around 900 cm^{-1} most likely is a background signal of the reaction cell, because it was present already from the beginning of the experiment and observed in the glass and solution spectra in almost equal intensity.

Indications for fully hydrolyzed MSA, especially under hyperalkaline conditions, are given by the bands around 780 to 785 cm^{-1} [199,200]. The relatively low intensity, even at high concentration considering the solution analysis, is also consistent with the fact, that the fraction of this dissolved silica species is quite low at high pH.

6.2.2 Post corrosion observations

Backscattering electron (BSE) images of cross-sections through the SAL reveal a greater am-SAL thickness with increasing reaction time and different corrosion products such as am-SAL, zeolites, calcite, and aragonite (Figure 28 and Figure 29). The am-SAL of the sample from the *in operando* experiment is permeated by gaps and cracks that were filled with epoxy resin (Figure 28a). These structures are likely formed by drying induced collapse and shrinking of the amorphous, water-rich, and hydrolyzed alteration product. Such drying features were already observed for ISG samples altered in hyperalkaline solutions and dried in the same way[43]. Interestingly, the mere exchange of pore solution with ethanol as an intermediate step before drying, as applied to the *ex situ* samples, seems to minimize the shrinking and cracking, even without a supercritical drying procedure. Note that the sample area shown here is not identical to the region that was monitored *in situ* by the Raman measurements, because most of the corrosion products detached completely after drying. Only the parts of the sample closest to the sample holder were preserved. Therefore, the am-SAL extension might not quantitatively reflect the corrosion extent observed *in operando*. Nevertheless, the qualitative interpretation reveals a distinct outer am-SAL layer covered by zeolites, which is fully consistent with the *in operando* observations presented in the previous section.

The BSE images of the samples altered for 8, 31, 80, and 274 days are also shown in Figure 28 along with representative elemental distribution maps from the 274 days sample. All samples show the presence of a distinct outer layer of about 5 ± 1 µm that is enriched in Zr and Ca with respect to the pristine glass and the rest of the am-SAL (c.f. elemental distribution line scan of Ex_situ_080d in the appendix in Section 12.4). While the sample corroded for only 8 days (Ex_situ_008d) was covered by a single layer, the other samples that have been corroded for 31 days or longer formed an internally layered am-SAL. For these, the inner am-SAL is in general more enriched in Al and Si while it is depleted in Zr with respect to the outermost layer. The inner am-SAL of sample Ex_situ_274d can be subdivided in minimum four parts, while the one that formed next to the Zr-rich outer am-SAL is characterized by an inwardly decreasing concentration gradient of Al and K. This is followed by a K-rich, but Si and Al depleted layer that seems to have a less dense structure. The third layer was seen to be speckled in the BSE image and the inhomogeneities reflect fluctuating Ca and K enrichments. A more homogeneous am-SAL formed adjacent to the pristine glass at the end of the experiment, which is characterized by the highest Si concentrations of all am-SALs.

The samples that were altered for 80 and 274 days were covered by secondary phases, identified as $CaCO_3$ (aragonite & calcite) and different zeolites (Si-K-Al-Na-rich phase in false color images of Figure 29). Because the secondary phases and am-SALs covering the pristine glass are fragile and tend to detach from the glass surface during drying and sample preparation, the massive formation of secondary phases is not visible in Figure 28e. Therefore, these parts of the corrosion products were embedded separately. An example from the sample corroded for 274 hours is shown in Figure 29. The Outwardly directed growth of crystalline phases (calcite, aragonite, and zeolites) on the outer am-SAL surface is apparent in the BSE image.

Aragonite and calcite can morphologically be distinguished by their acicular-elongated and typical rhombohedral shapes, respectively. Both polymorphs were also identified by Raman spectra (Figure 30), measured at the locations marked with colored stars in the BSE image of Figure 29. The observed $CaCO_3$ crystals were covered by two consecutive layers of zeolites which are visible by the differences in brightness in the BSE image and the simultaneous change of the phase specific elemental concentrations (Al, Si, K, Na) from the inner to the outer zeolite zones. A reliable quantitative chemical analysis of the zeolites by electron microprobe was not possible, because of their dispersion, their porosity, and the water content that was not determined. Furthermore, the similarities of the chemical composition make it difficult to distinguish between zeolites, which is why the phase identification by Raman spectroscopy was favored.

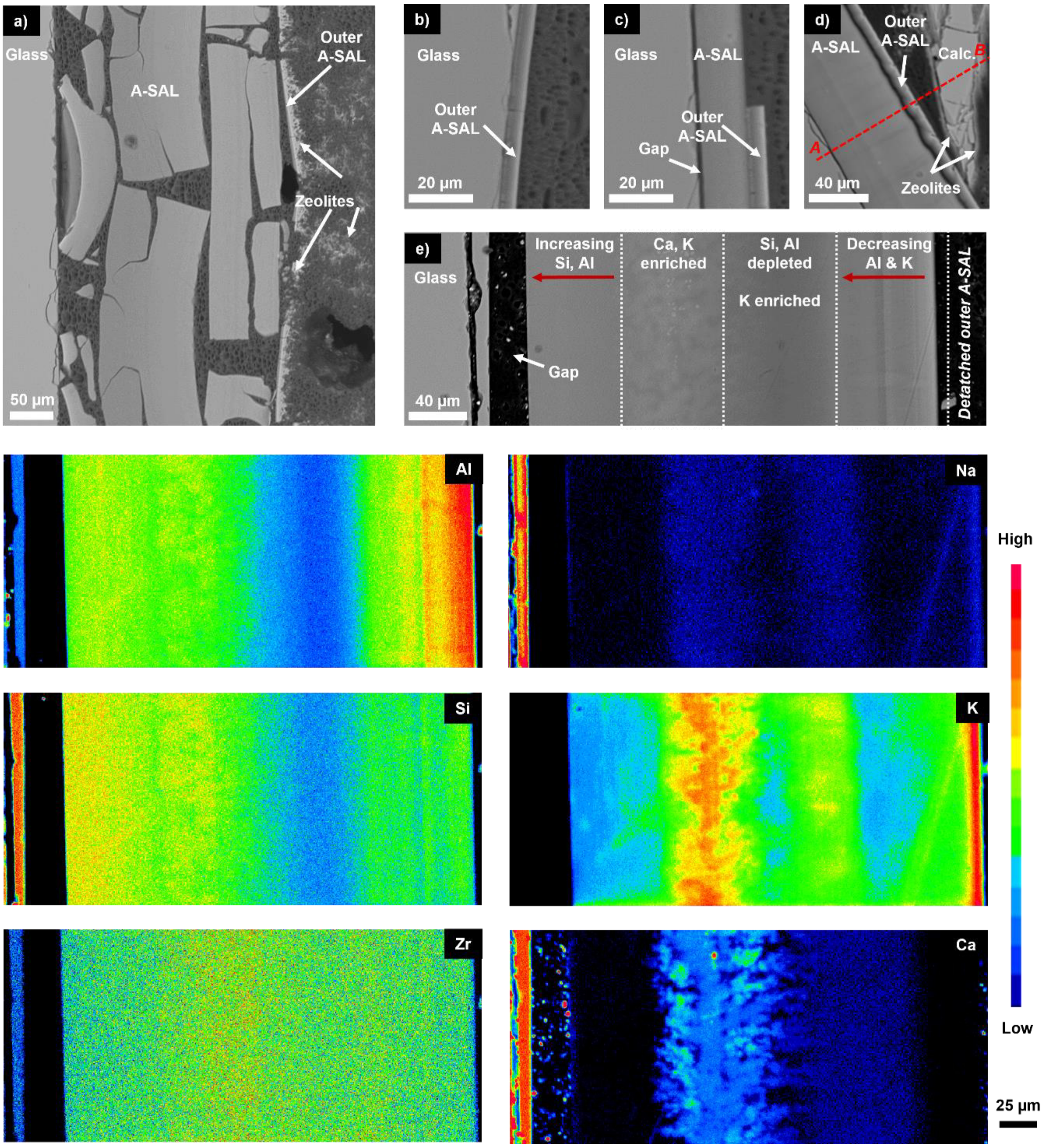

Figure 28: Backscattered electron image of cross sectioned ISG samples after alteration in a 0.25*M* KOH, 025*M* K_2CO_3 solution for **(a)** t=198 days in a in situ Raman reaction cell and ex situ for **(b)** *t* = 8 days, **(c)** *t* = 31 days, **(d)** *t* = 80 days, and **(e)** *t* =274 days in PTFE lined steel autoclaves. An elemental distribution line scan is shown in Figure S 2 that was measured along the red dashed line in (d). The false color images show the element distribution of Al, Si, Zr, Na, K, and Ca (blue to red colors reflect low to high relative concentrations, respectively) of the sample shown in (e). The samples were rinsed with Milli-Q® water, washed in ethanol for 48 h, dried at 90 °C for 48 hours and embedded in epoxy resin (dark colored area on the right-hand side in the images). The elemental distributions and brightness in BSE images indicate some sublayers of the am-SALs that are different in composition and density.

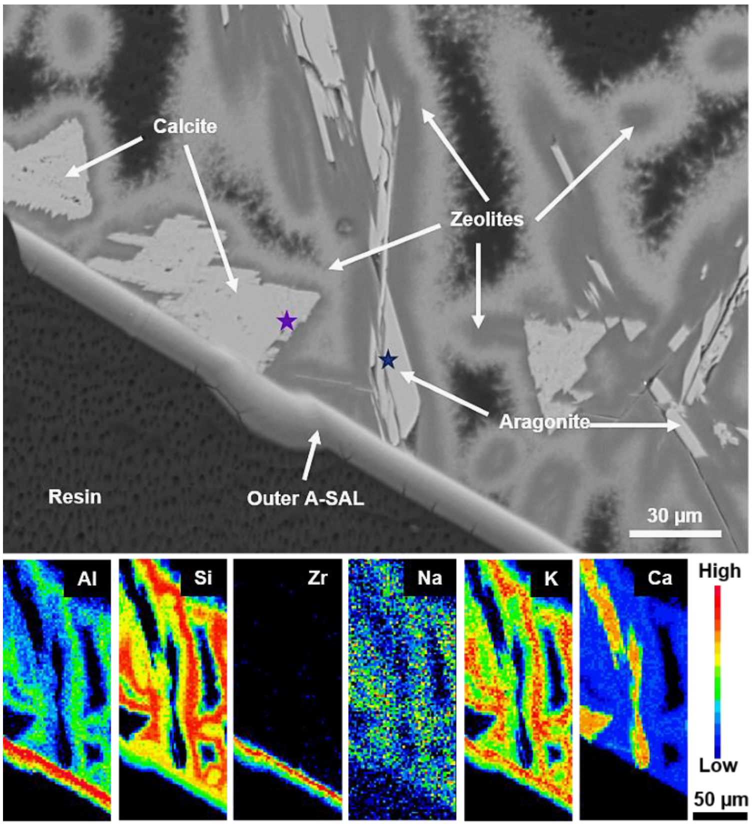

Figure 29: Backscattered electron image of secondary phases and outer am-SAL that detached from the altered ISG sample altered for 274 hours shown in Figure 28e. The false color images show the elemental distribution of Al, Si, Zr, Na, K and Ca (blue to red colors are reflecting low to high relative concentrations, respectively). Presence of calcite and aragonite was confirmed by Raman spectra measured at the points marked with stars (blue = aragonite, purple = calcite). Both $CaCO_3$ polymorphs are covered by zeolites which are mainly composed of Si, Al, Na, and K. Note the Zr- and Al-rich outer SAL that was also observed in samples altered for shorter time periods.

Raman measurements were performed at different regions of the embedded and polished 198 hours sample. These measurements were difficult, because of the high background signal of the epoxy resin. Nevertheless, spectra taken from near-surface area of the outer am-SAL (Inner zeolite) and from a distance of about 20 µm in direction of the bulk solution (Outer zeolite(s)) reveal the presence of different zeolites phases (Figure 25). The good agreement of bands located at 424 cm^{-1} and around 460 to 490 cm^{-1} with those of reference spectra of paulingite $(K,Ca_{0.5},Na,Ba_{0.5})_{10}[Al_{10}Si_{32}O_{84}] \cdot 27\text{-}44H_2O$ [201] (paulingite-K - R070604, paulingite-Na - R060457) and phillipsite $(K,Na,Ca_{0.5},Ba_{0.5})_x[Al_xSi_{16}\text{-}xO_{32}] \cdot 12H_2O$ [201] (phillipsite-K – R140774) from the RRUFF database clearly verify the occurrence of these zeolites [190]. Four-membered tetrahedral ring based zeolites exhibit a strong symmetrical bending mode $\delta(T-O-T)$ (T = Al, Si) between 480 and 520 cm^{-1} [191,192] and a smaller band near 422 cm^{-1} (472 respectively 424 cm^{-1} for phillipsite) [192]. The Raman data suggest the formation of K-rich paulingite and/or K-rich phillipsite next to the outer am-SAL surface. An increasing ratio of extra-framework alkali elements (Na + K) to framework elements (Si + Al) from inner to outer zeolite layers can also be seen in the elemental distribution maps, which agree well with the stoichiometric chemical composition of both identified zeolite phases. Even if the existence of Na-rich paulingite may also affect the convoluted band between 480 and 520 cm^{-1}, especially later in the reaction process with increasing Na release by glass dissolution, its formation cannot explain the pronounced shoulder at 472 cm^{-1}. Furthermore, solution analysis (Table 3) revealed a minimum 10 times higher K than Na concentration, which likely made K the preferred alkali element to be incorporated. Similar S4F-Zeolite-group minerals were also observed in a *in situ* Raman study of a Ba- and Mg-bearing soda-lime-glass using the same experimental setup (solution composition was 0.25M Na_2CO_3 and 0.5M NaOH) [45]. Although an amorphous alteration layer did not form in this study, the glass was partly replaced by paulingite, witherite ($BaCO_3$) and, saponite ($[Ca,Na]_{0.3}Mg_3[Si,Al]_4O_{10}[OH]_2 \cdot 4H_2O$). Mann et al. (2019) also observed phillipsite (K-rich) precipitation during the alteration of ISG at 70 °C in artificial cement water (YCWCa) [187].

As anticipated already before, calcite and aragonite were observed in the BSE images of the 274 hours sample. Confirmation by Raman measurements at the spots marked with colored stars in Figure 29 and the similar colored spectra are displayed in Figure 30. The position of the symmetrical stretching mode $\nu_1(CO_3)$ is located at 1085.5 cm^{-1} and 1086.6 cm^{-1} for aragonite and calcite, respectively. Additionally, the phases can be differentiated more easily by the asymmetric bending mode(s) (ν_4) at 712.5 for calcite and about 702 and 706 cm^{-1} for aragonite. However, the most unambiguous bands are lattice modes located between 100 and 300 cm^{-1}, which can be assigned to the external vibration modes between cations (M) and the anionic carbonate group ($T(M,CO_3)$) [202]. Calcite was also observed *in operando* after 1086, 1117, 1488, 1849, and 2090 hours of corrosion. Afterwards, the Raman signal disappeared with the appearance of zeolites bands, suggesting a zeolite coverage of $CaCO_3$ as observed *ex situ* in the quenched samples (c.f., Figure 28 and Figure 29). A representative spectrum acquired *in operando* after 1086 hours is also plotted and colored green. The strong band at 1332 cm^{-1} corresponds to diamond [203] and reflects a polishing grain pressed into the surface and can be considered as a marker of the initial glass-solution interface. As described already concerning the am-SAL spectra, the convoluted bands between 900 and 1000 cm^{-1} can be addressed to symmetric vibration of nonbridging Si-O-(X) groups [195] and originates as out-of-focus background signal from the outer am-SAL, on whose surface the calcite had grown. The same is valid for the bands about 490 and 550 cm^{-1}.

After the reaction cell of the Raman experiment was opened, white precipitates were found at the bottom of the cell, which could be identified as K-Bicarbonate ($KH(CO_3)$) based on its good agreement with kalicinite (R130026) of the RRUFF database [190] and is also shown in Figure 30 (red spectrum). As this phase has not been observed in the *in situ* measuring sessions, it remains unclear, whether it was part of the corrosion process or formed during quenching the experiment. However, the latter is rather unlikely due to the increasing carbonate solubility with decreasing temperature. Formation of kalicinite during corrosion at the bottom of the reaction cell is also plausible since here the temperature was slightly higher due to an almost unavoidable temperature gradient in the cell.

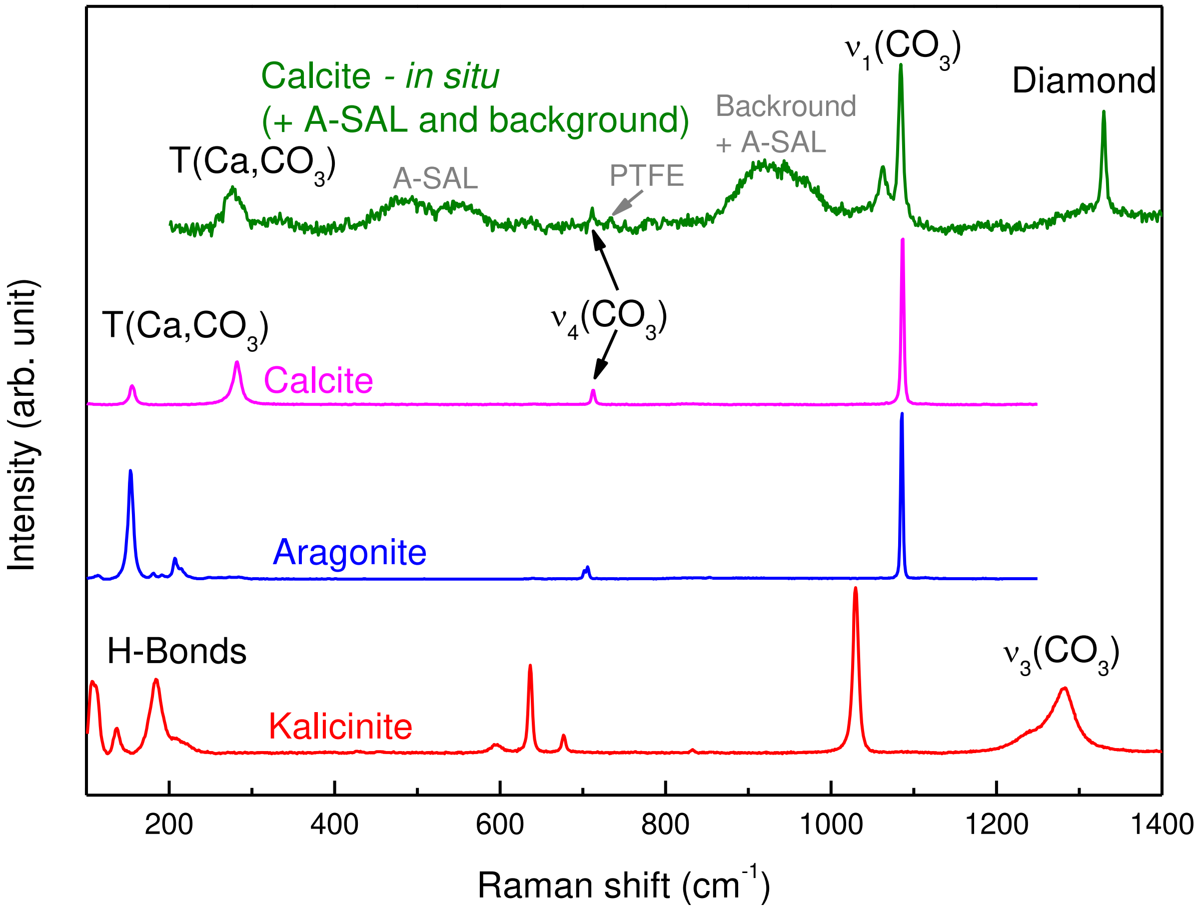

Figure 30: Background-corrected Raman spectra of different carbonates identified in this study. The green convoluted calcite and amorphous silica spectrum was acquired in operando corrosion at 1086 h, using the *in situ* fluid-cell Raman setup. The crystalline calcite was formed at the surface of the outer am-SAL. This solid phase and dissolved carbonate (~1063 cm^{-1}) were identified by the symmetric stretching mode of the carbonate anion. A residual diamond grain from the polishing paste can be observed (1332 cm^{-1}) which was trapped in the corrosion layer. The other diffuse bands between 400 - 600 cm^{-1} and 850 - 1000 cm^{-1} correspond to the am-SAL right underneath the calcite grain. Kalicinite (red), i.e., K-bicarbonate, was observed at the bottom of the reaction cell after quenching the experiment. The calcite (purple), and aragonite (blue) were identified at the marked spots in Figure 29 of sample Ex_situ_274d.

6.2.3 Solution analysis

The chemical composition and measured pH of the starting and leaching solutions are given in Table 3 and Table 4. The same initial solution was used for all experiments and the determination of the fraction of altered glass f_{AG}, given in %, reflects the amount of glass that has been dissolved based on solution composition. Based on B concentration, the f_{AG} of the samples are shown as blue points in Figure 31. To compare the temporal evolution of f_{AG} with reference data of experiments performed under quite similar conditions (ISG at $pH_{90°C}$ 11.5 adjusted with KOH), the f_{AG}-data from Gin et al. [43] are displayed as well (grey squares). Although the two datasets differ slightly they agree surprisingly well, considering the different experimental setups and the low number of solution data in case study I. Despite initials fluctuations of the corrosion rate, an overall corrosion rate of 0.30 ± 1 %/h altered glass per day can be estimated. The dissolution rate measured *in situ* was also expressed as $f_{AG_{Raman}}$ (black squares in Figure 31) and calculated according to Equation (31) to directly compare both methods. The $f_{AG_{Raman}}$ based on *in situ* Raman data diverges from bulk solution data after 85 days, reflecting the two different corrosion rate regimes (Figure 26). The differences between solution data f_{AG} and *in situ* $f_{AG_{Raman}}$ arises most probably from the fact that the *in situ* method is spatially resolved and local corrosion rate variations are not considered in more averaged bulk solution analysis. This is supported by the larger corrosion intensity at the edges of the sample, as observed in *post mortem* acquired BSE images of the samples from the *in situ* Raman experiment.

The $pH_{90°C}$ reduced continuously from 11.4 to almost 10.5 with increasing f_{AG}. The sigmoidal shape of pH transition and steep increase between 20 and 80% f_{AG} indicates a buffing effect at $pH_{90°C}$ ~ 11. The pks values at 90°C of dissolved monomeric silicic acid (MSA) was calculated for a solution containing 200 ppm dissolved Si and can be described by the following reaction equations:

$$H_4(SiO_4) + OH^- \leftrightarrow H_3(SiO_4)^- + H_2O \qquad \text{pks}_{90°C}\text{: } 8.9 \qquad \text{(XVIII)}$$

$$H_3(SiO_4)^- + OH^- \leftrightarrow H_2(SiO_4)^{2-} + H_2O \qquad \text{pks}_{90°C}\text{: } 11.5 \qquad \text{(XIX)}$$

Solution pH buffering must be considered in glass corrosion models and was discussed in the Weak-Acid-Strong-Base-Equilibria concept ([WA]-[SB]) [204]. Boric acid and its role as a buffering agent is important as well, particularly in pH ranges of about 10 to 12 [204]. Due to its high concentration up to the g/l level, boron speciation may also affect the pH, through the conversion of double deprotonated to single deprotonated MSA.

Table 3: Composition solution samples. Composition was measured by ICP-MS. The initial B concentration in the corroding solution was below the detection limit (< d.l.).

	Si *(mg/l)*	*B* *(mg/l)*	*Na* *(mg/l)*	*Al* *(mg/l)*	*Ca* *(mg/l)*	*K* *(g/l)*
Initial solution	2.6 ± 0.1	< d.l.	50.19 ± 0.51	0.254 ± 0.003	3.53 ± 0.26	25.50 ± 0.29
Ex_situ_008d	435.1 ± 2.4	123 ± 4	247.7 ± 3.8	50.1 ± 0.6	8.43 ± 0.23	26.31 ± 0.33
Ex_situ_031d	688.7 ± 1.5	245 ± 1	433 ± 6	21.96 ± 0.21	7.29 ± 0.33	26.05 ± 0.30
Ex_situ_080d	1357.7 ± 9.1	549 ± 3	891 ± 11	6.02 ± 0.08	13.50 ± 0.39	26.77 ± 0.27
Ex_situ_166d	2457 ± 22	1316 ± 25	2052 ± 22	13.19 ± 0.16	79 ± 1	26.45 ± 0.42
Ex_situ_274d	2685 ± 11	1728 ± 25	2622 ± 27	3.35 ± 0.03	18.29 ± 0.49	23.12 ± 0.19
In_situ_198d	1489 ± 8	1170 ± 12	1825 ± 18	2.83 ± 0.03	19.4 ± 0.2	17.7 ± 0.02

Table 4: Measured solution pH and corresponding temperature after quenching the experiment. f_{AG} and r_{BN} were calculated based measured boron concentration in the leaching solution (concentration in initial solution was below detection limit). Setup A corresponds to ex situ quench experiments and B to the in situ fluid-cell Raman setup.

	pH	*Temperature (°C)*	f_{AG} *(%)*	r_{BN} *(g/m²/d)*
Initial solution	13.4 ± 0.2	20.9 ± 0.1	-	-
Ex_situ_008d	13.2 ± 0.2	23.0 ± 0.1	*5.0* ± 0.1	*5.89* ± 018
Ex_situ_031d	12.8 ± 0.2	25.6 ± 0.1	*10.2* ± 0.1	*2.00* ± 0.01
Ex_situ_080d	13.0 ± 0.2	17.7 ± 0.1	*22.5* ± 0.1	*2.34* ± 0.01
Ex_situ_166d	12.8 ± 0.2	22.8 ± 0.1	*54.9* ± 1	*3.43* ± 0.06
Ex_situ_274d	12.4 ± 0.2	29.2 ± 0.1	*79.5* ± 1.2	*1.57* ± 0.02
In_situ_198d	12.6 ± 0.2	17.6 ± 0.1	*84.9* ± 1.3	*4.22* ± 0.09

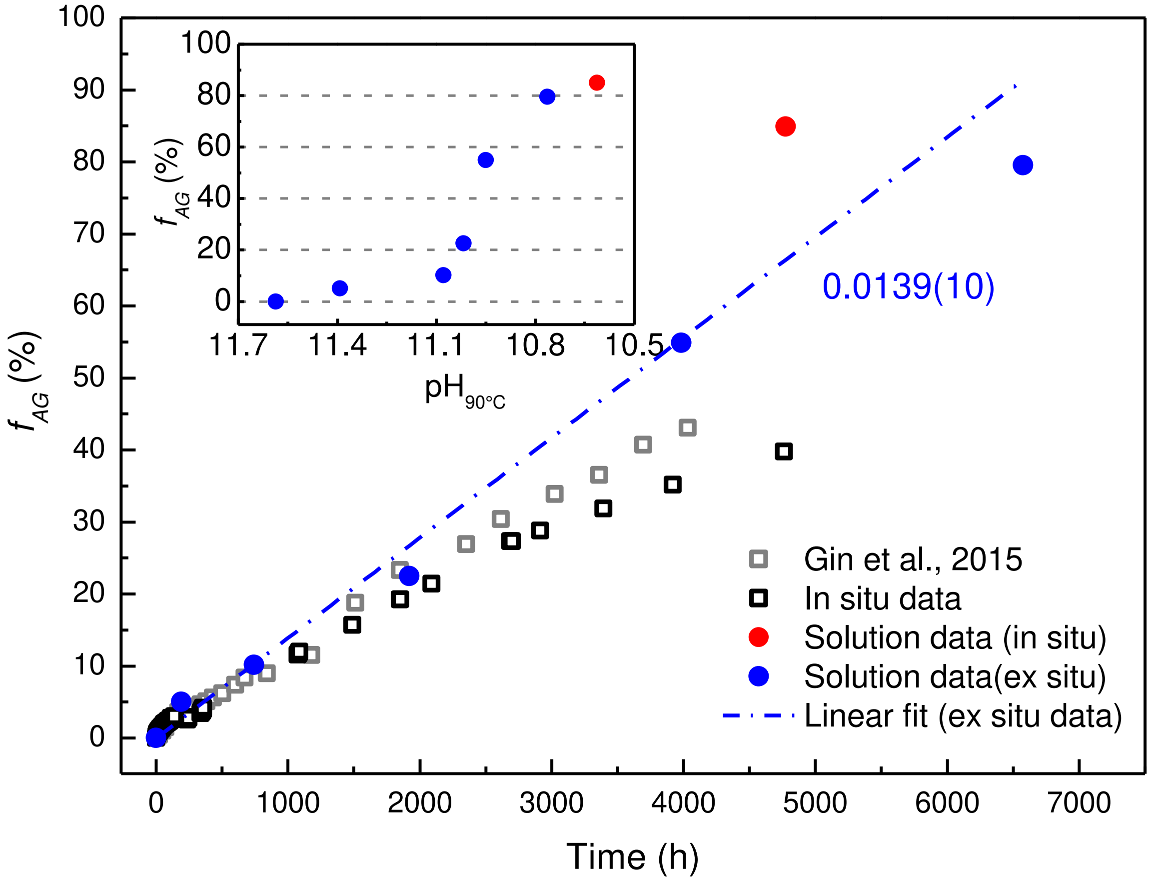

Figure 31: Alteration kinetics of ISG under hyperalkaline conditions and advance of solution pH (inset diagram) compared with data of Gin et al. [43]. The altered glass fraction (f_{AG}) was calculated according to Equation (32) and (33) using solution data (Table 4), and reference data of Gin et al., respectively [43]. The f_{AG} was also calculated based on glass retreat with respect to the initial glass sample thickness. Note that the *in situ* data rather represents local corrosion kinetics, while bulk solution analysis reflect an average reaction rate. The sigmoidal shaped pH decreases with increasing f_{AG} (inset diagram) indicate a buffering reaction about $pH_{90°C}$ 11. The pH was measured at RT and converted to 90 °C using the software PHREEQC [133] and the Thermochimie V9b [136] database.

6.2.4 Geochemical calculations

Based on the solution analysis, the geochemical software PHREEQC V.3 [133] (c.f., Chapter 5.6) was used to calculate the solution pH at the nominal reaction temperature (90 °C) and the saturation state of the observed precipitating phases or appropriate equivalent phase (am-SAL, amorohpus SiO_2 and $Zr(OH)_4$, calcite, aragonite, kalicinite, and some zeolites) at thermodynamic equilibrium. Even if the dominating zeolite phases were identified as paulingite-K and phillipsite-K, only phillipsite-K was considered in the model, because paulingite was not available in the SIT or any available phreeqc database. To account for the am-SAL, consisting primarily of Si, Zr, and Al, the amorphous phases SiO_2(am) and $Zr(OH)_4$(am, fresh) as well as gibbsite were considered as a possible product phase. The input values for the calculations were the measured pH at RT, the boron equivalent amount of dissolved glass constituents (Table 5) based on measured boron concentration (Table S 3) and the initial KOH and K_2CO_3 concentration (0.25*M* each).

Table 5: Oxide components input data for geochemical calculations (and their phase names in the database) that were assumed to dissolve completely, according to a stoichiometric dissolution of a boron equivalent amount of ISG.

	B_2O_3 B_2O_3(cr) mmol/L	Na_2O Na_2O(cr) mmol/L	Al_2O_3 Corundum mmol/L	SiO_2 SiO_2(am) mmol/L	CaO CaO(cr) mmol/L	ZrO_2 ZrO_2(cr) mmol/L	K_2CO_3 K_2CO_3 mol/L	KOH K(OH)(s) mol/L
Ex_situ_008d	5.71	4.50	1.36	21.48	2.03	0.61	0.25	0.25
Ex_situ_031d	11.34	8.93	2.69	42.68	4.04	1.21	0.25	0.25
Ex_situ_080d	25.38	19.99	6.03	95.49	9.04	2.70	0.25	0.25
Ex_situ_166d	60.88	47.94	14.46	229.06	21.69	6.47	0.25	0.25
Ex_situ_274d	79.90	62.92	18.98	300.62	28.46	8.49	0.25	0.25
In_situ_198d	54.11	42.61	12.85	203.58	19.28	5.75	0.25	0.25

6.3 Discussion

6.3.1 Kinetics of glass dissolution and surface alteration layer formation

The glass retreat rate was observed to decrease with time already from the beginning as indicated by the course of glass retreat with time in Figure 26. Other *in situ* Raman studies also showed that dissolution rate decreases from the beginning even in absence of alteration layers [29,41,42,45]. A strong decrease of the alteration rate at the beginning becomes even clearer by plotting the glass retreat rate vs. time as shown in the supplementary material (Figure S 3). However, even if this plot highlights the strong initial decrease of the alteration rate, it is less suitable for the overall dissolution rate behavior than it is for Figure 26. This is a result of a relatively low dissolution rate, the short time intervals between measurements in one measuring session, and the uncertainty of the determined glass/solution interface. This combination results in an apparent fluctuation in the alteration rate that merely reflects the uncertainty of the method at low alteration rates.

The reduction at the beginning could be partially explained by the enrichment of glass components in the solution according to the chemical affinity theory, but even this concept alone is not sufficient to explain the overall glass dissolution kinetics [15,103]. In general, the affinity effect describes the dissolution rate dependency with respect to the saturation state of a specific rate limiting component in the reacting solution, e.g., amorphous silica [15,68]. However, especially at the high pH and temperature applied to the experiments in this study, amorphous silica remains highly undersaturated, although the Si concentration was remarkably high at the end of the experiments (c.f., Table 3). Even if amorphous silica saturation state is not limiting under these conditions a general inadequacy of such an affinity approach has already been criticized by other authors [103] such as the additional impact of other components on the affinity effect [10], e.g.,Al activity [98,150] was also considered in past studies. However, no generally valid affinity concept has yet been proven. Nevertheless, there is clear evidence that the accumulation of glass constituents reduce dissolution rates despite the absence of precipitates [67,68] which is also revealed by the *in situ* Raman data. The assumption is that the affinity concept might work, but the limiting phase must necessarily be defined and is rather a multicomponent amorphous phase than pure amorphous silica. Apart from this, the rapid reduction of the glass dissolution rate within the first hours can be explained by preferential dissolution of high energy sites [68] and higher reactive surface area at the glass surface due to sample preparation.

Following the non-linear declining of the glass retreat rate in the beginning, the rate proceeds more constant after the first signal of a hydrated am-SAL was detected at the glass surface at about 76 hours. Raman data and elemental distribution maps (Figure 29) indicates that the outer silica rich am-SAL is composed mainly of Si, Al, Zr, and K. Especially Zr is highly enriched, compared to the other phases, probably due to the fact that the solubility of ZrO_2/$Zr(OH)_4$ is very low, even at very low pH [205,206]. This is supported by aqueous geochemical calculations, indicating oversaturation of amorphous $Zr(OH)_4$ in all solutions that were modelled. This is, of course, a rough simplification scince Zr coprecipitates with other elements in amorphous silica and does not form distinct $Zr(OH)_4$ precipitates in our experiment.

Presumably, the GRAAL (glass reactivity in allowance of the alteration layer) model that is implemented in the CHESS/HYTEC code [21,43,86,99,120,146,206,207] could predict more realistically the formation of the am-SAL. Although the model does not consider the formation of alteration layers on a molecular level, it is able to simulate the SALs by six end-members made up mainly by the less soluble glass components Si, Al, Zr, and Ca [43,206]. Debure et al. [206] performed corrosion experiments in pH ranges from 8 to 9 and their complementary modelling results using GRAAL suggest that the Zr-bearing end-member (*SiZrNa*) is practically proportional to the quantity of altered glass. This could explain the Zr-rich am-SAL formation very quickly after starting our experiments, even amorphous SiO_2 stayed highly undersaturated. Since it is quite difficult to precisely define the amorphous phases making up the SALs, especially due to their chemical and structural variations [26,39,46,47,76,78], the mixed end-member model in combination with a spatially resolved reactive transport code seems highly promising for modeling glass corrosion. Nevertheless, the thermodynamic properties of these representative and rather hypothetical, amorphous phases do not seem determinable, because it is paradoxical to describe metastable phases at thermodynamic equilibrium.

The formation of Zr-rich and Zr-poor SAL regions was also observed in other corrosion experiments under hyperalkaline conditions [43,44]. Gin et al. [43] also observed a single ZrO_2 rich outer layer and explained this observation by the reprecipitation of a less soluble Zr-bearing phase. On the other hand, Backhouse and coworkers [44] observed multiple banding of Zr-rich and Zr-poor layers formed at 50 °C in a $Ca(OH)_2$ solution (pH 11.6) and assumed a self-organizing phenomenon being responsible for this pattern formation that could be explained by an ICDP mechanism, as proposed by Geisler et al. [36]. In contrast to this, when ISG was corroded at 65°C in Tetramethylammonium hydroxide (pH 13), an even Zr distribution within the corrosion product was observed [184]. Wang and coworkers [184] compared the results with other experiment of a Ca-free glass, where no hydrated surface layer was formed and concluded that Ca, not Zr is crucial for am-SAL formation under hyperalkaline conditions and proposed an ICDP mechanism being suitable to explain their observations.

The higher, linear rate of 0.0767±0.0003 µm/h was established after 338 hours and at the beginning of this rate regime a Zr-poor am-SAL continued replacing the ISG. Beside elemental analysis (c.f. Figure S 2 and Figure 29), this was observed *in operando* by the Raman spectra shown in Figure 27, revealing also structural differences of the different am-SAL types. An increasing Si-O-H concentration at the reaction front might indicate the presence of a interface fluid proposed by Geisler et al. for an ICDP mechanism and observed in another Raman experiment for a Na-borosilicate glass [29,36], or at least a more hydrolyzed silica network. Coinciding with the appearance of zeolites at the outer am-SAL surface, the linear glass retreat rate was reduced to 0.0510 ± 0.0008 µm/h. Representation as f_{AG} shows the same course of alteration with time, but allowed a comparison with solution data of our study and those of Gin et al. [43]. In the corresponding reference study of, 16 ISG coupons were placed in a single vessel containing 380 ml of a solution that was enriched with ^{29}Si as an isotopic tracer until saturation with respect to amorphous silica at $ph_{90°C}$ 9 was archived. The samples were corroded at $pH_{90°C}$ 9 for 209 days before the $pH_{90°C}$ was raised to 11.5 by adding 10*M* KOH. Then the pH was kept constant for the rest of the experiment. Sampling of the solution in regular time intervals and consecutive analyzation of its composition lead to the f_{AG} dataset, displayed in Figure 31. Note that just the data from samples after rising the $pH_{90°C}$ up to 11.5 are displayed, because this pH region is of interest in this study. Even the pre-alteration of 209 days at slightly alkaline pH is different from our experiments, the significantly higher alteration rates at higher pH (increases by a factor of 3000) [43] makes this period negligible, especially because the thin am-SAL, that has formed during the first 209 days, will quickly be re-dissolved. This becomes clear by the good agreement of f_{AG} data over long time periods, except the value from the *in situ* experiment what is due to its different experimental setup and parameters (c.f. Table S 3).

The normalized dissolution rate r_{BN} based on boron concentration was also calculated according to Equation (34) and summarized in Table 4 [102]. The rate within the first 8 days was about 5.89 ± 0.18 $g/m^2/d$ and thus twice as high as for the samples altered for longer timer periods (31, 80, 166, 274 d) which were about 2.7 ± 1.1 $g/m^2/d$. The overall r_{BN} of the *in situ* Raman experiment is sifnificantly higher at 4.22 ± 0.09 $g/m^2/d$, although its interpretation may be problematic because it is based on just one solution sample and fluctuations of the corrosion rates of about 50 % were observed, also for the rates from Gin et al. under these extreme conditions [43]. Note, though the SA/SV ratios of the *ex situ* and *in situ* were different, it was found that its impact on the *residual rate* is little relevant [43]. The highest normalized corrosion rate of the first 8 days (5.89 ± 0.18) $g/m^2/d$) in the hyperalkaline carbonate solution was higher than the one published by Gin (2.8 $g/m^2/d$), but the order of magnitude matches. The initial dissolution rate of ISG at pH 11.5 is much higher (18 $g/m^2/d$) [43,102,208], consistent with the very rapid glass retreat (1.427 µm/h) between the first two measurements of the *in situ* study that is 28 times higher than the final linear retreat rate. The fast rate at the beginning has already been addressed to preferential dissolution of high energy sites [68] on the sample surface and the absence of affinity effects and passivating surface layers enables unimpeded dissolution.

Boron was used as a dissolution tracer analogous to other studies, because it is assumed to not be incorporated in the corrosion products formed during the corrosion process [43,206]. However, it should be noted that B retention was recognized for hyperalkaline solutions in presence of Ca, allowing the formation of calcium borates [78] and also at 150°C at moderate pH (8 at RT) [34]. It should be noted, that B can also be adsorbed by corrosion products, especially if clay minerals are involved [209,210]. Nevertheless, no B bearing phases was detected by Raman spectroscopy and no detectable amount of B was found in the corrosion products. Furthermore, the f_{AG} based on B concentration should be rather reduced compared to the one that is based on glass retreat data, if B would be incorporated. The opposite has been observed, which in turn can be explained by locally lowered dissolution kinetics.

This local difference in corrosion rates reflect spatial variations induced by e.g., thermal gradients and the geometric arrangement of the sample in the reaction vessel and the sample geometry, presence of defects/cracks in the glass, or even stochastically determined reactions. Due to the experimental setup used for the *in situ* measurements, a gradient in temperature could not be avoided, because the heating is placed at the bottom of the reaction cell. The maximum difference in temperature was determined to ~ 5 °C at nominally 90 °C [29]. Moreover, the local SA/SV ratio also varies because of the geometric arrangement of the sample in the reaction vessel, even if the overall ratio is the same for the single experiment. For example, a small fluid film between the glass sample and the covering sapphire window may affect the local corrosion kinetics at this location as the solution can be expected to progress much faster compared to the bulk solution.

6.3.2 Retention of chemical components

To highlight the incongruency of the overall corrosion process, the retention of each element (as oxide phase) in corrosion products (am-SAL & crystalline phases) was calculated according to Equation (35). Accordingly, the boron equivalent amount of the glass constituents was calculated, which will be theoretically dissolved by stoichiometric glass dissolution. The differences between the equivalent amounts and the measured concentrations were expressed as retention fraction in %, while 100 % indicates a complete incorporation in the corrosion products (incongruent behavior) and 0 % a total dissolution (congruent behavior). Note that the high K_2O concentration reflects the solute K_2CO_3 and KOH and does not originate from the glass. However, it will also be incorporated in the corrosion products.

In general, the oxide specific retentions were found to be in line with elemental distribution observed by SEM analysis (Figure 28, Figure 29, and Figure S 2). According to Figure 32, more than 90 % CaO is incorporated in the corrosion products, already in the beginning, while Na_2O stays almost completely dissolved (< 10 %) at any point in time, even a slightly stronger congruent dissolution at the beginning (Ex_situ_008d & Ex-Situ_0031d) can be concluded. It is known that the forward dissolution rate of glasses increases with increasing Ca content in the glass and reacting solution at neutral and slightly basic pH [69,73,78]. Furthermore, Ca tends to be incorporated in the SAL, but at very high pH and reaction progress, CSH phases will form, consuming most of the Ca [78]. One of the major differences between the experiments conducted in this study and in the main reference study by Gin et al. [43] was the observation of calcite/aragonite instead of CSH phases, even though their role as Ca-sink and zeolite substrate seems to be equivalent.

A high amount of Al_2O_3 remained dissolved during the beginning of the reaction, while it is completely incorporated in alteration products at later stage, especially if zeolites were also noted in BSE images of the samples after 80 days of corrosion. Considering the zeolite composition it is quite obvious that Al is consumed by zeolite formation, which is in line with the results of experiments under similar conditions [43,114,185,186,211]. The amount of SiO_2 that dissolves incongruently increases continuously with the altered glass fraction f_{AG} for all samples (indicated by black dashed arrow in Figure 32). This means that the fraction of dissolved SiO_2 is reduced with increasing reaction progress, possibly due to zeolite precipitation that consumes Si. Another reason could be the lowered solubility of SiO_2 and/or the formation of am-SALs that are more enriched in silica due to the decreasing solution pH (c.f., Table 4). This theory is supported by the increasing Si concentration observed in elemental distribution maps towards the glass, implying that the Si concentration is higher in the am-SAL formed at the late stage. Furthermore, the Si variations parallel to the reaction front correlates with those of Ca, Al and K (false color images in Figure 28) indicating the existence of different types of am-SALs formed here. Concerning K_2O retention, its concentration was about 10 % below the one assumed for the nominally 0.25*M* KOH and 0.25*M* K_2CO_3 solution. In addition to the enrichment in the outer Zr-rich am-SAL, this strong decrease already after 8 days is possibly caused by $KHCO_3$ precipitation observed in the *in situ* Raman experiment at the bottom of the reaction cell. The increasing K_2O retention at high reaction progress (Ex_situ_274d, In_situ_198d) is equivalent to a strong extraction of K from solution due to K-rich zeolite precipitation, more precisely paulingite-K and phillipsite-K.

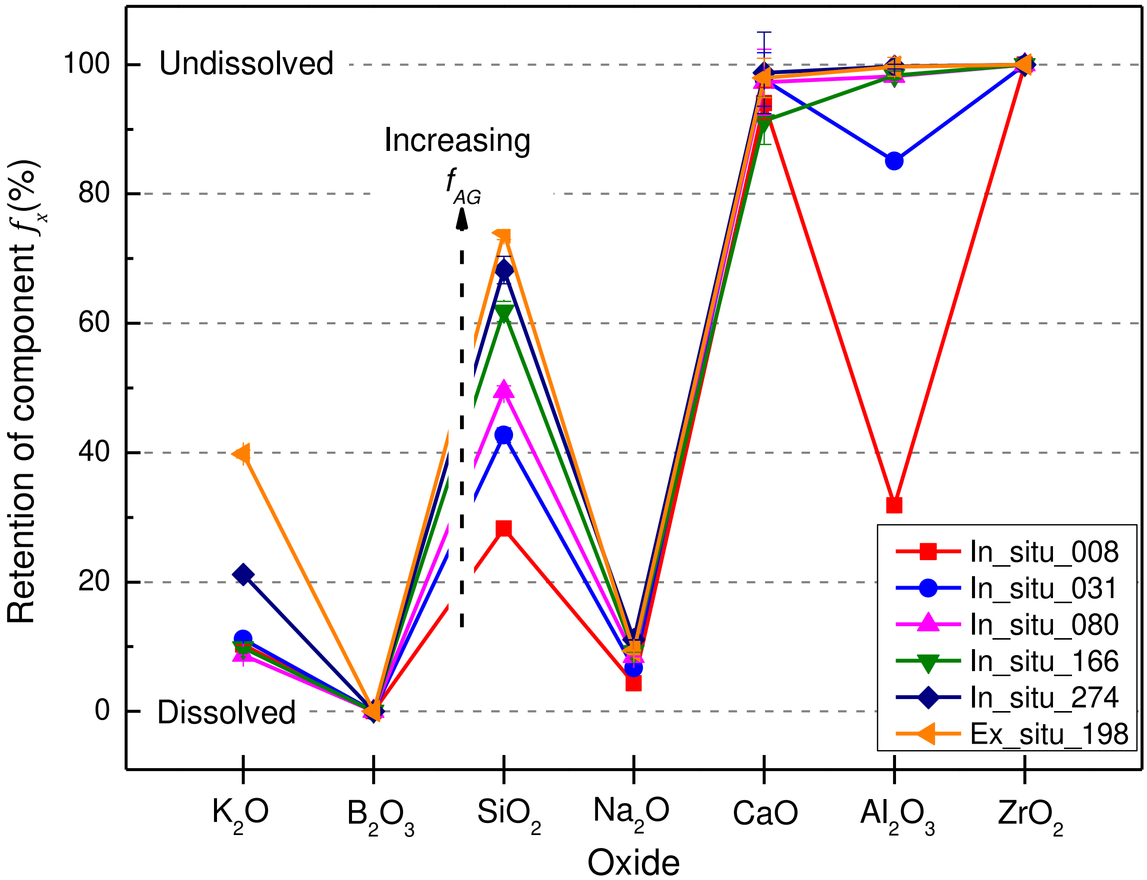

Figure 32: Retention of components (%) based on solution analysis and the calculated boron equivalent amount of theoretically dissolved glass constituents according to Equation (32). A low value indicates the component to stay dissolved (congruent dissolution) and a high value suggests that it is incorporated in the corrosion products (incongruent dissolution). Because B was assumed to stay dissolved completely and Zr was below detection limit their corresponding oxide values were set to 0 and 100 %, respectively. It was observed that SiO_2, Al_2O_3, and K_2O were incorporated more strongly with increasing f_{AG}. Note that ISG is almost free of K and that the increasing retention of K_2O therefore represents the incorporation of K in corrosion products, that originates from the reacting solution (nominal initial composition: 0.25*M* KOH and 0.25*M* K_2CO_3).

6.3.3 Precipitation of crystalline phases

6.3.3.1 Zeolite formation

In addition to amorphous SALs, crystalline phases, i.e., aragonite, calcite, and zeolites, precipitated at a later reaction stage onto the previously formed Ca-carbonates. This coincided with the establishment of a slightly reduced glass retreat rate. Interestingly, an acceleration of the glass corrosion rate through precipitation of crystalline, so called secondary phases, such as, e.g., zeolites, clay minerals, or CSH phases, has already been observed several times in other studies [10,43,44,99,114,185,186,211]. Their formation and the coinciding resumption of alteration rates are characteristic for the *Stage III* of glass corrosion, which follows a low, approximately constant corrosion rate during *Stage II* [10,42,64]. A link between zeolite precipitation and resumption of alteration rates through the consumption of dissolved elements and resupply from the previously formed am-SAL is suggested, weakening its protective properties[208,212]. Especially at $pH_{90°C}$ values between 10.5 and 11.0, zeolites can grow unimpeded and glass dissolution continues [185], which is in line with our results. These observations are relevant for nuclear waste repositories that are backfilled with cement or for cemented waste forms, because a cement-equilibrated solution can reach high pH values even between 12 and 14 [44,71,185–187]. Below $pH_{90°C} = 10.5$ the dissolution rate is less constant, which may be attributed to the fact that zeolite growth conditions at this pH becomes thermodynamically more unfavorable [100,185]. This, in turn, may again change the effect of precipitates on the dissolution rate. For example, SAL structures or secondary phases can result in reduced diffusivity, which in turn would reduce the removal of glass components from the reaction front into the bulk solution. Since precipitation of phases affects the solution chemistry, another phase will change the solution composition in a different way, which in turn can affect the dissolution rate of the glass. In the discussed experiments, the $pH_{90°C}$ leveled out at about 10.7 ± 0.2 for long time corroded samples (Ex_situ_166d, Ex_situ_274d , and In_situ_198d) and the final corrosion rate remained constant until the experiment was stopped. Theoretically, further glass dissolution and solution advance should reduce the solution pH below 10.5. Then, the growth of zeolites would be impeded. It is also possible that zeolites or am-SALs re-dissolve or become replaced by other phases when they become thermodynamically favored. However, the most advanced experiment had to be stopped before they could fall below this threshold. Further long-term batch experiments of much longer periods of time might be useful to possibly reach the situation of a completely replaced glass and a thermodynamically equilibrated phase assemblage with the corresponding reaction textures (as far as can be preserved). Another *in situ* Raman corrosion study performed on a glass containing Ba and Mg revealed Na-K-Ba enriched S4F zeolite formation in a hyperalkaline carbonate solution (0.5*M* NaOH, 0.25*M* Na_2CO_3). This zeolite crystal formed together with a witherite coating, and carbonate pore-fillings on a previously formed saponite layer without any am-SAL formation [45].

Usually, the precipitation of zeolites or other crystalline silicates is accompanied with an increase in the glass dissolution rate when a *Stage II* has been established before. But how exactly the silicate precipitation at the outer am-SAL surface will affect further glass dissolution is not yet clear. It is assumed, that Si (and Al) consumption due to (alumo-)silicate mineral precipitation (mainly zeolites) destabilizes the passivating layer [10,78,86,208].But what does this actually mean? An effective redissolution of the am-SAL formed under hyperalkaline conditions and its replacement by zeolites seems unlikely, considering our experimental results that show preservation of the am-SAL while a lot of zeolites were formed on its outer, Zr-rich surface. However, an am-SAL that had formed at lower pH could become unstable and re-dissolved when the pH is raised. One can also ask whether the precipitation of crystalline phases determine the composition of am-SAL formed at the same time or *vice versa*, taking into account the compositional variations within the am-SAL [43,44,46,47,187]. Despite its enigmatic nature, some sort of strong coupling of the precipitation reactions at the outer am-SAL surface and at the glass dissolution front likely exists. Temporal and µm-scale differences in solution chemistry are also indicated by the formation of different phases at the corrosion front and along the outer am-SAL surface. Consequently, a spatial decoupling, e.g., due to transport limitations by the am-SAL, might limit the reaction rates on both sides, affecting subsequent phase stabilities.

6.3.3.2 Calcium carbonate formation and geochemical calculations

Calcite and aragonite were observed right next to each other (c.f. Figure 29), while the third polymorph of anhydrous crystalline $CaCO_3$, i.e., vaterite, was not detected. Although the polymorphism of $CaCO_3$ has been studied intensively in the past, it is still not yet fully understood [213,214]. Especially, the coexistence of aragonite and calcite is frequently observed in nature at ambient temperature, whereas thermodynamics suggests aragonite to be metastable under these conditions [213,215]. It is thus not surprising that thermodynamic calculations (c.f. Table 6) only indicate the formation of calcite under the applied experimental conditions.

Nevertheless, it is known that aragonite forms under certain conditions in addition to calcite, especially with increasing temperature under hydrothermal conditions, and the distribution of different $CaCO_3$ polymorphs also depends on pH, ionic strength, saturation state, and organic additives [216]. Furthermore, Debure et al. [206] observed the formation of aragonite in batch corrosion experiments, while calcite was formed in a diffusion cell setup. Aragonite formation is promoted in the presence of Mg^{2+} even at room temperature [206,215] or in nanometer-sized pores [214]. Sun et al [215]. explained the dominating aragonite formation at room temperature at high Mg^{2+} to Ca^{2+} ratios by an increasing nucleation barrier of calcite compared to the that of aragonite. Apart from Mg^{2+}, the presence of other cations, including Al^{3+} that is also contained in ISG, favor the formation of aragonite [216]. Zeng et al. [214] showed that the fraction of aragonite formed under ambient conditions in pores of track-etched membranes increases dramatically by reducing the pore diameter, even at low and constant Mg^{2+} and SO_4^{2-} concentration. This observations were explained by the effect of the pore surface on the ion activity caused by surface effects [213,214]. This, in turn, highlights the importance of local surface effects and suggests the existence of different local quasi-equilibria right next to each other, which is particularly noticeable in Figure 29 for this study. Interestingly, both polymorphs are covered by zeolites and therefore probably act as a nucleating seed. Debure et al. also concluded that the inclusion of aragonite or calcite in thermodynamic models does not significantly affect the results [206]. It can be concluded that the glass corrosion kinetics does not significantly depend on whether calcite and/or aragonite crystallizes. It should be mentioned that kalicinite was observed in the *in situ* experiment, while no aragonite could be identified. It could follow that the formation of aragonite or kalicinite is somehow competitive, which may be related to the competing demand for carbonate anions. Under this assumption, the formation of kalicitnite in the *in situ* experiment acts as a sink for carbonate anions in the bulk solution, which in turn could reduce the affinity for aragonite formation due to the lowered concentration of its educts.

Interestingly, no zeolites and calcium carbonates were formed when ISG was corroded in $Ca(OH)_2$ solutions at 50 °C by Backhouse et al. [44], but CSH precipitation was verified by experiments and thermodynamic calculations. The absence of calcium carbonates is explained by the fact that all leach tests and solution preparations of the said study were carried out in a nitrogen atmosphere, in a glovebox, to prevent carbonation. A nonlinear declining corrosion rate was observed, which becomes extremely low like *Stage II* type *residual rates,* and the absence of zeolites was assumed to be the reason for not switching to *Stage III*. Beside the temperature differences in the case study I experiments, the excess Ca in the experiments of Backhouse and co-workers promotes CSH formation which also consumes Si that is no longer available for zeolite formation. The absence of CSH phases in another study, when ISG was corroded in artificial cement water at 70 °C, was also explained by the low Ca concentration and its affinity to be preferentially incorporated into the silica-rich amorphous corrosion product [187]. In the experiments of case study I, the high dissolved CO_3^{2-} concentration promotes $CaCO_3$ precipitation instead, which suppresses CSH formation by Ca consumption. Consequently, the fraction of Si and Al that is not incorporated into the am-SAL is entirely available for zeolite formation.

This theory is supported by geochemical calculations (calculated phase assemblage in Table 6), in which the precipitation of CSH phases was absent. More precisely, no CSH precipitation occurred when $CaCO_3$ polymorphs are considered in the calculations, while carbonate suppression stabilizes these CSH-phases, which explains CSH formation when the leaching solution is free of carbonates [43]. The boron equivalent amount of glass components that were dissolved stoichiometrically, as well as the initial KOH, K_2CO_3 concentration of 0.25 mol/L was used as input parameters for the geochemical model. The phases calcite, amorphous $Zr(OH)_4$, and K-rich phillipsite are predicted to precipitate at thermodynamic equilibrium at 90 °C. Even the solution of Ex_situ_274d was undersaturated with respect to amorphous SiO_2 (SI -0.392).

Table 6: Concentration (mol/l) of precipitated phases and final solution pH after equilibration of the boron equivalent amount of stoichiometrically dissolved ISG. Additionally, the saturation index (SI) of amorphous silica is given.

	Ex_situ_ 008d	*Ex_situ_ 031d*	*Ex_situ_ 080d*	*Ex_situ_ 166d*	*Ex_situ_ 274d*	*In_situ_ 198d*
Calcite	2.02E-03	4.03E-03	9.03E-03	2.17E-02	2.85E-02	1.93E-02
$Zr(OH)_4$(am, fresh)	6.05E-04	1.20E-03	2.69E-03	6.47E-03	8.49E-03	5.75E-03
Phillipsite-K	2.11E-03	5.32E-03	1.21E-02	2.89E-02	3.80E-02	2.57E-02
$pH_{90°C}$ (equilibrated)	11.4	11.3	11.2	10.8	10.5	10.9
SI of SiO_2(am)	-2.630	-2.322	-1.788	-0.833	-0.392	-1.002

Note that complementary thermodynamic modelling of the residual leaching solutions at 90 °C based on solution composition and measured pH still indicates supersaturation of Ca-, Si-, and Al-bearing phases, e.g., phillipsite-K. Nevertheless, the carbonate concentration was unknown and the Zr concentration was below detection limit, so the boron equivalent data were used for geochemical equilibrium modelling. Differences between calculated (Table 6) and measured pH values (Table 4) were to be expected because no phase was considered that simulates the formed am-SAL and no precipitation kinetics were considered. The am-SAL precipitation may also reduce the pH, the concentration of pH buffering silica specie, and/or the overall alkalinity. Reference phases are postulated in the GRAAL model [206] that was discussed already above and can probably account for the pH misfit. A relatively well soluble Zr-species (amorphous $Zr(OH)_4$) was considered to demonstrate Zr supersaturation, even if only small amounts of glass had been dissolved. Note that K-rich phillipsite and paulingite were identified as the zeolites formed in our experiments, but just phillipsite was considered here, because paulingite was not included in the database. Since Si and Al are not consumed by amorphous precipitates, they were still available to support the formation of saponite, phillipsite, witherite, and calcite, which was confirmed by additional equilibrium solution modeling. This glass was free of Zr, leading to the assumption that this component is crucial to observe an am-SAL under certain conditions due to its low solubility and its affinity to coprecipitate with Si and Al to form a hydrolyzed gel. In contrast, Wang et al. [184] suggested that the presence of Ca rather than Zr is crucial for am-SAL formation, as the congruent glass dissolution without any SAL formation was observed in the presence of Zr without Ca.

However, a synergistic effect of CaO and ZrO_2 for SAL formation was suggested, what is in line with the observations made here, even if Ca was just slightly enriched in the Zr-rich phases.

The presented experiments in combination with other studies performed at high pH conditions show that the alteration kinetics and phase assemblage is dictated by the initial solution chemistry and its evolution through coupled dissolution, precipitation and speciation reactions, and is especially sensitive to the solutes that are highly enriched [43,44]. Beside pH and temperature, a high concentration of reactants like Ca^{2+} or CO_3^{2-} ions determine whether CSH phases, carbonates and/or zeolites will preferentially form. This highlights the importance of completeness and consistency of the databases for thermodynamic models to correctly simulate the glass alteration process, because the appearance of resumption seems strongly connected with the forming phases.

6.3.4 Indications for the corrosion mechanism

The observations made here, and the mentioned reference studies [43,44,100,184,185,187] suggest an ICDP mechanism for glass corrosion, at least under hyperalkaline conditions. Accordingly, stoichiometric glass dissolution occurs continuously at the reaction front , even when solution analysis shows an incongruent dissolution behavior by retention of certain components, as shown in Figure 32. As sketched out in Figure 33, the stoichiometric dissolution (Figure 33a) quickly becomes complemented by back precipitation of a highly porous hydrated am-SAL that is enriched by Zr with respect to the glass, and contains some Al, Si, Ca, and K (Figure 33b). This happens because the Zr-rich outer am-SAL phase exceeds critical oversaturation very fast. At this time, Al and Si are less enriched with respect to their solubility and a greater fraction remains dissolved. It is important to understand that the composition and microstructure of the am-SAL that forms at a certain time can change abruptly or rather transiently and is not easily predicted compared to a stoichiometrically well-defined crystalline phase. Instead, its composition reflects the local environmental conditions within the interface solution at the reaction front from which it precipitates. The interface solution must also be coupled to the bulk solution, despite certain transport limitations. On the one hand, a spatial separation of simultaneously precipitating phases were observed at the glass interface (new am-SAL) and at the outer am-SAL surface (zeolites as shown in Figure 29). On the other hand, the correlation of glass retreat kinetics and zeolite growth kinetics (c.f. Figure 26) indicates a coupling of both processes. Apparently, the formation of the am-SAL layers seems to cause a different local chemistry within an interface fluid layer at the corrosion front compared to the chemical conditions in the bulk solution. However, a high porosity of the am-SAL still enables transport between both regimes and explains the chemical coupling. A significant porosity and solute mobility are also revealed by the high carbonate anion concentration that was detected *in operando* throughout the am-SAL (Figure 27) and by the K ions detected inside the am-SAL by EMPA (Figure 28).

Because Al and Si are getting more enriched in solution, especially within the interface fluid layer at the reaction front, their fraction making up the amorphous phase is higher for the inner am-SAL, where Zr concentration is rather constant and slightly enriched compared to the pristine glass (Figure 33c). Alkali elements, especially K, that was already highly concentrated in the reacting solution from the beginning, are as well incorporated in all corrosion products and reflect an unhindered diffusional transport through the am-SAL. These cations are assumed to act as charge compensators for terminal oxygens and, e.g., for Al^{3+} that is incorporated in the silica-based gel structure, mainly made up by SiO_4 tetrahedra. This is supported by a good correlation between K and Al concentrations, for the first 25 µm of the Zr-poor layer. Ca is less concentrated in this part of the am-SAL, which is probably due to the onset of calcite/aragonite formation at the surface of the outer am-SAL, also indicated in Figure 33c. The higher concentration of carbonate ions in the bulk solution and the outwardly directed diffusion of Ca from the reaction front into the bulk solution probably promotes the precipitation at the outer solid-fluid interface. Another reason could be pH differences between the bulk and pore or interface solution, so observed for a *in situ* fluid-cell Raman study at moderate pH [29].

Calcite seems to be a nucleation substrate for zeolites, which probably also applies to previously formed CSH-phases in carbonate-free solutions with regard to results observed by Gin et al. [43]. The precipitation of zeolites (Figure 33d), in which paulingite-K was probably formed first, is manifested by consumption of Si, Al, and alkali and earth alkali elements. This is reflected by a less dense, inner am-SAL zone, where Al and Si concentration were observed to be decreased. While glass dissolution continues, the lack of elements that are available for formation of hydrous corrosion products due to additional and coupled zeolite precipitation inevitably requires a less dense, i.e., more porous am-SAL to replace the dissolved glass volume. The higher amount of K-rich pore solution is the reason for the high K concentrations in this inner am-SAL, although the Al concentration is lowered. The Ca- and K-rich, patchy am-SAL zones observed in some samples (c.f. Figure 28) are assumed to represent solid carbonate or bicarbonate in former pore space induced by quenching and drying.

In general, the Si and Al concentration of the consecutively formed am-SAL increased gradually as the lowered pH in turn decreased the solubility of SiO_2 and Al_2O_3 (Figure 33e). The strong pH decrease is mainly caused by zeolite formation and the reason for the lowered glass retreat after 2699 hours of corrosion (c.f., Figure 26) that exceeds the buffering capacity of dissolved $H_2SiO_4^{2-}$. This observation is rather counterintuitive, because zeolite precipitation is frequently accompanied with an acceleration of glass dissolution [64,113,208]. However, without pH adjustment, it will change the pH dependent dissolution rate and a reverse correlation can be observed.

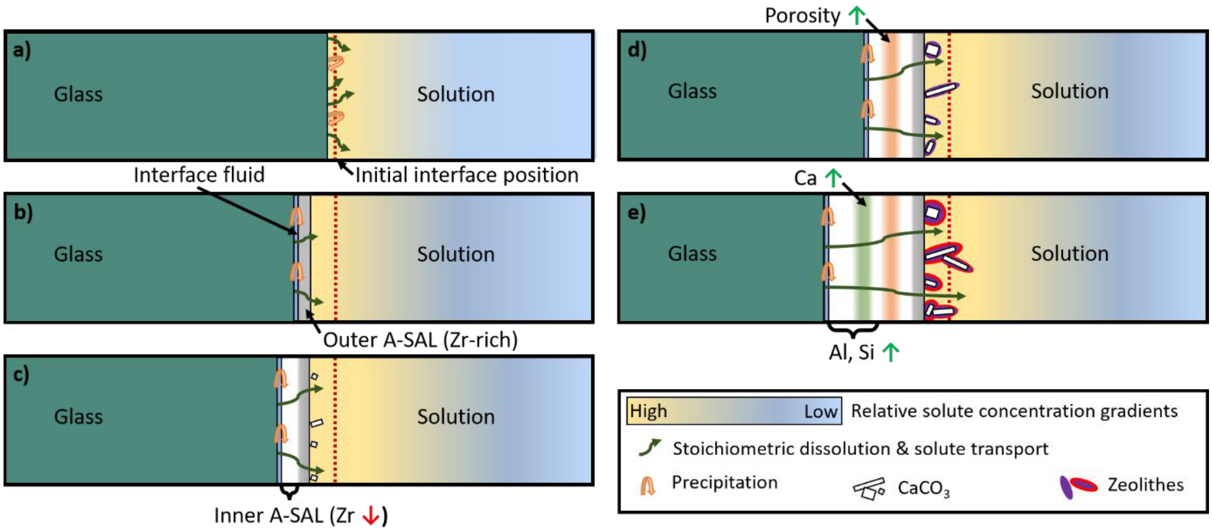

Figure 33: Schematic representation of the proposed corrosion mechanism for ISG in hyperalkaline carbonate solutions at around 90 °C, mainly based on interface-coupled glass dissolution and alteration product precipitation reactions.

6.4 Conclusion

The ISG is prone to corrode under hyperalkaline conditions ($pH_{90°C}$ between 10.5 and 13) and will be replaced by amorphous and/or crystalline phases, while the phase assemblage depends primarily on temperature, pH, and the concentration/saturation state of their limiting components. While the type of alkali that is present appears to be less relevant for the course of corrosion under these conditions, Ca and Zr seems to strongly affect the am-SAL formation [44,78,184]. Based on the results shown here, the low Zr solubility is assumed to be the reason for the relatively fast formation of a Zr-rich and quite dense outer am-SAL. This initializes the formation of an interface fluid layer underneath, wherein glass dissolution and am-SAL precipitation takes place. The amorphous corrosion products observed here can be subdivided into minimum two distinct layers, an outer Zr-rich and an inner Zr-poor am-SAL. Further gradual and abrupt compositional fluctuations in the inner am-SAL were observed that reflect the secondary phases formed at the outer am-SAL surface and the solution pH changes. The interface-coupled dissolution-precipitation mechanism is suitable to explain the compositional variations. Additionally, strong coupling of the interface solution at the reaction front with the bulk solution is assumed under certain conditions. This explains the interdependence of am-SAL composition and the secondary phases formed simultaneously, since the corrosion products did not cause significant transport limitations (passivating properties). However, the separation of the interface fluid layer at the reaction front and the bulk solution by the am-SAL leads to different local chemical conditions. In contrast, the am-SAL formed at moderate alkaline pH may develop passivating properties which in turn decouples the reactions at the interface fluid from those of the am-SAL/bulk solution interface, especially in Ca-rich solutions [78].

In contrast to other studies, no CSH phases were observed, likely because Ca was consumed by $CaCO_3$ precipitation. The coexistence of calcite and aragonite is in contradiction to thermodynamic calculations, but is often observed in nature and experiments [213–216]. Aragonite formation can be promoted even at room temperature, e.g., in the presence of cations like Al^{3+} [216] or in small pores, while its fraction compared to that of calcium increases by reducing the pore size [214]. It can be assumed that very local differences in composition affects the $CaCO_3$ modification that is preferred to nucleate. Both $CaCO_3$ polymorphs formed at the outer am-SAL surface were observed to act as nucleation substrates for zeolites (paulingite-K & phillipsite-K), quite similar to the role of CSH phases formed in equivalent carbonate-free solutions [43].

In situ and *in operando* characterization methods are very useful to directly bring changes in corrosion kinetics in relation to product phases that will form, as shown by our *in situ* Raman study. Furthermore, one of these experiments reflects several conventional quench experiments where the samples are analyzed after the experiment. Both approaches seem to be useful to complement each other in capturing the complex dynamics of glass corrosion and explaining the variable incongruency of glass component release. Note that solution exchange with ethanol before drying the sample avoided massive shrinking, cracking and detachment of the corrosion products even without a supercritical drying procedure.

To model the glass corrosion process and to account for the variations in am-SAL composition and their interdependence to secondary phases formed at the outer surface, as well as the impact of transport limiting effects, a spatially resolved geochemical reactive-transport model on pore scale could be a promising approach. But such a model must consider representative phases that can simulate the am-SAL composition, like the GRAAL model, and even the thermodynamic data of these metastable phases are difficult to estimate with reasonable accuracy.

7

Case study II: International simple glass (ISG) corrosion under acidic conditions

7.1 Introduction

Understanding the glass corrosion process and its basic reactions is crucial for predicting the long-term durability of nuclear waste glasses which are the preferred matrix material for immobilization of high-level radioactive waste from reprocessing fuel elements [3–5]. Although an acidic environment seems unlikely in most geological repositories for nuclear disposal, since alkaline backfill materials such as bentonite or cements are usually part of the safety strategy [32,44,187,217], understanding the corrosion process over a wide pH range is important to develop a universal glass corrosion mechanism as a basis for adequate numerical corrosion models. Furthermore, understanding glass corrosion in contact to acids is crucial for storage of chemicals or sensitive drugs [8] and for the use of glassware in experimental setups in the laboratory. Apart from this, Guo et al. [138,218] highlighted the possibility of local acidic environments that may form at the glass surface in contact with stainless steel making up a canister for terminal storage, leading to formation of Fe-silicates. In the corresponding study, a new feedback mechanism between ISG and stainless steel was observed which may affect the initial mobilization rate of radionuclides which, in turn, highlights the importance of considering manifold interactions between different components of a nuclear waste repository. However, the study shows little significance for real case scenarios as it has been conducted under oxidative conditions which is not expected to occur in a nuclear repository.

The chemical durability of glasses depends on glass composition and the environmental conditions (e.g., solution pH, relative humidity in gaseous environments, temperature, and composition of the corroding solution) [2,4,5,10,16,17,219]. There is a broad scientific consensus that (boro-)silicate glasses undergo pure glass dissolution under far from equilibrium conditions when affinity effects or the impact of (am-)SALs can be neglected [17,44,63,220]. As shown in the previous Chapter 6 (case study I), ISG corrosion under hyperalkaline conditions leads to intense corrosion and formation of am-SALs, zeolites, and Ca-carbonates. In order to get a full understanding of the mechanism of corrosion, however, glass corrosion studies need to cover a broad pH range. Geisler et al. [35] have proposed that the formation of an amorphous SAL in highly acidic solutions can also be explained by an ICDP process, whereas other authors favor a leaching-based, diffusion-controlled formation mechanism, where the SAL is considered as a relic but chemically and structurally modified glass [123].

The silicate network dissolution is assumed to occur according to the reaction Equation (III) given in Chapter 3.2.2 [123] and is generally assumed to be catalyzed by $\mathrm{OH^-}$ ions [123], which is why the forward dissolution rates increase with increasing solution pH [17,102,220,221]. This is also in line with the dramatic increasing SiO_2 solubility at pH values exceeding 9 to 10 at 90 °C [108]. However, the dissolution of glasses under acidic conditions was observed to also increase with increasing acidity [63,102], indicating also catalyzation by $\mathrm{H^+/H_3O^-}$ ions. In addition, ID reactions, i.e., diffusion-controlled ion exchange between alkali network modifiers of the glass and hydrogen ions from solution, is assumed to dominate under acidic conditions [123], but also at late reaction stage under alkaline conditions [31,34] and even near neutral pH, where the V- or U-shaped, pH-dependent glass dissolution rate reaches a minimum [44,48,49,63,98,102]. This exchange reaction is represented by the reaction Equation (XX) [35,123]

$$\equiv \mathrm{Si-O-Na} + \mathrm{H^+} \rightarrow \equiv \mathrm{Si-O-H} + \mathrm{Na^+} \qquad \text{(XX)}$$

i.e., leads to the formation of silanol groups ($\mathrm{Si-OH}$) which may re-condense *in situ* according to reaction Equation (XVI) [35] given in Chapter 3.2.8. It follows that the glass structure is assumed to restructure in the solid state.

This chapter (case study II) focuses on long-term corrosion behavior of nuclear waste glasses under acidic conditions for which only relative few studies have been carried out in the past [30,31,35,50,158]. Consequently, there is a relative lack of knowledge about the corrosion behavior at low pH, compared to alkaline conditions. In order to clarify the corrosion mechanism in general, the aim of this study was (i) to determine the glass retreat rate of ISG under acidic conditions *in situ* and compare the results to those measured at higher pH (previous Chapter 6), (ii) to reveal structural differences of the am-SAL at different pH, (iii) to study maturation of the am-SAL with time and after drying, and, importantly, (iv) to test the hypothesis that an ICDP-based corrosion mechanism is also operating under acidic conditions as proposed by Geisler et al. (2010) [35]. Therefore, an ISG cuboid (8.8 mm x 5.5 mm x 1.0 mm) was corroded for about 205 days in a 0.1M HCl and $\mathrm{KH_2PO_4}$ solution in the setup described in Chapter 5.1.1. As demonstrated already in previous studies [29–31,41,42,45] and chapters of this thesis, glass corrosion experiments using the *in situ* fluid-cell Raman technique provides a wide range of chemical and mineralogical information.

7.2 Results

7.2.1 Kinetics of glass dissolution and surface alteration layer formation

Figure 34 shows hyperspectral Raman images shown in for ISG corrosion in a 0.1M HCl and 0.1M $\mathrm{KH_2PO_4}$ solution visualize the temporospatial phase distribution at the glass/(am-SAL/)solution interface(s). More precisely, the temporal evolution of the distribution of water

(Figure 34a) and the corrosion product, i.e., amorphous silica (Figure 34b), is shown. Because the am-SAL has also a strong H_2O signal, the visualization of the glass phase would be redundant, as only high and low intensity of Figure 34a would be interchanged. The am-SAL was visualized by calculation of the parameter R_n from the Raman spectra, which reflects the time dependent structure of amorphous silica [30,31,40,41], as shown in Figure 35b. *In situ* Raman spectra were acquired continuously during the first 215 hours. After this initial measurement period, regular consecutive measurements have been performed until the experiment was terminated after 4913 hours.

As can already be seen in the false color images of Figure 34, after an initial stagnation of the glass/solution interface, the glass started to retreat after about 50 hours and comes to a near standstill again after about 20 µm glass retreat at the end of the experiment. At the same time, the retreated part was replaced by an am-SAL which arose already on the glass surface after a few µm of glass were dissolved. This relatively fast am-SAL formation, with respect to case study I, led apparently to an increase of the volume of the solid cuboid (c.f., initial interface position in Figure 34b). This becomes also clearer by having a look at Figure 35a, where the glass retreat and am-SAL thickness is shown as a function of time. The final glass retreat was 24.8 ± 0.6 µm for the last four determined interface positions between about 3430 and 4905 h, when the glass retreat came nearly to halt. Between approximately 100 to 3000 hours of corrosion the glass retreat decreased nonlinearly with time and begun to stagnate after the am-SAL reached a thickness of 22 ± 1 µm.

Both, the main and the inset diagram show the glass retreat and am-SAL thickness. However, beside plotting the data on different scales at the x-axis (linear vs. logarithmic scale), the data of the main diagram were generated by averaging five consecutive measured glass retreat values of the entire dataset (inset diagram) for better visibility. The results shown in Figure 35a indicate that the am-SAL thickness was higher than the dissolved glass volume for about 900 hours (highlighted by the gray dashed lines) after beginning. Later, the opposite was the case. Having a look at the inset diagram reveals a stagnation of the glass/solution interface position for about 40 hours and an increasing glass retreat until the sigmoidally shaped glass retreat curve reached a plateau after approximately 3000 hours of corrosion that can be interpreted as establishment of a residual rate regime (*Stage II*). Fitting of a sigmoidal shape function to the glass retreat and a exponential function to the am-SAL thickness clearly reveals the change from volume-positive to volume-negative replacement reaction (colored red and blue curves in Figure 35a, inset diagram). The initial glass dissolution rate was found to be 0.032 ± 0.001 µm/h and was estimated by a linear fit (R^2= 0.9838) of the averaged datapoints (17 in total) of the main diagram of in Figure 35a between 53 h and 208 h. Although the trend

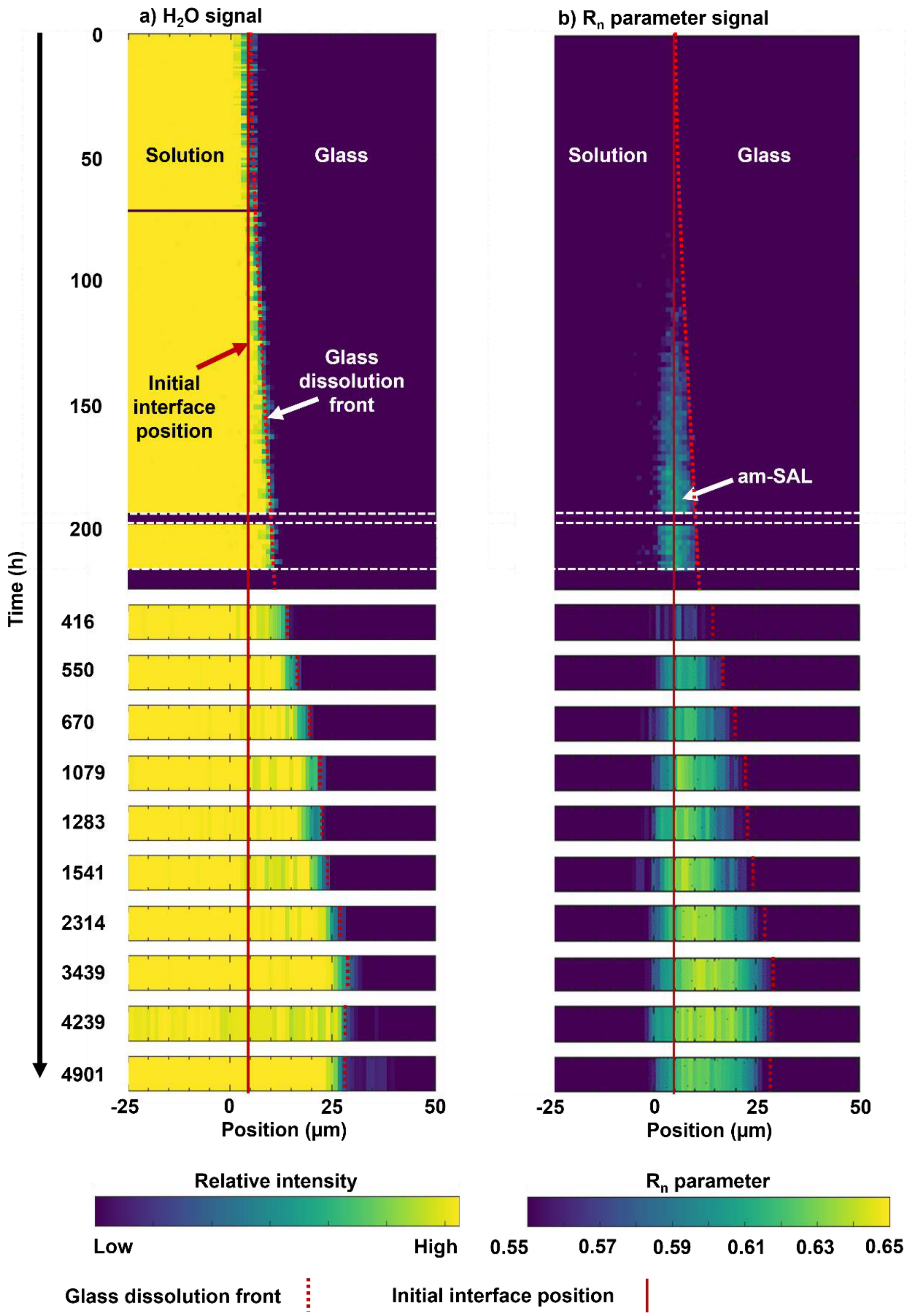

Figure 34: Temporospatial evolution of the glass/solution interface monitored *in situ* and *in operando* at 85 °C using fluid-cell Raman spectroscopy. In these hyperspectral Raman images, yellow reflects a high and blue a low intensity of water in **(a)**, showing the H_2O signal, i.e., the intensity of bands between 3050 - 3750 cm^{-1}. The R$_n$ signal in **(b)** reflects the fraction of higher order Si-O rings relative to four-fold Si-O rings. R$_n$ is given as the intensity between 250 and 460 cm^{-1} divided by the intensity of bands between 250 and 600 cm^{-1} after linear background subtraction [29–31,41].

is almost linear, the induction time and the am-SAL has already started to form, which is why the initial rate is probably already affected and not fully equivalent to the forward dissolution rate.

In the second main diagram of Figure 35b, the temporal evolution of the R_n parameter of the am-SAL is presented and fitted by a sigmoidal function. To ensure that the R_n value is not significantly affected by out of focus Raman signals, only those data were considered that were taken after the am-SAL reached a thickness of about 10 µm. After an initial increase of this structural parameter it reached a plateau at 0.614 ± 0.002 after about 1000 hours of corrosion until the end of the experiment. Additional Raman analysis of the quenched and dried sample showed a much higher R_n value of 0.66 ± 0.01 for the same am-SAL. It is notable that for a second ISG sample, that was altered for 308 hours in an *ex situ* setup as described in Chapter 5.7, an almost identical R_n value of 0.653 ± 0.004 was determined, showing the robustness of the parameter and that drying has a measurable effect on the silica structure.

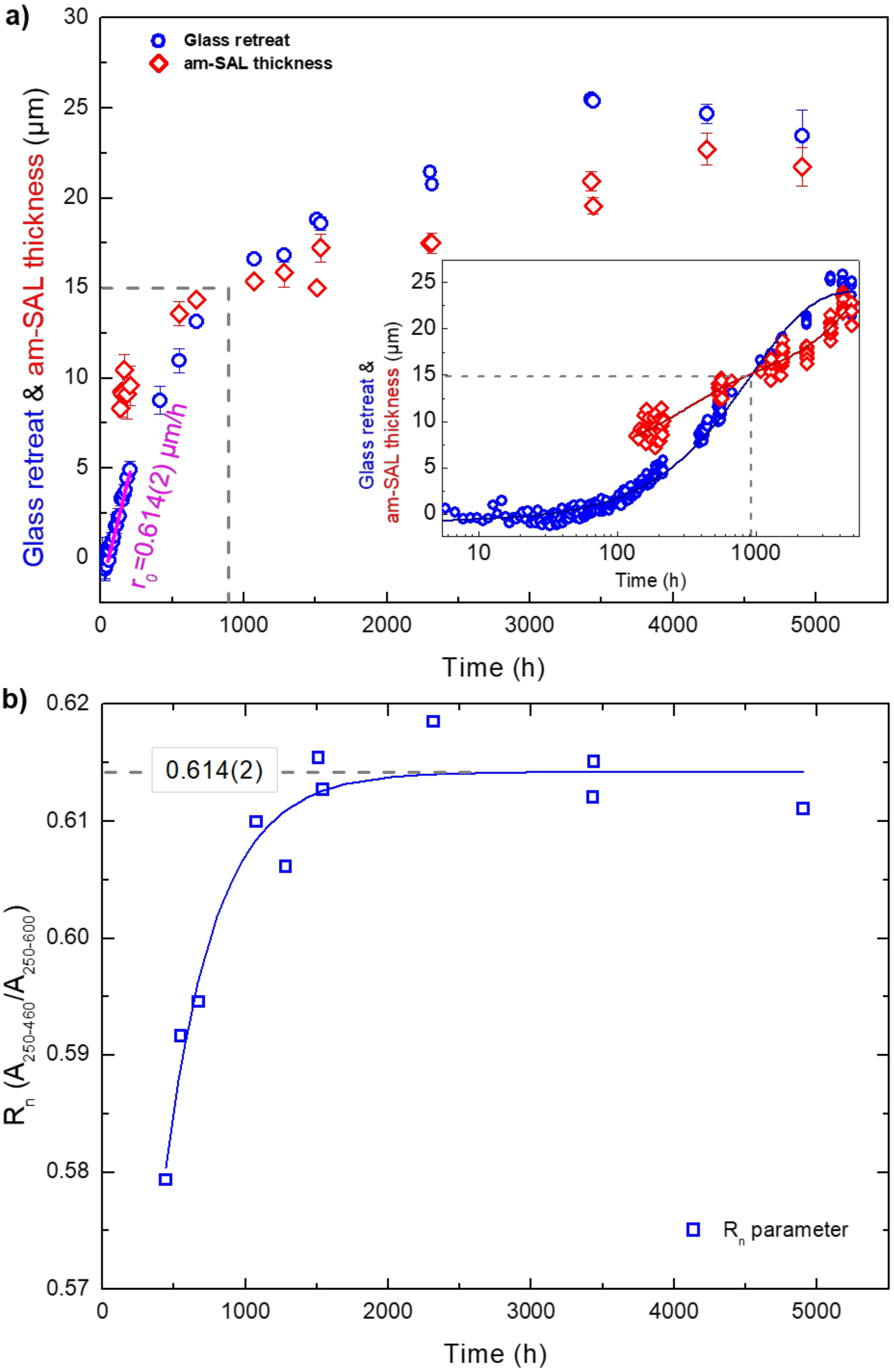

Figure 35: **(a)** glass retreat and thickness of the amorphous surface alteration layer (am-SAL) and **(b)** the R_n parameter of the am-SAL as a function of time fitted by a sigmoidal shape function (R^2= 0.9239). Each data point in the main diagram of (a) was generated by averaging five consecutive glass retreat values and the purple line indicates a linear fit (R^2= 0.9838) for estimation of r_0. The inset diagram shows the entire data set for glass retreat and am-SAL thickness and a sigmoidal (R^2= 0.9896) and exponential (R^2= 0.9519) fit, respectively, but with the time axis in the logarithmic scale.

7.2.2 Structural evolution of the amorphous surface alteration layer

For better understanding of the structural differences and chemistry of the am-SAL, a closer look at the Raman spectra is given in the following. However, it is sometimes difficult to clearly identify the Raman bands of the SALs in the spectral region between 200 and 1200 cm^{-1} due to the multiple overlaps of several bands from different solid phases and aqueous species. For example, an orthophosphate stretching vibration band can be observed near 940 cm^{-1} in P-bearing silicate glasses [222] and non-bridging $Si-O-(Na, K, charge, H)$ and $Si-O-Zr$ linkages are also located between 900 and 975 cm^{-1} [31,193,194,196,197].

Time-dependent spectral changes and some phosphate bands are shown in the representative Raman spectra from the bulk and pore solution (Figure 36b). Additionally, Figure 37a shows Raman spectrum of the am-SAL acquired *in operando* and *post mortem*. Note that in general the frequency position of a Raman band depends on temperature and therefore *in situ* measured Raman frequencies are not expected to exactly fit the frequencies of RT reference spectra.

Some structural similarities were found in the Raman spectra of the pristine ISG and the am-SAL (c.f., Chapter 5.8.2). For example, the $Si-O-Si$ rocking bands of silicate ring structures of varying size ranging from about 350 to 500 cm^{-1}, and the band around 990 cm^{-1}. However, the absence of danburite-like ring structures and Q^n bands of $n > 2$ in the spectra from the am-SAL, which might indicate a higher degree of polymerization/connectivity of SiO_4 tetrahedra, demonstrates unambiguous structural differences (c.f, Figure 36a).

These structural differences in the low-frequency region of the spectrum were used to determine the R_n parameter for the silica rim. While the temporal evolution of this structural indicator of amorphous silica (c.f., Figure 35b) was already mentioned, the basis for estimation of this value are the *in situ* acquired Raman spectra shown in Figure 36a, while the color of the spectra indicates the relative time of acquisition (dark blue = first value, bright yellow = last value).

The R_n value is a useful tool to reveal structural differences of amorphous silica formed under different conditions and at different reaction stages [30,31,40,41]. A larger value is equivalent to a larger fraction of $(Si-O)_{n>4}$ rings and the comparison of these *in operando* Raman spectra also reveals an increasing relative signal intensity between 300 and 450 cm^{-1} with increasing reaction time. Note that the sapphire band around 416.5 cm^{-1} does not affect the R_n value, because its intensity is considered to the same degree in both spectral ranges that were used to calculate the R_n ratio, i.e., its intensity cancels out.

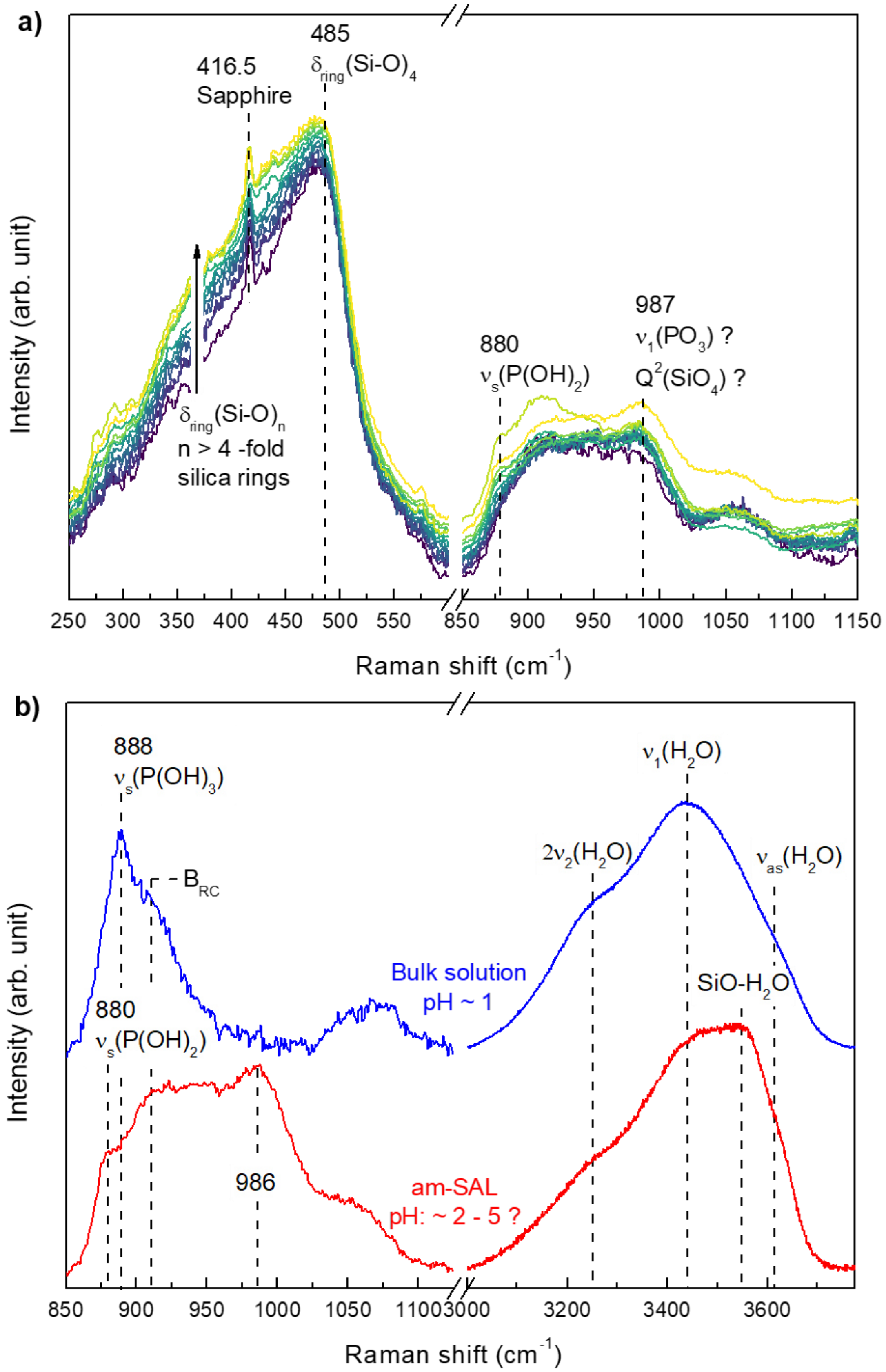

Figure 36: Representative, background-corrected Raman spectra that were acquired *in operando* ISG corrosion: **(a)** Average *in situ* Raman spectra of the am-SAL, including the spectral range between 250 and 600 cm^{-1} that was used for quantification of the structural parameter R_n. **(b)** low and high frequency region of Raman spectra of bulk solution (blue) and am-SAL, permeated with pore solution (red), measured at the end of the experiment.

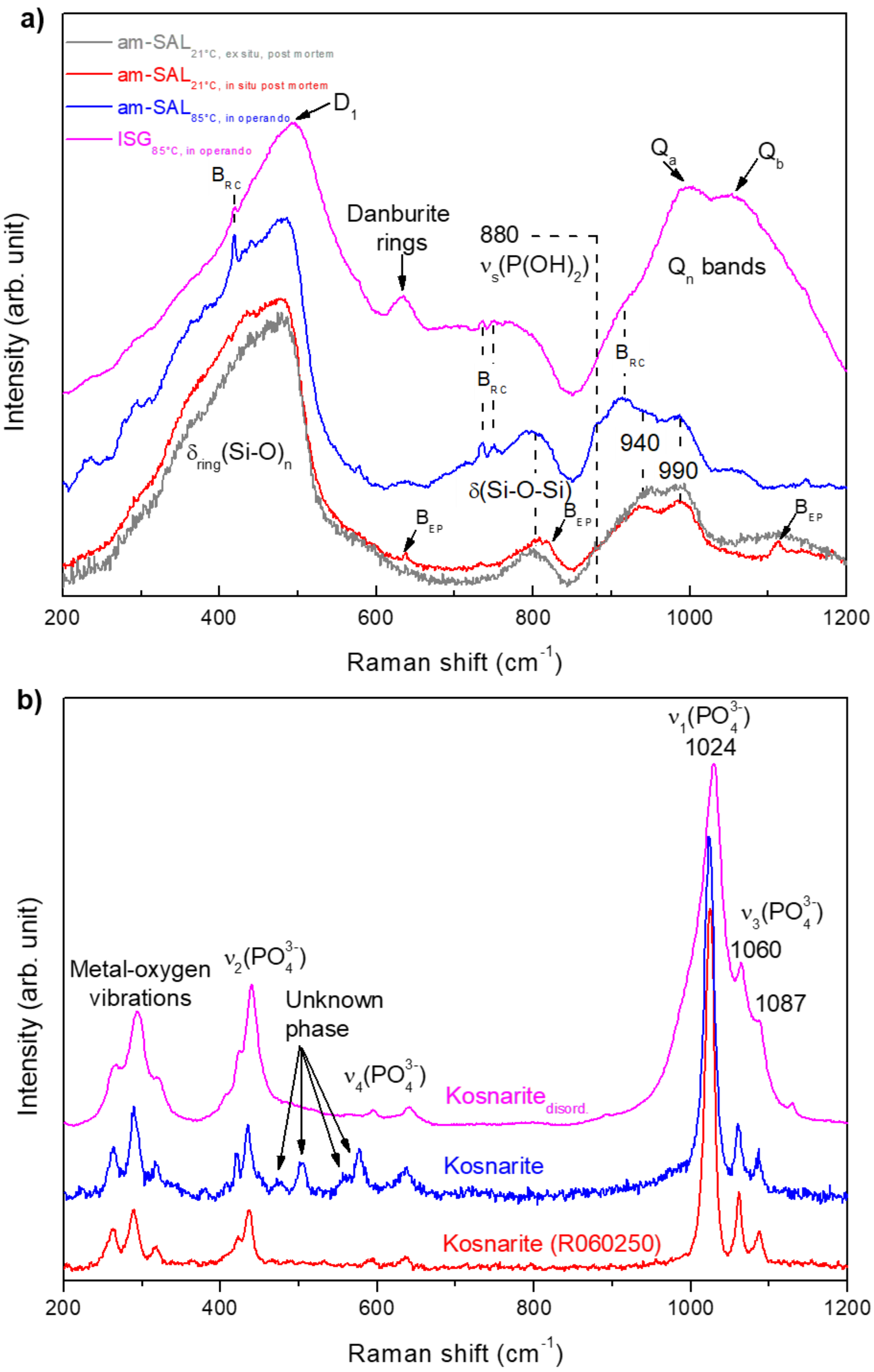

Figure 37: Representative, background-corrected Raman spectra of pristine ISG, and the identified corrosion products: **(a)** Average *in situ* Raman spectra of the ISG (purple) and am-SAL (blue) measured during the last measuring session after 4913 hours. The other spectra were acquired at RT by measuring the am-SAL of embedded altered ISG samples from the *in situ* (red) and *ex situ* (grey) experiments. **(b)** Disordered (purple) and ordered (blue) kosnarite ($KZr_2(PO_4)_3$) that was identified by the kosnarite reference spectrum R060250 (red) of the RUFF database [190]. No reference spectrum was found in the reference database that matches with the bands that are labeled as unknown.

7.2.3 Determination of the pH from dissolved phosphate speciation

So far, the focus has been on the analysis of solid phases that dissolved or formed during ISG corrosion under acidic conditions. However, the spectra also contain information on the dissolved species in aquatic solutions which in turn reflect the local pH [40,41]. Phosphoric acid was added to the initial leaching solution as KH_2PO_4 (0.1*M*) to make it possible to recognize strong local pH changes in the acidic pH scale regime, where the carbonate speciation cannot be used anymore.

The *in situ* Raman spectra are also in agreement with the low bulk solution pH (c.f., Table 7), measured at the termination of the experiment, since only H_3PO_4 was detected as a dissolved phosphate species in the bulk solution. This species is characterized by the $\nu_s(P(OH)_3)$ band around

888 cm^{-1} (blue *in situ* spectrum in Figure 36b). To assign the pH dependent phosphate species, additional reference measurements of KH_2PO_4 solutions at different pH values and temperatures using the fluid-cell setup were conducted (Figure 38). The observation of a band at 891 cm^{-1} for H_3PO_4 at 23 °C is in line with a reported band around 887 - 891 cm^{-1} at 25 °C [223,224]. It is also known that the frequency position will shift to lower wavenumbers with increasing temperature, e.g., down to 884 cm^{-1} at 155 °C in a 2 mol/kgw aqueous phosphate solution [223].

In contrast to the blue colored bulk solution Raman spectrum in Figure 36b, the assignment of the bands in the red colored am-SAL spectrum in the frequency range from 850 to 1125 cm^{-1} is more complicated due to overlap of Raman bands from different phases. The am-SAL spectrum was generated from *in situ* measurements by averaging the spectra of the am-SAL region that were taken just before the experiment had been terminated. The band around 913 cm^{-1} and the broad hump ranging from 1025 to 1075 cm^{-1} are background signals of the fluid-cell and can be found in all Raman spectra taken *in situ*. Furthermore, they were absent in subsequent Raman analysis of the dried sample, which can be clearly seen by comparing the gray and blue spectrum in Figure 37a. Both spectra belong to the same sample studied *in situ*, but the red and gray spectra were acquired *in situ* and *post mortem* after the sample was removed from the fluid cell, respectively. The band around 986 cm^{-1} and 987 cm^{-1} in the am-SAL spectrum in Figure 36a and b, respectively, probably belongs to the solid am-SAL and may be addressed to Q^2 coordinated SiO_4 tetrahedra [80,183] or Q^4 (2T) tetrahedra, like those assumed to be present in the ISG [80]. However, due to the possible overlap with the $\nu_1(PO_3)$ band of PO_4 within the pore solution, this band cannot unambiguously be assigned Because of its highly porous character, which is reflected by the strong water signal between 3000 and 3750 cm^{-1} in the am-SAL spectrum, the presence of dissolved phosphate species seems very likely. The band around 3540 cm^{-1} is assigned to $Si-O-H$ surface silanol groups that originate from molecular water attached to surface $Si-O$ sites. This assignment is supported by similar observations in porous silica and an am-SAL formed under initially acidic conditions by corrosion of TBG [30,31,225]. Indeed, phosphate was just observed *post mortem* in the outer Zr-phosphate layer or kosnarite phase of the dried sampl, which is further evidence for the assignment of the band near 880 cm-1 to a dissolved phosphate species. In fact, the $\nu_s(P(OH)_2)$ band at 880 cm-1 indicates the presence of $H_2PO_4^-$ anions in the pore solution that corresponds to a pH value between 2 and 5, at least higher than the corresponding bulk solution pH. This would suggest that the band around 987 cm-1 is more likely to be associated with the silicate tetrahedron, as the two phosphate bands indicate different species and are practically mutually exclusive according to the reference spectra of Figure 38. However, the second specific band of $H_2PO_4^-$ at 1077 cm-1, assigned to $\nu_s(PO_4)$, was not observed.

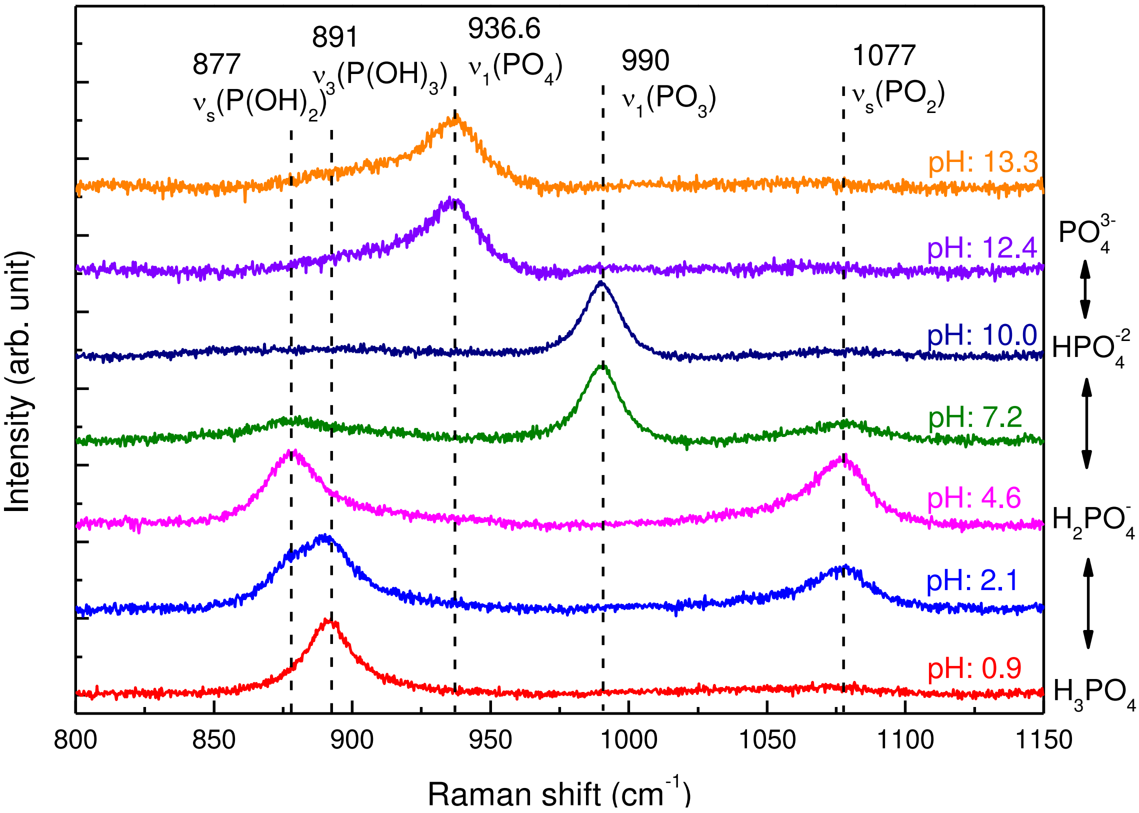

Figure 38: Representative baseline corrected (2nd order polynomial function, 10 baseline points) Raman spectra of KH_2PO_4 solutions at different pH (adjusted by adding diluted NaOH or HCl solutions to an initially 0.5*M* KH_2PO_4 solution) acquired *in situ* at ~ 85 °C in the Raman fluid cell. The phosphate concentration in the adjusted solutions ranged from 0.2 to 0.5 mol/l.

7.2.4 Bulk solution chemistry

At the end of the experiment pH measurements were performed and revealed that the bulk solution pH did not change during the experiment (c.f., Table 7). Additionally, the solution composition was determined for the initial and final solution to estimate the amount of altered glass constituents that remained dissolved, i.e., did not co-precipitate in the am-SAL. Although the glass corrosion process typically increases the pH of the leaching solution, the buffering effect of phosphate species and the high hydrogen activity seem to have prevented significant pH changes. Furthermore, just a small glass fraction of 6.1 ± 0.6 % was dissolved, based on the boron equivalent altered glass fraction (f_{AG}, c.f. , Chapter 5.2.1). The amount of f_{AG} determined from B solution data is in line with the of altered glass fraction of 6.5 ± 0.2 % that has been calculated based on Raman data ($f_{AG_{Raman}}$, c.f., Chapter 5.1.6.4), more precisely from the glass retreat.

Table 7: Solution pH and composition.

Solution parameter	*Initial solution*	*Final solution*
Si (mg/l)	0.060 ± 0.008	45.48 ± 0.43
B (mg/l)	0.024 ± 0.006	84.21 ± 0.64
Na (mg/l)	0.269 ± 0.006	98.896 ± 0.063
Al (mg/l)	0.0202 ± 0.0004	4.784 ± 0.002
Ca (mg/l)	0.108 ± 0.003	15.936 ± 0.051
K (mg/l)	7048 ± 11	8686 ± 62
P (mg/l)	5068 ± 127	5831 ± 35
$pH_{21°C}$	1.5 ± 0.2	1.4 ± 0.2
f_{AG} *(%)*	-	6.11 ± 0.56
$f_{AG_{Raman}}$ *(%)*	-	6.5 ± 0.2

7.2.5 Micro-texture and composition of the surface alteration layer

After termination of the *in situ* experiment, the sample was rinsed with pure water and dried at 90 °C for 48 hours before it was embedded in resin, polished, and analyzed by electron microprobe. The am-SAL thickness was measured based on backscattered electron (BSE) images at different positions of the cross-sectioned sample and found to be 22 ± 3 µm (standard deviation of the mean value, based on 20 representative, randomly selected length measurements), which agrees very well within the errors with the *in situ* measured thickness of 22 ± 1 µm. In general, the am-SAL thickness was smaller and rather irregular in regions, where the sample was close to the PTFE sample holder (Figure 39). Here, a wavy outer surface of the am-SAL was observed, especially at the curved edges. Within the recesses of the outer am-SAL a second solid phase, mainly composed of Zr, P, and K, was detected and identified by Raman spectroscopy (Figure 37b) as more or less well crystallized kosnarite ($KZr_2(PO_4)_3$). The frequencies and relative intensities of the symmetrical stretching mode $\nu_1(PO_4)$ near 1024 cm^{-1} and the asymmetrical stretching modes of $\nu_3(PO_4)$ near 1060 and 1087 cm^{-1} [226] match well with those of a kosnarite reference spectrum (R060250) from the RRUFF database [190]. Additional metal-oxygen (M-O) vibrations at 265, 290, and 318 cm^{-1} as well as in plane bending modes $\nu_2(PO_4)$ at 423 and 436 cm^{-1} were also observed [226]. However, the small bands around 595 and 636 cm^{-1} found in the blue spectrum of Figure 37b could not be assigned to kosnarite and their origin remained unknown, since no phase match with the RRUFF database was found. Although crystalline kosnarite was also detected, e.g., at the position marked with the blue star symbol in Figure 39a, most of the kosnarite was characterized by a spectrum equivalent to the purple one in Figure 37b. The broad $\nu_1(PO_4)$ band indicates a disordered, weakly crystalline and possibly nano-crystalline kosnarite type that predominates. However, the band maximum of the $\nu_1(PO_4)$ band is blue shifted, indicating a shorter average $P - O$ length and rather a higher crystallinity.

Figure 39a shows an BSE and elemental distribution images that extent across the ISG/am-SAL/kosnarite/resin sequence. Beside the two layers of corrosion products (am-SAL and kosnarite) covering the pristine ISG, a gap can be observed between the glass and am-SAL. A BSE image of the same area selected for the images of Figure 39a was recorded before (area that is outlined by yellow dots in the BSE image) and after the elemental analysis (rest of the BSE image). Comparison of both images reveals significant differences in electron beam resistance between inner am-SAL parts next to the reaction front/gap and the rest of the am-SAL. The increasing porosity of the inner am-SAL induced by the electron beam indicates evaporation of volatile components of corrosion products or resin that filled the porosity of the am-SAL.

Additionally, two elemental profiles are plotted in Figure 39. Figure 39b reflect the averaged compositions in x-direction for the area outlined with red dots in the BSE image of Figure 39a (direction from the red colored 1 to 2). In Figure 39c, a second elemental profile is shown that crosses the corrosion sequence of the same sample at another part of the glass sample that was hanging free in the solution,i.e., it was not in direct contact with the PTFE sample holder. A Zr and P enrichment was also observed in the thin layer covering the thick, silica based am-SAL. However, compared to kosnarite, this phase was almost free of K.

Note that the enrichment of Na at the ISG surface in Figure 39b was probably artificially induced by the electron beam during measurement. This is supported by the fact that the presence of Na enrichment was depending on the scan direction (compare profiles from Figure 39b and c, scan direction was from left to right side for both). Both, the false color images and the line scans are revealing a Ca-gradient with a maximum at the reaction front and a gradual decrease towards the outer surface of the corrosion layers. Such a gradient was also observed in previous ISG corrosion studies performed at low pH and addressed to incorporation into the SAL [34] or trapping in pores [158].

In contrast to the irregular outer surface of the corrosion products at parts of the samples that were close to the sample holder, a rather even SAL formed in the regions where the glass surface has been exposed freely to the bulk solution. These faces of the sample were polished very evenly,

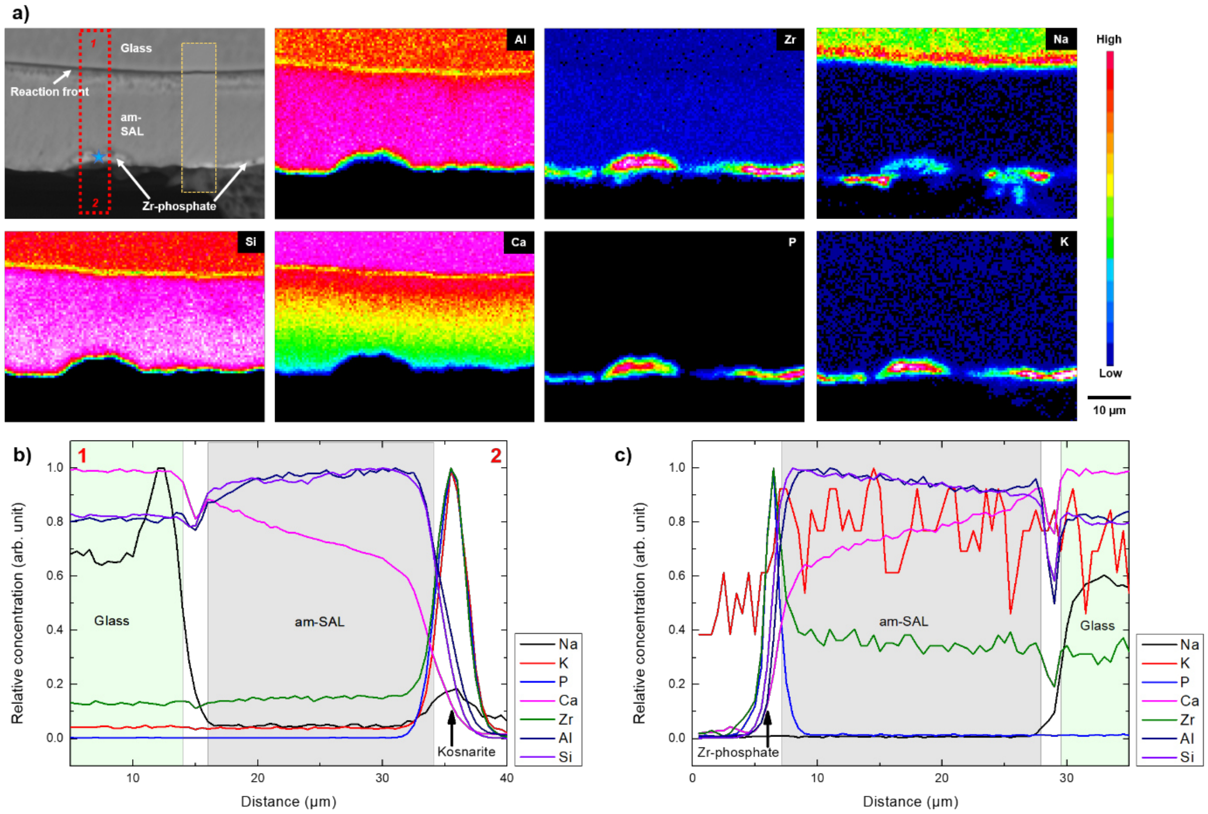

Figure 39: SEM analysis ISG altered in acidic phosphate bearing solutions at ~ 85 °C. **(a)** BSE image and elemental distribution maps (false color images) of an altered *in situ* ISG sample (showed part was close to the PTFE sample holder during corrosion) revealing an irregular outer am-SAL surface. **(b)** Relative elemental concentrations across the ISG/am-SAL/kosnarite/resin-sequence in the area outlined by red dots in the BSE image of (a), which shows a strong Zr, P, and K enrichment at the outer surface and an electron beam-induced artificial Na enrichment at the ISG surface close to the reaction front. **(c)** Representative relative elemental concentrations across the resin/outer am-SAL/inner am-SAL/ISG-sequence of a sample area that was not in contact to the PTFE sample holder (c.f., Figure S 4 for elemental distribution maps and BSE image), revealing a quite similar elemental distribution except the artificial Na enrichment.

in comparison to the curved edges, before starting the corrosion experiment. In Figure 39c, the elemental distribution profile crossing a laminar am-SAL shows a thin (< 2 µm) Zr-P-bearing outer layer that covers the predominantly Si-Al-Ca-based am-SAL. The small thickness of this layer was probably the reason, why it was not detected *in operando* due to the spatial resolution limitation of the *in situ* fluid-cell setup. Additionally, a distinct outer am-SAL could not be identified by *post mortem* Raman measurements, because of the dominating background signal of surrounding epoxy resin. Note that total am-SAL thickness in the consecutive *ex situ* sample not shown here was observed to vary, depending on whether the surface was directly contacted to the PTFE lining as the sample was placed on the floor of the reacting cell (13 ± 2 µm) or freely exposed to the reacting solution (20 ± 3 µm).

7.3 Discussion

7.3.1 Mechanism of surface alteration layer formation in acidic solutions

There are a few studies addressing the aqueous durability of silicate glasses under acidic conditions [30,31,35,50,158] and no general consensus about the mechanism leading to the formation of an SAL [30,35]. This is probably because there are only few technical applications of silicate glasses in strongly acidic solutions. In particular, in the near-field geochemical conditions in a geological nuclear waste repository are usually assumed to be slightly or strongly alkaline, which also depends on the disposal concept and surrounding host rocks, reducing the interest to study glass corrosion in highly acidic solutions. The forward dissolution rate of ISG in acidic solutions was, however, studied among others by Backhouse et al. [44] and Inagaki et al. [102]. These studies have confirmed a V-shaped pH-dependency of the forward dissolution rate with a minimum near a $pH_{70°C}$ of 4. Furthermore, an Arrhenius-type temperature dependency with an apparent activation energy between 62 and 68 kJ/mol (pH 3 - 8) was observed.

Fournier et al. [79] studied ISG alteration at 90 °C between pH 1.0 and 10.7 in silica-free and silica-saturated solutions to clarify the pH-depending impact of dissolved silica on silicate glass durability. Therefore, the solution pH was kept constant by frequent adjustment. The quite comprehensive study focused on analyzing leaching solution data and the calculation of equivalent dissolution rates, albeit solid samples were at least studied by XRD and SEM. The experiments were performed in silica-free solutions as well as in solutions that were initially saturated with respect of amorphous silica. It is noteworthy that no effect of dissolved silicic acid on glass alteration was observed under acidic conditions. Based on an ID based corrosion mechanism, the authors concluded that the preferential leaching of Na and B is responsible for am-SAL formation under acidic conditions. Furthermore, the effect of an Si-rich am-SAL was concluded to be negligible at low pH.

Although this hypothesis seems to be plausible at a first glance, the formed am-SAL becomes a more crucial element of the mechanism by considering it forms by stoichiometric glass dissolution and coupled precipitation reactions, which are inherent to the ICDP model [30,31,35,36]. Consequently, the amorphous gel-like corrosion product would be a newly precipitated phase instead of being a residual, partially leached glass relic. The congruent release of B and Na, following a square root of time dependency, in turn, may be explained by the increasing am-SAL thickness and its maturation that impedes the diffusional transport from the reaction front into the bulk solution. Therefore, this dependency of the concentration of glass constituents on time cannot be a clear argument for a pure leaching mechanism. The apparently preferred dissolution of Na and B compared to Si can be easily explained by the low silica solubility under acidic conditions, while other glass constituents (Na, B) may stay dissolved. Nevertheless, the dissolution process at the reaction front takes place stoichiometrically for all glass components.

Element or phase specific solubilities apply to silicate glass dissolution under different pH conditions, but the remarkable low silica solubility at low pH is crucial for the relatively fast am-SAL precipitation, probably making it hard to observe a different corrosion behavior between initially silica free and silica saturated solutions. Note that the composition and solubility within the solution layer at the solid surfaces may differ a lot from those of the bulk solution [29,41,65], which makes the sole interpretation of bulk solution data and models derived from them questionable.

7.3.2 Kinetics of glass dissolution and surface alteration layer formation

The *in operando* determined glass retreat data indicate an induction period of approximately 50 hours, because no shifting of the interface position was recognized for so long. This might be explained by the spatial resolution limitations, which are in the range of 6 to 16 µm [29,30,41,42,45]. Note that the lateral resolution depends on the measuring depth and intensity contrast of the chosen characteristic spectral region reflected in the false color Raman images. Nevertheless, the fact that a glass retreat of just about 1.9 µm was clearly observed in an equivalent time period between 60 and 120 hours, an initial induction period seems to be a real feature in this experiment. This is surprising above all because in the beginning the reacting solution was completely free of MSA and consequently the absence of any affinity based effect that might reduce forward dissolution should lead to a fast initial glass retreat [29,41,42], as has also been observed by Lenting and Geisler in 2021°[30], who studied the corrosion of the TBG in a 1*M* HCl solution by fluid-cell Raman spectroscopy.

If one assumes an ID dominated mechanism under acidic conditions to be responsible for am-SAL formation, an initial induction time is hard to explain as well. Theoretically, the highest gradient and therefore the highest glass retreat or alteration rate is expected to prevail at the very beginning of the reaction when the unhydrolyzed outer glass surface is directly exposed to the hydronium-enriched bulk solution. Glass network dissolution was found to also take place under acidic conditions in silica undersaturated solutions and could be recognized e.g., by enrichment of Al and Si in leaching solution [79,98,102]. However, in the experiment presented here the network dissolution reaction seems to be kinetically inhibited at the beginning. Most probably, ID reactions and accompanying hydrolyzation of terminal oxygen groups partly hydrolyze the silica glass structure, even an apparent low network dissolution rate, i.e., hydrolytic breaking of $\mathrm{Si-O-Si}$ bonds, limits the overall glass retreat at the very beginning. Once the glass started to dissolve the glass retreat was nearly linear with time with a rate of 0.612 ± 0.002 µm/h, but continuously decreased after an am-SAL started to form. A strong decrease of the glass dissolution rate by the formation of this layer has frequently been denoted passivation, as long as it is strong and leads to a *Stage II* behavior in long-term corrosion experiments. This was already discussed intensively in Chapter 2.1.4 and 3.2.8 and is mainly attributed to the effect of the SAL as a diffusion barrier between bulk solution and reaction front, regardless of the assumed corrosion mechanism [10,29,31,59]. The explanation is in line with a generally reduced glass alteration rate that goes along with an increasing am-SAL thickness.

The glass retreat and the simultaneous quantified am-SAL thickness (c.f., Figure 35a) seems to be somewhat inconsistent, because at the beginning, the precipitated am-SAL is even thicker than the glass that it is replacing. Additionally, this ratio is changing during the experiment and finally the am-SAL is even a little bit thinner than the glass retreat length. The almost complete cessation of the glass retreat over the last ~1500 hours of alteration also coincides with the thickness remaining relatively constant.

The reason for the increased corroded glass sample volume at the beginning is the porous microstructure that results in a lower density of the am-SAL compared to the pristine primary ISG (2.41 g/cm^3) [31]. Assuming an SAL structure that is similar to precipitated or sol gel derived amorphous silica, the density typically ranges from 2.0 to 2.3 g/cm^3, depending on the applied conditions [108]. In fact, this also supports the assumption that the am-SAL is formed by ICDP reaction, because a pure ID process cannot explain a volume increase at the beginning. The fact that the increasing volume changes to a volume reducing, non-isovolumetric replacement of the ISG is explained by the maturation and densification of the am-SAL with time, similarly to synthetic sol-gels [108,109].

Ongoing maturation is also reflected by the evolving R_n parameter that increased with time (Figure 35b) and reached a constant value of 0.614 ± 0.002 after the volume-positive replacement changed to a volume-negative one. The R_n increase indicates further condensation and maturation reactions of the amorphous silica after it was formed. Hydrolyzed free NBO of silica tetrahedra condense, which in turn increase the silicate network density and causes expulsion of water. This hypothesis is also supported by further increase of R_n up to 0.66, observed by Raman analysis after drying the sample. Such drying induced removal of pore solution and densification reactions highlight the relevance of *in operando* analytical techniques.

Interestingly, another *in situ* Raman study of Lenting et al. [30,31] observed a final R_n value of 0.65 *in operando* for an am-SAL formed by corrosion of TBG in a 0.1*M* HCl solution at ~70 °C. In this study, the R_n value did not change after drying. To explain this discrepancy, it should be mentioned that despite the relatively similar initial pH conditions, the solution in the study of Lenting et al. [30,31] was free of buffering phosphate species and the initial glass alteration rate was more than ten times higher. Therefore, the pH increased to 7.9 during a much shorter reaction time of about 250 hours due to the alkaline acting dissolution of the poorly durable TBG [30,31]. In contrast, the pH of the ISG experiment remained constant considering the measurement errors (c.f. Table 7). The different compositions of the am-SALs that formed by corrosion of ISG and TBG under initially acidic conditions had almost no measurable effect on the final R_n values after drying. The values measured *in situ* at different pH were slightly different. In comparison to this, am-SALs formed under neutral to weakly alkaline conditions were found to have higher R_n values that range from 0.64 to 0.74 and vary spatially [29,41].

It can be concluded that after the induction period passed, a few µm of glass dissolved stoichiometrically before am-SAL formation begun, which also caused the reduction of the dissolution kinetics of the underlying pristine ISG. Due to the lack of solution composition analyses during the experiment, it remains unknown if ID or glass dissolution already occurred before glass retreat was detected by the Raman measurement and when the bulk solution reached the silica saturation level. Nevertheless, the experimental results discussed so far are fully in line with results from previous *in situ* Raman corrosion studies and indicate that the R_n value of silica-based am-SALs to generally increase with increasing pH due to slower condensation (back-)reaction under acidic than under basic pH [79,108]. Drying promotes condensation of silanol groups and, in turn, also induces water expulsion and am-SAL densification. It follows that this is probably the reason for rising R_n values of less condensed gels formed under acidic conditions after they had been dried.

7.3.3 Precipitation of Zr-rich corrosion products

The formation of Zr-bearing, partly crystalline and Si-free phases indicates the complete dissolution of the Zr-bearing ISG, i.e., the release of Zr into solution. The textural relationship suggests that the glass was replaced first by an amorphous Zr-Phosphate layer until a silica-rich am-SAL began to form. Later, the outer Zr-P-layer in turn was replaced by kosnarite. It is noteworthy that no Zr-P-enriched outer layer was observed in a much shorter complementary reference experiment. However, it is assumed that an outer, separate layer may have detached from the sample during drying and preparation, because large parts of the stronger, thicker, and underlying am-SAL detached as well. A supplementary test series of conventional quench experiment combined with gentle drying and preparation would probably be helpful for clarification.

Thermodynamic calculations based on measured solution composition and the initially adjusted concentrations of KH_2PO_4 (0.1*M*) and HCl (0.1*M*) were carried out for a reaction temperature of 85 °C, using PHREEQC (c.f., Chapter°5.6). This was done to check the assumption that a Zr-P-bearing phase formed first and represents the outer surface layer, followed by further glass replacement by a silica-rich am-SAL. The calculated pH at room temperature (1.61 and 1.73) was a little higher than the one measured (1.40 ± 0.02 and 1.46 ± 0.02), which can potentially be attributed to the inaccuracies of (i) weighing the added components, (ii) the pH measurements, (iii) the geochemical modelling, and (iv) the measured solution composition. Nevertheless, the values are in a similar order of magnitude and the Zr-P-bearing reference phase ($Zr(HPO_4)_2$(alfa)) as well as amorphous silica (SiO_2(am)) were observed to be oversaturated in the residual leaching solution by $4.14 \cdot 10^{-4}$ and $9.74 \cdot 10^{-3}$ mol/l, respectively. Additional calculations also showed that extremely low concentrations of dissolved ZrO_2 (e.g., $1.0 \cdot 10^{-7}$ mol/l) already leads to an oversaturation of zirconium(IV) hydrogen phosphate, while SiO_2(am) remained undersaturated, even at higher concentrations of dissolved SiO_2 (e.g., $1.0 \cdot 10^{-6}$ mol/l). This suggests a Zr-P-bearing phase being favored to precipitate, before a silica-based am-SAL will form, and can explain the enrichment of Zr an P in the outer am-SAL layer, observed by EMPA for the *in situ* corroded glass sample (c.f. Figure 39c). It should be considered that a reliable modelling of the corrosion products is not possible without a sufficient thermodynamic description of the am-SAL phase(s) and the detected kosnarite. Therefore, the thermodynamic calculations and conclusions derived from them are only indicative. Nevertheless, they confirm that a Zr-P-phase has a high affinity to form, which in turn is consistent with the interpretation of the observations made so far.

The observation that structurally variable crystalline Zr phosphate phase (kosnarite) as well as a K-free Zr-P-bearing layer formed at the outer surface of the indicates different local environmental regimes within the reaction cell of one experiment, having caused different chemical and structural patterns observed in the SAL. This variation can be explained by the different local reaction kinetics caused by geometric constrains of the reaction cell. As described already in Chapter 5.1.1, the sample is fixed by a sample holder in the lid of the reaction cell, directly below the transparent sapphire window (c.f., Figure 17). The holder is made of PTFE and carries just the sample edge area, while the middle part is free hanging in the solution. Consequently, there is merely a thin fluid film between the sample and the sample holder in the edge area. Here, a high SA/SV ratio accelerated the reaction kinetics significantly when compared to the alteration reactions at the glass surface that freely hung in the bulk solution. Such small solution volumes become oversaturated to a certain phase very quickly, because the glass dissolution rate is relatively high compared to the transport into bulk solution and just a little bit of glass has to be dissolved to reach oversaturation within this solution volume. The more intense oversaturation and faster achievement of this stage next to the sample holder might be the reason for a fast re-precipitation of corrosion products, because nucleation rates in turn increase with the grade of supersaturation. This might be the reason why no well crystalline kosnarite was observed, where the glass was freely exposed to the bulk solution and evenly polished. Here, supersaturation was probably not reached that early in the experiment and the degree of supersaturation was much lower. In this context it should be mentioned that the critical supersaturation in general is assumed to becomes much higher within small solution volumes [227,228], which might be the reason for the absence at the very beginning, even the solution is probably oversaturated immediately with respect to a certain phase in very small voids between the sample holder and glass sample.

7.3.4 Passivating effect of the surface alteration layers

Raman spectra of the am-SAL acquired *in situ* and *in operando* indicate a higher pH within its pore space, compared to the bulk solution, which is in agreement with the study of Geisler et al. [29], who also observed a difference of the pH value in the pore and bulk solution by *in situ* fluid-cell Raman spectroscopy. Although the transport between bulk and pore or interface solution at the reaction front is impeded by the porous am-SAL, one would expect the pH to equilibrate gradually when the glass dissolution reaction is slowed down and the alkaline acting dissolution reaction almost comes to still stand. However, the $\nu_s(P(OH)_2)$ band even increases with reaction time in the spectra of Figure 36a. The observations that the second specific band of $H_2PO_4^-$ at 1077 cm^{-1} could not be detected in the spectra, indicating anion-anion interactions [229] and that a lot of the pore water was identified to be physiosorbed indicate the pores to be very small, even though the water signal intensity is relatively strong in the am-SAL region.

This assumption is based on a comparative Raman study of $2M$ KH_2PO_4 bulk solutions and droplets at different relative humidity (RH) that was performed by Syed et al. [229]. The authors observed that the $\nu_s(PO_4)$ band intensity strongly decreases and gets extremely asymmetric by reduction of the RH while the $\nu_s(P(OH)_2)$ band was not affected that much. This observation was explained by anion-anion interaction, because of the increasing anion concentration when RH is reduced and H_2O evaporates [229]. An analogous effect may also arise in the small pores of the am-SAL, where only low amounts of water are available, and its activity is very low. A relatively low concentration of free mobile H_2O molecules can also be concluded from the high frequency region of the Raman spectrum that indicates a great fraction of the pore water to be physiosorbed (c.f., Figure 36b). This can be interpreted as reflecting a highly porous microstructure with very small pores. It follows that a reason for the high pore solution pH might be the high reactive surface of the am-SAL, which at the same time results in a high number of terminal oxygens and a high surface charge density. The local surface equilibrium led to an increased amount of adsorbed counter ions (hydronium) which, in turn, rose the pore space pH very locally (inverse reaction Equation (I)).

The changing pore size, especially for the SAL that formed at late stage, correlates with a changing chemical composition, e.g., Ca increase (c.f., Figure 39). Such observations has already made in previous studies [34,158] and has been attributed to the incorporation of various elements into the amorphous silica phase of the SAL or to pore trapping, also influenced by pores sizes. A porous am-SAL can be responsible for the passivation in several ways. For example, the broadest consensus of how the passivation of glass is generated by the covering corrosion products is due to acting as a diffusion barrier which in turn depends on its porosity and pore connectivity. Related to the results shown here, the small pores may significantly delay the diffusional transport through the am-SAL by increasing the length of the transport distance or even inhibit the transport of certain dissolved species due to geometric constraints. Isotopic transport experiments performed *in situ* with corroded TBG at different pH also revealed anomalous diffusion and a pH dependence of the SAL diffusivity [141]. The observed power-law dependence with time indicates confined diffusion even for H_2O/D_2O molecules. Apart from such diffusional transport limiting or molecular sieve-like effects, the re-precipitation of a large fraction of previously dissolved glass constituent to form a less dense phase can end up with a closure of the aqueous reaction interface volume between the am-SAL and the underlying pristine glass (the interface fluid layer), which in turn ceases the dissolution reaction. Another factor might be the high reactive surface area and the anticipated associated rise of the solution pH in the pore solution, which shifts the pH value at the reaction front and within the pores closer to the dissolution rate minimum that is located near neutral pH for most silicate glasses [9,44,49,63,66] and near 4 for the ISG [44,102].

It is indeed likely that a combination of all these effects are responsible for the passivation and the establishment of the *Stage II*. Passivation by the am-SAL explains the rapid corrosion of glasses under acidic conditions at the beginning of alteration and at the same time the rapid slowdown of the dissolution rate as well as the low thickness of the am-SALs at the end of the experiment.

7.3.5 Glass corrosion under acidic conditions via interface-coupled dissolution-precipitation reactions

In summary, ISG dissolves congruently in acidic aqueous solutions at the beginning of the experiment, as sketched out in Figure 40a. However, a relatively short induction period of about 40 hours was observed, where glass dissolution seems to be inhibited. Because of the very low Zr solubility, this element tends to precipitate back on the glass surface to form Zr-phosphates while glass dissolution continues (Figure 40b), which is in line with simple thermodynamic predictions. The formation of Zr phosphate nominally free of Si clearly demonstrates that the glass was completely hydrolyzed, even under acidic conditions.

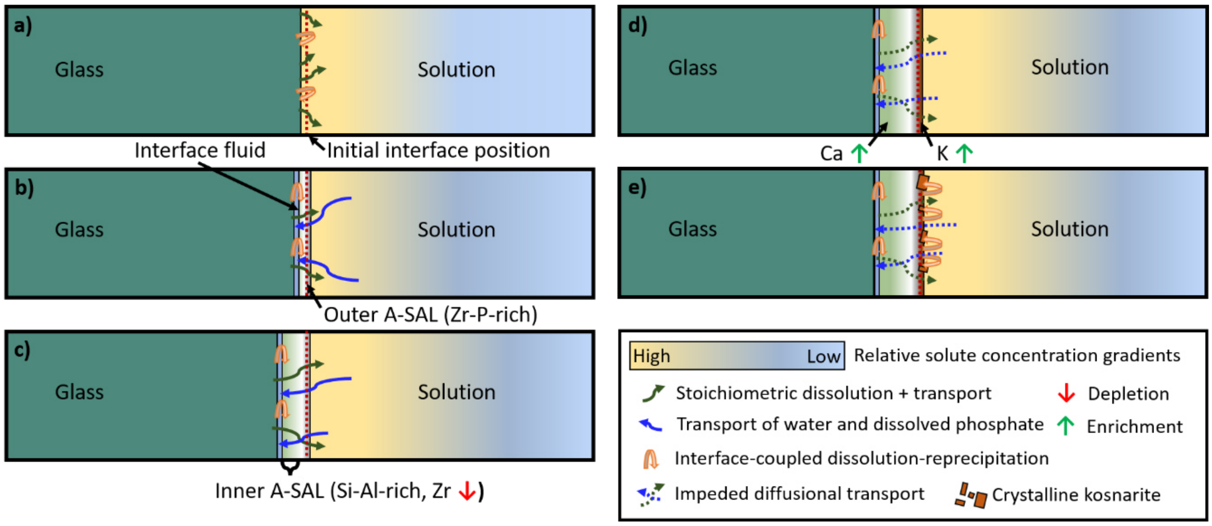

Figure 40: Schematic representation of the proposed corrosion mechanism for ISG in acidic phosphate solutions at around 90 °C, mainly based on interface-coupled glass dissolution and precipitation reactions.

However, further glass dissolution leads to increasing Si concentrations at the reaction interface which in turn allows a silica-rich am-SAL to form between the Zr-and P-rich layer and the pristine glass (Figure 40c). After this am-SAL reached a thickness of about 20 µm, its transport limiting properties were sufficient to passivate the underlying glass (Figure 40d). Additionally, the amorphous Zr phosphates seemed to be replaced again by weakly or well crystalline kosnarite by an ICDP process which in turn consumes K that originates from the initial solution (c.f., Figure 40d and e). Two distinct ICDP reactions, i.e., the glass/am-SAL-replacement and Zr-P/kosnarite-replacement, which take place at different interfaces. The observations highlight the relevance of considering local solution properties and steady states instead of constant glass dissolution rates to capture the dynamic replacement and manifold secondary replacement reactions, which may lead to a resumption of the alteration rate.

7.4 Conclusion

The described observations from the second ISG case study confirm that the ICDP mechanism is also suitable to explain ISG corrosion features arising under acidic conditions [30]. Although the distinct water-rich zone at the am-SAL/glass interface was not detected *in operando*, an ICDP process only needs a very thin water layer to operate [37,93,111,112] that cannot be resolved by the applied *in situ* method. However, a gap between the SAL and the underlying glass can be observed in BSE images from the dried and polished sample (Figure 39). In addition, in other *in situ* Raman studies the gap could clearly be observed in hyperspectral Raman images [29,41,45], because its extension reached the lateral resolution, which in turn is due to a higher pH and higher solubilities of the glass and its constituents. However, the small gap between the pristine glass and am-SAL and the easy detachment of the different corrosion products support the existence of an atomically sharp interface and, in turn, of an interface fluid layer.

7.4 Conclusion

To the best of the authors' knowledge, this is the first time that crystalline corrosion products were detected during corrosion of the ISG in an acidic solution. However, rutile (TiO_2) crystals have been observed at the outer SAL surface after corrosion of a chemically complex, Ti-bearing borosilicate glass in a 1*M* HCl solution at 150 °C [35]. The formation of crystalline corrosion products under these conditions is important for the debate about an universal glass corrosion mechanism, because crystalline secondary phase formation is usually assumed to coincide with an accelerated glass corrosion rate and was so far mainly observed in hyperalkaline solutions [18,43,61,64,67,79,94,96,99,114,185]. In this study, however, the formation of crystalline phases had no observable effect on the glass retreat rate. The reason for this is probably that the identified crystalline secondary phase kosnarite did not incorporate the main network building elements (Si and Al), making up the parental glass and the am-SAL. Therefore, the formation of Zr-bearing phosphate does not affect the saturation state of amorphous silica, i.e., the chemical affinity of glass dissolution. However, the formation of well or weakly crystalline kosnarite or amorphous Zr-phosphates, which are nominal free of Si, implies the complete hydrolyzation of ISG bonds, especially $Zr-O-Si$ bonds. This is in contradiction to the *in situ* reconstruction and ID based alteration mechanism presented in Chapter 2.2 that has rarely been questioned so far [30,35,36] for aqueous glass alteration under acidic conditions.

Apart from the fact that the method used here makes it possible to observe the dynamics of glass corrosion with a high spatial and temporal resolution in only one experiment, the Raman spectra also indicate a different pH value in the pore space, as reflected by the pH-dependent phosphate species and their specific Raman bands. Furthermore, the Raman data suggest a small pore size and a high porosity for the am-SAL. These results highlight the value of using *in situ* techniques to analyze reactions *in operando* with a high spatial resolution and thereby the local hydrochemical conditions during glass alteration.

Moreover, the *in situ* Raman data reveal a maturation of the am-SAL by an increasing R_n value over time, which is equivalent to an increase of the proportion of silica ring structures larger than 4-fold rings [29–31] and a decreasing molar volume due to ongoing condensation and densification. Also, a significant increase of R_n after drying was observed, which highlights how important it is to analyze the structure and properties of the corrosion products before quenching and drying. Another indication for maturation and densification of the am-SAL is given by the observation of the changing ratio of glass retreat to SAL thickness. At the beginning, the am-SAL thickness increased more strongly than the ISG retreated, while this behavior was reverse at the end.

In contrast to the recently published study of Lenting and Geisler [30], who did not use a buffer agent in their experiment with a 0.1*M* HCl solution, the addition of phosphate as a buffering species in combination with the significantly lower amount of corroded, alkaline-acting borosilicate glass kept the pH value relative constant and strongly acidic. The use of such buffering agents, whose species can be distinguished by Raman spectroscopy, is recommended to ensure the pH to be constant or at least to recognize significant pH changes *in operando* in order to avoid deriving false conclusions from the results. However, as in this case, such an addition of phosphate or other elements to the system can lead to the formation of new phases which in turn may change the course of the alteration. Nevertheless, the presence of phosphate did not prevent passivation, although it led to the formation of crystalline secondary phases (kosnarite).

The complex SAL and the crystalline kosnarite that has been observed in this study are assumed to be formed via ICDP reactions at two different interfaces. At the reaction front, the glass is dissolved and coupled to am-SAL precipitation, leading to an inwardly moving replacement of the glass. A second ICDP process was identified at the outer surface of the sample, where the initially amorphous Zr-phosphate-rich corrosion product is replaced by crystalline kosnarite. This result again demonstrates the complexity of glass corrosion under acidic conditions and suggests that a single dissolution or glass hydrolyzation/reconstruction rate is probably not able to correctly predict the long-term stability of a silicate glass. Reliable corrosion models must appropriately consider the establishment of local equilibria, steady states, and the occurrence of feedbacks in order to correctly predict the dynamic corrosion rate.

8

Case study III: Glass corrosion under flow-through conditions

8.1 Introduction

In the field of glass corrosion, experimentally corroded glass samples and the experimental aqueous solutions are commonly analyzed after quenching the experiments at different stages of reaction progress. However, the structure and chemistry of the surface alteration layer alter during the drying and preparation procedure. More precisely, the microstructure and chemistry of the hydrous am-SALs may change, or additional secondary mineral precipitation may be triggered, particularly inside porous SALs. In addition, conventional isothermal corrosion experiments require the use of a new glass sample for each time step. These limitations complicate the study of non-linear dynamic reaction kinetics of glass dissolution and glass replacement. This becomes even more difficult when glass dissolution is studied under dynamic conditions, induced by different fluid exchange rates, which multiplies the required number of conventional experiments. Flow through conditions are usually applied to determine the intrinsic forward dissolution rates of glasses to avoid SAL formation by keeping the reacting solution undersaturated with respect to amorphous SiO_2 [10,15,68,69]. However, most of these studies are focusing on solution analysis and do not consider the actual local changes on the glass samples surface, i.e., the corrosion reaction front, to validate the data from bulk solution analyses. A combination of solution analysis and *in situ* techniques to monitor the sample surface advance allows studying the forward dissolution rate, as previously shown for ISG alteration under hyperalkaline conditions in case study I (Chapter 6). In addition, both complementary methods are useful for inferring specific details about corrosion behavior that may not be visible in bulk solution and *post mortem* analyses.

To overcome the drawbacks of *ex situ* quench experiments, *in situ* fluid-cell Raman spectroscopy was used to investigate the corrosion of a simple ternary sodium borosilicate glass (TBG) that has also been used in other studies [30,31,40–42,141], under varying solution exchange rates for different reacting solutions. For the flow-through experiments, polished coupons (approximately $8 \times 5 \times 2\ mm^3$, half of the edges rounded) were prepared according to the procedure described in Chapter 5.8.1. The reaction cell was linked to the syringe pump for the flow-through studies of this case study, as shown in Figure 17. The fresh leaching solution was pumped continuously in the fluid cell and the displaced solution was collected in a vessel that was linked to the outlet valve. This vessel was renewed at regular time intervals to get multiple solution samples over different time periods of the experiment. Subsequently, these samples were analyzed to obtain time-averaged information about the bulk solution composition and solution pH.

In this chapter, the results from three different corrosion experiments (Exp. I, Exp. II, and Exp. III), performed at nominally 90 °C, will be presented, differing mainly in the solution chemistry and exchange rate. Exp. I and Exp. II were in particular designed to study the influence of the solution exchange rates and different buffers (borate and carbonate species) on the corrosion of silicate glass. The third corrosion experiment (Exp. III) was carried out at a constant solution exchange rate and in a silica-supersaturated solution (about two times the saturation level) to examine possible chemical affinity effects and to *in situ* and *in operando* investigate the am-SAL structure as it forms either from silica originating from the initial solution or from the dissolving glass.

For the first experiment (Exp. I) boric acid (isotopically pure ^{10}B) was dissolved in deionized water (Milli-Q®) to get a 0.075*M* $^{10}B(OH)_3$ solution. A target $pH_{85°C}$ of 7 was adjusted by adding minor amounts of a 0.5*M* NaOH solution at 85 °C. The aims of adding boric acid were (i) to test the application of dissolved boron species as an additional *in situ* pH tracer instead of carbonate species [29,41,230], (ii) to buffer the solution pH to avoid dramatic changes during glass dissolution, and (iii) to study the effect of boron on the glass alteration rate of TBG. At the beginning, the exchange rate was set to 5 ml/h and reduced to 0.5 ml/h after 54 hours. After 141 hours, the pump rate was further reduced to 0.25 ml/h for the rest of the experiment that was terminated after 212 hours.

The second experiment (Exp. II) was carried out with deionized water with pH $7_{90°C}$, adjusted with minor amounts of a 0.1*M* NaOH solution under varying flow rates and stagnant conditions. The initial pump rate was again set to 5 ml/h and was reduced to 3 ml/h and to 1 ml/h after 23 and 53 hours, respectively. After 225 hours the pump was switched off, the valves were closed, and the experiment continued under stagnant conditions until it was terminated after 476 hours.

Finally, a third experiment (Exp. III) was conducted with the TBG under silica-supersaturated (about 1200 mg/l SiO_2) and constant solution exchange (5 ml/h) conditions. The silica-rich liquid was prepared from a commercial concentrated sodium silicate solution by dilution and addition of HNO_3 (2.5 wt.%) to reduce the $pH_{85°C}$ to 9 at 85 °C while continuously monitoring the pH.

The results of these three experiments presented in the following impressively demonstrate that *in situ* fluid-cell Raman spectroscopy can open up new avenues for studying glass-water reactions and that the use of *in operando* methods can avoid misleading interpretations induced by quenching and drying of the samples before analysis.

8.2 Results and Discussion

8.2.1 Impact of solution composition and exchange rates on initial dissolution rates

All three experiments include the initial stage of glass dissolution at different applied solution exchange rates. Later in the course of the reaction, only in Exp. II and Exp. III an am-SAL, more precisely, multiple am-SALs formed. Exp. I was performed under silica-free conditions in a 0.075 M $B(OH)_3$ solution at neutral pH and revealed a clear dependence between the forward dissolution rate of TBG and the solution exchange rate (Figure 41a). At the beginning, when the pump rate was set to 5 ml/h, the glass retreat rate was 1.91 ± 0.02 µm/h. This value is in the same order of magnitude of forward dissolution rates obtained for this glass under very similar conditions which range between 0.75 ± 0.08 and 2.1 ± 0.7 µm/h (Table 8) [29,41,42].

After 58.5 hours the pump rate was drastically reduced from 5.0 to 0.5 ml/h, causing an abrupt drop of the glass retreat rate to 1.09 ± 0.01 µm/h. The rate decreased further to 0.78 ± 0.01 µm/h after the solution exchange rate was halved to 0.25 ml/h. Although the exchange rate was low at the end of the first experiment and a significant amount of glass was dissolved considering a total glass retreat of more than 250 µm after 201 hours, no corrosion product could be detected at the glass surface. This contrasts with results from experiments performed under stagnant conditions at similar pH in B-free solutions, which show the formation of an am-SAL made up of hydrous amorphous silica after about 60 hours [29,41]. It appears that the continuous solution exchange prevents the solution at the surface of the glass from reaching silica saturation. Consequently, no amorphous SiO_2 precipitated onto the glass surface, even though the local solution properties at the glass surfaces was found to differ greatly from those of the bulk solution [29,65], which in turn is much stronger affected by the solution exchange rate. Beside applying flow-through conditions, the solution composition (initial B concentration) and salinity (initial alkali concentration) were also different than those in previous studies [29,41]. So far, it remains unknown if and how the presence of boric acid influences the glass dissolution and silica condensation reactions directly. However, it is clear that the initial salinity of the pH adjusted $0.075M$ $B(OH)_3$ solution was about three times lower than those of a $0.5M$ $NaHCO_3$ solution. In addition, this lower salinity was maintained by regular solution exchange, which reduced the extent of glass constituent accumulation in the bulk solution compared to stagnant conditions.

The observation that the lower the pumping rate, the lower the corresponding forward dissolution rate is partially inconsistent with increasing solution pH, as shown in Figure 41b in which the time evolution of the pH is shown. The solution pH increases with decreasing flow rate and after a transition stage the pH value forms a plateau at about 7.47 ± 0.01 and 7.83 ± 0.02 for solution exchange resolution 5.0 ml/h and 0.5 ml/h, respectively. Unfortunately, the experiment had to be terminated before a pH plateau for the pump rate of 0.25 ml/h could have been established due to technical problems. However, it would likely be above a pH of ~ 8, considering the already observed pH values for the transition regime. Interestingly, it has been observed in several studies that above the neutral point glass dissolution rates commonly increase with increasing solution pH [44,48,63], which is in severe contrasts to the decreasing dissolution rate observed. However, this observation may be explained by the affinity effect of dissolved silica, because this component can become more concentrated in the solution with a reduced solution exchange rate. It follows that in this experiment the rate decreasing affinity effect has superimposed the rate increasing effect of a higher solution pH. It can be concluded that the alkaline glass dissolution reaction affects the solution pH and the feedback of the rising pH on glass dissolution is less dominant. The results of this experiment further highlight the impact of solution exchange rates on (i) the solution pH, (ii) the salinity, and (iii) the silica saturation state. These parameters in turn influence the forward dissolution rate at the ICDP interface in different ways and are also crucial for am-SAL formation.

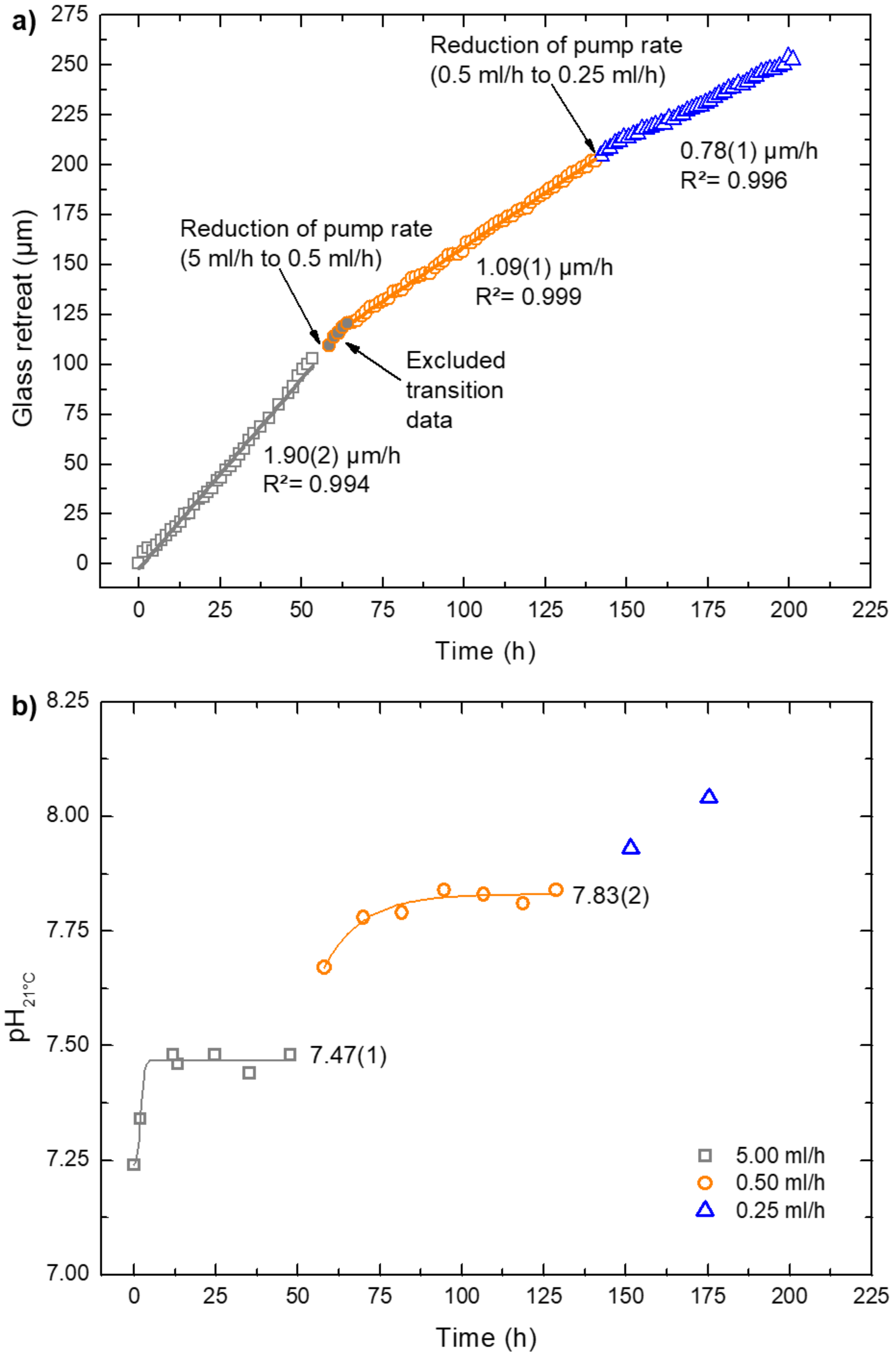

Figure 41: (a) Temporal shift of the glass retreat based on the glass/solution interface position for different pump, i.e., solution exchange rates (Exp. I). **(b)** The corresponding pH of the exchanged solution as a function of time at 21 °C. Sigmoidal curves were fitted to the pH data of 5.00 and0.50 ml/h pump rate to determine the plateau values which is equivalent to the pH of the steady state of glass dissolution and solution exchange. The R^2 was 0.9503 for the gray and 0.8903 for the orange curve, respectively.

Table 8: Comparison of the initial dissolution rates for the ternary Na borosilicate glass (TBG) obtained by fluid-cell Raman spectroscopic experiments under batch and flow-through conditions in this and previous studies.

Solution composition	***T*** *(°C)*	*Initial pH at T **	*Pump rate (ml/h)*	r_0 *(µm/h)*	*Reference*
0.075M $B(OH)_3$	84 ± 2	*7.0 ± 0.1* (measured and adjusted with NaOH)	5.00 0.50 0.25	1.91 ± 0.02 1.09 ± 0.01 0.78 ± 0.01	This study (Exp. I)
Deionized water	84 ± 2	*7.0 ± 0.1* (measured and adjusted with NaOH)	5.00 3.00 1.00	0.81 ± 0.02 0.80 ± 0.02 0.70 ± 0.03	This study (Exp. II)
Diluted sodium silicate solution (1200 mg/l SiO_2*)*	84 ± 2	*9.0 ± 0.2* (measured and adjusted with HNO_3)	5.00	0.66 ± 0.03	This study (Exp. III)
0.5M $NaHCO_3$	80.0 ± 0.2	7.1	-	1.8 ± 0.2	Lönartz et al. [42]
0.5M $NaHCO_3$	82.6 ± 0.3	7.1	-	1.5 ± 0.1	Lönartz et al. [42]
0.5M $NaHCO_3$	81.7 ± 0.1	7.0	-	1.00 ± 0.03	Dohmen [41]
0.5M $NaHCO_3$	85.1 ± 0.7	6.8	-	2.10 ± 0.01	Dohmen [41]
0.5M $NaHCO_3$	85.2 ± 0.2	7.1	-	1.61 ± 0.04	Geisler et al. [29]
0.5M $NaHCO_3$ *adjusted with HCl*	84 ± 2	*4.91 ± 0.02* (measured at RT)	-	1.46 ± 0.20	Egger [141]
0.5M $NaHCO_3$	84 ± 2	*8.37 ± 0.02* (measured at RT)	-	0.75 ± 0.08	Egger [141]
0.3M $NaHCO_3$ *and 0.1M* Na_2CO_3	84 ± 2	*9.95 ± 0.02* (measured at RT)	-	0.12 ± 0.03	Egger [141]
0.1M HCl	~ 70	1.0	-	~ 9	Lenting & Geisler [30]

* Calculated with PHREEQC [133] according to the method described by Geisler et al. [40], with the exception of values in italic that were measured at room temperature.

To estimate the influence of B addition or generally the addition of other buffering species (e.g., dissolved carbonates [29,41]) on the corrosion process, a buffer-free experiment in deionized water, containing only minor quantities of NaOH for pH adjustment, was carried out. Again, the initial flow rate was 5 ml/h, but the measured forward dissolution rate of 0.81 ± 0.02 µm/h is relatively small when compared to the other initial dissolution rates observed for this glass (Table 8), i.e., the dissolution rate was generally lower without dissolved species such as boric acid or bicarbonate. It has been observed that buffering agents, including organic buffers, are able to increase the dissolution kinetics of borosilicate glasses, as, e.g., shown by Tournié et al. for (TRIS) molecules [75]. These authors assumed that the increase of glass dissolution kinetics can be explained by surface complexation of TRIS on specific boron surface sites, which in turn accelerates glass dissolution. In this context, it is important to note here that an *in situ* fluid-cell Raman spectroscopic experiment has revealed a decoupling of TRIS molecule transport through the SAL and the ICDP reaction front velocity so that the buffer cannot be considered as being inert with respect to the glass-water reaction process [41]. The buffering agents used here, however, are smaller in size and it is therefore conceivable that borate and bicarbonate ions affect the dissolution reactions at the ICDP interface by complexation of silicon surface sites similar to hydroxyl anions. However, further experiments are needed to first confirm this observation and then to clarify the underlying molecular mechanisms.

Whereas the reduction of the solution exchange rate down to 3 ml/h did not significantly change the forward dissolution rate, a further reduction to 1 ml/h has eventually led to a significantly reduced rate of 0.70 ± 0.03 µm/h. However, this abrupt rate drop coincides with the first detection of amorphous silica replacing the glass rather than with the change in pumping rate (Figure 42), which is evidence that the drop is related to the formation of a protective SAL [36,57,60,94].

The lowest initial dissolution rate of TBG listed in Table 8 originates from the third *in situ* fluid-cell Raman experiment (Exp. III), which was likely due to the high concentration of dissolved SiO_2 (1200 mg/l), i.e., the chemical affinity effect of amorphous silica that goes along with it. The glass retreat data used to derive r_0 is shown in Figure 46a. They were fitted with a piecewise function that combines three linear functions, yielding an initial glass dissolution rate of 0.570 ± 0.001 µm/h for the first 180 ± 5 hours. Note that first silica signals were detected already from the beginning, which is why in this time period the rate value might be affected already by passivating effects.

The findings from this experiment are also stimulating for the interpretation of experiments in which an initially silica saturated solution was used to accelerate the reaction progress and skip *Stage I* of glass corrosion, especially for relatively durable glasses, such as the ISG [43,53,92]. However, whether this approach influences the corrosion process beyond a mere acceleration has usually not been considered.

8.2.2 *In operando* observation of surface alteration layer formation under flow-through conditions

At the beginning of Exp. II at a 5 ml/h solution exchange rate only congruent glass dissolution was observed. Still, no significant change in glass retreat rate was observed after the exchange rate had been reduced to 3 ml/h (c.f., Figure 42). However, precipitation of amorphous silica started after ~ 70 hours when the exchange rate was further reduced to 1 ml/h. At that same time, the glass retreat stopped rapidly which becomes very clear from the glass retreat *versus* time plot shown in Figure 42a. After the reaction front remained in the same position for about 10 hours, the glass retreat gradually increased non-linearly until a linear rate of change was restored after about 175 hours. Interestingly, despite the short halt of the glass retreat after the first silica was detected, glass dissolution underneath continued and the first am-SAL, named

SAL#1 in the following, grew until it reached a thickness of 19.9 ± 1.8 µm. A second order polynomial fit describes very well the glass retreat vs. time behavior during this period, while the glass dissolved and the SAL#1 grew with a rate of 0.17 ± 0.01 µm/h until 175 hours. When the SAL#1 reached its final thickness, a linear glass retreat rate of 0.59 ± 0.01 µm/h was simultaneously observed, which lasted until the pump was turned off after 225 hours. As a consequence of ongoing glass retreat and a constant SAL#1 thickness after 175 hours, a water-rich zone formed between the SAL#1 and the underlying glass. This gap formation is clearly visible in the hyperspectral Raman images, especially when having a look at water signal intensity map (Figure 44b). Figure 44a shows the glass interface shift with time (c.f., Figure 42). The water signal (Figure 44b) indicates a water-rich interface and also a porous SAL structure, since Raman signals of H_2O can also be seen here, albeit at a lower intensity level compared to bulk and interface fluid regions. This water-rich interface between SAL#1 and SAL#2 was about 65 µm thick. Furthermore, intensity variations can be observed the final line scan after 476 hours also in-between the reaction front and the outer surface of SAL#2. This is in line with silica signal variations (c.f., Figure 44c) in the same domain, which may indicate differences in silica density and porosity. While no silica or glass signal (Figure 44a and c) is present below the SAL#1 between 175 and 250 hours, the high H_2O signal intensity indicates the presence of a water-rich interface fluid layer.

From the moment the pump was switched off, the glass retreat had an almost linear progression with time, but the final trend can be better described by a polynomial fit when considering the last measurement after 476 hours. This also applies to the thickness of the second am-SAL that was observed *in operando* (SAL#2), although it should be emphasized that there was a large time period of about 165 hours without any data (grey region in Figure 42). Changing the solution exchange rate is also reflected in the pH of the bulk solution that was measured at the outlet valve of the fluid cell. In general, a higher pH was measured in the solutions of Exp. II when decreasing the pump rate (c.f., Figure 42b). A rising pH with advancing corrosion was already observed in many other glass corrosion studies, especially for TBG [30,31,39], and is related to the alkaline components of the dissolving glasses (such as Na). Interestingly, the outflow $\mathrm{pH}_{23^\circ\mathrm{C}}$ remained stable at 8.27 ± 0.03 between 120 and 170 hours. This coincides with the observed constant growth of SAL#1 and the nonlinear-glass retreat in Figure 42a. After a transient period, when the pump rate was reduced to 1 ml/h, a steady state between glass dissolution, silica precipitation, and bulk solution exchange and a constant pH has apparently been established until further SAL growth ceased and an acceleration of the glass retreat was observed. Because more glass was dissolved at this time while the pump rate

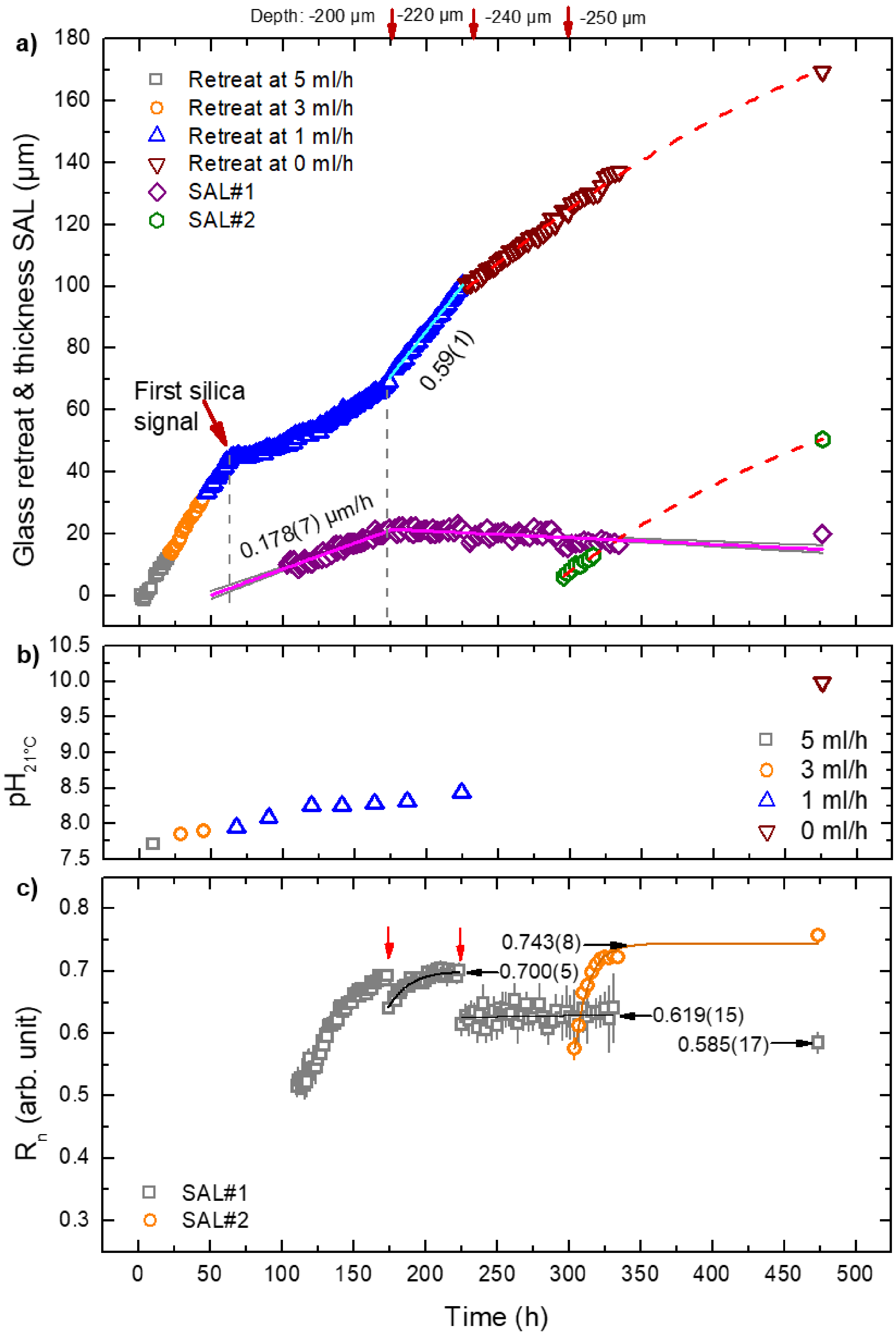

Figure 42 (see previous page): (a) Glass retreat and the thickness of two am-SALs (SAL#1, SAL#2) as a function of time (Exp. II). The glass retreat symbols are differentiated based on the pump rate (solution exchange rate). The dashed red lines are showing 2nd grade polynomial fits. Least-squares fitting errors are smaller than symbol size. The piecewise fit and extrapolation of SAL#1 thickness data indicate silica precipitation started at about 50 ± 2 hours (gray lines adjacent to the purple fit represent the 95 % confidence interval). The advance of the solution pH of the exchanged bulk solution was measured for some samples, shown in **(b)**. In **(c)**, the structural parameter R_n, which has been calculated based on the *in situ* Raman data of the am-SAL, is plotted as a function of time. Note that the discontinuities in the gray data of SAL#1 is due to the changing analysis depth, highlighted by the red arrows. If possible, the plateau values were estimated by fitting of a sigmoidal shape function (black curve with R^2= 0.945, orange curve with R^2= 0.907) or linear regression (black horizontal line).

remained constant, the pH started to increase again, as observed for the sample taken after 225 hours. The final solution $pH_{23°C}$ that was measured after 476 hours was 10.0 ± 0.2, which is in line with TBG corrosion experiments performed for much shorter time periods various conditions [39,41]. This is might have been caused by the buffering effect of dissolved MSA, more precisely the deprotonation of $H_3SiO_4^-$ to $H_2SiO_4^{2-}$. This change of the silica speciation is also the reason for the increasing amorphous silica solubility at pH values above $9_{25°C}$ [108]. The sequence of the underlying reactions is as follow:

$$SiO_2 + 2H_2O \rightarrow H_4SiO_4 \qquad \text{(XXI)}$$

$$H_4SiO_4 + OH^- \rightarrow H_3SiO_4^- + H_2O \qquad \text{(XXII)}$$

$$H_3SiO_4^- + OH^- \rightarrow H_2SiO_4^{-2} + H_2O \qquad \text{(XXIII)}$$

For the am-SALs formed in Exp. II and Exp. III all R_n values were calculated for the individual layers formed to examine a spatiotemporal variation of the silica structure. As described already in Chapter 5.1.6.3, a larger R_n value implies a larger fraction of $(Si\text{-}O)_{n>4}$ rings and allows to evaluate the silica structure and its dependence on other parameters. The average Rn was observed to be slightly smaller for SAL#1 than that of SAL#2, which is also shown in Figure 42c and discussed in more detail in the following.

It should be noted that the increase of the R_n value at the beginning of any SAL growth does probably not exclusively reflects the silica structure. Depending on experimental conditions and corrosion progress, the signal can be affected to different degrees by the background signals. The complex optical system in which the laser beam passes successively through air, sapphire, the top water layer to be finally focused in the silica layer has undergone several refraction and scattering processes, all of which are wavelength specific. This also have effects on the background that in turn is dynamic if a very thin SAL is measured, where the fraction of out of focus signal increases. To reduce such effects the R_n value was averaged (mean of the R_n values from position -49 µm to -53 µm for SAL#1 and from -120 to -125 µm for SAL#2, c.f., SAL-positions in Figure 44) over several micrometer of the SALs, after it has reached a thickness of about 10 µm to increase the silica-to-background ratio.

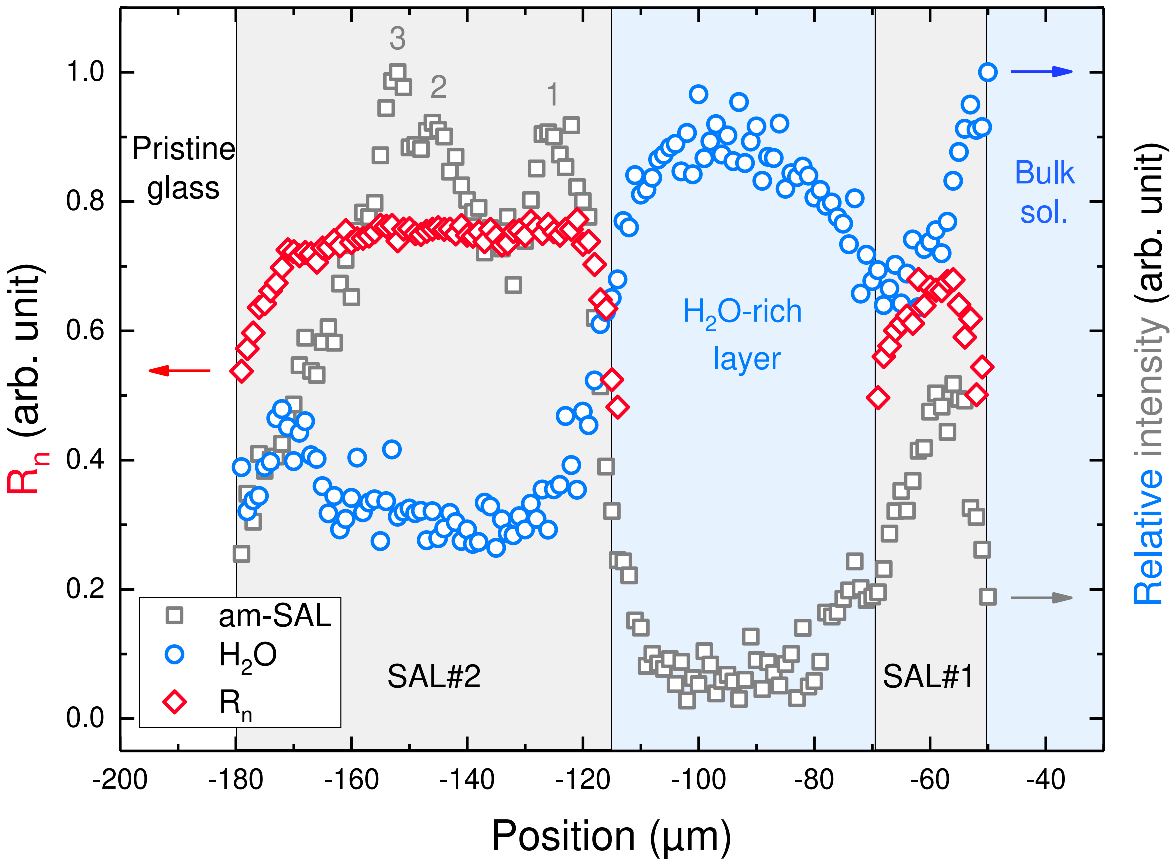

Figure 43: Spatially distributed relative signal intensity of the H_2O and silica signal of the final line scan after 474 hours, also presented as a false color bar in Figure 44 (Exp. II). Additionally, the structural parameter R_n is showed for the different SALs, revealing a slightly higher value for SAL#2, compared to SAL#1. The silica signal intensity shows that SAL#2 can be subdivided in minimum three sub-SALs (labeled with 1, 2, and 3). The H_2O and am-SAL signals clearly demonstrate a water layer between both main SALs. Location of am-SALs is indicated by the gray shaded background and the blue background represents the presence of aqueous solutions.

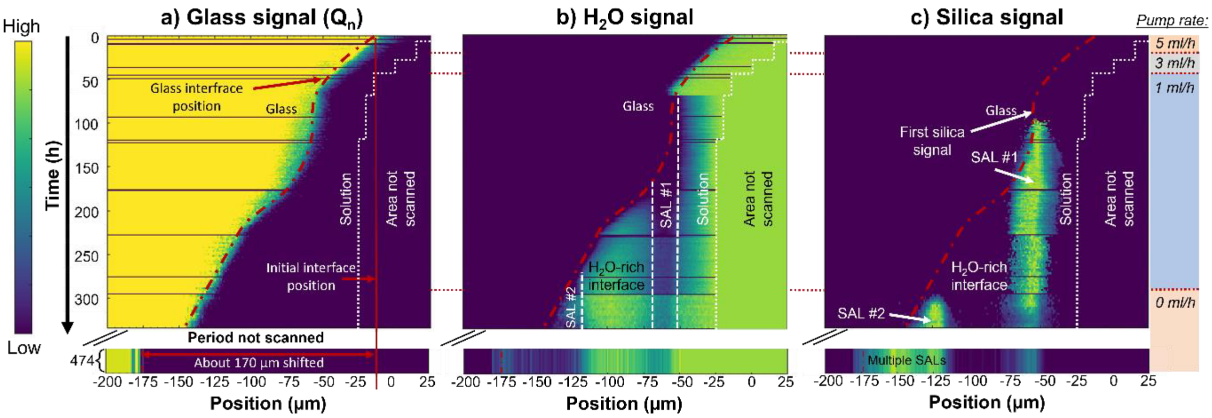

Figure 44: The temporospatial evolution of various Raman parameters during Exp. II with a ternary borosilicate glass (TBG) that was performed with different solution exchange rates, given in the panel at the right-hand side of the images. (a) The signal intensity of the Q_n species (1000 - 1250 cm^{-1}), marking the glass dissolution front. (b) Integrated Raman signal of water specific bands (3050 - 3750 cm^{-1}), showing the presence of porous, water-interpenetrated am-SALs and a H_2O-rich interjacent solution layer between SAL#1 and SAL#2. (c) Integrated Raman signals from amorphous silica (200 - 525 cm^{-1}), showing the formation of at least two distinct corrosion layers (SAL#1 and #2). Each pixel row in the upper part of the images represent a line scan. Only the bar at the bottom represents a single line scan that was acquired after 474 hours before the experiment was terminated.

To highlight the differences between both superordinate SALs, the R_n value of the am-SAL, reflecting the silica ring structure, and the intensity profiles of H_2O and amorphous silica are plotted in Figure 43 as a function of time, complementary to the spatiotemporal false color hyperspectral images (Figure 44). Here, the differentiation of SAL#2 by multiple sub-SALs is obvious and at least three different sub-SALs (labeled with 1, 2, and 3) can be identified. Neither the H_2O intensity distribution nor the structural parameter R_n allows a clear identification of the SAL#2 internal structure. The decrease of the R_n value at the interfaces is probably caused by the fact that the laser beam has very complex optical pathways in this transition zone and that the spatial resolution limitation of about 11 to 16 µm [45]. It can be assumed that the Raman signal at the interface is therefore a mixture of both, amorphous silica and the acjacent solution. The background of both phases was observed to be different in the frequency range used for R_n estimation. Even though water has no bands in this frequency range, the R_n value, which basically is an intensity ratio, can be determined in water as well, though it has no actual meaning and is background driven. Therefore, only R_n values of several micrometer thick SALs have been taken into account, in order to be able to exclude values close to the interface. This way, it can be ensured that the structural parameter R_n only reflects real time-dependent changes during corrosion

The results of ISG corrosion under acidic conditions (c.f., Chapter 7) indicated a correlation between the R_n of am-SALs and the solution pH. This seems very plausible, considering the strong influence of pH on condensation reactions of dissolved silica [108,109]. The effects of the pH value are manifold and, in addition to silica solubility, it also affects the rates of Si-O-Si hydrolysis. A main reason for the impact on silica condensation is that the pH determines the charge surface groups and MSA speciation. Depending on pH, temperature, and salinity, the negative surface charge of dissolved silica species and solid particles increases with the pH above the isoelectric point, which is at pH 2.0 for amorphous silica [135]. Increasing the negative charge also increases electrostatic repulsion, which is why under alkaline conditions the attachment and condensation of silica particles is more difficult. This is effect is used in sol-gel chemistry to create isometric spherical silica particles ranging from just a few nm to up to hundreds nm in diameter [108,109]. While slow growth by condensation of dissolved silica species is still possible, the large silica particles repel each other due to their high negative surface charge at high pH. As a result, aggregation or precipitation is avoided.

Getting back to the effect of pH changes on R_n value for Exp. II (Figure 42c), the bulk solution pH that is shown at the same time scale in Figure 42b, has to be considered. The R_n values were determined for the outer SAL#1 and the inner SAL#2 which formed subsequently. While SAL#1 formed during ongoing solution exchange (1 ml/h), SAL#2 formed after having turned off the pump to stop solution exchange. Then, as to be expected, the solution became more enriched in glass constituents by ongoing glass dissolution and the $pH_{21°C}$ rose significantly from about 8.5 up to 10. A higher pH should be reflected by a higher R_n value. Indeed, the final R_n value of the inner SAL#2 was higher, while the solution pH measured at the outlet of the fluid cell was higher as well for the same time period. The maximum R_n of SAL#2 measured before the experiment was terminated at 474 hours was 0.758 ± 0.009. After 210 hours, the maximum R_n of SAL#1 was 0.704 ± 0.012. However, it is also notable that the R_n value of the SAL#1 in Exp. II changes with time and an absolute increase of up to 0.08 can be observed, e.g., between 173 and 223 hours. The maxima coincide with the start of new Raman measurements at a lower z level, i.e., the laser was focused at a deeper spot in the fluid cell. This was necessary for further analysis of the interfaces in lateral direction, likely due to the simultaneous top side corrosion of the sample. On the one hand, the additional dependence of the R_n value with depth is problematic to unambiguously evaluate the R_n changes with time. On the other hand, the fact that R_n changes not only temporally, but also spatially is intriguing and highlights the control of local conditions of the interface solution chemistry on silica precipitation and growth. The different alteration kinetics and corrosion products at different locations of the glass coupon within the fluid cell possibly reflects the impact of local geometric constraints, temperature gradients, and possibly also the influence of stochastic effects, e.g., nucleation, hydrolyzation, and condensation. Although the course of the R_n of SAL#1 for Exp. II is not resilient on its own, the relative comparison with the R_n value from the SAL#2 is still useful, as both were acquired at the same depth. From this it can be concluded once more that a higher R_n value correlates with the solution pH during am-SAL formation, as the pH was higher while SAL#2 formed.

8.2.3 Surface alteration layers formed in a silica oversaturated solution

In the third TBG corrosion experiment performed at $pH_{85°C} = 9$, with a silica oversaturated solution and a constant solution exchange rate of 5 ml/h (Exp. III), multiple SALs were observed as well. The relatively low initial forward dissolution rate (c.f. Chapter 8.2.1) is a consequence of the high oversaturation which in turn reduces the affinity for hydrolysis of the silicate network [219], although the pH was higher than in Exp. II. In contrast to Exp. I and II the solution exchange rate was kept constant at 5 ml/h until the bulk solution was exchanged with D_2O after 240 hours. This was done to quantify the diffusion coefficient for D_2O within the SAL or at least test if water transport through the SAL was transport-limited. However, the evaluation of the D_2O/H_2O Raman bands showed that the equilibration between bulk and interface solution via transport through SALs was too fast to be recorded with the used acquisition parameters. At least it can be concluded that the apparent diffusion coefficient of water in the SAL was larger than $5 \cdot 10^{-13}$ m^2/s. At this time, after 8 ml of solution were exchanged, the pump was switched off for

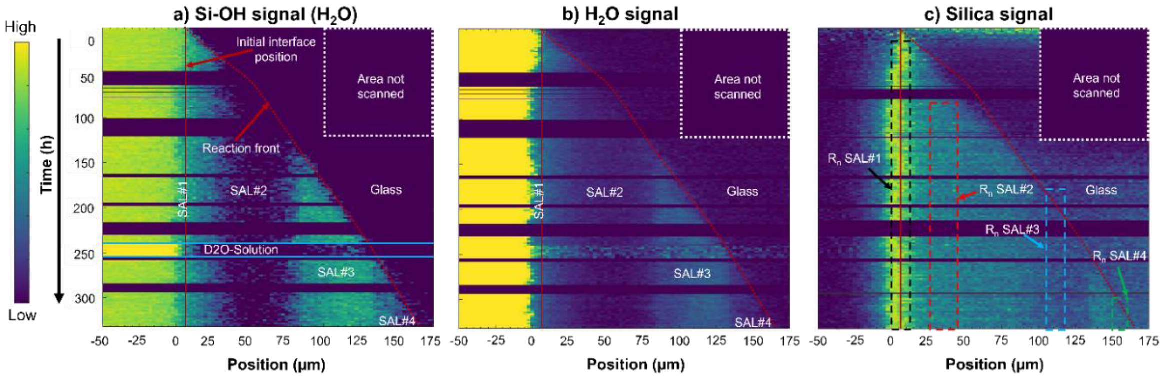

Figure 45: The temporospatial evolution of various Raman parameters with a ternary borosilicate glass (TBG) during Exp. III . The false-color images showing the time dependent and spatial distribution of **(a)** the fraction of Si-OH Bonds reflecting adsorbed water on the silica surface (integrated intensity ratio of spectral regions between 3500 - 3550 vs. 3050 - 3750 cm^{-1}), **(b)** the relative water concentration (specific spectral range was 3050 - 3750 cm^{-1}) revealing a H_2O-rich SAL#3, and **(c)** the silica signal (200 - 525 cm^{-1}) distribution that clearly allows a separation between the outer SAL#1 and the inner SAL#2. In this experiment, a regular solution exchange rate of 5 ml/h was applied and a silica-oversaturated solution with $pH_{85°C}$ 9 was used. After a D_2O-tracer was introduced after about 240 hours, the pump was switched of for 16.5 hours. This stagnant period is labeled with D_2O-Solution in (a) and also highlighted by a higher (more intense yellow color) signal intensity in the bulk solution. Subsequently, the pump was switched on again and a silica-free H_2O solution was exchanged continuously until termination of the experiment. The vertical red line represents the initial interface position. Gray areas were not imaged and the red dashed line represents the actual pristine glass interface. The dashed colored boxes in c) outline the regions from which the spectra were used to calculate the structural R_n.

16.5 hours to enable a diffusional equilibration between bulk and interface solution. Thereupon, the pump was switched on again (5 ml/h), but the exchange solution was free of Si from now on (adjusted $pH_{70°C}$ 9 by adding NaOH).

Furthermore, the H_2O signal contrast at the am-SAL/glass interface was low until 162 hours have passed, which is why there is a gap between both glass retreat datasets. Nevertheless, the glass retreat can be subdivided in two different kinetic regimes, with a linear retreat rate of 0.576 ± 0.002 µm/h that dropped abruptly to 0.410 ± 0.015 µm/h after 200 hours (Figure 46). The measured Raman data reveal an apparent final glass retreat of almost 140 µm after 332 hours. But a look on the time-position images in Figure 45 reveals that the kink around 275 hours in the glass retreat curve is probably an artifact of the data evaluation procedure. The glass continues to retreat until the end of the experiment, even if the SAL seems to has a different density, which is indicated by the varying signal intensities. The glass retreat data in Figure 46, however, suggests a still stand during the last 60 hours, but this is because the water signal intensity contrast between the SAL and glass became too low to distinguish them from each other by the automated data evaluation method used here. A continuous glass retreat can, however, be deduced from the spatiotemporal false color images by mere visual evaluation of (Figure 44, green dashed line).

The plot of Si – OH signal of adsorbed water in Figure 45a compared to the plot of the water intensities in Figure 45b shows that much more water is adsorbed to silica surfaces in SAL#1 and

SAL#3 than in SAL#2. Even if the total water concentration in SAL#1 is almost as low as in SAL#2, a bigger fraction of these molecules seems to be adsorbed instead of being mobile within the silica pores. This is indeed plausible, since the silica signal intensity from the outer SAL#1 is higher than from SAL#2, indicating a denser microstructure (Figure 45c). The denser a silica layer structure, the smaller the pores are and more water is adsorbed to silica surfaces compared to free water molecules. It is assumed that therefore the very high $Si-OH$ signal in the H_2O-rich SAL#2 indicates a silica colloid-based sol gel that is still highly hydrolyzed and porous, but rather a solid am-SAL. These results and the derived conclusions are in line with previous experimental studies of TBG [31,40,41].

It should be mentioned, however, that the overall Raman data quality was relatively poor in Exp. III, because there was a large distance between the sapphire window and the investigated sample already from the beginning, resulting in a worse spatial resolution and significantly lower overall Raman intensities. Nevertheless, this experiment and Exp.#2 are the first experiments in which the structural self-organization of a glass corrosion layer was observed *in situ* and *in operando*, which clearly confirms the suggestion that the self-organization process is part of the SAL formation process rather than a secondary, post-formation phenomenon [39]. These experiments further highlight how important it is to combine different analytical methods to derive to reliable conclusions. In this respect, analyzing the solution composition to estimate dissolution rates based on the release of glass constituents is useful for validation of local corrosion rates. Solution analyses were carried out for this purpose and the results are shown and discussed in the following section.

Interestingly, the pH value of the exchanged solution of Exp. III indicates that the absence of dissolved amorphous silica in the input solution has an influence on the final pH, even though the initial pH was quite similar. The initial solution pH of the silica-bearing solution was about 9.95 at 25 °C (9.00 at 83 °C). The observed temperature-dependent pH increase by cooling the silica-bearing solution is in good agreement with hydrogeochemical calculations, which suggests a pH of 9.87 at 25 °C. Analogously, the silica-free solution was adjusted to an initial pH of 8.69 at 83 °C, which corresponds to a calculated pH of 10.28 at 25°C. Here, the missing buffering capacity of dissolved siliceous acid becomes clear, which is why the temperature dependent pH difference is much higher for a solution that is free of dissolved MSA. The final pH of the bulk solution in the second part of the experiment with an initially silica-free bulk solution was observed to be much lower compared to the first experimental time period. This is in contradiction to the behavior during the first 240 hours of the experiment, during which the pH of the silica oversaturated solution increased from about 9.95 to 10.26 ± 0.06 at 21 °C, based on the pH values between 15 and 240 hours. Here, the initial rise of the pH is a result of the release of alkaline sodium oxide components of the glass. However, for the second D_2O solution an average value of about

9.28 ± 0.16 was measured at 21 °C. Concerning the solution exchange of H_2O solutions with D_2O solutions, its necessary to mention the different response of H^+ and D^+ ions to pH electrodes. This observation reflects the different ion products K_w of light (pK_w^H= 13.995) and heavy (pK_w^D = 14.951) water, which in turn results in a systematically higher pD value compared to pH [231]. However, this discrepancy alone cannot be explained by this effect, because the measured pH of the D_2O solution was higher compared to the H_2O solution. However, this may influence the solubilities at the reaction interfaces if the pH/pD differences are not considered when the corrosion solution is exchanged.

To explain the pH drop, it helps to have a look on the hyperspectral images in Figure 45, which show that there are also increasing silica and decreasing H_2O signal intensities from the SAL formed during this period, suggesting that under these conditions a much denser SAL has formed. Consequently, the transport properties of the SAL change and less dissolved glass constituents could be released from the reaction front into the bulk solution. More Na and a higher solution pH of the interface solution ahead the SAL#4 is expected, so indeed observed in another *in situ* fluid-cell Raman study [29]. It remains unclear whether the stagnant period of 16.5 hours after D_2O exchange (marked in Figure 46b) or the different exchange solution chemistry was the reason for the formation of another am-SAL with individual properties. In any case, the observations demonstrate how sensitive the system is, especially at the reaction front, to changes in the bulk solution chemistry, even in such chemically relatively simple system.

But even if transport of glass constituents from the reaction front into the continuously exchanging bulk solution is impeded, which in turn explains why the pH has not increased, the question remains, why did the pH decrease in the first place? A plausible explanation is given by the solution compositional data, especially by the released amount of B (c.f., Table S 2). The fact that almost the same amount of B is released into the solution after switching the exchanging solution from Si-oversaturated to an Si-free solution confirms ongoing glass matrix dissolution. Also, B may affect the solution pH and its dissolution, more precisely the B_2O_3 part of TBG. The pH depending speciation can be summarized by the following reactions:

$$B_2O_3 + \; 3H_2O \rightarrow 2B(OH)_3 \qquad \text{(XXIV)}$$

$$B(OH)_3 + OH^- \rightarrow B(OH)_4^- \qquad \text{(XXV)}$$

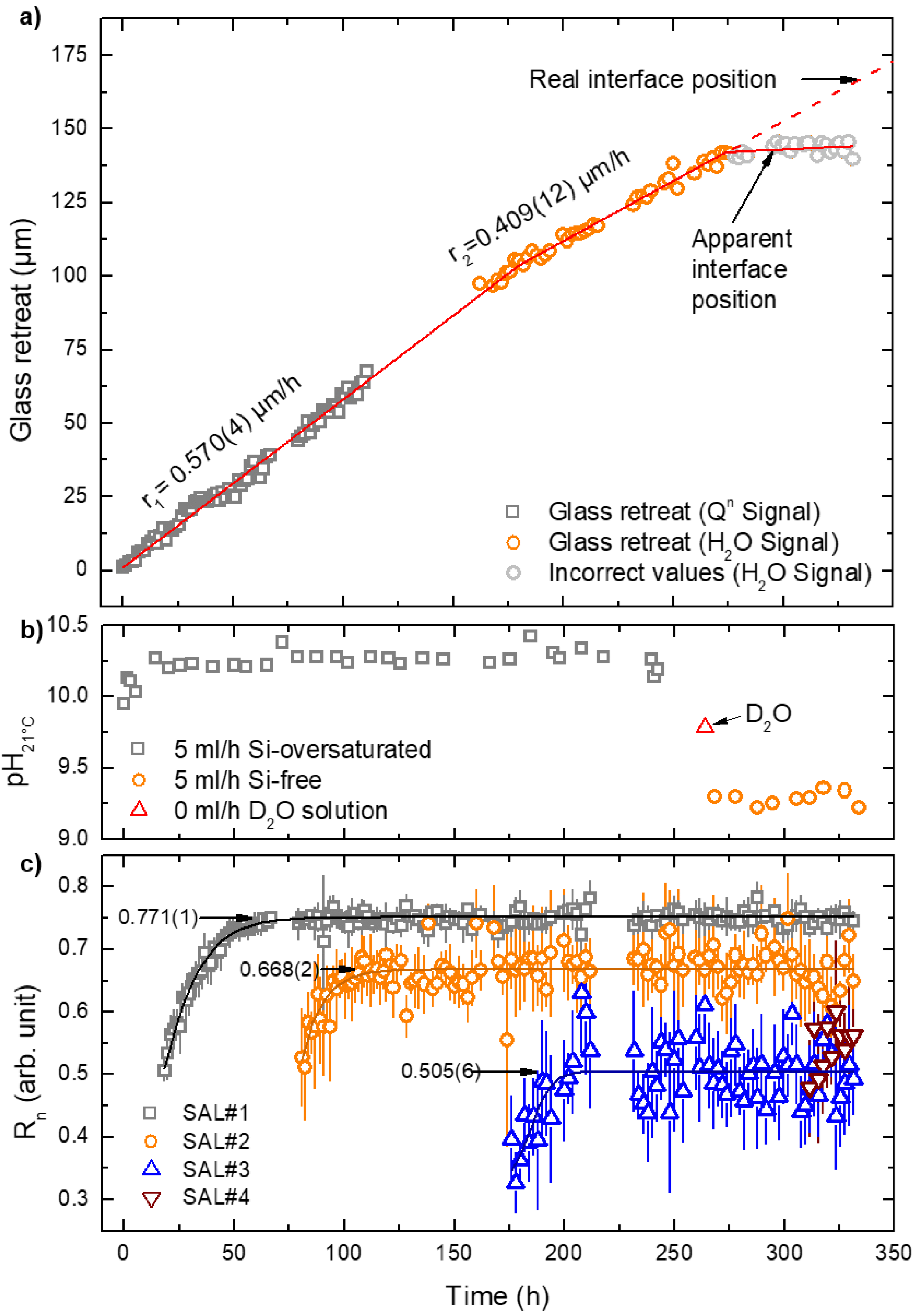
a)
Glass retreat (µm)
0
25
50
75
100
125
150
175
Real interface position
r_1= 0.570(4) µm/h
r_2=0.409(12) µm/h
Apparent interface position
□ Glass retreat (Q^n Signal)
○ Glass retreat (H_2O Signal)
○ Incorrect values (H_2O Signal)
b)
$pH_{21°C}$
9.0
9.5
10.0
10.5
D_2O
□ 5 ml/h Si-oversaturated
○ 5 ml/h Si-free
△ 0 ml/h D_2O solution
c)
R_n (arb. unit)
0.3
0.4
0.5
0.6
0.7
0.8
0.771(1)
0.668(2)
0.505(6)
□ SAL#1
○ SAL#2
△ SAL#3
▽ SAL#4
0
50
100
150
200
250
300
350
Time (h)

Figure 46 (see previous page): **(a)** Glass retreat of TBG as a function of time based on the intensity distribution of glass specific Q_n species (gray symbols) and the H_2O signal (orange symbols) (Exp. III). For the glass retreat versus time plot the H_2O signal was used for the second half of the experiment to determine the glass interface position, because the signal intensity of the Q^n species was too low at late reaction stage. Nevertheless, the Q^n species were used as long as possible to determine the glass retreat until the use of intensity of the water-specific Raman bands yielded statistically better results. The apparent glass retreat stagnation at the end of the experiment does not correspond to the actual interface position and thus to the glass retreat, because of a low signal intensity contrast, and is thus an artefact of the automated fitting routine. **(b)** Solution pH of the exchanged bulk solution for some samples as a function of time. **(c)** The structural parameter R_n of the am-SAL, calculated based on the *in situ* Raman data, plotted for all four am-SALs as a function of time. The data of SAL#1, SAL#2, and SAL#3 were fitted by a sigmoidal function to determine the saturation level of the R_n value for each layer (R^2= 0.900 for SAL#1, R^2= 0.270 for SAL#2, R^2= 0.530 for SAL#3).

Based on these equilibria, the pH drop could be a result of ongoing glass dissolution, including the boron oxide components, and the transformation of boric acid to dissolved boron anions under consumption of hydroxyl molecules. The reason why this effect does not occur in the Si oversaturated solution may be due to a dominating buffering effect of the large amounts of dissolved MSA. Another reason may be the selective release of dissolved glass constituents into bulk solution. As indicated by the Raman data, a denser SAL has formed when a Si-free solution is pumped through the fluid cell. This in turn leads to selective transport of mobile B from the reaction front into the bulk solution, because it is assumed to be not incorporated into the SAL in most cases due to its high solubility [158]. At the same time, transport of dissolved Si species, especially of larger oligomers, may be hindered due to steric limitations in a denser SAL structure [36] and the affinity of condensation onto reactive Si-O surface groups of the am-SAL. A higher amount of dissolved and precipitated silica also binds more alkali metals, i.e., Na, at their surface for charge balance. This in turn also retains the alkali release from interface into bulk solution. Because a charge balance in the solution between $OH^-$and Na^+ can be assumed to be required [48], this proportionality may also be a reason for the pH difference.

Looking at the R_n values of Exp. III (Figure 46c), the different pH values of the leaching solutions measured at 21 °C, i.e., 10.26 ± 0.06 for the silica oversaturated and 9.28 ± 0.16 for the silica-free solution, might be misleading. At the reaction temperature of about 85 °C this pH difference will be adjusted by the stronger temperature dependent pH change of the silica free solution, which has its cause in the missing MSA buffering effect. However, there is a difference between the R_n values of the different am-SALs. Specifically, the R_n values of SAL#1, SAL#2, and SAL#3 are 0.771 ± 0.01, 0.668 ± 0.02, and 0.505± 0.06, respectively. Based on all the experiments shown in this study and in additional reference studies using the same glass [29–31,41], it can be concluded that the pH significantly influences the R_n and the silica structure. In contrast, the changes of the salinity, MSA concentration, and pH buffer capacity had no discernible effect on the structural parameters of the amorphous silica layers after they had formed and the R_n value plateaued. Nevertheless, the changing solution chemistry at the SAL/glass interface led to formation of the third am-SAL (SAL#3), which continued replacing the glass. Although some R_n values are plotted for the SAL#4 as well, the plateau could not be established and a final R_n estimation was not possible based on the small amount of data. In general, due to the overall bad Raman signal at the end of the experiment these values should be interpreted with caution. Low Raman signal intensity and contrasts was also the reason for the evaluation artifact in the glass retreat curve (Figure 46a), that indicated an apparent stagnation during the last ~60 hours. Although the pH at the outlet was observed to change slightly, it still remained alkaline. However, the pH at the reaction front may differ from bulk solution pH. This may be reflected by the generally inwardly decreasing R_n values of the various am-SALs identified in Exp. III. Once the outer SAL was established and increased in thickness, the coupled glass dissolution and silica precipitation reactions at the glass surface probably became (partly) decoupled from the bulk solution chemistry, so observed also in previous *in situ* fluid-cell Raman studies [29,41]. The transport-limiting properties and species-dependent filtering due to the porous structure of the corrosion products are likely responsible for this observation and may have also impacted the bulk solution pH. It can be concluded that of the reactions taken place here seems to act acidifying, at least for the pH at the reaction front. This was also observed in previous studies under strong alkaline conditions [45] and is in line with the lowered bulk pH at the outlet and the decreasing R_n value of am-SALs formed at a later stage.

8.2.4 *Post mortem* analysis of the altered glass samples

For validation of the *in situ* Raman data and visualization of the am-SALs, several BSE images of the embedded and polished sample of Exp. II and Exp. III were made (Figure 47). A finely stratified microstructure of the corrosion layers can be observed, which agrees with the results of conventional experiments with the same glass [39]. This confirms the assumption that the am-SAL Raman signal intensity variations (c.f., Figure 44 and Figure 43) reflecting density variations or distinct layers within the superordinate am-SALs. (e.g., SAL#1 and SAL#2 in Exp. II) However, due to the limitation of the spatial resolution such fine layers cannot be differentiated clearly in the hyperspectral images. Nevertheless, combining the *in situ* Raman data with *post mortem* characterization by SEM imaging complement each other and allows a more accurate interpretation of the Raman data. It should be mentioned that the gap between SAL#1 and SAL#2 in Figure 47a is much thinner compared to the values measured *in operando*, which is probably due to the shrinking of the SALs, caused by drying before it was embedded into epoxy resin. The observed thickness of the outer SAL#1 was 22 ± 2 µm, according to several SEM line measurements, which agrees very well with the thickness of 20 ± 2 µm derived from *in situ* Raman data, whereas the second SAL#2 was observed to be much thinner in the BSE image of the cross sectioned sample, i.e., the thickness *post mortem* was only half the size, i.e., 24 ± 3 µm, than estimated from the *in situ* Raman data (~ 50 µm). This can be explained by the observation of several alternating silica and interface fluid layers building up SAL#2. Consequently, the thickness difference is explained by the smaller fraction of solid silica, respectively by the higher fraction of water layers, which are no longer present after drying the sample. Additionally, it should me mentioned that the region displayed here was at the edge of the sample that was in contact with the PTFE sample holder, whereas the *in situ* Raman data were acquired at another part of the TBG sample that was freely exposed to the bulk solution. As demonstrated in the previous chapter, such local geometric conditions also affect the corrosion behavior and product phases. The BSE images of Exp. III also show a complex multiple am-SAL structure (Figure 47) and interestingly, an entirely different microstructure was observed on both sides of the cross-sectioned glass cuboid. Simultaneously, laminar and wavy SALs formed in one single experiment, as clearly seen by comparison of Figure 47c and Figure 47d. The four distinct am-SALs in Figure 47d can be assigned to the four consecutive am-SALs identified already *in operando* (c.f., Figure 45). Unfortunately, the opposite glass surface, *post mortem* image in Figure 47c, was not measured during the *in situ* experiment. However, at least three distinct SALs can be observed.

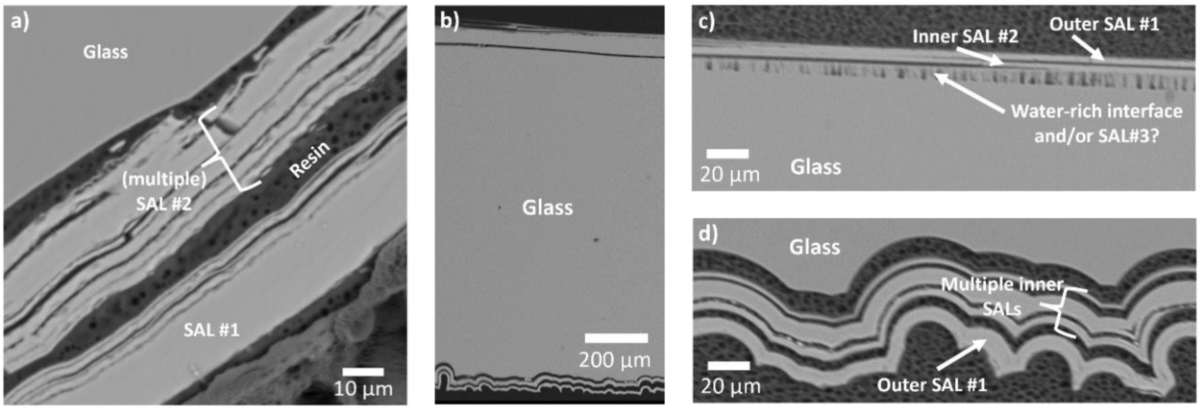

Figure 47: Backscattered electron images of a cross sectioned glass sample (TBG) of Exp. II and Exp. III after alteration. All images reveal multiple SALs and their different characteristics. The sample in **(a)** was corroded for 474 hours at $pH_{85°C}$ = 7 (adjusted by adding small amounts of NaOH) under varying solution exchange rates at the beginning and stagnant conditions at the end of the experiment (Exp. II). In **(b)** the entire cross section of TBG is shown, which was altered in a silica oversaturated solution at $pH_{85°C}$ 9 (Exp. III). In **(c)** and **(d)** the very different corrosion layers of the two sides of the glass sample (b) are enlarged and show simultaneously formed laminar and wavy layers in a single experiment.

8.2.5 Comparison of altered glass fraction based on Raman and solution composition data

Beside post mortem analysis of the corroded glass samples, the collected bulk solution at the outlet value of the fluid cell was also analyzed by ICP-MS. To compare bulk solution analysis and *in situ* Raman data, the altered glass fraction (f_{AG}) was calculated based on B concentration data, listed in Table S 1 and Table S 2. The f_{AG} was calculated according to Equation (36) that is quite similar to Equation (33), but modified by an additional summation term to account for the flow through conditions.

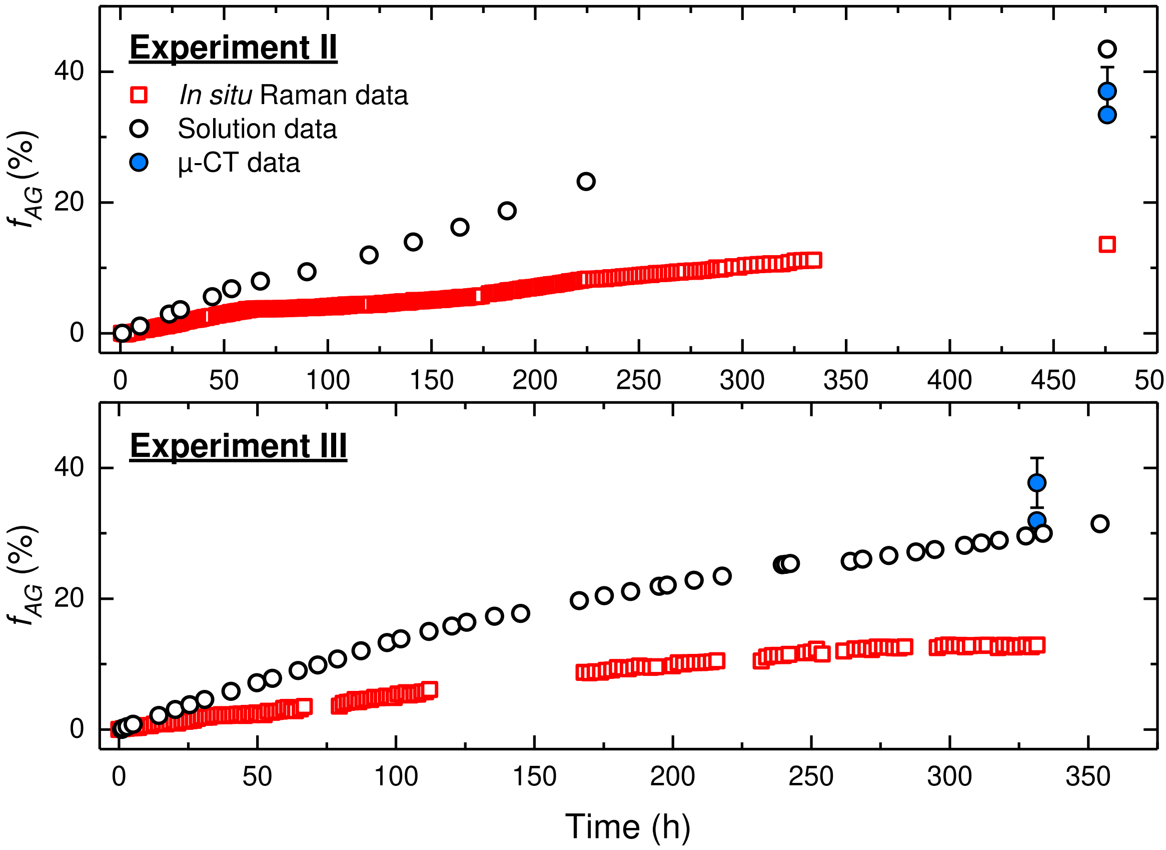

Figure 48: Comparison of estimated altered glass fractions f_{AG} of TBG at a constant fluid exchange rate for Exp. II (top) and Exp. III (bottom), based on *in situ* Raman data and bulk solution composition analysis. The solution based f_{AG} was calculated according to Equation (36) and the Raman data based f_{AG} was calculated by assuming the locally measured glass retreat rate to be equal for the whole surface of the glass cuboid and using the measured geometric dimensions of the glass sample at the beginning.

$$f_{AG}(\%) = \frac{\sum_{t=1}^{n}(C(\mathrm{B})_t - C(\mathrm{B})_{ini}) \times V}{m \times x_B} \times 100\ (\%) \qquad (36)$$

where $C(\mathrm{B})_t$ is the concentration of B at time t of sample n, $C(\mathrm{B})_{ini}$ the initial boron concentration that was almost zero, V the solution volume of the fluid-cell (about 4.75 ml), m the initial mass of the glass sample (0.195 ± 0.001 g for Exp. II and 0.216 ± 0.001 g for Exp. III), and x_B the mass fraction of B (0.06926) in TBG.

For comparison, these values are plotted in Figure 48 with the $f_{AG_{Raman}}$ based on glass retreat (c.f., Chapter 5.1.6.4) for both, Exp. II and Exp. III. In general, the estimated f_{AG} based on different methods differ significantly from each other and obviously it is not possible to extrapolate the glass retreat rate measured by *in situ* Raman spectroscopy to the entire sample. The overall corroded volume fraction of the glass based on solution data was found to be about more than three times higher than expected from the retreat data. To validate the solution data, both samples were scanned with a SkyScan 1272 desktop µCT device of Brucker microCT (c.f., Chapter 5.5) and the residual glass volume was estimated to determine the bulk volume fraction

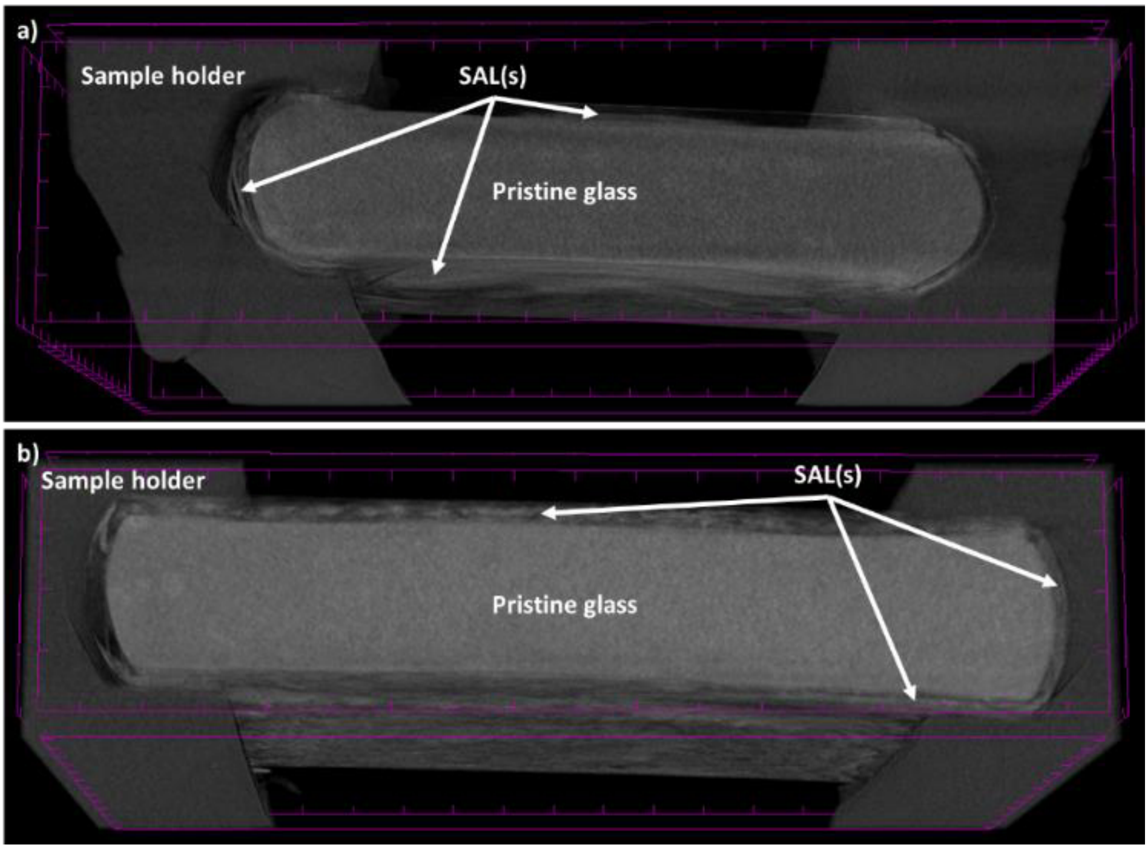

Figure 49: Micro-computed tomography (µCT) images of altered TBG samples of **(a)** Exp. II and **(b)** Exp. III that were dried and measured in the PTFE sample holder of the fluid-cell to avoid any damage of the am-SALs.

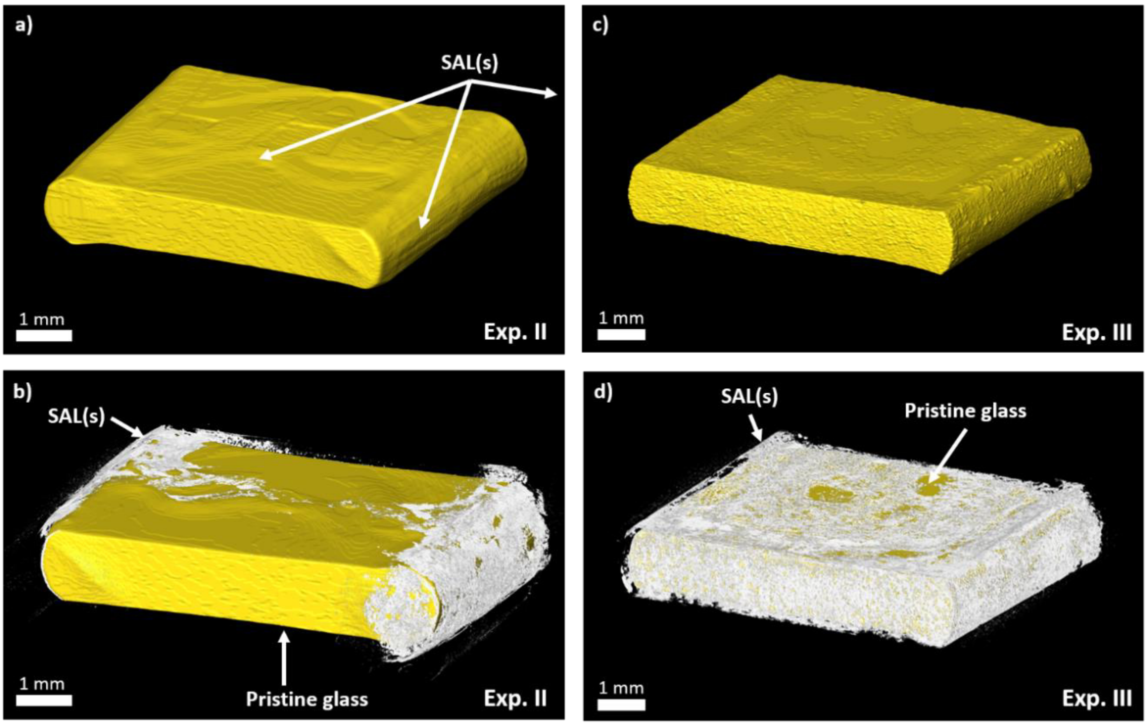

Figure 50: Micro-computed tomography (µCT) images of altered glass (TBG) samples of **(a,b)** Exp. II and **(c,d)** Exp. III. The residual pristine glass volume and SALs is shown in yellow and white, respectively. The volumes of (a) and (c) were used for residual glass volume estimation.

that was corroded in two different ways. For the first approach, twenty manual line measurements (point-by-point) were averaged to determine the sample dimensions of the pristine glass cuboid and the outer am-SAL surface, which yielded a within the errors identical corroded glass volume of 38 ± 4 and 37 ± 4 % for Exp. II and III, respectively. The second approach was based on a more complex analysis of the data via preparation, segmentation, visualization (Figure 50), and volume determination of the resulting voxel size dimensions (c.f., Chapter 5.5). The approach yielded lower values for f_{AG}, i.e., 31.9 ± 0.6 % for Exp. II and 33.4 ± 0.7 % for Exp. III.

These values are more or less in line with the f_{AG} that was calculated from solution data, confirming the deviation of locally determined corrosion from bulk corrosion rates. A comprehensive volume analysis of the µCT images would have been desirable, but was not possible due to the low contrast between the pristine glass and the am-SALs and the lack of a scan that was made before the experiment (c.f., Kral et al. [232]).

8.2.6 Further notes on the corrosion mechanism

The results of all the three experiments discussed in this chapter are fully in support of an ICDP mechanism. They revealed the stoichiometric dissolution of TBG. The glass dissolution kinetics were observed to depend on solution pH, pump rate, solution composition, and especially on the silica saturation level. While the impact of solution pH on the glass forward dissolution rate is well investigated for even more complex glasses [17,19,63], a direct feedback of the released glass constituent on the solution pH is usually not discussed. On the one hand, the glass dissolution and interdiffusion reactions act alkalinizing due to the consumption of hydronium by hydrolyzation reactions. On the other hand, precipitation and condensation reactions on the molecular level can reduce the pH, especially locally, e.g., within confined interface fluid layers that arise when am-SALs are formed. Because of the spatial decoupling of the bulk and the interface solution by the growing SAL, the pH of both solutions is not in equilibrium, which affects the glass corrosion process in different ways. Once amorphous silica starts to cover the glass surface, the bulk solution and the solution at the reaction front start to become separated by the growing am-SAL. Thus, both further glass alteration and silica precipitation reactions are highly dependent on the am-SAL thickness, density, and microstructure, which in turn determines its transport properties.

The results of Exp. II and Exp III indicate that maturation of the am-SAL occurs, which is evident from the time- and spatial dependent change in the structural parameter R_n for amorphous silica (Figure 42c and Figure 46c). Such a maturation of am-SALs may change its transport properties and, in turn, may affect further corrosion.

In Figure 51 (left side) the different processes observed in Exp. II are schematically displayed, including the information about the solution exchange rate. At the beginning the glass dissolved stoichiometrically and the solution was kept undersaturated with respect to amorphous silica due to the high solution exchange rate (Figure 51a, Exp. II). After lowering the pump rate to 1 ml/h (Figure 51b, Exp. II), the enrichment of glass constituents and the reduced convective motion allowed the precipitation of silica at the glass surface. At this stage, the retreat rate was reduced for a transitional period, because the precipitated silica likely covered a lot of the $Si-O$ surface sites of the glass, until the underlying glass dissolved in significant amounts and a gap had formed between the pristine glass and the SAL#1. Despite ongoing silica precipitation on the inner side of the SAL#1, the lower molar volume of the SAL compared to the glass resulted in the formation of a gap at the reaction interface and porosity in the am-SAL.

Interestingly, the SAL#1 layer ceased growing after having reached a thickness of about 20 µm, which is in the same order of magnitude as observed in another experiment under stagnant conditions with the same glass [29]. However, the glass dissolution continued and a large gap formed between the SAL#1 and the glass (Figure 51c, Exp. II). Apparently, the interface solution properties and the continuous removal of silicic acid from bulk solution suppressed silica precipitation at this stage. This steady state between silica supply by ongoing dissolution and removal by solution exchange was disturbed by inducing stagnant conditions, which again enabled SiO_2 oversaturation and silica precipitation at the glass surface (Figure 51d, Exp. II).

Observation of two distinct SALs and fine-scale multiple internal layering observed *post mortem* in BSE (Figure 47) as well as *in situ* by Raman spectroscopy (Figure 44) suggests a complex self-organization process. As already explained previously (c.f., Chapter 5.7), the am-SAL structure depends on the local chemical conditions at a certain point in time. The feedback of dissolution and precipitation reactions on the solution chemistry, in turn, affects the further course of corrosion. Such multiple, separated layers of amorphous silica were already observed in naturally and artificially corroded glasses, as shown in Chapter 2.1.1. They were commonly attributed to drying and shrinking effects, but it has also been suggested that they form by the corrosion process itself [35,36,39]. However, our *in operando* results prove (c.f., silica signal fluctuations in Figure 43), for the first time, that such patterns can indeed form in the course of the replacement process. The observation that amorphous silica precipitated onto the glass surface and not onto the already formed first SAL#1 further demonstrates the importance of local conditions at the glass surface for am-SAL formation and that even small distances can result in spatial decoupling of dissolution and precipitation reactions at SAL#1.

Despite the fact that the initial solution pH in Exp. III was higher compared to Exp. II, the formation of the SAL#1 was initiated in an initially silica-oversaturated solution immediately after the start of the experiment, even at high pump rates of 5 ml/h (Figure 51a, Exp. III). It can be assumed that most of the Si that has been incorporated in the outer SAL originates from the solution, since little glass has been dissolved at this stage. This is basically supported by silicon isotope tracer experiments which have indicated that the silica formed initially incorporates significant amounts of Si from solution if present in solution [36,94]. Once the glass surface was covered by a silica layer, the transport of solution MSA to the reaction front was inhibited with increasing thickness and density of the outer SAL#1. The filtering properties of the corrosion layers covering the glass are strongly depending on the local physicochemical conditions, which are partly determined by the chemical composition of both glass and solution.

In contrast to a pure affinity-driven dissolution reaction, a silica-oversaturated bulk solution does not prevent the metastable glass to dissolve. Dissolution and release of glass constituents including dissolved SiO_2 unambiguously occurred in Exp. III and the generated MSA reprecipitated together with MSA originating from solution at the inner side of the outer SAL#1 (Figure 51b, Exp. III). The thicker the SAL#1 became, the lower the incorporated proportion of material that was already dissolved from the beginning, since transport of MSA from bulk solution to the reaction front became more and more restricted. That led to the formation of SAL#2 adjacent to SAL#1, whose structure is clearly different (c.f., Figure 46c) and whose MSA has probably a different origin (Figure 51c, Exp. III). This has already been discussed in Chapter 3.2.7 and is in line with results from isotope tracer experiments, where different silicon isotopes were present in the glass sample and the initial corrosion solution. Some studies revealed a strong difference in isotopic composition of the outermost SAL compared to the rest of the SAL [20,34,56,94,105].

However, it can be concluded that the am-SAL structure is probably not directly related to the origin of Si, but depends more on other parameters such pH, Si concentration, and salinity, which all have an influence on the silica micro-structure during its formation [108]. The interface and bulk solution are probably partly decoupled by the transport limitations imposed by the growing am-SAL so that with increasing thickness of the am-SAL the interface solution may become more and more highly saline and oversaturated [29,36]. This shift of the interface solution away from equilibrium with the bulk solution is a key prerequisite for the self-organization process. At this time, a water-rich silica layer establishes in the interface solution layer that is equivalent to a sol gel (Figure 51d, Exp. III). This is in line with the observed combination of high water and silica signals in the hyperspectral images discussed in Chapter 8.2.3. Interestingly, switching the continuously exchanging solution from a silica-oversaturated to a silica-free solution changed the course of alteration and again a less hydrous silica layer formed that completes the sequence of SAL#1, SAL#2, a water-rich SAL#3, and another SAL#4, whose structure appears to be similar to that of SAL#2 (Figure 51e, Exp. III). The effect of changing the bulk solution on the structure of silica that forms at a certain time at the reaction front implies a coupling between both solutions, even if the transport of aqueous silica species through the am-SALs is impeded. It remains unclear whether the slightly different pH and missing buffer capacity in the silica free solution or the lower salinity are crucial for this feedback. In fact, a combination of all these is also conceivable and can potentially be proven in future studies by, e.g., *in situ* pH measurements and/or the use of isotope tracers. Both experiments, in which a corrosion layers were formed, impressively demonstrate that multiple am-SALs are a real glass corrosion feature that arises *in operando* and is thus an important feature of the corrosion process. It, however, has not yet been considered in any of the currently proposed corrosion models.

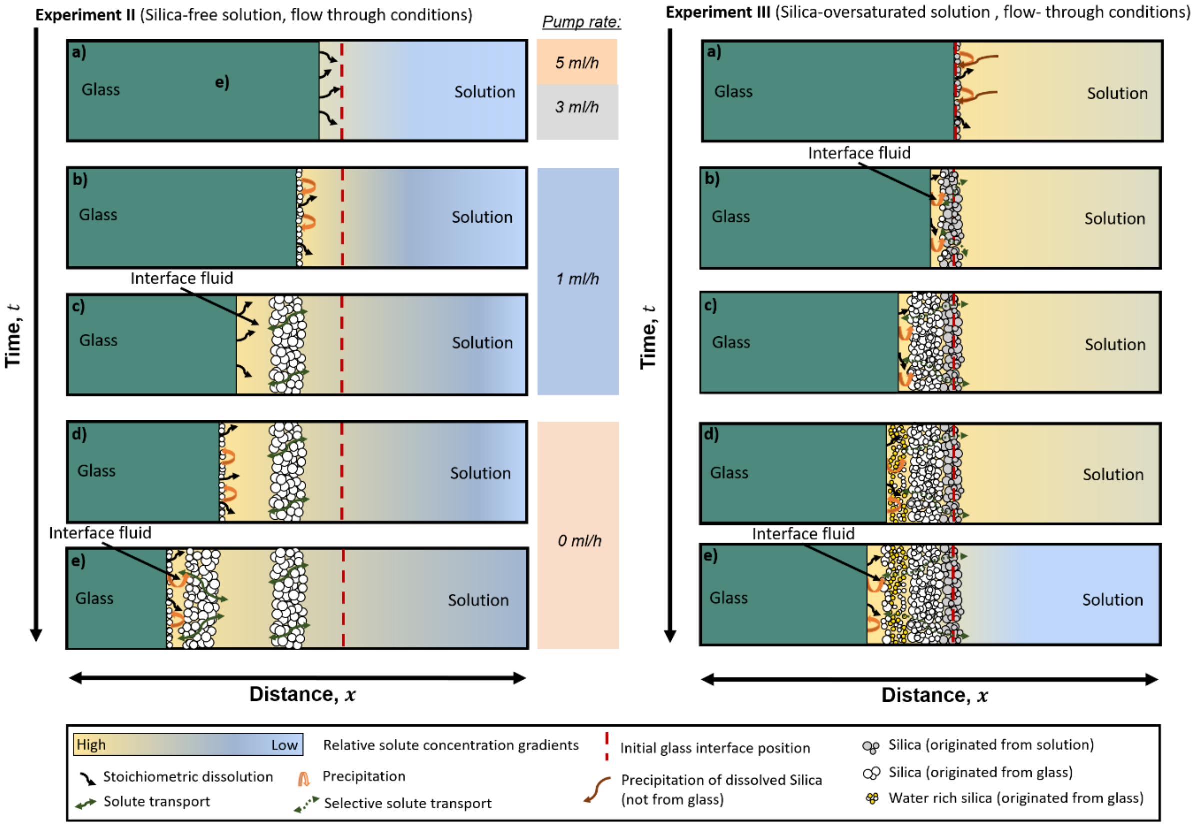

Figure 51: Simplified mechanistic sketches of the individual glass corrosion process, observed at different solution exchange rates in Exp. II (left) and under stagnant conditions in Exp. III (right).

8.3 Conclusion

The results of the three different experiments presented in this chapter demonstrated the opportunities of using *in situ* fluid-cell Raman spectroscopy to *in operando* study glass alteration not only under stagnant but also under dynamic conditions. Many information about the formation kinetics of am-SALs, their molecular structure and transport properties, the glass dissolution kinetics, and the interdependence of glass dissolution rates and solution exchange rates can be gathered by just one experiment. The experiments also showed that the solution composition has a great impact on the glass corrosion behavior of TBG, as indicated by different observations although the glass composition, the temperature, and the pump rates were the same. Exp. I clearly revealed an increasing solution pH with increasing mean residence time of the leaching solution in the reaction cell. A higher residence time is equivalent to a reduced solution exchange rate which was observed to go along with lower forward dissolution rates. It was concluded that the retreat rate decreasing silica affinity affect dominates the rate increasing pH rise for this experiment. Another experiment without a buffering agent (Exp. II) did not show such a clear interdependence between solution exchange rate and glass retreat. Furthermore, the forward dissolution rate in an unbuffered solution was lower, even if the solution was initially silica-free. It can be concluded that borate and bicarbonate ions may catalyze the dissolution reactions by complexation of silicon surface sites, similar to hydroxyls. Such buffer-enhanced corrosion rates were already observed by using organic buffers, such as TRIS [75]. In order to resolve the influence of buffers on glass alteration, more spatially resolved experiments with isotope tracers and *in situ* pH measurements are required.

The Raman data of the Exp. II and Exp. III clearly reveal that multiple am-SALs are not just a quenching and drying feature, but are an integral part of the glass corrosion process. In both experiments the formation of distinct am-SALs and solution layers was observed *in operando*, i.e., without stopping the experiment and quenching the sample. The spatial variation of the structural R_n, parameter of precipitated amorphous silica was found to be a useful parameter for distinguishing differently structured am-SALs.

It was observed that the glass retreat and solution exchange can establish a steady state, where glass dissolution and solute removal continued but silica precipitation stopped, until the steady state was disturbed by stopping the solution exchange. Furthermore, the local solution chemistry at the glass surface seems to be crucial for the amorphous silica precipitation, because the second am-SAL (SAL#2) precipitated at the glass surface instead of growing on the already existing SAL#1, which was just about 60 µm away.

Comparison of the altered glass fraction (f_{AG}) based on data from solution analysis, from Raman data, and from µ-CT scans showed that large difference can exist between *in situ* determined corrosion rates and those that are derived from bulk solution chemistry or whole glass sample analysis. Therefore, to fully understand the glass corrosion features on different length scales, it is recommended to combine *in situ* fluid-cell Raman spectroscopy with complementary solution analyses and investigations of the corroded glass with SEM, µ-CT, and nano-analytical techniques such as transmission electron microscopy, nano-scale secondary ion mass spectrometry, and/or atom probe tomography.

The presented results cannot be explained by the classical glass corrosion models that are based on ID reactions and *in situ* reconstruction without complete glass matrix dissolution. Rather, they confirm the notion of an ICDP process for am-SAL formation that is also a well-established alteration mechanism responsible for numerous mineral replacement reactions [110]. This mechanistic model is capable to explain all observations made in this and other studies, including multiple am-SALs, interstitial fluid layers, and the structural differences of the alteration layers that are determined by the specific local solution properties at the reaction front.

9

Implications for upcoming numerical aqueous glass corrosion models

9.1 Existing approaches for ICDP modeling and limitations of pore scale models

The aim of this chapter is, to suggest implications for upcoming numerical models for simulation of aqueous silicate glass corrosion, because they are important for i) the customized development of a selection of glass types for technical applications and glassware, and for ii) the prediction of long-term stability of nuclear waste glasses, as it represents the first barrier for a large fraction of HLW. Numerical models are useful to confirm the validity of any mechanistic corrosion model and quantitative experiments. Therefore, based on the implications, an approach for modeling glass corrosion by a simple reactive transport code is presented for TBG corrosion in pure water at 85 °C as a preliminary modelling approach.

The proposed approach is based on just a few, but pivotal processes, whose coupling may lead to a self-organized formation of multiple layered SALs. Such a numerical model should be able to capture the SAL formation process including the reviewed corrosion features (Chapter 2.1) and the corrosion kinetics (Chapter 2.3). These observations and the results of the three case studies presented above cannot be explained by classical glass corrosion models that are based on interdiffusion (ID) reactions and *in situ* reconstruction. A stoichiometric glass dissolution that is spatially and temporally coupled to precipitation of corrosion products is basically able to explain all so far observed corrosion features, as demonstrated for all observations made in the presented case studies. Most of the basic ideas of the model can be partly found in some other, already existing models for long-term glass corrosion, reviewed in Chapter 3.3, and the basic mechanism has also been proven for numerous mineral replacement reactions [110]. An interface solution layer at the reaction front in combination with locally thermodynamic (quasi)equilibria and the accompanying spatial coupling of reactions are crucial [29,35,36]. It follows that a realistic model for silicate glass corrosion in aqueous solutions by an ICDP process should consider the following aspects and subprocesses, respectively:

i) The local solution chemistry, especially of the
ii) interface solution between the SAL and the underlying glass,
iii) stoichiometric glass dissolution that is coupled to the
iv) precipitation of amorphous and/or crystalline secondary phases forming the SAL, and
v) (transient), species depending transport properties through the bulk solution and SAL.

To model the broad variety of possible SALs observed in naturally and experimentally corroded glass samples, especially the chemical and structural patterns (c.f., Chapter 2.1.1), the local environmental conditions at a given time have to be considered, as it determines the type of SAL that will form. The specific microstructure and porosity, surface charge, and composition affect the transport though the SAL and thus the composition of the interface, pore, and bulk solution. Consequently, the glass corrosion rate is the result of such interdependent reactions and their feedbacks. A promising model which could potentially decipher that is the KμC model [146,157] (c.f., Chapter 3.3.3.2), where the rate limiting process may change with reaction progress, which in turn is reflected by the structurally and chemically patterned SAL.

Such geochemical reactive transport models with a spatial resolution on μm scale are promising for modelling SAL formation in the same spatial resolution as that of the *in situ* Raman images. However, a realistic model also needs to incorporate a valid thermodynamic description and the corresponding thermodynamic data for relevant phases making up the (am)-SALs. Such an approach exists for example in the GRAAL model [21,99] (c.f., Chapter 3.3.3.1), although thermodynamic and kinetic data for metastable SAL-phases are difficult to determine.

Reactive transport codes are also used to model other solid-fluid reactions, especially ICDP reactions, for mineral alteration in natural environments [233,234]. They are able to describe complex interactions and kinetics of dissolution, precipitation, and transport via diffusion or convective flow. However, description of ICDP reactions, especially within porous media, and their coupling is non-trivial, because they all are happening simultaneously [233,235]. In practice porous media are frequently represented by an continuum, where the system properties are averaged over a macroscopic length, i.e., a control volume containing many solid grains [236,237].

Basically, according to Steefel and coworkers [236,237], continuum formulations assume that:

i) Solid, liquid, and gaseous phases coexist at a single point in space for a certain control volume.
ii) Heterogeneous reactions of separated phases, that interact across a reaction interface, is simplified by treating the reactions as being homogeneously distributed throughout a given control volume.
iii) Fluid, solid, and gas phases are well-mixed, resulting in absence of concentration gradients and uniform reaction rates within the control volume, i.e., a continuum.

However, since many of the chemical, physical, and biological processes are pore scale processes and determine the large-scale observations, such an approximation is questionable for complex processes that involve a lot of feedbacks. In other words, continuum scale models represent a simplification of a bulk volume, the reactions and processes, and their effect on the properties of the modelled phases. The physical system is mathematically idealized as a fictive continuum, without an explicit representation of the spatial phase distribution on pore scale. Therefore, this modeling approach does not allow modeling and validation of the mechanistic understanding of the hydrogeochemical reactions and physical processes that take place on pore scale during mineral alteration or glass corrosion [146]. To model fluid-rock interactions in environmental systems or glass-water interaction in experiments sophisticated numerical methods need to handle variations of the system properties in both space and time at a smaller scale [236].

However, a relatively low requirement for computing capacity compared to a pore scale model for large volumes are still a great advantage. Furthermore, as long as bulk parameters of the solid and fluid samples are measured by analytical methods and high resolution spatial resolved data are missing, the modelling at the scale of analytical data can also be very instructive. Furthermore, it is a quite advanced approach to treat multicomponent chemical processes [236]. Nevertheless, continuum or volume averaging approaches are known to introduce significant errors, which is why more rigorous approaches are used to capture the reactions and transport processes correctly and considering pore-scale gradients [237].

Beside general continuum models, pore scale, hybrid/multiple continuum, and micro-continuum models can be used for modelling such complex ICDP reactions more properly [66,146,157,233,236,237], or allow upscale the pore-scale network modeling to calculate reaction rates at the continuum scale [238]. But even if pore-scale reactive transport models, e.g., models using the Lattice Boltzmann method, are able to capture the complex feedbacks between dissolution, transport, and precipitation, they are quite difficult to validate by *in situ* observed experimental data [233]. In this context, the relevance of the *in situ* fluid-cell Raman technique that was used in this work is further highlighted.

To account for the limitations of modeling micro-scale reactions and processes on a macro length scale, some simplifications and approximations are necessary and used for multiple continuum or hybdrid models [236]. Because a description based on a single continuum formulation is not able to capture unique features of a fractured system that involves multiple characteristic length scales [236], a hierarchical set of continua with characteristic length scales is recommended that are coupled to the next continuum in the hierarchy [236]. For example, a porous material can be modelled by dual-continuum approach, where the solid phase and the pore volume of the reference volume is subdivided into sub-volumes of each domain and coupled by mass transfer [157,239].

To model ICDP reactions on the micro-scale, the so-called micro-continuum approach seems to be a promising approach. This approach allows tracking of solid-fluid interfaces, considering transport via flow or diffusion on pore-scale, and the kinetics of dissolution and precipitation reactions at the same time [146,233]. Especially, a precipitation-driven diffusivity change, which is also considered decisive for the passivation of the glass by formation of surface covering porous SALs, can be modelled this way [233]. The great advantage of this approach is also that no *a priori* assumptions about a rate-limiting reaction step is made and implemented in such a model, in contrast to, e.g., the GRAAL model that involves a passive reactive interface (PRI) [86,146]. The passivation properties of the SAL directly follows from the relative rates of SAL formation/precipitation, SAL maturation, glass dissolution, and transport through the SAL and bulk solution.

To model glass corrosion on the basis of an ICDP process, the micro-continuum approach seems to be most favorable. This multi-scale approach in which a continuum domain and a pore-scale domain can be simulated simultaneously offers a capability of computing sub-grid processes, which is useful to model small pores that are present within precipitates [233]. The porous SAL that will precipitate during glass corrosion is treated as a continuum of solid and pore space, which in turn allows consideration of diffusive flux through these precipitates. However, the continuum formulation of sub-grid properties by using simplified empirical relations like Archie's law [233] bears large uncertainties and requires experimental validation. This can be done, e.g., by *in situ* and *in operando* determined measurement of effective diffusion coefficients for SALs formed by glass corrosion [29,41,141]. The interplay between empirical observations, advances in theoretical mechanistic models, and the numerical implementation of such conceptional models is essential to move closer and closer to a full understanding of such complex processes.

9.2 Approach for a simplified numerical glass corrosion model

From the reviewed approaches in the previous chapter, it can be concluded that a micro-continuum model is suitable for modelling glass corrosion including (am-)SAL formation on a micrometer scale. Different chemical reactions and physical processes (c.f., Chapter 3.2) can readily be implemented in such a numerical model and the modeling results can be compared directly with the *in situ* observations made by fluid cell Raman spectroscopy, as long as the scales are in same order of magnitude. Therefore, a simple 1D reactive transport code in combination with the software PHREEQC was used to model the corrosion of TBG in pure water at $pH_{RT} = 7$ at 85°C, considering:

i) Nonlinear glass dissolution, described by a TST-type rate equation,

ii) Multicomponent diffusion through SALs and bulk solution, considering effective Diffusion coefficients that depend on local porosity,

iii) Kinetically and thermodynamically controlled precipitation of amorphous silica (including Na incorporation) forming the SAL.

Some simplifications are also necessary due to the lack of data for reaction kinetics of some chemical reactions that take place on molecular level, e.g., sorption, polymerization, hydrolyzation or nucleation/growth of silica particles. Moreover, stagnant conditions are assumed, i.e., just diffusional transport was considered.

Modeling of glass corrosion considering glass dissolution and silica re-precipitation leads inevitably to discontinuities, which in turn lead to computational difficulties by approximating numerical solutions of PDEs. Classical finite difference methods, in which derivatives are approximated by finite differences, such discontinuities may be a limit for validity of the numerical approximation [240]. Therefore, finite volume method (FVM) is widely used in reactive transport codes to represent partial differential equations (PDEs) in the integral form, instead of the differential equation. Using this method, the model domain (1D profile that crosses the reaction interface) is separated into grid cells and the integral divided by the cell volume, i.e., cell average, is calculated over each grid cell instead of a pointwise approximation at each grid point in finite difference methods [240]. The averaged parameters of each grid cell, e.g., Si concentration, is modified in each time step depending on the fluxes through the edges of the adjacent cells, which is why the numerical flux functions are crucial for reliable approximation results. Because the fluxes are just entering adjacent volumes and are calculated explicitly, the method is conservative. In comparison to classical finite difference methods, the FVM is more suitable for modeling of, e.g., flow dynamics, because it exactly represents the physical process [241]. Related to the TBG corrosion model, which is presented in more detail below, a column of cell volumes that represents the glass/(SAL/)water interface(s) is considered to be able to simulate the empirical results obtained by *in situ* Raman experiments.

9.2.1 Numerical implementation

Here, a grid spacing of 10 μm between the different micro-continuums, i.e., the grid cells, were chosen, because the spatial resolution of the *in situ* Raman setup was in the same range (c.f., Chapter 5.1.4). This allows comparison of the numerical and experimental results at same scale without a full computationally expensive and inevitably simplified and unreliable modelling of the manifold molecular reactions.

The transport (diffusion) and reaction (dissolution and precipitation) reaction steps are solved sequentially by an operator splitting approach. This is common in subsurface environmental reactive transport simulators [157] and was used in a non-iterative manner here. In a sequential iterative approach the solve of transport and reaction is repeated until convergence is achieved [157]. The entire Matlab code is given in the Appendix (Chapter 12.7) and is subdivided into the main body (Chapter 12.7.1) and the definition of functions for dissolution (Chapter 12.7.3), precipitation (Chapter 12.7.4), and transport (Chapter 12.7.1). Both split main bodies of the model, i.e., transport and the reaction, are coupled by a global reaction time step of 100 seconds, while the diffusional transport equation was solved for much smaller time steps to enable numerical stability. This method is based on the quasi steady state assumption, i.e., within the coupling global time step, no significant reaction (dissolution and precipitation) takes place [233]. While, the global time step was kept constant, the internal transport time steps were reduced so that the Neumann stability criterion [241] is valid at all the times:

$$\Delta t_{int} < \frac{\Delta x^2}{2 \cdot \overline{D_{eff}}} \tag{37}$$

Here, Δt_{int} is the internal transport time step size, Δx is the distance and lengt in x-direction of one cell volume that is modeled, and $\overline{D_{eff}}$ is the averaged effective diffusion coefficient. The distance Δx (1 µm) dictates the amount of modelled solution cell volume N that is necessary to model a system of a given total length L of the solution cell column:

$$\Delta x = \frac{L}{N} \tag{38}$$

To estimate the length L, the conditions of the fluid-cell Raman setup were simplified to a representative 1D column model. For the numerical model, a column of 1000 cubic glass volumes with the size of 1 x 1 x 1 µm^3 of glass was simulated and one end of this column was exposed to a column of solution cells. Following the experiments of case study 3 in Chapter 8, about 0.1 g of TBG was immersed into a solution volume of about 4.5 ml of solution. Taking into account the density of TBG (2.5179 g/cm^3 [29]), this results in a solution/glass volume ratio of ~ 11.335. Based on this case study, 1000 glass volumes and 11335 solution volumes were considered for the model in an equally discretized numerical grid.

In Figure 52, the reaction interface of such an 1D micro-continuum model and some surrounding cell volumes are sketched out schematically, illustrating (i) diffusional transport (black double arrows) between solution cells, (ii) SAL formation (purple layers), and (iii) glass dissolution that will release glass constituents into the adjacent boundary solution cell. Note that due to its porous character the silica bearing cell volumes are simulated as fluid cells, which is why diffusion is still possible, even if diffusion is reduced due to the presence of silica. After complete dissolution of a glass cell volume, it is transformed to a solution cell volume and diffusional transport and silica precipitation is then also considered in this cell volume. This micro-continuum is now the new adjacent interface fluid cell volume. This way the inwardly directed glass dissolution reaction and shift of the reaction front can be approximated pseudo-explicitly and the SAL, considered as a pseudomorphic replacement of glass, can also be modelled as well as their influence on the transport of solutes from the reaction front into the bulk solution.

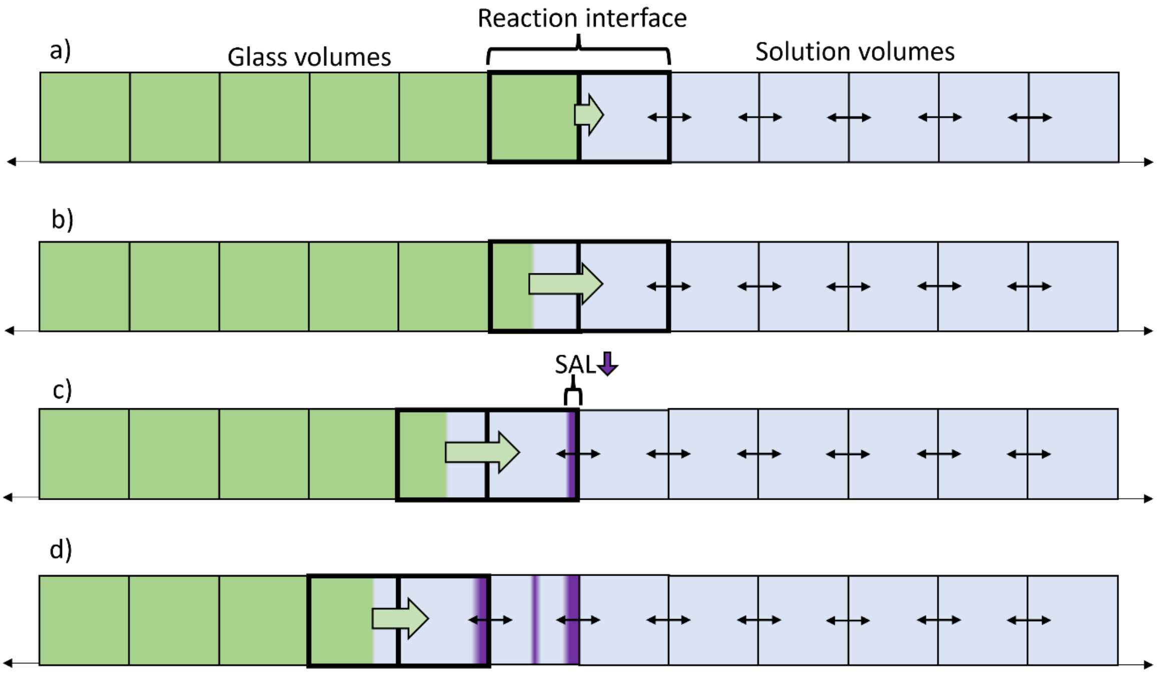

Figure 52: Conceptional illustration of the 1D micro-continuum model to simulate glass corrosion based on an ICDP process. Diffusion is considered to operate within solution volumes. The interface solution volume adjacent to the glass (part of the reaction interface) represents the solution boundary layer, which is where silica precipitation takes place and glass constituents from dissolution enter the solution volumes.

The probably simplest method for solving partial differential equations explicitly is by using the Euler method in a Forward-Time-Centered-Space (FTCS) scheme, where the central spatial derivative at a known time t^n is used to explicitly approximate the new concentration at a node i for a new time t^{n+1}, provided the concentration c at time t^n is known [241].

This scheme is frequently used for diffusional transport and assumed to be numerically stable, as long as the Neumann stability is satisfied. In order to be able to model both advection and diffusion, an advective transport term was also considered.

Therefore, an Upwind scheme was used according to the following equation:

$$\frac{c_i^{n+1} - c_i^n}{\Delta t} + \frac{1}{\Delta x} \cdot \left((uc)_{i+\frac{1}{2}} - (uc)_{i-\frac{1}{2}} \right) = D_{eff} \frac{c_{i-1}^n - 2c_i + c_{i+1}^n}{\Delta x^2} \tag{39}$$

with

$$(uc)_{i+\frac{1}{2}} = \frac{u_i + |u_i|}{2} c_i + \frac{u_{i+1} + |u_{i+1}|}{2} c_{i+1} \tag{40}$$

and

$$(uc)_{i-\frac{1}{2}} = \frac{u_{i-1} + |u_{i-1}|}{2} c_{i-1} + \frac{u_i + |u_i|}{2} c_i \tag{41}$$

where u_i, u_{i+1}, and u_{i-1} are the flow velocity (m/2) at position i, $i+1$, and $i-1$.

Nonetheless, the advection term u was assumed to be zero for the glass corrosion calculations presented here, which is why in fact just the following equation was solved by the FTCS scheme:

$$\frac{c_i^{n+1} - c_i^n}{\Delta t} = D_{eff} \frac{c_{i-1}^n - 2c_i + c_{i+1}^n}{\Delta x^2} \tag{42}$$

The numerical realization of the FTCS and Upwind scheme in Matlab was implemented and partly adapted according to the example of A. Malcherek [241]. However, the automated time-step adjustment that is proposed in this example was replaced by a different function in order to fulfil the Neumann stability criterion instead of the Courant criterion, since diffusion was the main focus here.

PHREEQC is a software to model aqueous geochemical reactions. It is possible to model several physical and chemical processes that take place in aqueous geochemical systems and one-dimensional transport. Kinetically determined and equilibrium reactions at different temperatures and, depending on the used database, ion-association models like the Debye-Hückel formulation or the specific-ion theory can be used [133,146]. Although it is also possible to calculate 1D advective and dispersive or diffusive transport with PHREEQC, the IPhreeqcCOM module (Version 3.7.3) with the Thermochimie V9b [136] database was only applied to couple the geochemical equilibration model to a Matlab script. In fact, PHREEQC was merely used to calculate the solution pH and saturation state of amorphous silica and the amount of Si that is transformed to amorphous silica if silica precipitation or growth takes place. The coupling of the precipitation reaction, diffusional transport, and feedback of SAL formation on diffusional transport by calculating effective diffusion coefficients for each finite volume for each global timestep was performed by the Matlab code.

As mentioned already above, this model is a simplification and should be understood as an outlook for future work that may build on the findings of this study to create a more comprehensive numerical model that more correctly describes the individual reactions. Here, some variables/fitting parameters of the equations that are given in Table 9 are still estimated and not based on reliable empirical data. Nonetheless, the mechanistic framework of ICDP reactions and the numerical model approach can at least be tested qualitatively. A entirely quantitative evaluation is not yet meaningful.

Table 9: Selection of crucial model parameters for the reactive transport model to simulate glass corrosion based on the ICDP mechanism and their relative effects.

	Value	*Origin*	*Effect*
Diffusion coefficient D of Si	$1.10\cdot10^{-9}\ \mathrm{m^2/s}$	PHREEQC [133] database PITZER	Larger *D* leads to more diffusional transport per timestep
Diffusion coefficient D of Na	$1.33\cdot10^{-9}\ \mathrm{m^2/s}$		
Diffusion coefficient D of B	$1.10\cdot10^{-9}\ \mathrm{m^2/s}$		
Initial glass retreat rate r_0	0.8 µm/h	Exp. II of case study III (Chapter 8.2.2)	Larger r_0 leads to higher dissolution length per timestep
pH	Initial: 7, afterwards calculated after each reaction step	Calculated using IPhreeqcCOM module and SIT database [133,136]	Larger *pH* leads to higher dissolution rates
Exponent a for pH term	0.5	Estimated	Larger *a* leads to higher dissolution rates
Activation energy E_a for Arrhenius term	90 kJ/mol	Estimated based on literature data [42]	Larger E_a leads to smaller dissolution rates
Fraction factor b for affinity term	0.75	Estimated	Larger *b* leads to stronger rate reducing impact of dissolved silica concentration on glass dissolution rate
Critical supersaturation SI_{crit} for burst nucleation and growth	0.05	Estimated	Larger SI_{crit} leads to delayed or suppressed burst nucleation and growth
Density of precipitated amorphous silica particles	$2.2\ \mathrm{g/cm^3}$	Based on sol gel literature data [108]	Larger *density* leads to larger SAL volumes and, in turn, less diffusional transport through SAL per timestep

9.2.2 Diffusional transport and effective diffusion coefficients

Multi-diffusional transport of dissolved components was calculated for the solution micro-continua and can be generally written as:

$$\frac{\partial c}{\partial t} = D\frac{\partial^2 c}{\partial x^2} \tag{43}$$

Where the changing concentrations c (mol/l) with time t (s) is given by the second derivative of the concentration gradient Δu for the transport distance Δx multiplied by the coefficient D, i.e., the diffusion coefficient ($\mathrm{m^2/s}$). To consider the impact of porous SALs on the diffusional transport through this micro continuum that is not a pure aqueous volume, an effective diffusion coefficient has been calculated, meaning that the D also depends on the spatial variable x according to the following differential equation:

$$\frac{\partial c}{\partial t} = \frac{\partial}{\partial x}\left(D_{eff}(x)\frac{\partial c}{\partial x^2}\right) \tag{44}$$

The effective diffusion coefficient D_{eff} was computed based on the porosity at a certain solution volume as follows:

$$D_{eff}(x) = D \cdot \theta_{eff} \tag{45}$$

where the effective porosity θ_{eff} is, in turn, defined by the following equation:

$$\theta_{eff} = \frac{(1 - V_{sil})}{(V_{con} \cdot f)} \tag{46}$$

where the ratio of the volume that is occupied by precipitated silica V_{sil} relative to the total volume of the solution continuum V_{con} and the parameter f is the effective porosity that is accessible for diffusional transport. The parameter f was set to 0.74048, based on the assumption that the primary silica particles are equally sized spherical particles that will lead to ~26 % ineffective pore volume for an idealized close-packing of equal spheres in a cubic volume. Therefore, this pore volume is assumed to be not accessible for diffusional transport. Note that according to this equation the effective porosity value theoretically could be negative, which is why all values $\theta_{eff} < 0$ were set to be zero. The assumption that non-Fickian diffusion in porous am-SAL has recently been verified by hydrogen isotope tracer experiments analyzed *in situ* by fluid-cell Raman spectroscopy [141] which revealed anomalous diffusion through SALs formed by TBG corrosion in acidic and basic solutions while water diffusion through an SAL that formed under rather neutral conditions follows a linear dependence of the mean square water transport with time. It is noted here that the GRAAL model was also extended recently to consider non-linear diffusivity [120], although the authors assumed that the diffusivity depends on the local water content.

9.2.3 Glass dissolution

Stoichiometric glass dissolution is described by a transition state theory (TST) type rate equation (c.f. Chapter 3.3.1) which depends mainly on the solution pH and amorphous silica saturation state at the reaction front. Based on this concept the dissolution length for each global time step was calculated according to the following equation for homogeneous surface dissolution:

$$l_{dissolution} = \Delta t \cdot S_{glass} \cdot r_0 \cdot pH_{i+1}^{-a} \cdot \exp\left(\frac{-E_a}{R \cdot T}\right) \cdot \left[1 - \left(10^{\,SI_{SiO2(am)}} \cdot b\right)\right] \tag{47}$$

Where Δt is the global time step, S_{glass} is the surface area that is exposed to the solution, i.e., the length of a solution or glass volume in y and z direction, r_0 is the intrinsic forward dissolution rate of the glass, pH_{i+1} is the pH at the adjacent solution cell and the pH dependency is described by an empirical fitting parameter a (set to 0.5 for TBG in this study). The Arrhenius term accounts for the temperature dependency by assuming a mean activation energy of 90 kJ/mol for TBG, based on data given by Lönartz et al. [42] that ranged from 71 to 116 kJ/mol. A typical activation energy been 60 and 80 kJ/mol has been reported in literature for TST type glass dissolution rate laws [17,67]. The last term is equivalent to an affinity term using the saturation index (SI) of amorphous silica at the solution volume adjacent to the glass surface calculated with PHREEQC ($SI_{SiO2(am)}$) and a fitting parameter b (set to 0.75) to account for the lower solubility of TBG compared to the corrosion product, i.e., amorphous silica. The reason for this was the fact that glass dissolution continued, even if the bulk solution is supersaturated with respect to amorphous silica (c.f., Chapter 8).

The SI is defined by the ion activity product (IAP) of the ions A and B with stoichiometric coefficients a and b, respectively, and the thermodynamic solubility constant K_s.

$$SI = log_{10}\left(\frac{IAP}{K_s}\right) = log_{10}\left(\frac{[A]^a[B]^b}{K_s}\right) \tag{48}$$

9.2.4 Silica precipitation

Precipitation of amorphous silica was implemented based on the following assumptions (c.f., Chapter 3.2.9):

1. Silica nucleation and growth (precipitation) occurs within the adjacent interface fluid cell volume, whether initial or already transformed, after a glass cell volume is dissolved completely.
2. A burst nucleation and growth (precipitation) [143,145] process is implemented for silica precipitation whenever a critical supersaturation (SI_{crit}) threshold of 0.05 for amorphous SiO_2 is achieved. Then, the Si concentration was reduced to a level so that the SI for amorphous SiO_2 is reduced down to a tenth of the initial value. The Si difference is subtracted and transformed via precipitation to solid amorphous silica.
3. A prerequisite for nucleation and growth of amorphous silica is that silica has already precipitated via burst nucleation and growth and that the SI of amorphous SiO_2 lies between zero and the critical supersaturation. Then, dissolved Si is removed from the interface solution volume to half the SI. The Si difference is then as well transformed into solid amorphous silica.

Whether dissolved Si was removed and transformed to amorphous silica via precipitation or growth route, the volume of precipitated silica V_{sil} is calculated assuming a typical density (2.2 g/cm^3) of sol gel derived anhydrous SiO^2 [108] particles. This, in turn, is considered in the effective diffusion coefficient according to Equation (45) and (46).

9.3 Preliminary results and discussion

First results of the application of the proposed model, that was set up to simulate the corrosion of TBG on a similar spatial resolution as monitored *in situ* by fluid cell Raman spectroscopic experiments, are discussed briefly in the following. In Figure 53 the elemental distribution of dissolved Si, Na, and B are shown the for the whole modeled 1D profile crossing the glass/reaction interface/solution-sequence for two different chosen times. While in Figure 53a the strong concentration gradient can be identified easily after about 7 h of modeled TBG corrosion, there is just a small difference between the concentrations at the reaction front and the rest of the solution at the end of the model period of 555.6 h, shown in Figure 53b. The observation that there is a higher Na to B ratio close to the glass, while it decreases with increasing distance from the reaction front and even reverses after a certain distance, is due to the higher assumed diffusion coefficient of Na ($1.33 \cdot 10^{-9}$ m^2/s) compared to the diffusion coefficient of B ($1.1 \cdot 10^{-9}$ m^2/s). However, this effect was no longer really noticeable by the end of modeling.

The calculated glass retreat for the TBG corrosion at initial $pH_{21°C}$ 7 in pure water is shown in Figure 54a, combined with SAL growth. Using the previously mentioned input parameters, the first silica precipitation was observed after 52 h, which is indicated by a slight kink in the glass retreat curve and highlighted by a red arrow. The solution pH and SI of amorphous silica within the interface solution cell volume adjacent to the glass reaction interface is assumed to be decisive for the occurrence of silica growth or precipitation, because SAL formation usually takes place at the surface of pristine TBG (c.f., Chapter 8.2.2). Because silica precipitation is assumed to not occur before a sufficient supersaturation of amorphous silica is reached, defined by an SI_{crit} > 0.05, the SI also raised until this threshold was reached and dropped abruptly (c.f., Figure 54c). Because the precipitation of amorphous silica is also reflected by a reduction of dissolved Si, more precisely dissolved silicic acid, the precipitation event also causes a pH rise at the same time (c.f., pH-increase in Figure 54d). Interestingly, after initial precipitation, the critical oversaturation was always exceeded in the consecutive reaction steps and the SI of amorphous silica was even greater than the predefined Si_{crit} at late stage.

The modeling results are also in line with experimental observations and identified feedbacks discussed in this study. For example, a first silica signal was recorded after about 50 h of TBG corrosion in a 0.5*M* $NaHCO_3$ solution at 85 °C by Geisler et al. [29]. However, as disclaimed already in Chapter 0, a quantitative interpretation of the modeled data is not recommended due to the roughly estimated parameters and the lack of empirically evidence, e.g., for empirically validated pH dependent dissolution rates. This may be one of the reason for misfit between the extent of glass retreat and SAL thickness, compared to reference experiments for TBG from case study III

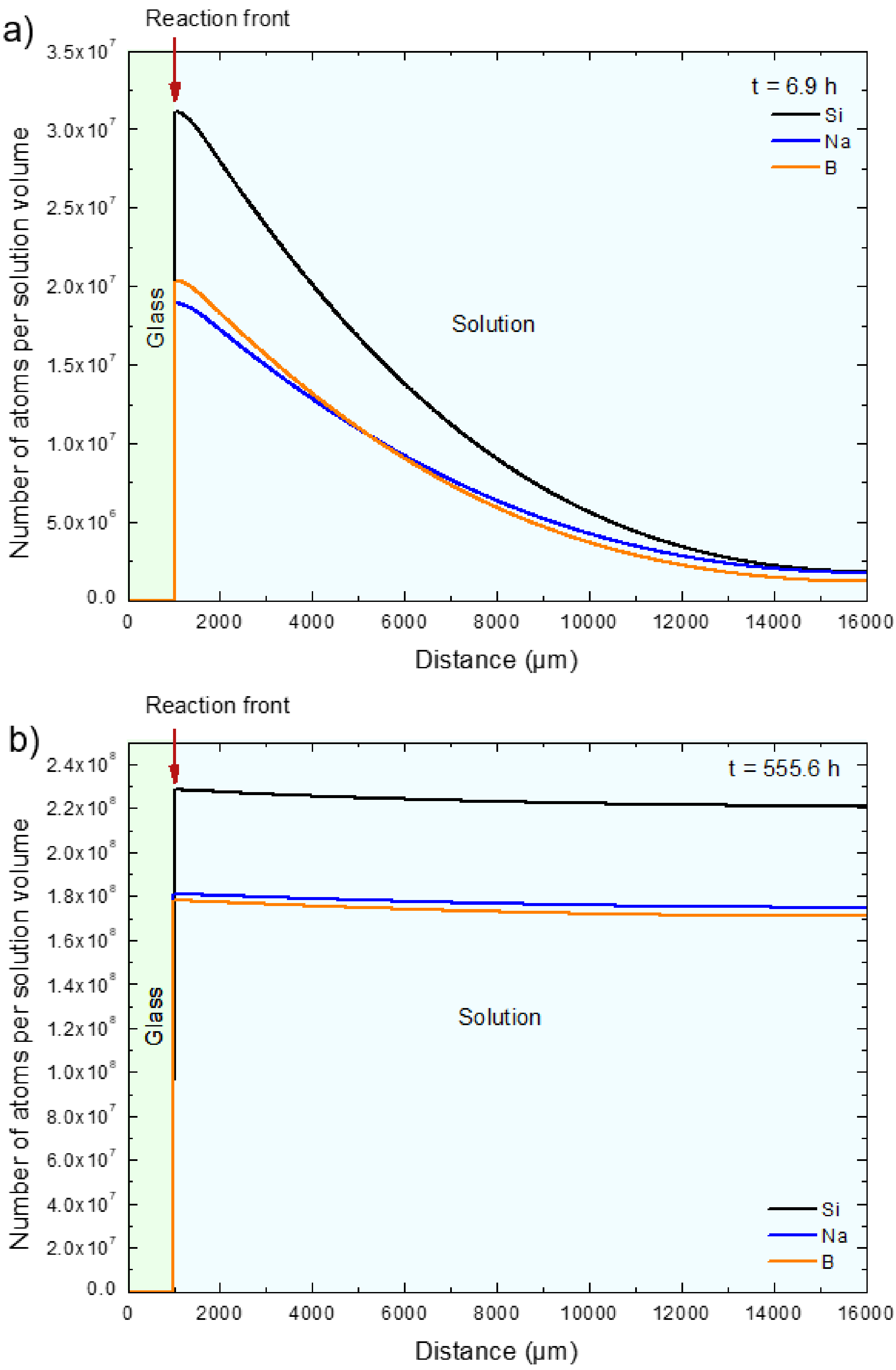

Figure 53: Exemplary element concentration profiles of dissolved glass constituents that are plotted as number of atoms per modeled solution volume (10 µm) as a function of position. The snapshot like results represent the state of the elemental distribution after **(a)** 6.9 h of corrosion, and **(b)** at late stage, after 555.6 h. Diffusional transport and amorphous silica precipitation was assumed here to only occur in solution.

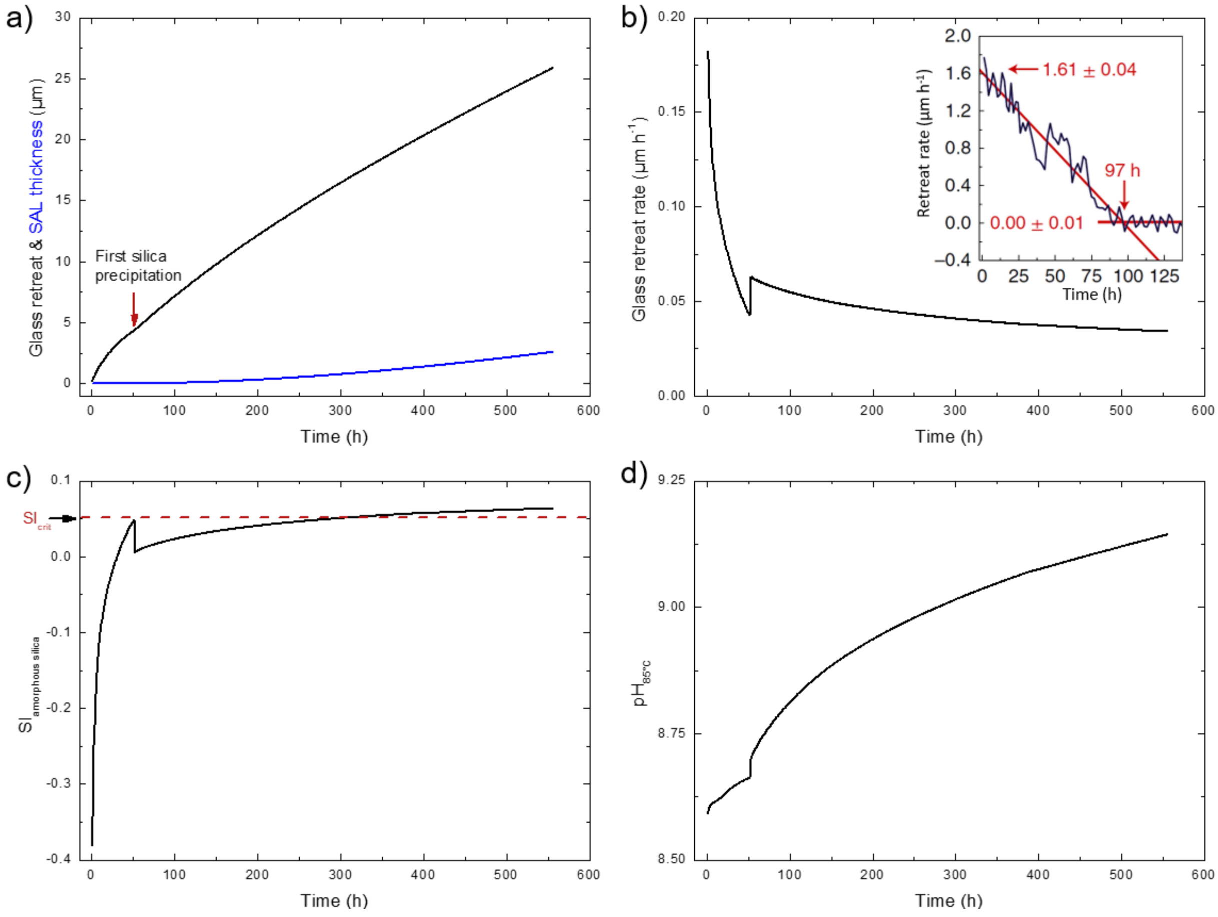

Figure 54: Results of TBG corrosion in pure water at 85 °C modeled by a 1D reactive transport code that was coupled to the geochemical software PHREEQC. **(a)** Calculated glass retreat and thickness of the SAL, based on the volume of precipitated amorphous silica, as a function of time. **(b)** The simulated glass retreat rate as a function of time. Inset diagram shows experimental fluid-cell Raman data from the same glass altered in a bicarbonate solution [29]. In **(c)** and **(d)** the saturation index (SI) of amorphous silica and the solution pH are plotted against time for the solution cell volume adjacent to the glass surface that represents the solution boundary layer after equilibration (possible silica precipitation).

and other studies [29,30,41,42]). Besides general limitations of reactive transport and thermodynamic models (e.g., lack of knowledge on actual molecular reactions, high computational effort of pore scale models for large model domains, inconsistent or incomplete thermodynamic databases, missing kinetic data) the presented approach simplifies the glass corrosion process by not considering i) interdiffusion reactions, ii) incorporation, sorption or trapping of alkali and earth alkali elements within the amorphous silica structure, iii) water diffusion through the SAL, iv) silica maturation, and v) convective flow. Furthermore, some quantitative assumptions of the model are not based on empirical data, but rather have been estimated for this study. However, the calculation of the forward glass dissolution rate and its activation energy is based on experimental data, namely from case study II (c.f., Chapter 8.2.2) and from literature data [42]. However, the parameter a was just set to 0.5 to consider typically higher glass dissolution rates for higher pH in the alkaline regime [17], even if TBG specific data are missing. Inevitable limitations of the model are also the simplification of molecular reactions by rate equations and the spatial resolution limitation that is defined by the cell volume size.

However, the results can be analyzed qualitatively and show that the basic features of TBG alteration by an ICDP mechanism can be modeled by only considering the most important feedbacks between the dissolving glass and precipitating silica on solution properties and *vice versa* (c.f., Chapter 3.2). For example, changing solution properties, such as pH and SI of amorphous silica within the interface solution, shown in Figure 54c and d as a function of time, are the direct result of glass dissolution. It is noteworthy that such a pH evolution in the bulk solution was also observed in case studies I, II, and III. Also, a pH gradient from the glass surface towards the bulk solution, which is reflected in the simulation by the chemical gradients and defines the fluid-boundary layer (Figure 52a), which was observed by fluid-cell Raman spectroscopy [29].

Moreover, the simulated continuous reduction of the glass retreat rate already from the beginning has also been observed experimentally [29,42] , i.e., is also well simulated by the simple model (Figure 54b). This observation can be explained by affinity effects in the proposed fluid boundary layer. The affinity effect is considered in the dissolution equation by the SI of amorphous silica and adjusted by the fraction factor *b* at the adjacent reaction cell. It continuously decreases the dissolution rate by rising silica concentration during the first 52 h. After the solution has passed the critical oversaturation threshold, precipitation occurs. This causes a drop of the glass retreat rate, an abrupt pH increase, and a simultaneous reduction of the SI. The two feedbacks I and II (c.f., Chapter 3.2.5 and 3.2.7, respectively) are operating here, when considering the glass dissolution rate and the precipitation of amorphous silica are both being affected by the properties of solution boundary layer, especially the silica saturation state and solution pH the reaction front. In fact, the solution boundary layer is implemented here as the adjacent solution cell volume that was in contact with the glass surface. The other feedbacks III and IV (c.f., Chapter 3.2.7 and 3.2.8, respectively) are less obvious represented in this simple corrosion model, because the established SAL was still very thin (< 3 µm) after the entire simulation time. Even the spatially resolved (10 µm mesh) effective diffusion coefficient that is affected by presence of precipitated amorphous silica, the transport limiting effect was very low for the set of parameters used for the preliminary modeling. Conversely, a much thicker SAL or a stronger reducing impact of silica on the diffusion coefficient would probably lead to different transport properties of the SAL or possibly even to complete passivation of the glass.

In general, the pH and SI is increasing continuously after a discontinuity that occurs when the first silica precipitation takes place. Interestingly, beside burst nucleation events of silica precipitation when $SI_{amSiO2} > Si_{crit}$, the second possible silica forming reaction, i.e., nucleation and growth when $SI_{amSiO2} < Si_{crit}$ and $SI_{amSiO2} >$ zero, was not observed to take place in the model using this specific set of parameters (c.f., Table 9). Once burst nucleation and growth of amorphous silica occur, the SI and pH of this solution boundary layer is calculated assuming equilibrium conditions. These parameters in turn were considered for the consecutive glass dissolution reaction step in the next simulation time step. Tuning the variable input parameters in the numerical model, e.g., rising the critical oversaturation threshold, may have led to a time dependent change of the formation route from burst nucleation and growth to classical nucleation and growth of amorphous silica. In future, by trying different input parameter combinations, it even seems possible that the precipitation route probably switches several times between the two variants for certain parameter combinations, which in turn would result in a multi-layered SAL than a coherently precipitated SAL (c.f., Chapter 3.2.9).

9.4 Conclusion

For validation and refinement of mechanistic models such as the ICDP model for glass corrosion, a numerical model is an ideal complement to *in operando* experiments. As demonstrated in this study, using the most crucial chemical reactions and physical processes inherent to the ICDP model (c.f., Chapter 3), the results of *in situ* fluid-cell Raman experiments (c.f., Chapter 6, 7, and 8) can be well reproduced by a simple one-dimensional reactive transport code using finite volume methods. This model is particularly characterized by the implementation of an distinct fluid boundary layer, represented by the solution volume cell adjacent to the glass surface, where i) silica precipitation takes place, ii) the dissolved glass constituents are added for each dissolution reaction step, and iii) the solution properties are calculated to determine the actual glass dissolution rate for the consecutive dissolution reaction step.

The idea was to set up a model on a micrometer scale that would allow a comparison with results from *in situ* fluid-cell Raman experiments. This in turn allows an iterative improvement of our understanding of the glass corrosion process. On the one hand, new experiments may reveal new observations that have to be considered in the numerical model. On the other hand, the systematic change of parameters, such as, e.g., different pH, temperature, or additional convective flow, in a comprehensive numerical model can be useful to systematically study the effect of these parameters on the corrosion process, which is difficult to achieve by relatively time-consuming experiments.

10 Conclusion and outlook

This study shows that the interface-coupled dissolution-precipitation (ICDP) model is suitable to explain all observed glass corrosion features that can be found in literature and the experiments presented in this work. By using *in situ* fluid-cell Raman spectroscopy it is possible to study glass corrosion *in operando* to determine kinetic data of glass dissolution and growth of amorphous or crystalline surface alteration layers (SALs). Advanced experimental setups that were used here in three individual case studies allowed studying corrosion of the international simple glass (ISG) over for time periods of several month by *in situ* Raman mapping in sequential measurement sessions with intermediate corrosion periods, where no Raman data were acquired. The results indicate that ISG undergoes transformation via ICDP reactions to amorphous and crystalline phases under strong alkaline as well as strong acidic conditions. The formation of multiple surface alteration layers (SALs) was observed *in operando* for the first time during the experimental corrosion of a ternary borosilicate glass (TBG) under varying fluid exchange rates, which is further evidence for a self-organizing corrosion process being responsible for the formation of complex chemical and structural patterns.

The analytical technique has already been further developed as part of this project, but there is also further potential for optimization. For example, inert coating of the glass samples top side, which protects this surface from corrosion in the fluid cell in order to avoid a deterioration in the Raman signal intensity and the spatial resolution with increasing top side corrosion is recommended. Furthermore, the reaction cell has always been positioned manually under the stage of the Raman microscope for long-term experiments and placed back on a heating station between the measurement sessions. Optimization through automated sampling and measurements of several corrosion cells one after another would make it possible to carry out a large number of experiments in parallel.

In order to further validate the ICDP model, numerical corrosion models based on assumed chemical reactions and physical processes are important. By using the spatial resolution of such a numerical model similar to that of *in situ* and *in operando* techniques, an empirical validation and adjustment of the model parameters is possible. Even the simplified 1D reaction-transport model presented here as a kind of outlook shows good qualitative agreement with experimental observations presented in this thesis and elsewhere. The iterative and combined development of such experimental and numerical approaches is promising for improving our understanding of the glass corrosion process. For example, based on numerical modeling of corrosion experiments for different conditions and glass types, it can be estimated which experiments could reveal new glass corrosion features. Furthermore, it is possible to estimate the effect of different environmental parameters and glass composition on empirically determined forward dissolution rates of glasses. A combination of both approaches also makes it possible to specifically collect input data for numerical modeling by performing *in situ* Raman experiments. For example, the dynamic glass dissolution rate and diffusion properties through porous SALs can be investigated through the use of isotope tracers. The new data presented here demonstrate that only focusing on the intrinsic dissolution rate or chemical durability of a glass is not sufficient to predict their long-term durability. In particular, the dependence of dissolution and precipitation kinetics on the local solution chemistry and *vice versa* are crucial for further course and the total extent of corrosion. With *in situ* fluid-cell Raman spectroscopy it is possible to study such feedbacks in real-time and on a micrometer scale while the process is operating, in order to validate numerical corrosion models which in turn can be used to estimate the long-term stability of nuclear waste glasses and to enable an application-oriented glass development of other technical glasses.

11 References

1. Jantzen, C. M. Development of glass matrices for high level radioactive wastes. In *Handbook of advanced radioactive waste conditioning technologies,* edited by M. I. Ojovan (Belgoprocess, Oxford, Philadelphia, s.l., 2011), pp. 230–292.

2. Conradt, R. Chemical Durability of Oxide Glasses in Aqueous Solutions: A Review. *J American Ceramic Society* **91,** 728–735; 10.1111/j.1551-2916.2007.02101.x (2008).

3. Gin, S. *et al.* An international initiative on long-term behavior of high-level nuclear waste glass. *Materials Today* **16,** 243–248; 10.1016/j.mattod.2013.06.008 (2013).

4. Grambow, B. Nuclear Waste Glasses - How Durable? *Elements* **2,** 357–364; 10.2113/gselements.2.6.357 (2006).

5. Gin, S. Open Scientific Questions about Nuclear Glass Corrosion. *Procedia Materials Science* **7,** 163–171; 10.1016/j.mspro.2014.10.022 (2014).

6. Gin, S., Ryan, J. V., Kerisit, S. & Du, J. Simplifying a solution to a complex puzzle. *npj Mater Degrad* **2,** 357; 10.1038/s41529-018-0057-y (2018).

7. Thorpe, C. L. *et al.* Forty years of durability assessment of nuclear waste glass by standard methods. *npj Mater Degrad* **5,** 1108; 10.1038/s41529-021-00210-4 (2021).

8. Iacocca, R. G. *et al.* Factors affecting the chemical durability of glass used in the pharmaceutical industry. *AAPS PharmSciTech* **11,** 1340–1349; 10.1208/s12249-010-9506-9 (2010).

9. Ngo, D. & Kim, S. H. Aqueous Corrosion of Glass. *The World Scientific Reference of Amorphous Materials,* 165–197 (2020).

10. Abdelouas, A., Neeway, J. & Grambow, B. Chemical Durability of Glasses. In *Springer Handbook of Glass,* edited by J. D. Musgraves, J. Hu & L. Calvez (2019), pp. 407–438.

11. Schalm, O., Nuyts, G. & Janssens, K. Some critical observations about the degradation of glass: The formation of lamellae explained. *Journal of Non-Crystalline Solids* **569,** 120984; 10.1016/j.jnoncrysol.2021.120984 (2021).

12. Melcher, M., Wiesinger, R. & Schreiner, M. Degradation of glass artifacts: application of modern surface analytical techniques. *Accounts of chemical research* **43,** 916–926; 10.1021/ar9002009 (2010).

13. Bouakkaz, R., Abdelouas, A. & Grambow, B. Kinetic study and structural evolution of SON68 nuclear waste glass altered from 35 to 125 °C under unsaturated H2O and

D2O18 vapour conditions. *Corrosion Science* **134,** 1–16; 10.1016/j.corsci.2017.12.035 (2018).

14. Chinnam, R. K., Fossati, P. & Lee, W. E. Degradation of partially immersed glass: A new perspective. *Journal of Nuclear Materials* **503,** 56–65; 10.1016/j.jnucmat.2018.02.040 (2018).

15. Pierce, E. M., Richards, E. L., Davis, A. M., Reed, L. R. & Rodriguez, E. A. Aluminoborosilicate waste glass dissolution under alkaline conditions at 40°C: implications for a chemical affinity-based rate equation. *Environ. Chem.* **5,** 73; 10.1071/EN07058 (2008).

16. Pierce, E. M., Rodriguez, E. A., Calligan, L. J., Shaw, W. J. & Pete McGrail, B. An experimental study of the dissolution rates of simulated aluminoborosilicate waste glasses as a function of pH and temperature under dilute conditions. *Applied Geochemistry* **23,** 2559–2573; 10.1016/j.apgeochem.2008.05.006 (2008).

17. Vienna, J. D., Neeway, J. J., Ryan, J. V. & Kerisit, S. N. Impacts of glass composition, pH, and temperature on glass forward dissolution rate. *npj Mater Degrad* **2,** 309; 10.1038/s41529-018-0042-5 (2018).

18. Strachan, D. M. & Neeway, J. J. Effects of alteration product precipitation on glass dissolution. *Applied Geochemistry* **45,** 144–157; 10.1016/j.apgeochem.2014.03.013 (2014).

19. Neeway, J. J., Rieke, P. C., Parruzot, B. P., Ryan, J. V. & Asmussen, R. M. The dissolution behavior of borosilicate glasses in far-from equilibrium conditions. *Geochimica et Cosmochimica Acta* **226,** 132–148; 10.1016/j.gca.2018.02.001 (2018).

20. Gin, S. *et al.* A General Mechanism for Gel Layer Formation on Borosilicate Glass under Aqueous Corrosion. *J. Phys. Chem. C*; 10.1021/acs.jpcc.9b10491 (2020).

21. Frugier, P., Minet, Y., Rajmohan, N., Godon, N. & Gin, S. Modeling glass corrosion with GRAAL. *npj Mater Degrad* **2,** 265; 10.1038/s41529-018-0056-z (2018).

22. Brewster, D. XIX.— On the Structure and Optical Phenomena of Ancient Decomposed Glass. *Trans. R. Soc. Edinb.* **23,** 193–204; 10.1017/S0080456800019372 (1863).

23. Fowler, J. III.— On the Process of Decay in Glass, and, incidentally, on the Composition and Texture of Glass at different periods, and the History of its Manufacture. *Archaeologia* **46,** 65–162; 10.1017/S0261340900006068 (1880).

24. Brill, R. H. & Hood, H. P. A new method for dating ancient glass. *Nature* **189,** 12–14 (1961).

25. Cox, G. A. & Ford, B. A. The long-term corrosion of glass by ground-water. *Journal of Material Science* **28,** 5637–5647 (1993).
26. Schalm, O. & Anaf, W. Laminated altered layers in historical glass: Density variations of silica nanoparticle random packings as explanation for the observed lamellae. *Journal of Non-Crystalline Solids* **442,** 1–16; 10.1016/j.jnoncrysol.2016.03.019 (2016).
27. SCHALM, O. *et al.* MANGANESE STAINING OF ARCHAEOLOGICAL GLASS: THE CHARACTERIZATION OF Mn-RICH INCLUSIONS IN LEACHED LAYERS AND A HYPOTHESIS OF ITS FORMATION. *Archaeometry* **53,** 103–122; 10.1111/j.1475-4754.2010.00534.x (2011).
28. Cagno, S. *et al.* Evaluation of manganese-bodies removal in historical stained glass windows via SR-µ-XANES/XRF and SR-µ-CT. *J. Anal. At. Spectrom.* **26,** 2442; 10.1039/c1ja10204d (2011).
29. Geisler, T., Dohmen, L., Lenting, C. & Fritzsche, M. B. K. Real-time in situ observations of reaction and transport phenomena during silicate glass corrosion by fluid-cell Raman spectroscopy. *Nature materials* **18,** 342–348; 10.1038/s41563-019-0293-8 (2019).
30. Lenting, C. & Geisler, T. Corrosion of ternary borosilicate glass in acidic solution studied in operando by fluid-cell Raman spectroscopy. *npj Mater Degrad* **5,** 8; 10.1038/s41529-021-00182-5 (2021).
31. Lenting, C. *GLASS CORROSION: Towards a Unifying Mechanistic Model* (Bonn, 2019).
32. IAEA. *Underground Disposal Concepts for Small Inventories of Intermediate and High Level Radioactive Waste* (IAEA, Vienna, 2020).
33. Stroncik, N. A. & Schmincke, H.-U. Palagonite – a review. *Int J Earth Sci (Geol Rundsch)* **91,** 680–697; 10.1007/s00531-001-0238-7 (2002).
34. Lenting, C. *et al.* Towards a unifying mechanistic model for silicate glass corrosion. *npj Mater Degrad* **2,** 18696; 10.1038/s41529-018-0048-z (2018).
35. Geisler, T. *et al.* Aqueous corrosion of borosilicate glass under acidic conditions: A new corrosion mechanism. *Journal of Non-Crystalline Solids* **356,** 1458–1465; 10.1016/j.jnoncrysol.2010.04.033 (2010).
36. Geisler, T. *et al.* The mechanism of borosilicate glass corrosion revisited. *Geochimica et Cosmochimica Acta* **158,** 112–129; 10.1016/j.gca.2015.02.039 (2015).
37. Hellmann, R. *et al.* Unifying natural and laboratory chemical weathering with interfacial dissolution–reprecipitation: A study based on the nanometer-scale chemistry of fluid–silicate interfaces. *Chemical Geology* **294-295,** 203–216; 10.1016/j.chemgeo.2011.12.002 (2012).

38. Hellmann, R. *et al.* Nanometre-scale evidence for interfacial dissolution-reprecipitation control of silicate glass corrosion. *Nature materials* **14,** 307–311; 10.1038/nmat4172 (2015).

39. Dohmen, L. *et al.* Pattern Formation in Silicate Glass Corrosion Zones. *Int J Appl Glass Sci* **4,** 357–370; 10.1111/ijag.12046 (2013).

40. Geisler, T., Dohmen, L., Lenting, C. & Fritzsche, M. B. K. Real-time in situ observations of reaction and transport phenomena during silicate glass corrosion by fluid-cell Raman spectroscopy. *Nature materials* **18,** 342–348; 10.1038/s41563-019-0293-8 (2019).

41. Dohmen, L. In situ observations of reaction and transport phenomena during silicate glass corrosion by fluid-cell Raman spectroscopy.

42. Lönartz, M. I. *et al.* The Effect of Heavy Ion Irradiation on the Forward Dissolution Rate of Borosilicate Glasses Studied in Situ and Real Time by Fluid-Cell Raman Spectroscopy. *Materials (Basel, Switzerland)* **12**; 10.3390/ma12091480 (2019).

43. Gin, S. *et al.* The fate of silicon during glass corrosion under alkaline conditions: A mechanistic and kinetic study with the International Simple Glass. *Geochimica et Cosmochimica Acta* **151,** 68–85; 10.1016/j.gca.2014.12.009 (2015).

44. Backhouse, D. J. *et al.* Corrosion of the International Simple Glass under acidic to hyperalkaline conditions. *npj Mater Degrad* **2,** 180; 10.1038/s41529-018-0050-5 (2018).

45. Müller, G., Fritzsche, M. B., Dohmen, L. & Geisler, T. Feedbacks and non-linearity of silicate glass alteration in hyperalkaline solution studied by in operando fluid-cell Raman spectroscopy. *Geochimica et Cosmochimica Acta,* 1–21; 10.1016/j.gca.2022.05.013 (2022).

46. Aréna, H. *et al.* Impact of Zn, Mg, Ni and Co elements on glass alteration: Additive effects. *Journal of Nuclear Materials* **470,** 55–67; 10.1016/j.jnucmat.2015.11.050 (2016).

47. Aréna, H. *et al.* Impact of Fe, Mg and Ca elements on glass alteration: Interconnected processes. *Geochimica et Cosmochimica Acta* **239,** 420–445; 10.1016/j.gca.2018.08.007 (2018).

48. Wang, Y., Jove-Colon, C. F. & Kuhlman, K. L. Nonlinear dynamics and instability of aqueous dissolution of silicate glasses and minerals. *Scientific reports* **6,** 30256; 10.1038/srep30256 (2016).

49. Wang, Y., Jove-Colon, C. F., Lenting, C., Icenhower, J. & Kuhlman, K. L. Morphological instability of aqueous dissolution of silicate glasses and minerals. *npj Mater Degrad* **2,** 182; 10.1038/s41529-018-0047-0 (2018).

50. Reiser, J. T. *et al.* Comparative Structural Investigations of Nuclear Waste Glass Alteration Layers and Sol-gel Synthesized Aerogels. *npj Mater Degrad* **4** (2020).

51. Hopf, J. *et al.* Toward an understanding of surface layer formation, growth, and transformation at the glass–fluid interface. *Geochimica et Cosmochimica Acta* **229,** 65–84; 10.1016/j.gca.2018.01.035 (2018).

52. Gin, S., Ryan, J. V., Schreiber, D. K., Neeway, J. & Cabié, M. Contribution of atom-probe tomography to a better understanding of glass alteration mechanisms: Application to a nuclear glass specimen altered 25years in a granitic environment. *Chemical Geology* **349-350,** 99–109; 10.1016/j.chemgeo.2013.04.001 (2013).

53. Gin, S. *et al.* Atom-Probe Tomography, TEM and ToF-SIMS study of borosilicate glass alteration rim: A multiscale approach to investigating rate-limiting mechanisms. *Geochimica et Cosmochimica Acta* **202,** 57–76; 10.1016/j.gca.2016.12.029 (2017).

54. Narayanasamy, S. *et al.* Influence of composition of nuclear waste glasses on vapor phase hydration. *Journal of Nuclear Materials* **525,** 53–71; 10.1016/j.jnucmat.2019.07.015 (2019).

55. Tribet, M. *et al.* New Insights about the Importance of the Alteration Layer/Glass Interface. *J. Phys. Chem. C*; 10.1021/acs.jpcc.0c02121 (2020).

56. Mir, A. H. *et al.* Effect of decades of corrosion on the microstructure of altered glasses and their radiation stability. *npj Mater Degrad* **4,** 300; 10.1038/s41529-020-0115-0 (2020).

57. Rebiscoul, D., Frugier, P., Gin, S. & Ayral, A. Protective properties and dissolution ability of the gel formed during nuclear glass alteration. *Journal of Nuclear Materials* **342,** 26–34; 10.1016/j.jnucmat.2005.03.018 (2005).

58. Gin, S., Frugier, P., Jollivet, P., Bruguier, F. & Curti, E. New Insight into the Residual Rate of Borosilicate Glasses: Effect of S/V and Glass Composition. *Int J Appl Glass Sci* **4,** 371–382; 10.1111/ijag.12048 (2013).

59. Grambow, B. Müller, R. First-order dissolution rate law and the role of surface layers in glass performance assessment. *Journal of Nuclear Materials* **298,** 112–124 (2001).

60. Gin, S. *et al.* Dynamics of self-reorganization explains passivation of silicate glasses. *Nature communications* **9,** 2169; 10.1038/s41467-018-04511-2 (2018).

61. Ebert, W. L. *The Effects of the Glass Surface Area/Solution Volume Ratio on Glass Corrosion: A Critical Review* (Illinois, 1995).

62. Gong, Y., Xu, J. & Buchanan, R. C. The aqueous corrosion of nuclear waste glasses revisited: Probing the surface and interfacial phenomena. *Corrosion Science* **143,** 65–75; 10.1016/j.corsci.2018.08.028 (2018).

63. Strachan, D. Glass dissolution as a function of pH and its implications for understanding mechanisms and future experiments. *Geochimica et Cosmochimica Acta* **219,** 111–123; 10.1016/j.gca.2017.09.008 (2017).
64. Vienna, J. D., Ryan, J. V., Gin, S. & Inagaki, Y. Current Understanding and Remaining Challenges in Modeling Long-Term Degradation of Borosilicate Nuclear Waste Glasses. *Int J Appl Glass Sci* **4,** 283–294; 10.1111/ijag.12050 (2013).
65. Ruiz-Agudo, E. *et al.* Control of silicate weathering by interface-coupled dissolution-precipitation processes at the mineral-solution interface. *Geology,* 567–570 (2016).
66. Aradóttir, E., Sigfússon, B., Sonnenthal, E. L., Björnsson, G. & Jónsson, H. Dynamics of basaltic glass dissolution – Capturing microscopic effects in continuum scale models. *Geochimica et Cosmochimica Acta* **121,** 311–327; 10.1016/j.gca.2013.04.031 (2013).
67. Icenhower, J. P., Samson, S., Lüttge, A. & McGrail, B. P. Towards a consistent rate law: glass corrosion kinetics near saturation. *Energy, Waste, and the Environment: a Geochemical Perspective,* 579–594 (2004).
68. Icenhower, J. P. & Steefel, C. I. Experimentally determined dissolution kinetics of SON68 glass at 90°C over a silica saturation interval: Evidence against a linear rate law. *Journal of Nuclear Materials* **439,** 137–147; 10.1016/j.jnucmat.2013.04.008 (2013).
69. Jollivet, P., Gin, S. & Schumacher, S. Forward dissolution rate of silicate glasses of nuclear interest in clay-equilibrated groundwater. *Chemical Geology* **330-331,** 207–217; 10.1016/j.chemgeo.2012.09.012 (2012).
70. Joe Ryan. *Chemical Durability of Nuclear Waste Glasses. Presented for Prof. Russell J. Hand* (Trieste, Italy, 2019).
71. Ferrand, K., Liu, S. & Lemmens, K. The Effect of Ordinary Portland Cement on Nuclear Waste Glass Dissolution. *Procedia Materials Science* **7,** 223–229; 10.1016/j.mspro.2014.10.029 (2014).
72. Oelkers, E. H. & Gislason, S. R. The mechanism, rates and consequences of basaltic glass dissolution: I. An experimental study of the dissolution rates of basaltic glass as a function of aqueous Al, Si and oxalic acid concentration at 25°C and pH = 3 and 11. *Geochimica et Cosmochimica Acta* **65,** 3671–3681 (2001).
73. Chave, T., Frugier, P., Gin, S. & Ayral, A. Glass–water interphase reactivity with calcium rich solutions. *Geochimica et Cosmochimica Acta* **75,** 4125–4139; 10.1016/j.gca.2011.05.005 (2011).

74. Burger, E. *et al.* Impact of iron on nuclear glass alteration in geological repository conditions: A multiscale approach. *Applied Geochemistry* **31,** 159–170; 10.1016/j.apgeochem.2012.12.016 (2013).

75. Tournié, A. *et al.* Impact of boron complexation by Tris buffer on the initial dissolution rate of borosilicate glasses. *Journal of colloid and interface science* **400,** 161–167; 10.1016/j.jcis.2013.03.009 (2013).

76. Aréna, H., Rébiscoul, D., Garcès, E. & Godon, N. Comparative effect of alkaline elements and calcium on alteration of International Simple Glass. *npj Mater Degrad* **3,** 3147; 10.1038/s41529-019-0072-7 (2019).

77. Collin, M., Fournier, M., Charpentier, T., Moskura, M. & Gin, S. Impact of alkali on the passivation of silicate glass. *npj Mater Degrad* **2,** 927; 10.1038/s41529-018-0036-3 (2018).

78. Mercado-Depierre, S., Angeli, F., Frizon, F. & Gin, S. Antagonist effects of calcium on borosilicate glass alteration. *Journal of Nuclear Materials* **441,** 402–410; 10.1016/j.jnucmat.2013.06.023 (2013).

79. Fournier, M. *et al.* Effect of pH on the stability of passivating gel layers formed on International Simple Glass. *Journal of Nuclear Materials* **524,** 21–38; 10.1016/j.jnucmat.2019.06.029 (2019).

80. Peuget, S., Tribet, M., Mougnaud, S., Miro, S. & Jégou, C. Radiations effects in ISG glass: from structural changes to long-term aqueous behavior. *npj Mater Degrad* **2,** 243; 10.1038/s41529-018-0044-3 (2018).

81. Mougnaud, S. *et al.* Heavy ion radiation ageing impact on long-term glass alteration behavior. *Journal of Nuclear Materials* **510,** 168–177; 10.1016/j.jnucmat.2018.07.046 (2018).

82. Boizot, B. *et al.* Irradiation effects in simplified nuclear waste glasses. *Nuclear Instruments and Methods in Physics Research Section B: Beam Interactions with Materials and Atoms* **240,** 146–151; 10.1016/j.nimb.2005.06.105 (2005).

83. Mir, A. H., Monnet, I., Boizot, B., Jégou, C. & Peuget, S. Electron and electron-ion sequential irradiation of borosilicate glasses: Impact of the pre-existing defects. *Journal of Nuclear Materials* **489,** 91–98; 10.1016/j.jnucmat.2017.03.047 (2017).

84. McLoughlin, S. D. *et al.* The long term corrosion of glasses: analytical results after 32 years of burial at Ballidon. *Glass Technology: European Journal of Glass Science and Technology Part A* **47,** 59–67 (2006).

85. Emami, M., Nekouei, S., Ahmadi, H., Pritzel, C. & Trettin, R. Iridescence in Ancient Glass: A Morphological and Chemical Investigation. *Int J Appl Glass Sci* **7,** 59–68; 10.1111/ijag.12182 (2016).

86. Frugier, P. *et al.* SON68 nuclear glass dissolution kinetics: Current state of knowledge and basis of the new GRAAL model. *Journal of Nuclear Materials* **380,** 8–21; 10.1016/j.jnucmat.2008.06.044 (2008).

87. Chave, T., Frugier, P., Ayral, A. & Gin, S. Solid state diffusion during nuclear glass residual alteration in solution. *Journal of Nuclear Materials* **362,** 466–473; 10.1016/j.jnucmat.2007.01.095 (2007).

88. Bouakkaz, R., Abdelouas, A., El Mendili, Y., Grambow, B. & Gin, S. SON68 glass alteration under Si-rich solutions at low temperature (35–90 °C): kinetics, secondary phases and isotopic exchange studies. *RSC Adv.* **6,** 72616–72633; 10.1039/C6RA12404F (2016).

89. Marquis, E. A., Geiser, B. P., Prosa, T. J. & Larson, D. J. Evolution of tip shape during field evaporation of complex multilayer structures. *Journal of microscopy* **241,** 225–233; 10.1111/j.1365-2818.2010.03421.x (2011).

90. Gin, S. *et al.* The controversial role of inter-diffusion in glass alteration. *Chemical Geology* **440,** 115–123; 10.1016/j.chemgeo.2016.07.014 (2016).

91. Marie Collin *et al.* ToF-SIMS depth profiling of altered glass (2019).

92. Ngo, D. *et al.* Spectroscopic ellipsometry study of thickness and porosity of the alteration layer formed on international simple glass surface in aqueous corrosion conditions. *npj Mater Degrad* **2,** 8; 10.1038/s41529-018-0040-7 (2018).

93. Putnis, A. Mineral Replacement Reactions. *Reviews in Mineralogy and Geochemistry* **70,** 87-124; 10.2138/rmg.2009.70.0 (2009).

94. Gin, S. *et al.* Origin and consequences of silicate glass passivation by surface layers. *Nature communications* **6,** 6360; 10.1038/ncomms7360 (2015).

95. Strachan, D. *et al.* On the dissolution of a borosilicate glass with the use of isotopic tracing – Insights into the mechanism for the long-term dissolution rate. *Geochimica et Cosmochimica Acta* **318,** 213–229; 10.1016/j.gca.2021.12.004 (2022).

96. Trivelpiece, C. L., Rice, J. A. & Pantano, C. G. *Glass Composition and Solution Speciation Effects on Stage III Dissolution* (Pennsylvania, 2017).

97. Ferrand, K., Abdelouas, A. & Grambow, B. Water diffusion in the simulated French nuclear waste glass SON 68 contacting silica rich solutions: Experimental and modeling. *Journal of Nuclear Materials* **355,** 54–67; 10.1016/j.jnucmat.2006.04.005 (2006).

98. Gislason, S. R. & Oelkers, E. H. Mechanism, rates, and consequences of basaltic glass dissolution: II. An experimental study of the dissolution rates of basaltic glass as a function of pH and temperature. *Geochimica et Cosmochimica Acta* **67,** 3817–3832; 10.1016/S0016-7037(03)00176-5 (2003).

99. Frugier, P., Fournier, M. & Gin, S. Modeling Resumption of Glass Alteration Due to Zeolites Precipitation. *Procedia Earth and Planetary Science* **17,** 340–343; 10.1016/j.proeps.2016.12.086 (2017).

100. Parruzot, B. *et al.* Multi-glass investigation of Stage III glass dissolution behavior from 22 to 90°C triggered by the addition of zeolite phases. *Journal of Nuclear Materials* (2019).

101. Grambow, B. & Strachan, D. M. Leach testing of waste glasses under near-saturation conditions. *Materials Research Society Symposium Proceedings* **26** (1984).

102. Inagaki, Y., Kikunaga, T., Idemitsu, K. & Arima, T. Initial Dissolution Rate of the International Simple Glass as a Function of pH and Temperature Measured Using Microchannel Flow-Through Test Method. *Int J Appl Glass Sci* **4,** 317–327; 10.1111/ijag.12043 (2013).

103. Frugier, P., Gin, S. & Jégou, C. Affinity Rate Law Failure to Describe Sodium Borosilicate Glass Alteration Kinetics. *Materials Research Society Symposium Proceedings* **807** (2004).

104. Crovisier, J. L., Honnorez. J. & Eberhart, J. P. Dissolution of basaltic glass in seawater: Mechanism and rate. *Geochimica et Cosmochimica Acta,* 2977–2990 (1987).

105. Valle, N. *et al.* Elemental and isotopic (29Si and 18O) tracing of glass alteration mechanisms. *Geochimica et Cosmochimica Acta* **74,** 3412–3431; 10.1016/j.gca.2010.03.028 (2010).

106. Reiser, J. T. *et al.* Sol-Gel Synthesis and Characterization of Gels with Compositions Relevant to Hydrated Glass Alteration Layers. *ACS omega* **4,** 16257–16269; 10.1021/acsomega.9b00491 (2019).

107. Bindini, E. *et al.* Following in Situ the Degradation of Mesoporous Silica in Biorelevant Conditions: At Last, a Good Comprehension of the Structure Influence. *ACS applied materials & interfaces* **12,** 13598–13612; 10.1021/acsami.9b19956 (2020).

108. Iler, R. K. *The Chemistry of Silica. Solubility, Polymerization, Colloid and Surface Properties, and Biochemistry* (John Wiley & Sons, New York, 1979).

109. Brinker, C. J. & Scherer, G. W. *SOL-GEL SCIENCE. The Physics and Chemistry of Sol-Gel Processing* (Academic Press, INC. An Imprint of Elsevier, San Siego, 1990).

110. Putnis, A. Materials science. Why mineral interfaces matter. *Science (New York, N.Y.)* **343,** 1441–1442; 10.1126/science.1250884 (2014).

111. Putnis, A. Mineral replacement reactions: from macroscopic observations to microscopic mechanisms. *Mineral. mag.* **66,** 689–708; 10.1180/0026461026650056 (2002).

112. Putnis, A. & Putnis, C. V. The mechanism of reequilibration of solids in the presence of a fluid phase. *Journal of Solid State Chemistry* **180,** 1783–1786; 10.1016/j.jssc.2007.03.023 (2007).

113. Fournier, M., Gin, S. & Frugier, P. Resumption of nuclear glass alteration: State of the art. *Journal of Nuclear Materials* **448,** 348–363; 10.1016/j.jnucmat.2014.02.022 (2014).

114. Fournier, M., Frugier, P. & Gin, S. Application of GRAAL model to the resumption of International Simple Glass alteration. *npj Mater Degrad* **2,** 89; 10.1038/s41529-018-0043-4 (2018).

115. Baucke, F. G. K. Functioning of glass electrodes. A discussion of interfacial equilibria. *Physics and Chemistry of Glasses* (2001).

116. Conradt, R. A proposition for an improved theoretical treatment of the corrosion of multi-component glasses. *Journal of Nuclear Materials,* 19–26 (2001).

117. Behrens, S. H. & Grier, D. G. The charge of glass and silica surfaces. *The Journal of Chemical Physics* **115,** 6716–6721; 10.1063/1.1404988 (2001).

118. Fleming, B. A. Kinetics of Reaction between Silicic acid and Amorphous Silica Surfaces in NaCl Solutions. *Journal of colloid and interface science* **110,** 40–64 (1986).

119. Doremus, R. H. Time Depencende of the Reaction of Water with Glass. *Nuclear and Chemical Waste Management,* 119–123 (1981).

120. Rieke, P. C., Kerisit, S., Ryan, J. V. & Neeway, J. J. Adaptation of the GRAAL model of Glass Reactivity to accommodate non-linear diffusivity. *Journal of Nuclear Materials* **512,** 79–93; 10.1016/j.jnucmat.2018.09.058 (2018).

121. Neeway, J. J. *et al.* Ion-Exchange Interdiffusion Model with Potential Application to Long-Term Nuclear Waste Glass Performance. *J. Phys. Chem. C* **120,** 9374–9384; 10.1021/acs.jpcc.6b03681 (2016).

122. Brantley, S. L., Kubicki, J. D. & White, A. F. *Kinetics of water-rock interaction* (Springer Verlag, New York, 2008).

123. Scholze, H. *Glas. Natur, Struktur und Eigenschaften.* 3rd ed. (Springer Berlin, Berlin, 1988).

124. Horacio E. Bergna and William O. Roberts. *COLLOIDAL SILICA. Fundamentals and Applications* (Taylor & Francis Group, LLC, 2006).

125. Rothbaum, H. P. & Rhode, A. G. Kinetics of Silica Polymerization and Deposition from Dilute Solutions between 5 and 180°C. *Journal of colloid and interface science* **71,** 533–559 (1979).

126. Tarutani, T. Polymerization of Silicic Acid - A Review. *Analytical Sciences* **5,** 245–252 (1989).

127. Weres, O., Yee, A. & Tsao, L. Kinetics of Silica Polymerization (1980).

128. Weres, O., Yee, A. & Tsao, L. Kinetics of Silica Polymerization. *Journal of colloid and interface science* **84,** 379–402 (1981).

129. Wilhelm, S. & Kind, M. Influence of pH, Temperature and Sample Size on Natural and Enforced Syneresis of Precipitated Silica. *Polymers* **7,** 2504–2521; 10.3390/polym7121528 (2015).

130. Kley, M. E. *Silica Particle Formation from Supersaturated Aqueous Solution and the Influence of Polymeric Additives* (Paderborn, 2017).

131. Schlomach, J. *Feststoffbildung bei technischen Fällprozessen. Untersuchungen zur industriellen Fällung von Siliziumdioxid und Calciumcarbonat* (Karlsruhe, 2006).

132. Pavlova, A., Trinh, T. T., van Santen, R. A. & Meijer, E. J. Clarifying the role of sodium in the silica oligomerization reaction. *Physical chemistry chemical physics : PCCP* **15,** 1123–1129; 10.1039/c2cp42436c (2013).

133. Parkhurst, D. L. & Appelo, C. Description of Input for PHREEQC Version 3—A Computer Program for Speciation, Batch-Reaction, One-Dimensional Transport, and Inverse Geochemical Calculations (2013).

134. Zhang, K., Li, S. Q. & Yan, Z. Optimization of high performance composite flocculant PFZSSB. *IOP Conf. Ser.: Earth Environ. Sci.* **68,** 12009; 10.1088/1755-1315/68/1/012009 (2017).

135. Wu, S.-H., Mou, C.-Y. & Lin, H.-P. Synthesis of mesoporous silica nanoparticles. *Chemical Society reviews* **42,** 3862–3875; 10.1039/c3cs35405a (2013).

136. Giffaut, E. *et al.* Andra thermodynamic database for performance assessment: ThermoChimie. *Applied Geochemistry* **49,** 225–236; 10.1016/j.apgeochem.2014.05.007 (2014).

137. Reiser, J. T. *et al.* Comparative structural investigations of nuclear waste glass alteration layers and sol-gel synthesized aerogels_Supplement. *npj Mater Degrad* **4,** 837; 10.1038/s41529-020-0109-y (2020).

138. Guo, X. *et al.* Near-field corrosion interactions between glass and corrosion resistant alloys. *npj Mater Degrad* **4,** 309; 10.1038/s41529-020-0114-1 (2020).

139. Lu, X., Deng, L., Kerisit, S. & Du, J. Structural role of ZrO2 and its impact on properties of boroaluminosilicate nuclear waste glasses. *npj Mater Degrad* **2,** 831; 10.1038/s41529-018-0041-6 (2018).

140. Ortoleva, P., Merino, E., Moore, C. & Chadam, J. Geochemical self-organization I; reaction-transport feedbacks and modeling approach. *American Journal of Science* **287,** 979–1007; 10.2475/ajs.287.10.979 (1987).

141. Egger, F. *Quantitative determination of water transport through porous alteration layers of borosilicate glasses in situ and in real time using fluid-cell Raman spectroscopy.* master thesis (2021).

142. Mercado-Depierre, S., Fournier, M., Gin, S. & Angeli, F. Influence of zeolite precipitation on borosilicate glass alteration under hyperalkaline conditions. *Journal of Nuclear Materials* **491,** 67–82; 10.1016/j.jnucmat.2017.04.043 (2017).

143. LaMer, V. K. & Dinegar, R. H. Theory, Production and Mechanism of Formation of Monodispersed Hydrosols. *Journal of the american chemical society* **72,** 4847–4854 (1950).

144. Milne, N. A. *et al.* Chemistry of silica scale mitigation for RO desalination with particular reference to remote operations. *Water research* **65,** 107–133; 10.1016/j.watres.2014.07.010 (2014).

145. Baronov, A., Bufkin, K., Shaw, D. W., Johnson, B. L. & Patrick, D. L. A simple model of burst nucleation. *Physical chemistry chemical physics : PCCP* **17,** 20846–20852; 10.1039/c5cp01745a (2015).

146. Steefel, C. I., Beckingham, L. E. & Landrot, G. Micro-Continuum Approaches for Modeling Pore-Scale Geochemical Processes. *Reviews in Mineralogy and Geochemistry* **80,** 217–246; 10.2138/rmg.2015.80.07 (2015).

147. Helebrant, A. Kinetics of corrosion of silicate glasses in aqueous solutions. *Ceramics,* 147–151 (1997).

148. Jégou, C., Gin, S. & Larché, F. Alteration kinetics of a simplified nuclear glass in an aqueous medium: effects of solution chemistry and of protective gel properties on diminishing the alteration rate. *Journal of Nuclear Materials,* 216–229 (2000).

149. Aagaard, P. & Helgeson, H. C. Thermodynamic and kinetic constraints on reaction rates among minerals and aqueous solutions. I. Theoretical considerations. *Journal of Science* **282,** 237–285 (1982).

150. Oelkers, E. H. General kinetic description of multioxide silicate mineral and glass dissolution. *Geochimica et Cosmochimica Acta* **65,** 3703–3719 (2001).

151. Köhler, S. J., Dufaud, F. & Oelkers, E. H. An experimental study of illite dissolution kinetics as a function of ph from 1.4 to 12.4 and temperature from 5 to 50°C. *Geochimica et Cosmochimica Acta* **67,** 3583–3594; 10.1016/S0016-7037(03)00163-7 (2003).

152. Wang, J. Thermodynamic equilibrium and kinetic fundamentals of oxide dissolution in aqueous solution. *J. Mater. Res.* **35,** 898–921; 10.1557/jmr.2020.81 (2020).

153. Gin, S. *et al.* Can a simple topological-constraints-based model predict the initial dissolution rate of borosilicate and aluminosilicate glasses? *npj Mater Degrad* **4,** 409; 10.1038/s41529-020-0111-4 (2020).

154. Krishnan, N. M. A. *et al.* Predicting the dissolution kinetics of silicate glasses using machine learning (2018).

155. Munier, I., Crovisier, J.-L., Grambow, B., Fritz, B. & Clément, A. Modelling the alteration gel composition of simplified borosilicate glasses by precipitation of an ideal solid solution in equilibrium with the leachant. *Journal of Nuclear Materials* **324,** 97–115; 10.1016/j.jnucmat.2003.08.033 (2004).

156. Doremus, R. H. *Treatise on materials science and technology, Vol. 17* (Acad. Press, New York, 1979).

157. Steefel, C. I. *et al.* Reactive transport codes for subsurface environmental simulation. *Comput Geosci* **19,** 445–478; 10.1007/s10596-014-9443-x (2015).

158. Gin, S. *et al.* Insights into the mechanisms controlling the residual corrosion rate of borosilicate glasses. *npj Mater Degrad* **4,** 310; 10.1038/s41529-020-00145-2 (2020).

159. Smith, E. & Dent, G. *Modern Raman spectroscopy. A practical approach* (Wiley, Hoboken NJ, 2019).

160. Everall, N. Depth Profiling with Confocal Raman Microscopy, Part II. *Spectroscopyonline* (2004).

161. Everall, N. The Influence of Out-of-Focus Sample Regions on the Surface Specificity of Confocal Raman Microscopy. *Applied spectroscopy* **62** (2008).

162. Everall, N. J. Confocal Raman Microscopy: Why the Depth Resolution and Spatial Accuracy Can Be Much Worse than You Think. *Applied spectroscopy* **54** (2000).

163. Everall, N. J. Confocal Raman microscopy: common errors and artefacts. *The Analyst* **135,** 2512–2522; 10.1039/c0an00371a (2010).

164. Smekal, A. Zur Quantentheorie der Dispersion. *Naturwissenschaften* **11,** 873–875; 10.1007/BF01576902 (1923).

165. RAMAN, C. V. & KRISHNAN, K. S. The Negative Absorption of Radiation. *Nature* **122,** 12–13; 10.1038/122012b0 (1928).

166. Gardiner, D. J. & Graves, P. R. (eds.). *Practical Raman Spectroscopy* (Springer Berlin Heidelberg, Berlin, Heidelberg, 1989).

167. Salzer, R. & Siesler, H. W. *Infrared and Raman Spectroscopic Imaging.* 2nd ed. (Wiley-VCH, Weinheim, 2014).

168. Hauke, K., Kehren, J., Böhme, N., Zimmer, S. & Geisler, T. In Situ Hyperspectral Raman Imaging: A New Method to Investigate Sintering Processes of Ceramic Material at High-temperature. *Applied Sciences* **9,** 1310; 10.3390/app9071310 (2019).

169. Stange, K., Lenting, C. & Geisler, T. Insights into the evolution of carbonate-bearing kaolin during sintering revealed by in situ hyperspectral Raman imaging. *J Am Ceram Soc* **101,** 897–910; 10.1111/jace.15209 (2018).

170. Böhme, N., Hauke, K., Neuroth, M. & Geisler, T. In Situ Hyperspectral Raman Imaging of Ternesite Formation and Decomposition at High Temperatures. *Minerals* **10,** 287; 10.3390/min10030287 (2020).

171. Böhme, N., Hauke, K., Neuroth, M. & Geisler, T. In situ Raman imaging of high-temperature solid-state reactions in the CaSO4–SiO2 system. *Int J Coal Sci Technol* **6,** 247–259; 10.1007/s40789-019-0252-7 (2019).

172. HORIBA Jobin Yvon Ltd. *Horiba LabRAM User Guide. An Introduction to the Software and Hardware* (2004).

173. Kim, S. B., Hammaker, R. M. & Fateley, W. G. Calibrating Raman Spectrometers Using a Neon Lamp. *Applied spectroscopy* **40** (1986).

174. Neuville, D. R. & Mysen, B., O. Role of aluminium in the silicate network: In situ, high-temperature study of oxide glasses and melts on the join SiO_2-$NaAlO_2$. *Geochimica et Cosmochimica Acta* **60,** 1727–1737 (1996).

175. Long, D. A. *Raman spectroscopy* (New York, 1977).

176. David, T. Headspace Raman Spectroscopy. *Spectroscopy Solutions for Materials Analysis* (2014).

177. Rudolph, W. W., Irmer, G. & Königsberger, E. Speciation studies in aqueous HCO3(-)-CO3(2-) solutions. A combined Raman spectroscopic and thermodynamic study. *Dalton transactions (Cambridge, England : 2003),* 900–908; 10.1039/b713254a (2008).

178. Meyer, E. F. A Note on Covariance in Propagation of Uncertainty. *Journal of Chemical Education* **74,** 1339–1340 (1997).

179. Malitson, I. H., Murphy, F. V. & Rodney, W. S. Refractive Index of Synthetic Sapphire. *J. Opt. Soc. Am.* **48,** 72; 10.1364/JOSA.48.000072 (1958).

180. Bashkatov, A. N. & Genina, E. A. Water refractive index in dependence on temperature and wavelength: a simple approximation, edited by V. V. Tuchin (SPIE2012), pp. 393–395.

181. Schindelin, J. *et al.* Fiji: an open-source platform for biological-image analysis. *Nature methods* **9,** 676–682; 10.1038/nmeth.2019 (2012).

182. Yadav, A. K. & Singh, P. A review of the structures of oxide glasses by Raman spectroscopy. *RSC Adv.* **5,** 67583–67609; 10.1039/C5RA13043C (2015).

183. Manara, D., Grandjean, A. & Neuville, D. R. Advances in understanding the structure of borosilicate glasses: A Raman spectroscopy study. *American Mineralogist* **94,** 777–784; 10.2138/am.2009.3027 (2009).

184. Wang, F. *et al.* Multiscale Investigation of the Mechanisms Controlling the Corrosion of Borosilicate Glasses in Hyper-Alkaline Media. *J. Phys. Chem. C*; 10.1021/acs.jpcc.0c08691 (2020).

185. Neeway, J. J. *et al.* Acceleration of glass alteration rates induced by zeolite seeds at controlled pH. *Applied Geochemistry* **113,** 104515; 10.1016/j.apgeochem.2019.104515 (2020).

186. Piovesan, V. *et al.* Chemical durability of peraluminous glasses for nuclear waste conditioning. *npj Mater Degrad* **2,** 927; 10.1038/s41529-018-0028-3 (2018).

187. Mann, C. *et al.* Influence of young cement water on the corrosion of the International Simple Glass. *npj Mater Degrad* **3,** 23; 10.1038/s41529-018-0059-9 (2019).

188. Deshpande, R., Hua, D.-W., Smith, D. M. & Brinker, C. J. Pore structure evolution in silica gel during aging/drying. III. Effects of surface tension. *Journal of Non-Crystalline Solids* **144,** 32–44 (1992).

189. Auerbach, S. M., Carrado, K. A. & Dutta, P. K. *Handbook of zeolite science and technology* (M. Dekker, New York, 2003).

190. Lafuente, B., Downs, R. T., Yang, H. & Stone, N. The power of databases: the RRUFF project. In *Highlights in mineralogical crystallography,* edited by R. M. Danisi & T. Armbruster (Walter de Gruyter GmbH, Berlin, Boston, 2016), pp. 1–30.

191. Wopenka, B., Freeman, J. J. & Nikischer, T. Raman Spectroscopic Identification of Fibrous Natural Zeolites. *Applied spectroscopy* **52,** 54–63 (1998).

192. Gatta, G. D. *et al.* A multi-methodological study of the (K,Ca)-variety of the zeolite merlinoite. *Mineral. mag.* **79,** 1755–1767; 10.1180/minmag.2015.079.7.03 (2015).

193. Aguiar, H., Serra, J., González, P. & León, B. Structural study of sol–gel silicate glasses by IR and Raman spectroscopies. *Journal of Non-Crystalline Solids* **355,** 475–480; 10.1016/j.jnoncrysol.2009.01.010 (2009).

194. Lee, S. Q. & Condrate Sr, R. A. The infrared and Raman spectra of ZrO2-SiO2 glasses prepared by a sol-gel process. *Journal of Materials Science* **23,** 2951–2959 (1988).

195. Halasz, I., Agarwal, M., Li, R. & Miller, N. Vibrational spectra and dissociation of aqueous Na2SiO3 solutions. *Catal Lett* **117,** 34–42; 10.1007/s10562-007-9141-6 (2007).

196. González, P. *et al.* Raman spectroscopic study of bioactive silica based glasses. *Journal of Non-Crystalline Solids* **320,** 92–99; 10.1016/S0022-3093(03)00013-9 (2003).

197. Celestian, A. J., Lively, J. & Xu, W. In Situ Cs and H Exchange into Gaidonnayite and Proposed Mechanisms of Ion Diffusion. *Inorganic chemistry* **58,** 1919–1928; 10.1021/acs.inorgchem.8b02834 (2019).

198. Kirkpatrick, R. J., Yarger, J. L., McMillan, Paul, F., Yu, P. & Cong, X. Raman Spectroscopy of C-S-H, Tobermorite, and Jennite. *Advanced Cement Based Materials* **5,** 93–99 (1997).

199. Gout, R., Pokrovski, G. S., Schott, J. & Zwick, A. Raman Spectroscopic Study of Aluminum Silicate Complexes at 20°C in Basic Solutions. *Journal of Solution Chemistry* **29,** 1173–1186 (2000).

200. Zotov, N. & Keppler, H. In-situ Raman spectra of dissolved silica species in aqueous fluids to 900 °C and 14 kbar. *American Mineralogist* **85,** 600–604; 10.2138/am-2000-0423 (2000).

201. Coombs, D. S. *et al.* Recommended nomenclature for zeolite minerals: report of the subcommittee on zeolites of the International Mineralogical Association, Commission on New Minerals and Mineral Names. *Mineral. mag.* **62,** 533–571; 10.1180/002646198547800 (1998).

202. Buzgar, N. & Apopei, A. I. The Raman study of certain carbonates. *Geologie* **55,** 97–112 (2009).

203. Krishnan, R. S. Raman Spectrum of Diamond. *Nature,* 171 (1945).

204. Jantzen, C. M., Brown, K. G. & Pickett, J. B. Durable Glass for Thousands of Years. *International Journal of Applied Glass Science* **1,** 38–62; 10.1111/j.2041-1294.2010.00007.x (2010).

205. KOBAYASHI, T., SASAKI, T., TAKAGI, I. & MORIYAMA, H. Solubility of Zirconium(IV) Hydrous Oxides. *Journal of Nuclear Science and Technology* **44,** 90–94; 10.1080/18811248.2007.9711260 (2007).

206. Debure, M., Windt, L. de, Frugier, P. & Gin, S. HLW glass dissolution in the presence of magnesium carbonate: Diffusion cell experiment and coupled modeling of diffusion and geochemical interactions. *Journal of Nuclear Materials* **443,** 507–521; 10.1016/j.jnucmat.2013.07.068 (2013).

207. Debure, M., Frugier, P., Windt, L. de & Gin, S. Dolomite effect on borosilicate glass alteration. *Applied Geochemistry* **33,** 237–251; 10.1016/j.apgeochem.2013.02.019 (2013).

208. Fournier, M., Frugier, P. & Gin, S. Resumption of Alteration at High Temperature and pH: Rates Measurements and Comparison with Initial Rates. *Procedia Materials Science* **7,** 202–208; 10.1016/j.mspro.2014.10.026 (2014).

209. Goldberg, S. & Glaubig, R. A. Boron Adsorption and Silicon Release by the Clay Minerals Kaolinite, Montmorillonite, and Illite. *Soil Science Society of America Journal* **50,** 1442–1448; 10.2136/sssaj1986.03615995005000060013x (1986).

210. Keren, R. Boron Adsorption by Clay Minerals Using a Phenomenological Equation1. *Clays and Clay Minerals* **29,** 198–204; 10.1346/CCMN.1981.0290305 (1981).

211. Fournier, M., Frugier, P. & Gin, S. Effect of Zeolite Formation on Borosilicate Glass Dissolution Kinetics. *Procedia Earth and Planetary Science* **7,** 264–267; 10.1016/j.proeps.2013.03.085 (2013).

212. Gin, S., Jollivet, P., Mestre, J. P., Jullien, M. & Pozo, C. French SON 68 nuclear glass alteration mechanisms on contact with clay media. *Applied Geochemistry* **16,** 861–881 (2001).

213. Xu, Y. & Sommerdijk, N. A. J. M. Aragonite formation in confinements: A step toward understanding polymorph control. *Proceedings of the National Academy of Sciences of the United States of America* **115,** 8469–8471; 10.1073/pnas.1811696115 (2018).

214. Zeng, M. *et al.* Confinement generates single-crystal aragonite rods at room temperature. *Proceedings of the National Academy of Sciences of the United States of America* **115,** 7670–7675; 10.1073/pnas.1718926115 (2018).

215. Sun, W., Jayaraman, S., Chen, W., Persson, K. A. & Ceder, G. Nucleation of metastable aragonite CaCO3 in seawater. *Proceedings of the National Academy of Sciences of the United States of America* **112,** 3199–3204; 10.1073/pnas.1423898112 (2015).

216. Ramakrishna, C., Thenepalli, T. & Ahn, J. W. A Brief review of Aragonite Precipitated Calcium Carbonate (PCC) Synthesis Methods and Its Applications. *Korean Chemical Engineering Research* **55,** 443–455 (2017).

217. Mann, C., Eskelsen, J. R., Leonard, D. N., Pierce, E. & Corkhill, C. L. The dissolution of simulant vitrified intermediate level nuclear waste in young cement water. *MRS Adv.* **5,** 131–140; 10.1557/adv.2020.40 (2020).

218. Guo, X. *et al.* Self-accelerated corrosion of nuclear waste forms at material interfaces. *Nat. Mater.* **16,** 243; 10.1038/s41563-019-0579-x (2020).

219. Gin, S., Delaye, J.-M., Angeli, F. & Schuller, S. Aqueous alteration of silicate glass: state of knowledge and perspectives. *npj Mater Degrad* **5,** 2; 10.1038/s41529-021-00190-5 (2021).

220. Neeway, J. J., Rieke, P. C., Parruzot, B. P., Ryan, J. V. & Asmussen, R. M. The dissolution behavior of borosilicate glasses in far-from equilibrium conditions. *Geochimica et Cosmochimica Acta* **226,** 132–148; 10.1016/j.gca.2018.02.001 (2018).

221. Elia, A., Ferrand, K. & Lemmens, K. Determination of the Forward Dissolution Rate for International Simple Glass in Alkaline Solutions. *MRS Adv.* **2,** 661–667; 10.1557/adv.2016.672 (2017).

222. Bjorn O. Mysen. Phosphorus solubility mechanisms in haplogranitic aluminosilicate glass and melt: effect of temperature and aluminum content. *Contrib Mineral Petrol* **133,** 38–50; 10.1007/s004100050435 (1998).

223. Marshall, W. L. & Begun, G. M. Raman spectroscopy of aqueous phosphate solutions at temperatures up to 450 °C. Two liquid phases, supercritical fluids, and pyro- to ortho-phosphate conversions. *J. Chem. Soc., Faraday Trans. 2* **85,** 1963–1978; 10.1039/F29898501963 (1989).

224. Preston, C. M. & Adams, W. A. A laser Raman spectroscopic study of aqueous orthophosphate salts. *J. Phys. Chem.* **83,** 814–821; 10.1021/j100470a011 (1979).

225. Anedda, A. *et al.* Surface hydroxyls in porous silica: a Raman spectroscopy study. *Materials Science and Engineering: C* **23,** 1069–1072; 10.1016/j.msec.2003.09.125 (2003).

226. Frost, R. L., Xi, Y., Scholz, R. & Belotti, F. M. Infrared and Raman spectroscopic characterization of the phosphate mineral kosnarite KZr2(PO4)3 in comparison with other pegmatitic phosphates. *Transition Met Chem* **37,** 777–782; 10.1007/s11243-012-9652-x (2012).

227. Kashchiev, D. Note: on the critical supersaturation for nucleation. *The Journal of Chemical Physics* **134,** 196102; 10.1063/1.3593401 (2011).

228. Kožíšek, Z., Sato, K., Ueno, S. & Demo, P. Formation of crystal nuclei near critical supersaturation in small volumes. *The Journal of Chemical Physics* **134,** 94508; 10.1063/1.3559453 (2011).

229. Syed, K. A., Pang, S.-F., Zhang, Y. & Zhang, Y.-H. Micro-Raman observation on the H2PO4(-) association structures in a supersaturated droplet of potassium dihydrogen phosphate (KH2PO4). *The Journal of Chemical Physics* **138,** 24901; 10.1063/1.4773585 (2013).

230. Parruzot, B. *et al.* Method for the in situ Measurement of pH and Alteration Extent for Aluminoborosilicate Glasses Using Raman Spectroscopy. *Analytical chemistry* **90,** 11812–11819; 10.1021/acs.analchem.8b00960 (2018).

231. Krezel, A. & Bal, W. A formula for correlating pKa values determined in D2O and H2O. *Journal of inorganic biochemistry* **98,** 161–166; 10.1016/j.jinorgbio.2003.10.001 (2004).

232. Kral, A. G., Ziegler, A., Tütken, T. & Geisler, T. Experimental Aqueous Alteration of Cortical Bone Microarchitecture Analyzed by Quantitative Micro-Computed Tomography. *Front. Earth Sci.* **9**; 10.3389/feart.2021.609496 (2021).

233. Deng, H., Poonoosamy, J. & Molins, S. A reactive transport modeling perspective on the dynamics of interface-coupled dissolution-precipitation. *Applied Geochemistry* **137,** 105207; 10.1016/j.apgeochem.2022.105207 (2022).

234. Poonoosamy, J. *et al.* Effects of solution supersaturation on barite precipitation in porous media and consequences on permeability: Experiments and modelling. *Geochimica et Cosmochimica Acta* **270,** 43–60; 10.1016/j.gca.2019.11.018 (2020).

235. Varzina, A. *et al.* A new concept for pore-scale precipitation-dissolution modelling in a lattice Boltzmann framework – Application to portlandite carbonation. *Applied Geochemistry* **123,** 104786; 10.1016/j.apgeochem.2020.104786 (2020).

236. Steefel, C. I. & Maher, K. Fluid-Rock Interaction: A Reactive Transport Approach. *Reviews in Mineralogy and Geochemistry* **70,** 485–532; 10.2138/rmg.2009.70.11 (2009).

237. Steefel, C. I., DePaolo, D. J. & Lichtner, P. C. Reactive transport modeling: An essential tool and a new research approach for the Earth sciences. *Earth and Planetary Science Letters* **240,** 539–558; 10.1016/j.epsl.2005.09.017 (2005).

238. Li, L., Peters, C. A. & Celia, M. A. Upscaling geochemical reaction rates using pore-scale network modeling. *Advances in Water Resources* **29,** 1351–1370; 10.1016/j.advwatres.2005.10.011 (2006).

239. Lichtner, P. C. Critique of dual continuum formulations of multicomponent reactive transport in fractured porous media. In *Dynamics of fluids in fractured rock,* edited by B. Faybishenko, P. A. Witherspoon, S. M. Benson, P. A. Witherspoon & S. Benson (American Geophysical Union, Washington, DC, 2000), Vol. 122, pp. 281–298.

240. LeVeque, R. J. *Finite Volume Methods for Hyperbolic Problems* (Cambridge University Press, 2012).

241. Malcherek, A. Numerische Methoden der Strömungsmechanik.

12

Appendix

12.1 Composition of the sampled solutions of Exp. II and Exp. III

Table S 1: Composition of the sampled solution of Exp. II including pH measurements. In addition, the altered glass fraction (f_{AG}) is given that is based on the measured dissolved boron according to Equation (32).

Sample name	*Sampling time (h)*	*Final $pH_{21\,°C}$*	*B (mg/l)*	*Si (mg/l)*	*Na (mg/l)*	f_{AG} *(%)*
Initial solution	0.00	6.81	0.04 ± 0.01	0.18 ± 0.03	2.67 ± 0.06	-
D_2O solution	0.00	7.59	0.14 ± 0.04	2.54 ± 0.37	3.73 ± 0.15	-
Sample 1	9.50	7.71	3.56 ± 0.19	20.05 ± 0.99	9.52 ± 0.05	1.10 ± 0.05
Sample 2	23.67		3.96 ± 0.01	17.68 ± 0.97	9.66 ± 0.38	2.93 ± 0.05
Sample 3	28.97	7.85	6.20 ± 0.15	21.27 ± 0.60	14.05 ± 0.22	3.58 ± 0.06
Sample 4	44.38	7.90	6.55 ± 0.23	22.89 ± 1.04	15.24 ± 0.65	5.57 ± 0.13
Sample 5	53.67		6.75 ± 0.09	21.67 ± 0.78	15.91 ± 0.17	6.81 ± 0.14
Sample 6	67.50	7.94	12.65 ± 0.07	32.95 ± 1.40	26.74 ± 1.34	7.97 ± 0.14
Sample 7	90.00	8.09	9.57 ± 0.28	22.42 ± 1.08	22.04 ± 0.08	9.40 ± 0.18
Sample 8	120.00	8.25	12.89 ± 0.19	38.58 ± 2.64	30.06 ± 0.76	11.96 ± 0.21
Sample 9	141.32	8.25	13.99 ± 0.28	45.46 ± 1.28	31.35 ± 0.32	13.94 ± 0.25
Sample 10	163.77	8.28	15.13 ± 0.28	46.40 ± 2.17	33.53 ± 0.63	16.20 ± 0.29
Sample 11	186.60	8.31	16.55 ± 0.33	56.36 ± 1.38	36.99 ± 0.29	18.71 ± 0.34
Sample 12	224.60	8.43	17.81 ± 0.60	64.15 ± 4.02	40.90 ± 0.31	23.21 ± 0.48
Sample 13 (D_2O)	476.00	9.99	637.8 ± 8.2	245.3 ± 3.5	1296.7 ± 24.8	43.44 ± 0.74

Table S 2: Composition of the sampled solution of Exp. III including pH measurements. In addition, the altered glass fraction (f_{AG}) is given that is based on the measured dissolved boron according to Equation (32).

Sample name	*Sampling time (h)*	*Final* $pH_{21°C}$	*B (mg/l)*	*Si (mg/l)*	*Na (mg/l)*	f_{AG} *(%)*
Initial solution A	0.00	10.0	0.08 ± 0.08	435 ± 10	274.55 ± 0.4	-
Initial solution B	0.00	10.0	0.02 ± 0.04	548 ± 12	257.96 ± 11.6	-
D_2O solution	0.00	9.9	0.11 ± 0.01	628 ± 44	307.0 ± 20.8	-
Sample 1 (A)	1.33	10.1	3.59 ± 0.07	434 ± 32	270.6 ± 12.3	0.17 ± 0.01
Sample 2 (A)	2.93	10.1	4.37 ± 0.21	436 ± 13	289.7 ± 25.8	0.43 ± 0.01
Sample 3 (A)	5.15	10.0	4.52 ± 0.04	43 ± 24	272.8 ± 4.6	0.79 ± 0.01
Sample 4 (A)	14.42	10.3	3.94 ± 0.44	413 ± 29	275.8 ± 24.5	2.1 ± 0.1
Sample 5 (A)	20.35	10.2	4.33 ± 0.04	429 ± 13	283.7 ± 4.2	3.1 ± 0.7
Sample 6 (A)	25.57	10.2	3.91 ± 0.30	424 ± 12	278.0 ± 26.0	3.8 ± 0.1
Sample 7 (A)	30.97	10.2	4.04 ± 0.08	443 ± 48	275.3 ± 4.6	4.6 ± 0.1
Sample 8 (A)	40.45	10.2	3.60 ± 0.49	427 ± 51	278.2 ± 32.9	5.82 ± 0.22
Sample 9 (A)	49.87	10.2	3.86 ± 0.03	444 ± 14	274.9 ± 4.9	7.14 ± 0.18
Sample 10 (A)	55.42	10.2	3.31 ± 0.07	399 ± 38	272.1 ± 8.7	7.80 ± 0.16
Sample 11 (A)	64.73	10.2	3.57 ± 0.01	410 ± 21	284.1 ± 1.6	9.01 ± 0.12
Sample 12 (A)	71.85	10.4	3.26 ± 0.06	355 ± 26	239.7 ± 1.2	9.85 ± 0.10
Sample 13 (A)	78.93	10.3	3.65 ± 0.41	406 ± 58	276.8 ± 16.7	10.78 ± 0.17
Sample 14 (A)	87.45	10.3	4.01 ± 0.13	425 ± 6	291.2 ± 17.2	12.02 ± 0.17
Sample 15 (A)	96.87	10.3	3.67 ± 0.12	399 ± 29	274.9 ± 32.05)	13.27 ± 0.16
Sample 16 (B)	101.80	10.2	3.33 ± 0.07	404 ± 10	261.9 ± 38.26)	13.87 ± 0.15
Sample 17 (B)	111.93	10.3	3.06 ± 0.06	434 ± 11	275.6 ± 5.22)	14.99 ± 0.12
Sample 18 (B)	120.25	10.3	2.71 ± 0.29	432 ± 57	285.4 ± 12.63)	15.80 ± 0.17
Sample 19 (B)	125.62	10.2	3.11 ± 0.05	433 ± 16	279.7 ± 3.09)	16.40 ± 0.16
Sample 20 (B)	135.63	10.3	2.47 ± 0.18	397 ± 10	259.3 ± 23.28)	17.29 ± 0.17
Sample 21 (B)	145.03	10.3	2.73 ± 0.20	424 ± 11	277.5 ± 24.91)	17.72 ± 0.18
Sample 22 (B)	166.25	10.2	10.7 ± 1.5	448 ± 28	277 ± 42)	19.69 ± 0.44
Sample 23 (B)	175.28	10.3	2.31 ± 0.04	445 ± 13	279 ± 37	20.44 ± 0.41
Sample 24 (B)	184.77	10.4	1.91 ± 0.27	434 ± 19	276.9 ± 42.6	21.08 ± 0.45
Sample 25 (B)	195.08	10.3	2.15 ± 0.02	420 ± 2	282.1 ± 3.1	21.88 ± 0.41

Sample name	*Sampling time (h)*	*Final $pH_{21°C}$*	*B (mg/l)*	*Si (mg/l)*	*Na (mg/l)*	f_{AG} *(%)*
Sample 26 (B)	197.98	10.3	1.87 ± 0.27	442 ± 41	272.1 ± 41.6	22.07 ± 0.42
Sample 27 (B)	207.72	10.3	2.12 ± 0.01	428 ± 10	280.0 ± 1.6	22.81 ± 0.38
Sample 28 (B)	217.87	10.3	1.77 ± 0.20	435 ± 60	265.1 ± 4.4	23.45 ± 0.40
Sample 29 (B)	239.58	10.3	2.21 ± 0.07	434 ± 11	290.7 ± 10.9	25.17 ± 0.34
Sample 30 (B)	240.80	10.1	1.74 ± 0.42	353 ± 33	275.7 ± 10.0	25.24 ± 0.36
Sample 31 (B)	242.48	10.2	1.92 ± 0.26	448 ± 7	280.9 ± 14.3	25.36 ± 0.36
Sample 32 (D2O)	264.08	9.8	6.09 ± 0.23	113.2 ± 4.1	86.8 ± 1.9	25.71 ± 0.37
Sample 33 (Si-free)	268.60	9.3	1.93 ± 0.15	14.1 ± 1.8	8.87 ± 0.25	26.02 ± 0.37
Sample 34 (Si-free)	278.00	9.3	1.66 ± 0.08	13.2 ± 0.6	7.84 ± 0.24	26.58 ± 0.35
Sample 35 (Si-free)	287.85	9.2	1.57 ± 0.07	10.7 ± 0.2	7.68 ± 0.28	27.12 ± 0.33
Sample 36 (Si-free)	294.63	9.3	1.58 ± 0.13	10.7 ± 1.0	7.74 ± 0.14	27.50 ± 0.32
Sample 37 (Si-free)	305.42	9.3	1.64 ± 0.03	10.9 ± 0.6	7.73 ± 0.34	28.13 ± 0.28
Sample 38 (Si-free)	311.43	9.3	1.75 ± 0.07	11.2 ± 0.4	8.01 ± 0.52	28.50 ± 0.27
Sample 39 (Si-free)	317.85	9.3	1.78 ± 0.13	11.7 ± 2.1	8.26 ± 0.70	28.90 ± 0.27
Sample 40 (Si-free)	327.57	9.3	1.90 ± 0.17	12.7 ± 0.4	8.46 ± 0.08	29.56 ± 0.28
Sample 41 (Si-free)	333.75	9.2	1.88 ± 0.17	13.5 ± 1.9	8.46 ± 1.49	29.98 ± 0.28

12.2 Experimental conditions case study I

Table S 3: Experimental conditions and sample dimensions. Numbers in brackets give the standard deviation and refers to the last digit.

	Time	*Solution* volume	*Sample size*			*SA/SV*	*Sample* weight
			Hight	*Length*	*Width*		
	(h)	(cm^3)	(mm)	(mm)	(mm)	(cm^{-1})	(g)
Ex_situ_008d	192	2.5(1)	9.96(1)	4.61(1)	0.99(1)	0.48(3)	0.1137(1)
Ex_situ_031d	744	2.5(1)	9.93(1)	4.67(1)	0.97(1)	0.48(3)	0.1122(1)
Ex_situ_080d	1920	2.5(1)	9.92(1)	4.67(1)	0.98(1)	0.48(3)	0.1134(1)
Ex_situ_166d	3984	2.5(1)	9.93(1)	4.57(1)	0.98(1)	0.48(3)	0.1114(1)
Ex_situ_274d	6576	2.5(1)	9.94(1)	4.21(1)	0.98(1)	0.45(3)	0.1009(1)
In_situ_198d	4776	4.8(1)	8.75(1)	5.40(1)	0.99(1)	0.26(3)	0.1216(1)

12.3 In situ acquired zeolite spectra

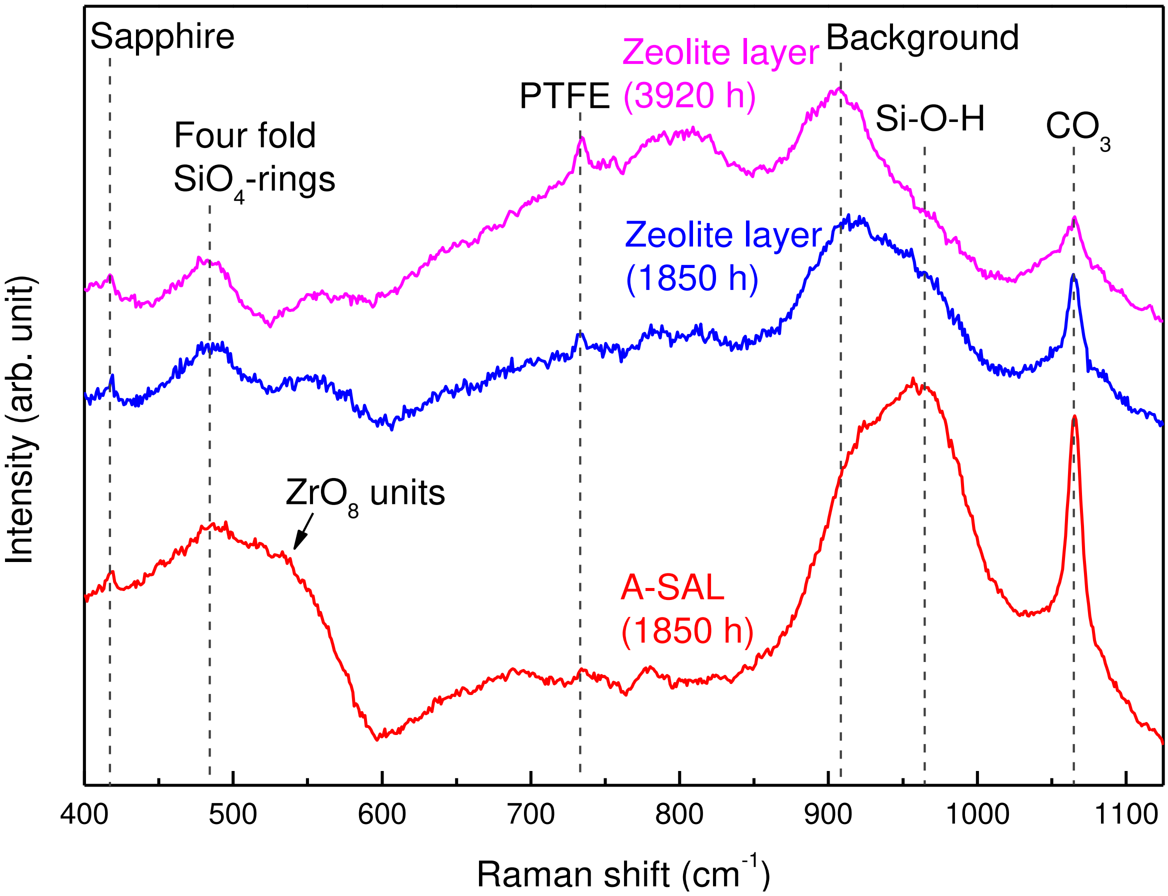

Figure S 1: Representative and corrected zeolite reference spectra acquired *in situ* and *in operando*. The overlap of sapphire band complicates zeolite identification by bands around 420 cm^{-1}. Due to the generally relative bad signal-to-background intensity, it is hard to distinguish between different types of zeolites and other silicates, which is why zeolite identification was performed by *post mortem* Raman analyses.

12.4 Elemental distribution line scans from SEM analysis

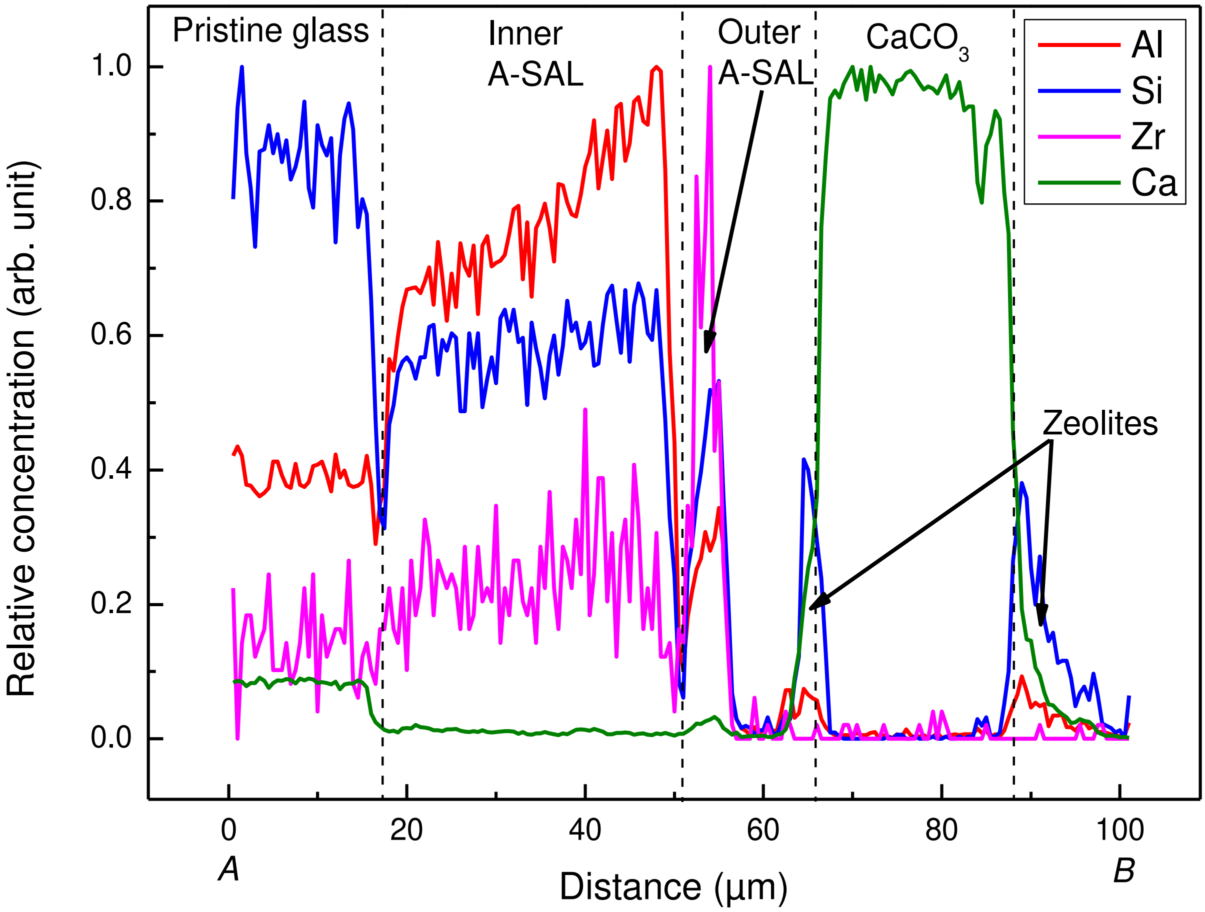

Figure S 2: Relative elemental concentrations crossing the inner and outer am-SAL and secondary phases of sample ISG_A_080 that is shown in Figure 28d (scanning direction is indicated by the location of A and B). The strong Ca enrichment correlates well with the identification of calcite in the BSE image. The $CaCO_3$ grain is covered by zeolites (enclosing Si-peaks). The outer am-SAL is mainly characterized by its high Zr concentration, while the inner am-SAL is more enriched in Al and Si. Note the gradual decrease of Al that probably becomes preferentially incorporated in growing zeolites with proceeding corrosion.

12.5 Glass retreat rate vs. time (ISG, hyperalkaline conditions)

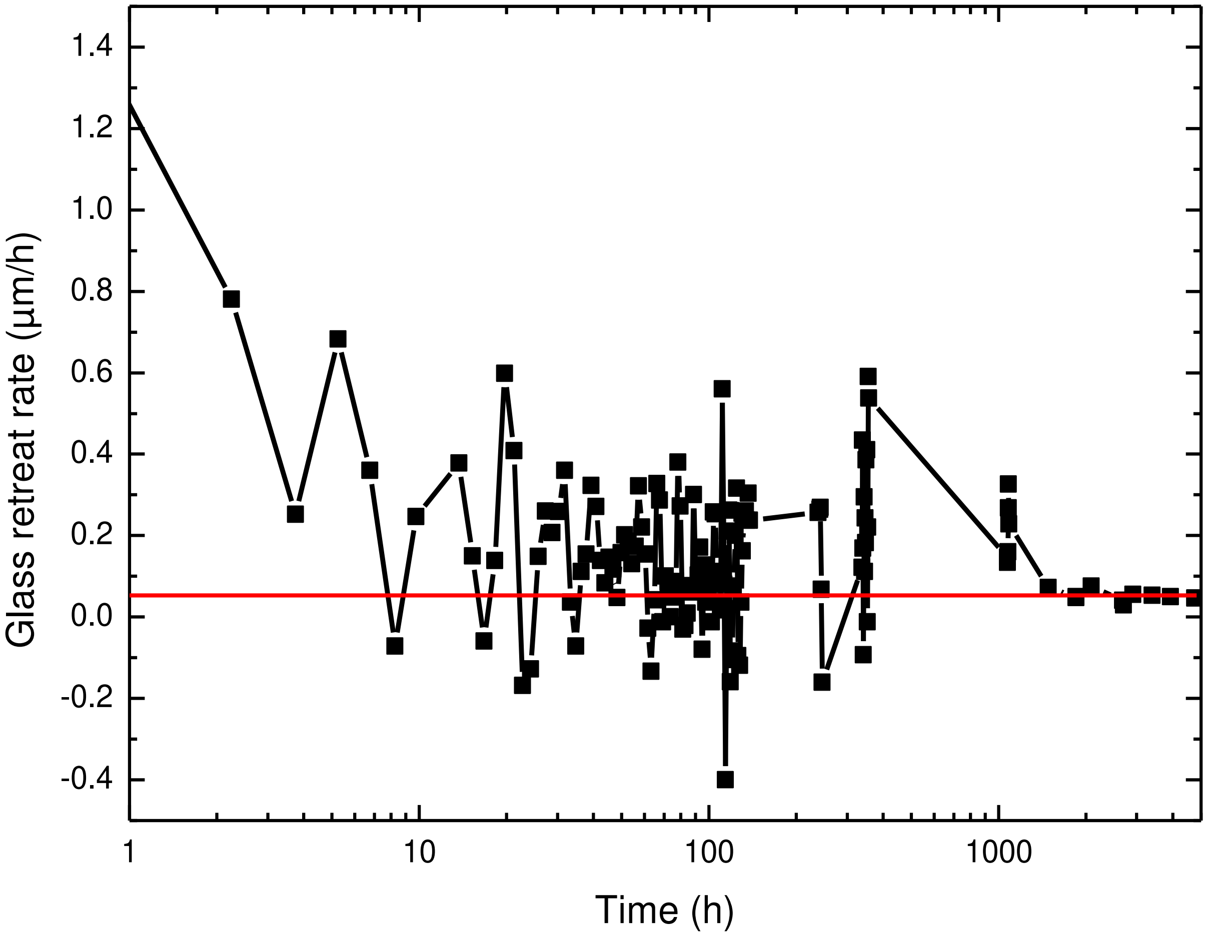

Figure S 3: The diagram shows the glass retreat rate as a function of time, showing a final rate of ~ 0.05 µm/h that is indicated by the red horizontal line. Due to the relatively low dissolution rate compared to the short time differences between the measurements during the Raman measurement sessions, the much higher uncertainty of the determined glass/solution interface values lead to strong scattering around the curve.

12.6 Elemental distribution map (ISG, acidic conditions)

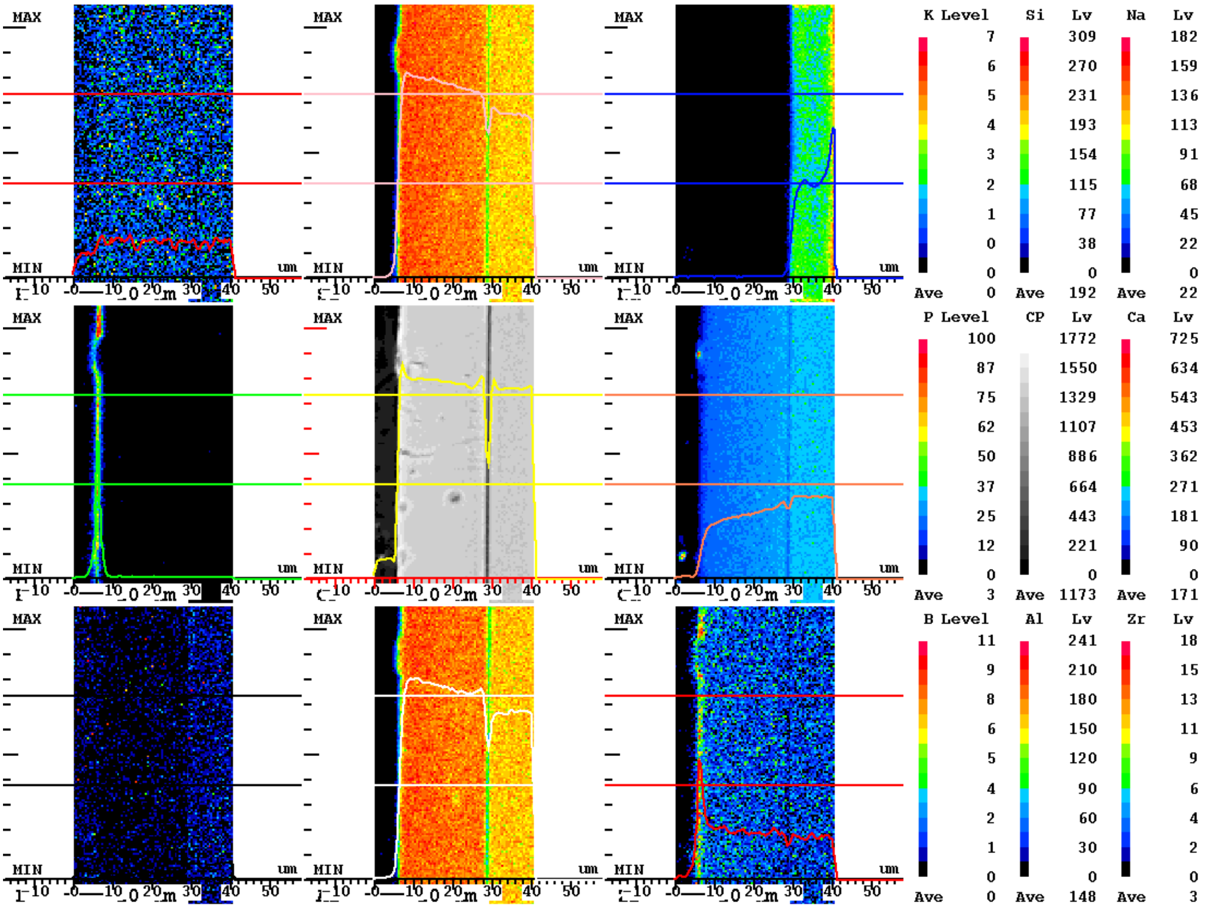

Figure S 4: BSE image and elemental distribution maps (false color images) of an *in situ* ISG sample that was altered in an acidic phosphate solution at ~ 85 °C and revealed an outer Zr and P enriched layer.

12.7 Matlab scripts

12.7.1 Main Code for 1D TBG reaction-diffusion-model

```
clear; clc; clf
% iput data
% Diffusion Coefficients taken from PITZER PHREEQC database
D_B=1.1e-9;               % B(OH)3(m²/s)
D_Na=1.33e-9;             % Na+(m²/s)
D_Si=1.1e-9;              % H4SiO4 (m²/s)
%atomic weight & constants
AW_B=10.811;AW_O=15.9994;AW_Na=22.989769;AW_Si=28.0855;AW_SiO2=AW_Si+AW_O*2;AW_Na2O=
AW_Na*2+AW_O;AW_B2O3=AW_B*2+AW_O*3; % g/mole
Avogadro=6.0221409*10^23;  % Avogadro constant
R=8.314;                  % Gas constant (J*mol^-1*K^-1)
% input data TBG density and composition - Geisler et al., 2019 - Supplement
Density=2.5179;                % g/cm³
mf_SiO2=round(57.9); mf_Na2O=round(19.7); mf_B2O3=round(22.3);      % wt%
% empirical experimental and fitting intput parameters
SI_crit=0.05;
m=0.5;                    % empirical pH factor for dissolution rate equation
Diff_SI_Glass_Silica=0.75;  % Fraction that considers the higher relative solubility of Glass compared to Silica
r0=0.8/60/60;               % forward dissolution rate of TBG (µm/h) based on data of case study III - glass
retreat rate unter flow-through conditions
AE=90;                    % activation energy (kJ/mol)~ 71 to 116 after Lönartz et al.(2019)
T=85;                     % reaction Temperature(°C)
%______________________________________________________________________
% Main Part: Explicit Method for Finite Volume Method (FVM)
NT=20000;                      % Number of time/dissolution steps
t_count_EQ= 25;                 % counter for Equilibration/reaction steps
l_solution=20000;               % 2 cm water surrounding the glass in (µm)
l_glass_ini=1000;               % glass sample thickness (µm)
dx=10;                         % node distance solution (µm)
dy=1;                          % node distance y direction(µm)
dz=1;                          % node distance z direction(µm)
dt=100;                        % timestep size (s)
Cell_volume=dx*dy*dz;                 % Volume of each modeled grid cell (µm³)
SA=dy*dz;                        % interface area cell volumes (µm²)
Solution_Volume_ini=l_solution*dy*dz;   % (µm³)      %4.5*10^12 ;    % (µm³)
Glass_Volume_ini=l_glass_ini*dy*dz;     % (µm³)

N_solution=round(Solution_Volume_ini/Cell_volume); % Number solution cell volumes
N_glass=round(Glass_Volume_ini/Cell_volume);      % Number of glass cell volumes
xL=0;                          % Left Interface (boundary) position(µm)
```

```
xR=N_solution;                    % Right Interface (boundary) position (µm)
N=xR-xL;                          % initial Number of (solution)elements
x=linspace(xL+dx/2,xR-dx/2,N);          % initialize soluction mesh --> equidistant
pH=7;                             % initial pH=7
SI_SiO2_am=zeros(1,N);
T_abs=T+273.15;                   % transformation of °C in K
% Initial conditions
u0=0;                             % convection (µm/s) - set to zero
u=u0*ones(size(x));
t=0;                              % global time record variable
t_count=0;                        % internal time record
c_Si=zeros(1,N); c_Na=zeros(1,N); c_B=zeros(1,N);   % concentration grids
prec_SiO2AM=zeros(1,N);           % matrix to record precipitated silica

% rate input parameters
l_glass=l_glass_ini;
r_l_IF_glass=0; % initialize counter
r_l_IF_glass_total=0; % second initial counter for total length
Record_interface=zeros((NT/t_count_EQ-1),4);
count_total=0; %xounter for Record Prec_growth matrix
Glass_and_solution_cells=zeros(1,(l_glass_ini+l_solution)/dx); % glass and solution cells =0 initialization
Glass_and_solution_cells(1:l_glass_ini/dx)=1; % set glass cells = 1
int_glass_cell=l_glass_ini/dx;                          %glass interface cell tracking
%initialize empty matrizes to record results
record_c_Si=zeros(NT/t_count_EQ,(l_glass_ini+l_solution)/dx);
record_c_Na=zeros(NT/t_count_EQ,(l_glass_ini+l_solution)/dx);
record_c_B=zeros(NT/t_count_EQ,(l_glass_ini+l_solution)/dx);

f_Porosity=0.74048;                      % fraction factor for effective porosity
SI_SiO2_am(1:N)=-99;                     %initial saturation Intex (SI)of SiO2
Count_Diss_Cells=0;
Na_incorporated=0;
EQ_SI_and_pH=zeros(N,2); % initialize results matrix for PHREEQC
% Time loop
for k=1:NT
t=t+dt;                    % Update global time
%__________Glass dissolution___________________
%Dissolution rate and length
r=Dissolution_rate(R,m,SA,r0,pH,AE,T_abs,SI_SiO2_am,Diff_SI_Glass_Silica); % calculate rate (µm/s)
r_l=r*dt;                                                             % Dissolution length (µm)
r_l_IF_glass_total=r_l_IF_glass_total+r_l;              % global total glass dissolution length for recording.
r_l_IF_glass=r_l_IF_glass+r_l;                          % Counter glass dissolution length for interface cell
```

```
if r_l_IF_glass>dx
  r_l_IF_glass=r_l_IF_glass-dx;
% extend mesh by additional solution cell
xR=xR+1;                    % Right Interface (boundary) position (µm)
N=xR-xL;                    % initial Number of (solution)elements for discretization ( )
x=linspace(xL+dx/2,xR-dx/2,N);
Count_Diss_Cells=Count_Diss_Cells+1;
int_glass_cell=int_glass_cell-1;
Glass_and_solution_cells(int_glass_cell+1)=0;
Record_shifts(Count_Diss_Cells)=k*dt/3600;              % time in (h)

%extent solution cell spanwidth
c_Si=horzcat(c_Si,0);c_Na=horzcat(c_Na,0);c_B=horzcat(c_B,0);% add zero Cell at the end
%average last new added cell for stability
c_Si(N)=round(c_Si(N-1)/2);c_Si(N-1)=c_Si(N);c_Na(N)=round(c_Na(N-1)/2);c_Na(N-
1)=c_Na(N);c_B(N)=round(c_B(N-1)/2);c_B(N-1)=c_B(N);
prec_SiO2AM=horzcat(0,prec_SiO2AM); % add zero cell at the front to imitate the interface shift
u=u0*ones(size(x));
else
end
%Dissolved glass constituents
Mass_glass_dissolved=r_l*dy*dz*Density/10^12;           % (g)
% Mass of each oxide
M_SiO2=mf_SiO2/100*Mass_glass_dissolved;M_Na2O=mf_Na2O/100*Mass_glass_dissolved;M_B2O3=mf_B
2O3/100*Mass_glass_dissolved;
% Amount of oxides and  atoms
N_SiO2_M=M_SiO2/AW_SiO2; N_Na2O_M=M_Na2O/AW_Na2O; N_B2O3_M=M_B2O3/AW_B2O3;
N_Si=N_SiO2_M*Avogadro;                % Concentration of Si as H4SiO4 Molecules per cell volume
N_Na=N_Na2O_M*Avogadro*2;              % Concentration of Na as Na+ ions per cell volume
N_B=N_B2O3_M*Avogadro*2;               % Concentration of B as B(OH)3 Molecules per cell volume
% Add dissolved glass constituents into inflow-cell
c_Si(1)=c_Si(1)+N_Si;c_Na(1)=c_Na(1)+N_Na;c_B(1)=c_B(1)+N_B;

%_________Diffusional Transport___________
% Calculate effective Diffusion coefficients
for i=1:length(c_Si)
Porosity= (1-prec_SiO2AM(i)/(Cell_volume*f_Porosity));
if Porosity <= 0
  D_eff_Si(i)=0;
  D_eff_Na(i)=0;
  D_eff_B(i)=0;
else
D_eff_Si(i)=Porosity*D_Si*10^12;     %(µm²/s)
```

```
D_eff_Na(i)=Porosity*D_Na*10^12;     %(µm²/s)
D_eff_B(i)=Porosity*D_B*10^12;       %(µm²/s)
end
end
%Execute diffusional transport function
c_Si=Transport1D(c_Si,u,x,dx,dt,D_eff_Si,0,0);
c_Na=Transport1D(c_Na,u,x,dx,dt,D_eff_Na,0,0);
c_B=Transport1D(c_B,u,x,dx,dt,D_eff_B,0,0);

%_________Precipitation & Growth reaction___
%counter
t_count=t_count+1;
if t_count==t_count_EQ
   t_count=0;
   count_total=count_total+1;      % Counter for precipitation & Growth loop
%  Equilibration and Precipitation & Growth

[prec_SiO2AM_new,c_Si,Record_pg,pH,SI_SiO2_am]=Precipitation_Growth(c_Si,c_Na,c_B,SI_SiO2_am,AW_SiO2,Avogadro,Cell_volume,dy,dz,Count_Diss_Cells,SI_crit,r_l_IF_glass_total);
  prec_SiO2AM= prec_SiO2AM+prec_SiO2AM_new; %Volume in (µm³) of SiO2 amorphous
% Update recors Tables of modeling results
  Record_interface(count_total,1)=k*dt/3600; % time (h)
  Record_interface(count_total,2)=Record_pg;%growth events ==1; precipitation events ==2;
  Record_interface(count_total,3)=r_l_IF_glass_total;% glas dissolution length/position (µm)
  Record_interface(count_total,4)=sum(prec_SiO2AM);% Sum of precipitated SiO2am Vol(µm³)
  Record_interface(count_total,6)=SI_SiO2_am;% interface SI after precip.
  Record_interface(count_total,7)=pH;% interface pH
record_c_Si(count_total,int_glass_cell+1:((l_glass_ini+l_solution)/dx))=c_Si;
record_c_Na(count_total,int_glass_cell+1:((l_glass_ini+l_solution)/dx))=c_Na;
record_c_B(count_total,int_glass_cell+1:((l_glass_ini+l_solution)/dx))=c_B;

else
end
end
```

12.7.2 Script for Diffusional transport in 1D

```
function cnew = Transport1D(c,u,x,dx,dt,D,fL,fR)
N=length(c);
tau=0;                       % initial local time
dtau=0.01;                   % size of internal timesteps
Iter_max=100;                % Iteration to reduce timestep size to reach Neumann stability
```

```
for k=1:Iter_max
Neumann=(dx^2)/2*mean(D); % Neumann stability criterion
    if dtau>Neumann
        dtau=dtau/2;
    else
    end
end
    if dtau>Neumann
'Neumann criterion not fulfilled!'
    else
    end
kmax=dt/dtau+2;
cnew=c;
for k=1:kmax                          %internal timesteps
% Calculate transport - FTCS
for i=1:N                             %For all nodes
if i==1                                %If its the first node --> Boundary
    ucp=(u(i)+abs(u(i)))/2*c(i)+(u(i+1)-abs(u(i+1)))/2*c(i+2); % advection first node (upwind scheme)
    fp=ucp-D(i)/dx*(c(i+1)-c(i));
    fm=fL;
elseif i==N                           %If its the last node --> Boundary
    ucm=(u(i-1)+abs(u(i-1)))/2*c(i-1)+(u(i)-abs(u(i)))/2*c(i); % advection last node (upwind scheme)
    fp=fR;
    fm=ucm-D(i)/dx*(c(i)-c(i-1));
else
    ucp=(u(i)+abs(u(i)))/2*c(i)+(u(i+1)-abs(u(i+1)))/2*c(i+1); % advection in (upwind scheme)
    ucm=(u(i-1)+abs(u(i-1)))/2*c(i-1)+(u(i)-abs(u(i)))/2*c(i); % advection out (upwind scheme
    fp=ucp-D(i)/dx*(c(i+1)-c(i)); % flux in including diffusion
    fm=ucm-D(i)/dx*(c(i)-c(i-1)); % flux out including diffusion
end
cnew(i)=c(i)-dtau/dx*(fp-fm);
end
c=cnew;                               % update concentration for next internatl transport step

tau=tau+dtau;                         % counter for internal time steps
if tau>=dt
    break                              % stop, if global time step was passed by sequentially internal time steps
end
if (tau+dtau>dt)
    dtau=dt-tau;                      % execute last time step to fit the global time step exactly
end
end
if tau<dt                             % if global time step was not reached by limited internal time steps
```

```
    'Not enought internal timesteps!'
end
end
```

12.7.3 Script for TBG dissolution rate law

```
function r_new = Dissolution_rate(R,m,SA,r0,a_pH,AE,T_abs,SI_SiO2_am_ini,Diff_SI_Glass_Silica)
r_new=SA*r0*(a_pH^-m)*exp(-AE/(R*T_abs))*(1-(10^SI_SiO2_am_ini(1))*Diff_SI_Glass_Silica);
if r_new<=0
    r_new=0;                                % Set rate to zero, if it becomes negative
else
end
end
```

12.7.4 Script for amorphous silica precipitation and PHREEQC coupling

```
function                                [prec_SiO2AM_new,c_Si,pH,SI_SiO2_am]                                    =
Precipitation_Growth(c_Si,c_Na,c_B,SI_SiO2_am,AW_SiO2,Avogadro,Cell_volume,SI_crit)
% Precipitation if oversaturated, reduce SI content depending on grade of supersaturation!
Denity_SiO2_Amorphous=2.2;              % (g/cm3)
prec_SiO2AM_new=zeros(1,length(c_Si));

for i=1                                 % set to 1 to just consider the adjacent solution cell
% Calculate solution properties and silica saturation state
% PHREEQC------------------- INITIAL SOLUTION ----------------------------
iphreeqc = actxserver('IPhreeqcCOM.Object');                       % run PHREEQC - COM-Object
iphreeqc.LoadDatabase('C:\Program Files\USGS\phreeqc-3.5.0-14000-x64\database\sit.dat');
iphreeqc.ClearAccumulatedLines;
% Defined special output
iphreeqc.AccumulateLine ('USER_PUNCH')
iphreeqc.AccumulateLine ('-head Spec_Cond');
iphreeqc.AccumulateLine ('PUNCH SC');
% Defined output
iphreeqc.AccumulateLine ('SELECTED_OUTPUT');
iphreeqc.AccumulateLine ('-pe');
iphreeqc.AccumulateLine ('-pH');
iphreeqc.AccumulateLine ('-totals Si');
iphreeqc.AccumulateLine ('-totals Na');
iphreeqc.AccumulateLine ('-totals B');
iphreeqc.AccumulateLine ('-saturation_indices SiO2(am)');
iphreeqc.AccumulateLine ('-equilibrium_phases SiO2(am)');
% Composition input "solution 1"
```

```
iphreeqc.AccumulateLine ('SOLUTION 1');
iphreeqc.AccumulateLine ('-pH 7 charge');          % initial pH
iphreeqc.AccumulateLine ('-temp 21');              % assumed room Temperature
iphreeqc.AccumulateLine ('-units mol/kgw');        % unit
% Concentration in solution cell volume (converted to mol/kgw)
iphreeqc.AccumulateLine (['Si ' num2str(c_Si(1)/Avogadro*1e15/Cell_volume)]);
iphreeqc.AccumulateLine (['Na ' num2str(c_Na(1)/Avogadro*1e15/Cell_volume)]);
iphreeqc.AccumulateLine (['B ' num2str(c_B(1)/Avogadro*1e15/Cell_volume)]);
iphreeqc.AccumulateLine ('REACTION_TEMPERATURE');
iphreeqc.AccumulateLine ('85');                    % reaction temperature
iphreeqc.RunAccumulated;
% get output
out_PHREEQC = iphreeqc.GetSelectedOutputArray;          % output as array
out_PHREEQC_mat=cell2mat(out_PHREEQC(3,7:15));          % convert to math
% Update output parameters of function
pH=out_PHREEQC_mat(1);                        % pH at reaction temperature after dissolution
SI_SiO2_am=out_PHREEQC_mat(8);                    % saturation index of amorphous SI

% precipitation and growht of amorphous silica below critical SI
if  SI_SiO2_am < SI_crit && SI_SiO2_am > 0 && prec_SiO2AM_new(1)> 0 % oversaturation, below critical SI
%PHREEQC------------------  INITIAL SOLUTION  ---------------------------
iphreeqc = actxserver('IPhreeqcCOM.Object');
iphreeqc.LoadDatabase('C:\Program Files\USGS\phreeqc-3.5.0-14000-x64\database\sit.dat');
iphreeqc.ClearAccumulatedLines;
% Defined special output
iphreeqc.AccumulateLine ('USER_PUNCH')
iphreeqc.AccumulateLine ('-head Spec_Cond');
iphreeqc.AccumulateLine ('PUNCH SC');
% Defined output
iphreeqc.AccumulateLine ('SELECTED_OUTPUT');
iphreeqc.AccumulateLine ('-pe');
iphreeqc.AccumulateLine ('-pH');
iphreeqc.AccumulateLine ('-totals Si');
iphreeqc.AccumulateLine ('-totals Na');
iphreeqc.AccumulateLine ('-totals B');
iphreeqc.AccumulateLine ('-saturation_indices SiO2(am)');
iphreeqc.AccumulateLine ('-equilibrium_phases SiO2(am)');
% Composition input "solution 1"
iphreeqc.AccumulateLine ('SOLUTION 1');
iphreeqc.AccumulateLine ('-pH 7 charge');
iphreeqc.AccumulateLine ('-temp 21');
iphreeqc.AccumulateLine ('-units mol/kgw');
iphreeqc.AccumulateLine (['Si ' num2str(c_Si(1)/Avogadro*1e15/Cell_volume)]);
```

```
iphreeqc.AccumulateLine (['Na ' num2str(c_Na(1)/Avogadro*1e15/Cell_volume)]);
iphreeqc.AccumulateLine (['B ' num2str(c_B(1)/Avogadro*1e15/Cell_volume)]);
iphreeqc.AccumulateLine ('REACTION_TEMPERATURE');
iphreeqc.AccumulateLine ('85');
iphreeqc.AccumulateLine ('EQUILIBRIUM_PHASES');
iphreeqc.AccumulateLine (['SiO2(am) ' num2str(SI_SiO2_am/2) ' 0']); % Calculate amount of precipitating
amorphous silica to half the current SI
iphreeqc.RunAccumulated;
% get output
out_PHREEQC = iphreeqc.GetSelectedOutputArray;
out_PHREEQC_mat=cell2mat(out_PHREEQC(2:3,9));
% transforming dissolved silicic acid into amorphous silica
c_Si_Delta=(out_PHREEQC_mat(1,1)-out_PHREEQC_mat(2,1))*Avogadro/1e15*Cell_volume;  % calculate
de Si difference for growth driven reduction
prec_SiO2AM_new(1)=c_Si_Delta/Avogadro*AW_SiO2/Denity_SiO2_Amorphous*10^12;  % calculate the
volume of formed amorphous silica
c_Si(1)= c_Si(1)-c_Si_Delta;          % execute Si concentration reduction due to growth of amorphous silica
pH=cell2mat(out_PHREEQC(3,7));                      % pH after precipitation and growth
SI_SiO2_am=cell2mat(out_PHREEQC(3,14));        % saturation index of amorphous SI after precipitation
and growth
% precipitation and growht of amorphous silica above critical SI
elseif SI_SiO2_am >= SI_crit   % supersaturation exceeds critical oversaturation level = burst nucleation
% PHREEQC------------------  INITIAL SOLUTION  ---------------------------
iphreeqc = actxserver('IPhreeqcCOM.Object');
iphreeqc.LoadDatabase('C:\Program Files\USGS\phreeqc-3.5.0-14000-x64\database\sit.dat');
iphreeqc.ClearAccumulatedLines;
% Defined special output
iphreeqc.AccumulateLine ('USER_PUNCH')
iphreeqc.AccumulateLine ('-head Spec_Cond');
iphreeqc.AccumulateLine ('PUNCH SC');
% Defined output
iphreeqc.AccumulateLine ('SELECTED_OUTPUT');
iphreeqc.AccumulateLine ('-pe');
iphreeqc.AccumulateLine ('-pH');
iphreeqc.AccumulateLine ('-totals Si');
iphreeqc.AccumulateLine ('-totals Na');
iphreeqc.AccumulateLine ('-totals B');
iphreeqc.AccumulateLine ('-saturation_indices SiO2(am)');
iphreeqc.AccumulateLine ('-equilibrium_phases SiO2(am)');
% Composition input "solution 1"
iphreeqc.AccumulateLine ('SOLUTION 1');
iphreeqc.AccumulateLine ('-pH 7 charge');
iphreeqc.AccumulateLine ('-temp 21');
```

```
iphreeqc.AccumulateLine ('-units mol/kgw');
iphreeqc.AccumulateLine (['Si ' num2str(c_Si(1)/Avogadro*1e15/Cell_volume)]);
iphreeqc.AccumulateLine (['Na ' num2str(c_Na(1)/Avogadro*1e15/Cell_volume)]);
iphreeqc.AccumulateLine (['B ' num2str(c_B(1)/Avogadro*1e15/Cell_volume)]);
iphreeqc.AccumulateLine ('REACTION_TEMPERATURE');
iphreeqc.AccumulateLine ('85');
iphreeqc.AccumulateLine ('EQUILIBRIUM_PHASES');
iphreeqc.AccumulateLine (['SiO2(am) ' num2str(SI_SiO2_am(1)/10) ' 0']);
iphreeqc.RunAccumulated;
% get output
out_PHREEQC = iphreeqc.GetSelectedOutputArray;
out_PHREEQC_mat=cell2mat(out_PHREEQC(2:3,7:14));
% transforming dissolved silicic acid into amorphous silica
c_Si_Delta=(out_PHREEQC_mat(1,3)-out_PHREEQC_mat(2,3))*Avogadro/1e15*Cell_volume;   % calculate de Si difference for precipitation driven reduction
prec_SiO2AM_new(1)=c_Si_Delta/Avogadro*AW_SiO2/Denity_SiO2_Amorphous*10^12;  % calculate the volume of precipitation driven formed amorphous silica
c_Si(1)= c_Si(1)-c_Si_Delta;                                   % execute Si concentration reduction due to precipitation of amorphous silica
pH=cell2mat(out_PHREEQC(3,7)); % pH after precipitation and growth
SI_SiO2_am=cell2mat(out_PHREEQC(3,14)); % saturation index of amorphous SI after precipitation and growth
else
end
end
end
```

Danksagung

Zunächst möchte ich mich bei allen Personen bedanken, die mich im Laufe der Zeit bei der Erstellung der Dissertation auf unterschiedlichste Weise unterstützt haben und die Qualität dieser Dissertation durch konstruktive Kritik und spannende Diskussionen gesteigert haben.

Mein größter Dank gilt meinem Doktorvater Thorsten Geisler-Wierwille, der mir die Promotion ermöglicht und mich mit seiner Begeisterung für das Thema sofort angesteckt hat. Er hatte immer ein offenes Ohr für fachliche Fragen, hat mir bei der Umsetzung des Vorhabens zur Seite gestanden und befähigte mich gleichzeitig durch ausreichend Freiraum, eigene Wege zu gehen, neue Ideen zu entwickeln und selbstständig umzusetzen.

Auch möchte ich meiner Zweitgutachterin Prof. Dr. Boriana Mihailova und den weiteren Mitgliedern der Promotionskommission Prof. Dr. Christian März und Prof. Dr. Wulf Amelung danken.

Ebenfalls möchte ich mich herzlich bei der SCHOTT AG und dem Otto Schott-Fonds bedanken, welche das Forschungsprojekt finanziert haben, in dessen ich meine Dissertation anfertigen konnte. Insbesondere Peter Nass und Detlef Köpsel möchte ich für ihr Engagement und die fachlichen Diskussionen danken.

Ferner möchte ich mich bei Christoph Lenting, Lars Dohmen, Gerrit Müller und Mara Lönartz bedanken, welche mich bei der Umsetzung meiner experimentellen Arbeiten und bei der Interpretation der Ergebnisse direkt und indirekt unterstützt haben. Markus Lagos danke ich für die Hilfe bei der Durchführung und Auswertung von ICP-MS-Analysen und Alexander Ziegler für die Unterstützung bei den µCT-Analysen.

Dieter Lülsdorf, Philipp Krämer, Henrik Blanchard danke ich für die Unterstützung bei der technischen Weiterentwicklung der *in situ* Flüssigzelle und Nils Jung für die Probenpräparationen. Ich möchte mich auch bei Daniela Bungartz und Dagmar Hambach für ihre tolle Arbeit im Sekretariat bedanken.

Besonders danke ich Nicole für ihre Geduld und Unterstützung auf der langen Zielgeraden und meinen Eltern, die mir ermöglicht haben, mich frei für ein Studium zu entscheiden und meine Begeisterung für die Wissenschaft zu entdecken.